Effective Field Theories for Metallic Quantum Critical Points

Effective Field Theories for Metallic Quantum Critical Points

By

SHOUVIK SUR, M.Sc.

A Thesis
Submitted to the School of Graduate Studies
in Partial Fulfillment of the Requirements
for the Degree Doctor of Philosophy

McMaster University

DOCTOR OF PHILOSOPHY, Department of Physics and Astronomy, McMaster University (2015), Hamilton, Ontario.

TITLE: Effective Field Theories for Metallic Quantum Critical Points

AUTHOR: Shouvik Sur, M. Sc. (McMaster University)

SUPERVISOR: Dr. Sung-Sik Lee

NUMBER OF PAGES: xiv, 113

ABSTRACT

In this thesis we study the scaling properties of unconventional metals that arise at quantum critical points using low-energy effective field theories. Due to high rate of scatterings between electrons and critical fluctuations of the order parameter associated with spontaneous symmetry breaking, Landau's Fermi liquid theory breaks down at the critical points. The theories that describe these critical points generally flow into strong coupling regimes at low energy in two space dimensions. Here we develop and utilize renormalization group methods that are suitable for the interacting non-Fermi liquids. We focus on the critical points arising at excitonic, and commensurate spin and charge density wave transitions. By controlled analyses we find stable non-Fermi liquid and marginal Fermi liquid states, and extract the scaling behaviour. The field theories for the non-Fermi liquids are characterized by symmetry groups, local curvature of the Fermi surface, the dispersion of the order parameter fluctuations, and dimensions of space and Fermi surface.

ACKNOWLEDGEMENTS

I thank my thesis adviser, Dr. Sung-Sik Lee, for his continual guidance, support, and kindness. The sheer novelty of his ideas, the intellectual bravery while pursuing them, and the ability to summon a diverse range of theoretical tools to aid the attacks on a problem are truly inspirational. However, the most important lesson that I imbibed from my association with Sung-Sik is to be a benevolent and patient mentor and teacher. Indeed, I have been very fortunate to have had his tutelage.

As a graduate student I benefited greatly from the courses taught by both Dr. Catherine Kallin and Dr. Cliff Burgess. They have also been on my supervisory committee, and have extended their support and encouragement over the years. I'm grateful for their contribution to my intellectual growth, and their guidance with my thesis work. I would also like to thank Rajatda and Dr. Murthy for their support and encouragement for close to a decade.

As I aged through my 20's, I have progressively realized the extent of sacrifice many parents make for their children. I'm fortunate to have such parents. I thank them for having faith in my aspirations, always standing by me and respecting my choices. Indeed I owe much of who I am to my early education, particularly to the trysts of my mother to provide me with the best education she could manage, and to the unceasing and unconditional love of my grandmother.

After leaving the comfort of the company of one's parents, it becomes important to form healthy friendships. Over the years I have been blessed with invaluable friends. I thank all who have generously extended their camaraderie, and have been great companions and, sometimes

unwitting teachers. Particularly, I would like to express my gratitude (in no particular order) to Rajesh, Prasanna, Rahulda, Shilo, Satyada, Arindamda, Ayush, Jayanth, Pramod, Bhanu, Arghya, Peter, Walid, Sedigh, Wen, Andreas, Laura, Mark, Meng, Xin, Subhroda, Kunal, Prajyot, Shreya, Saeed, Nilesh, Manraj, Bapon, Pikluda, Papaida, and Tuluda. Besides friends, I have been fortunate to have found many elements of a home-away-from-home in the hospitality of Boudi and Rajatda. Through my years in Hamilton, I have deeply treasured their kindness.

It is an incredible experience to have the company of someone who simply holds one's hand, and together set out on an undefined path. The entirety of my graduate school coincided with the evolution of the most important bond of my life. Riya has been the pillar around whom I have tried to find my love for intellectual engagements. For that, to her, I supplicate my sincerest gratitude.

Subscribing to an institution comes with its many requirements and paperwork, all of which have been made hassle-free by the excellent staff in the departmental office. I thank them for their patience and helpfulness over all the years I spent at McMaster.

PREFACE

This is a sandwich thesis based on three publications, which appear in the following order:

- **Chapter 2**

  S. Sur and S.-S. Lee, *Quasilocal strange metal*, Phys. Rev. B **91**, 125136 (2015).

  (DOI: `http://dx.doi.org/10.1103/PhysRevB.91.125136`)

- **Chapter 3**

  S. Sur and S.-S. Lee, *Anisotropic Non-Fermi Liquids*, to be submitted.

- **Chapter 4**

  S. Sur and S.-S. Lee, *Chiral non-Fermi liquids*, Phys. Rev. B **90**, 045121 (2014).

  (DOI: `http://dx.doi.org/10.1103/PhysRevB.90.045121`)

The first and the last papers are reprints of prior publications in Physical Review B, and appear with the permission of American Physical Society.

Shouvik Sur performed most of the computations and prepared the initial drafts. Sung-Sik Lee provided guidance and edited the drafts. Both authors participated in the discussions that shaped the contents in these papers.

TABLE OF CONTENTS

LIST OF TABLES

TABLE **Page**

LIST OF FIGURES

FIGURE **Page**

CHAPTER 1

INTRODUCTION

In a private communication to William Miller[1], Thomas Andrews reported [1],

> On partially liquefying carbonic acid by pressure alone, and gradually raising at the same time the temperature to 88° Fahr., the surface of demarcation between the liquid and gas became fainter, lost its curvature, and at last disappeared ...

In the letter Andrews introduced the term 'critical point' to describe the temperature and pressure at which visible demarcation between the gas and the liquid disappeared. However, it was not until his Bakerian lecture in 1869 that a full exposition of the critical point was provided. In the appropriately titled lecture [1], he showed that the discontinuous change in density accompanying the transition from liquid to gaseous state in carbonic acid disappeared when pressure was increased at temperatures higher than 87.7° F (30.92° C). Appearance of the continuous transition was accompanied by emergence of a fluid state which was neither purely gaseous nor liquid, but a fusion of the two. At the critical point, the fluid attained a new state of matter where the density fluctuated at all length scales, resulting in a critical opaqueness. Andrews's work was important, not only because it clarified the nature of the

[1] A summary of the letter was published in the third edition of Miller's *Chemical Physics* in 1863.

continuous transition that remained ill-understood since its discovery in 1822[2], but it also motivated subsequent theoretical advances, most notably the foundational works on critical phenomena by Josiah Willard Gibbs [2], Johannes Diderik van der Waals [3] and Pierre Weiss [4].

Although our understanding and characterization of critical phenomena have evolved extensively over the years, a central tenet that remains intact is the concept of universality. Since the earliest works on liquid-gas transition and ferromagnetism, it was realized that disparate systems can behave identically while undergoing continuous phase transitions, and the universal behaviour can be characterized by a handful of parameters. Although earlier works utilized the presence of universality, it was not until Lev Landau's work on λ-point transition in ^4He, in 1937, that the role of universality was clearly demonstrated [5, 6]. Landau noted the similarity of the equation of states for fluids (Van der Waals equation) and ferromagnets (Weiss's molecular field hypothesis) near respective critical points, and postulated that the underlying common structure holds for all continuous phase transitions. In his theory of phase transitions, Landau introduced *order parameters* to describe macroscopic degrees of freedom that distinguishes one phase from another. It also provided the guiding principles for subsequent developments in critical phenomena by emphasizing the role played by symmetry in determining the physical properties near critical points. Landau's theory of phase transition is the culmination of the mean-field based approach to continuous phase transition, where interactions between individual degrees of freedom in a system are replaced by a fictitious global potential or mean-field. The order parameters in Landau's theory are treated as rigid objects within the mean-field theory.

The success of mean-field theory was challenged by Lars Onsagar's exact solution of the two dimensional Ising model in 1949: the critical exponents derived from the exact solution deviated strongly from the predictions of all antecedent theories of continuous phase transition.

[2] Cagniard de la Tour first reported such a continuous transition in 1822. In subsequent years a number of people worked on this novel state of matter, including Faraday and Mendeleev.

It was subsequently realized that the deviation originates from the importance of thermal fluctuations near the critical point. The key role played by (thermal) fluctuations in the vicinity of a critical point necessitated the development of a new paradigm for studying continuous phase transitions, where effects of fluctuations are systematically incorporated. Thus, from a historical perspective, Onsagar's work was an watershed event in the field of critical phenomena, which separates the 'modern era' from the 'classical era' [7]. While the (mean-field) theories of the classical era considered the critical system as static, with or without spatial modulation of the order parameter, the modern approaches view the critical system as a dynamical entity, where the fluctuations of the order parameter play a central role.

A remarkable property of Landau's theory of phase transition is that it contains "the seeds of its own destruction" [8]. It is indeed possible to estimate the condition of applicability of Landau's theory, within its own framework. This condition is expressed by the *Ginzburg criterion* [9, 10], which states that when the ratio $\frac{\left|\int_V d^d\vec{r}\, G(\vec{r})\right|}{\int_V d^d\vec{r}\, \phi_0^2(\vec{r})} \gtrsim 1$, Landau's theory breaks down due to the dominance of order parameter fluctuations. Here V is the correlation volume, $G(\vec{r})$ is the two-point correlation function which encapsulates the magnitude of fluctuations of the order parameter, and $\phi_0(\vec{r})$ is the expectation value of the order parameter in the symmetry broken phase. A systematic study of the effects of fluctuations became possible only after the development of *renormalization group* (RG) techniques starting with the works of Leo Kadanoff in 1966 [11] and Kenneth Wilson in 1971 [12, 13]. Following these early works on the application of RG for understanding the effects of fluctuations, substantial progress has been made in the identification and classification of various critical points based on symmetries[3] and spacetime dimensions.

In 1970's a new kind of continuous phase transition, called *quantum phase transition* (QPT), came to focus through the works of Masuo Suzuki [16], M. T. Béal-Monod [17], and John A. Hertz [18]. QPTs are brought about by tuning non-thermal parameters such as magnetic

[3]Continuous phase transitions are possible between phases that are not distinguished by local symmetries, giving rise to *deconfined critical points* [14]. Although, deconfined critical points in itinerant systems maybe achieved upon doping [15], we do not consider these in this thesis.

field, pressure, doping, etc., at zero temperature. At the ensuing *quantum critical points* (QCPs) the fluctuations of the order parameter arise due to the non-commuting nature of quantum mechanical observables. QCPs can exist only at $T = 0$, because thermal fluctuations present at $T > 0$ tend to suppress quantum effects due to the loss of phase coherence between various quantum mechanical components of the system

QPTs in insulators are reasonably well understood and can be studied through conventional effective field theories [19]. However, QPTs in metals have proven challenging to analyze systematically, particularly due to the presence of extensive gapless modes near the Fermi surface[4]. In this thesis we focus on metallic criticality, and uncover three classes of novel metallic states that describe the respective QCPs. At the critical points, the strong fluctuations of the order parameter invalidates the Fermi liquid theory. In the rest of this chapter we will briefly outline the key properties of Landau's Fermi liquid theory, which is the canonical theory of metals, and discuss general aspects of metallic QCPs, where Fermi liquid theory is inapplicable.

1.1 Fermi Liquid Theory

It is often difficult to deduce the low energy properties of an interacting many-body system from its microscopic description. However, the low energy properties of the complicated microscopic model can be understood with relatively greater ease in terms of a simpler effective theory. Landau formulated such an effective theory for a large class of metals [21, 22], that reproduces the low energy properties of electrons in the presence of screened Coulomb interaction. This low energy description of electrons in metals came to be known as the *Fermi liquid theory*.

Landau's theory of Fermi liquids postulates the presence of excitations called *quasiparticles*, which carry the same quantum numbers as the non-interacting electrons, but have a finite

[4] Criticalities in metals with Fermi points are comparatively better understood. However, they still exhibit novelties that are missed by the traditional Hertz-Millis type description [20].

lifetime $\propto \left|\vec{k}-\vec{k}_F\right|^{-2}$, which increases as the momenta of the quasiparticles ($\vec{k}$) approaches the Fermi momentum ($\vec{k}_F$). Close to the Fermi surface the lifetime of a quasiparticle is much larger than the timescale associated with its de Broglie wavelength which $\sim \left|\vec{k}-\vec{k}_F\right|^{-1}$. Therefore, the quasiparticles in the vicinity of the Fermi surface may be considered as stable particles, similar to the non-interacting electrons. In fact, according to Fermi liquid theory, excitations in the interacting system bear a one-to-one correspondence to their non-interacting counterparts. When a bare electron is introduced in the ground state of N electrons, the resultant state has a finite overlap with the exact eigenstate with $N+1$ electrons [23],

$$\left|\Psi_{N+1}(\vec{k})\right\rangle = \sqrt{Z_k}\; c^\dagger(\vec{k})\,|\Psi_N\rangle + \ldots, \tag{1.1}$$

where $|\Psi_N\rangle$ is the N-particle ground state of the interacting electrons[5], $\left|\Psi_{N+1}(\vec{k})\right\rangle$ is an eigenstate with $N+1$ electrons with momentum $\vec{k}$, and $c^\dagger(\vec{k})$ is the creation operator for the bare electron. Z_k is the quasiparticle amplitude or weight, which is the overlap between bare electrons and quasiparticles. The ellipses at the end of Eq. (1.1) represents incoherent multiparticle excitations made up of electrons and holes. In the absence of interactions, $Z_k = 1$ and the terms represented by '…' are absent. An effect of interaction is to render $Z_k < 1$, at the cost of introducing a cloud of particle-hole excitations. As long as $Z_k > 0$, the quasiparticles remain sharply defined at the Fermi surface, and consequently, Fermi liquid theory retains its validity. A non-zero Z_k also implies that the states in the non-interacting system are adiabatically connected to the states in the interacting system[6].

Since Landau's proposal, Fermi liquid theory has been established as the low energy effective theory of interacting electrons at finite density through explicit diagrammatic computations [25] and RG methods [26, 27]. Because of its congruence with the content of this thesis, we focus on the latter approach and briefly outline the basis of validity of Fermi liquid theory.

[5]The spin indices are omitted in Eq. (1.1) in order to simplify notation.

[6] This is analogous to the fate of the eigenstates of a free particle in a box as a weak quadratic potential is turned on [24].

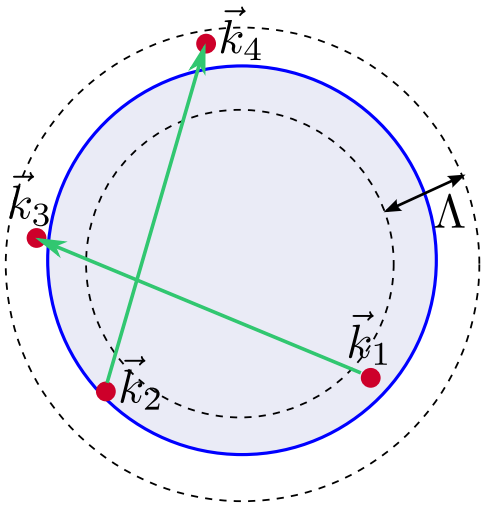

Figure 1.1: Schematic of electron-electron scatterings, as implied by Eq. (1.2), around a Fermi surface in the presence of an energy cutoff Λ. The solid circle is the Fermi surface, while the broken ones are energy cutoff contours. The small filled disks represent electronic states with momenta $\vec{k}_i$.

For electrons at finite density the low energy states lie close to the Fermi surface, such that the Wilsonian RG procedure involves coarse-graining towards the entire Fermi surface by lowering the energy cutoff Λ, as shown in Fig. 1.1. The short-range interaction among the electrons leads to the interaction vertex,

$$S_I = \int dk_1\, dk_2\, dk_3\, dk_4\, u(\hat{k}_i)\; \psi^*_\sigma(k_3)\psi^*_{\sigma'}(k_4)\psi_{\sigma'}(k_2)\psi_\sigma(k_1)\; \delta(k_1+k_2-k_3-k_4), \qquad (1.2)$$

where $dk \equiv \dfrac{dk_0 d^d\vec{k}}{(2\pi)^{d+1}}$. $u(\hat{k}_i)$ is the strength of four-fermion interaction, which is a function of the angular positions, $\hat{k}_i$, of the momenta $\vec{k}_i$. $\psi_\sigma(k)$ are electronic modes carrying spin σ, with momenta within the shell enclosed by the broken lines in Fig. 1.1. As Λ decreases, the phase space restriction weakens all scattering channels, except the forward and the Bardeen-Cooper-Schrieffer (BCS) [28, 29] channels. Thus, in the limit $\dfrac{\Lambda}{|\vec{k}_F|} \to 0$, only the scattering processes shown in Fig. 1.2 survive [26].

Through a one-loop analysis, it can be shown that the forward scattering channel is exactly marginal, while the BCS channel is either marginally relevant or irrelevant depending on the sign of its bare value [26, 27]. In particular, if it is negative at tree level, then the BCS channel

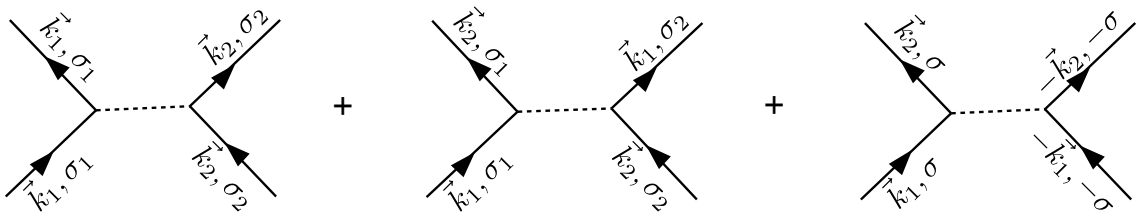

Figure 1.2: Dominant scattering channels in the low energy limit. The first two constitute the forward scattering, while the third is the BCS channel. Here we have introduced the spin index, σ_i, to distinguish between the two forward scattering channels. For spinless fermions they are identical.

grows logarithmically, eventually resulting in the BCS instability of the Fermi liquid.

Some of the key signatures of a Fermi liquid are obtained from the low temperature scaling behavior of its thermodynamic and transport properties. In particular, the resistivity $\rho = \rho_0 + AT^2$, specific heat $C_v = \gamma T$, spin susceptibility $\chi \sim \chi_0$, zero temperature compressibility $\kappa \sim \kappa_0$, etc., where $\rho_0, A, \gamma, \chi_0, \kappa_0$ are constants at low temperature [30]. Their violation indicates a breakdown of Fermi liquid theory, usually due to inapplicability of its defining assumptions.

1.2 Beyond Fermi Liquid Theory

Is the Fermi liquid the most general metallic state? Our experience with one dimensional itinerant systems suggests otherwise. In one space dimension, a generic metallic state is described by the Tomonaga-Luttinger liquid (TLL) [31–34], which lacks Landau quasiparticles. Instead the collective excitations in a TLL are independently propagating spin and charge waves, which result in spin-charge separation. Although spin-charge separation has long motivated the search for metallic states in higher dimensions that lie beyond the Fermi liquid paradigm, so far there has been no concrete experimental realization. However, there are numerous experimental signatures of exotic metallic states that lie beyond Fermi liquid theory.

1.2.1 General Strategy

A key assumption in Fermi liquid theory is the short range of the electron-electron interactions. The assumption holds for the Thomas-Fermi screened electrostatic interaction in metals, but is generally invalid. Interestingly, long-range interactions are already present in all metals. The current-current or Amperean interaction between electrons is not completely screened by electron-hole excitations, and remains long-ranged. Indeed, electronic interactions due to the transverse component of the electromagnetic field eventually leads to a breakdown of Fermi liquid theory[7], through the vanishing of the quasiparticle weight on the Fermi surface [35, 43]. The Amperean interaction arising from scatterings between electrons and the electromagnetic field requires very low temperatures to have significant effect on observable properties of the metal due to the small hyperfine constant. The non-Fermi liquid behavior due to the Amperean interactions has not been observed yet, because metals usually undergo transitions into a superconducting state at much higher temperature.

In order to find *non-Fermi liquids* (NFLs), we need to focus on other scenarios where long range interaction between electrons is present. These scenarios can be broadly classified into two categories: *critical phases* and *critical points*. A critical phase refers to an extended region in the zero temperature phase diagram where a gapless bosonic mode is present. Examples of critical phases include fermions such as spinons, etc., interacting with an emergent gauge field ($U(1)$, $SU(2)$, etc.) [35, 43–49], and symmetry broken itinerant systems where the generators

[7] Although, distinct deviation from Fermi liquid behavior was theoretically deduced as far back as 1973 [35], it did not garner much attention owing to the very low temperatures required for such deviations to become apparent. However, the situation changed markedly following the discovery of high temperature superconductivity in 1986 [36], specifically after the discovery of a linear-T resistivity in the metallic phase right above the superconducting phase at dopings where the highest transition temperatures (T_c) are realized [37, 38]. The inability of BCS theory to account for the high T_c, and discovery of similar anomalous metallic states in heavy-fermion compounds in 1991 [39] and iron pnictides in 2008 [40–42], further motivated the study of the anomalous metallic states whose properties do not follow from Fermi liquid theory. An interesting common thread that putatively unites the copper and iron based superconductors, and the heavy fermion compounds is the proximity of one or several QCPs to the region in the, respective, phase diagrams where deviations from Fermi liquid theory is observed. Therefore, an approach towards describing these non-Fermi liquid properties is to seriously consider the finite temperature effects of QCPs, which can extend to temperature scales that are far higher than the transition temperature of the superconducting phase that often covers the QCPs.

of the broken symmetry group does not commute with the momentum operators [50]. In the latter case, the Goldstone modes, associated with the broken continuous symmetry, provides the necessary gapless boson[8].

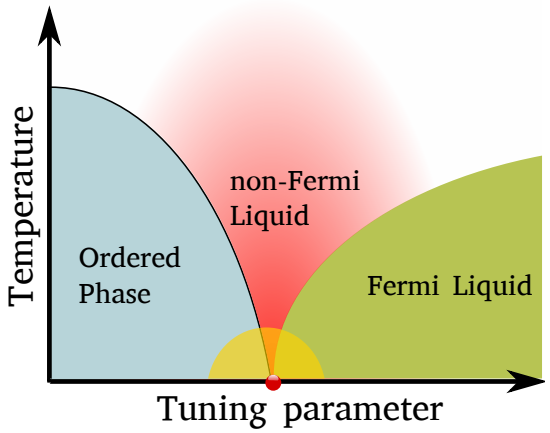

Figure 1.3: Schematic of the phase diagram in the presence of a symmetry breaking phase transition in a metal. The x-axis represents a non-thermal tuning parameter such as pressure, doping, or magnetic field, which drives the QPT. The (red) dot on the x-axis is the QCP, which may itself be unstable and remain hidden under a dome of a new stable phase. In spite of the instability, the QCP can affect the finite temperature properties in a fan shaped region that extends well beyond the dome. Thus, if a NFL state is realized at the QCP, the critical fan exhibits non-Fermi liquid scaling.

$\vec{Q}_{ord} = 0$	$\vec{Q}_{ord} \neq 0$
• Ferromagnetic	• Spin density wave
• Nematic	• Charge density wave
• Excitonic	

Table 1.1: The two subcategories of critical points.

A critical point, in contrast, is an isolated point on the zero temperature phase diagram where the critical fluctuations of an order parameter gives rise to a long-range interaction among electrons. Such critical points commonly arise at continuous QPTs in Fermi liquids, where

[8] Usually, the spatial modulation of Goldstone modes couple (derivative coupling) with electron density, which makes the interaction ineffective at low energies.

characteristic energy scales [9] vanish at the critical point (see Fig. 1.3). Critical points are further divided into two subcategories depending on the presence or absence of spatial modulation in the ordered state, which is expressed in terms of the ordering wave vector $\vec{Q}_{ord}$. In Table 1.1 we list a few examples of critical points that are classified according to the magnitude of $\vec{Q}_{ord}$.

1.2.2 Review of Earlier Works

Since the discovery of NFL properties in cuprate superconductors [37, 38], many theoretical works have addressed the issues concerning the origin and properties of NFL physics. The literature being extensive, in this subsection I attempt to provide a brief summary of those works that are most relevant to this thesis.

In the presence of long-range interaction between electrons, it is convenient to think in terms of the electrons and a gapless boson, where the boson mediates the long-range interaction between electrons. The electron-boson vertex is of the Yukawa form: $g\ \phi\psi^{\dagger}\psi$, where g is the interaction strength, and ϕ and ψ represent the boson and the electrons, respectively. The Yukawa vertex is relevant at the Gaussian fixed point in two space dimensions; consequently, the theory flows into strong coupling regime, where $g \sim 1$. Therefore, a perturbation series cannot be organized in powers of g.

In an attempt to control the theory, $1/N$ expansion has been used, where N represents the number of fermionic flavors [45, 46, 51]. The underlying motivation is that in a bath of a very large number of fermions the fluctuation of the boson would be subleading, such that in the large N limit the theory would closely resemble the $g = 0$ limit. However, following the work of Sung-Sik Lee [52] it became clear that the large N limit is not perturbatively controlled [53, 54].

Pursuing a different strategy, Chetan Nayak and Frank Wilczek showed that it is possible

[9] The energy scale on the symmetry broken side, such as the Néel temperature, is associated with a thermal transition into the symmetry broken state, while the energy scale on the Fermi liquid side is associated with the inverse correlation length of the order parameter fluctuations.

to obtain a controlled, perturbative NFL fixed point in two space dimensions by modifying the dispersion of the boson as $|\vec{q}|^2 \mapsto |\vec{q}|^{1+\varepsilon}$ [48, 55]. This modification, although non-local, helps in controlling the quantum fluctuations by reducing the low energy density of states of the boson. In the small ε limit it is also possible to have a well defined large N expansion as long as $\varepsilon N \sim 1$ and $N \gg 1$ [56]. Although promising, the introduction of non-locality is undesirable, since non-local terms remain unrenormalized within perturbative RG analysis, which is an artifact of the regularization procedure [57]. Denis Dalidovich and Sung-Sik Lee developed an analogous strategy based on the reduction of low energy density of states of the fermions by embedding the Fermi surface in a higher dimensional space [58]. An attractive feature of this strategy is that it preserves locality. However, it requires the introduction of a superconducting or charge density wave state with p-wave symmetry. The presence of an additional symmetry breaking state in the weak coupling limit may obscure its connection to the original strongly interacting theory. Nevertheless, as long as the symmetries on the plane of the one dimensional Fermi surface are intact in the weak coupling limit, it may be possible to obtain controlled understanding of the two dimensional theory.

1.2.3 Outline of the Thesis

The works presented in this thesis were initiated after the discovery of the failure of $1/N$ expansion at metallic criticality, which led to the development and usage of novel RG schemes that are tuned towards theories with extended Fermi surfaces. In the first two papers, which are the subjects of Chapters 2 and 3, respectively, we establish the existence of weak coupling NFL states at $\vec{Q}_{ord} \neq 0$ critical points near three dimensions. These states are shown to be perturbatively connected to marginal Fermi liquids (MFL) [59] in three dimensions. In Chapter 4 we present the third paper, where we study a representative case for $\vec{Q}_{ord} = 0$ critical point within the *one-patch theory* (to be defined in the same chapter). We develop a real-space RG scheme to non-perturbatively prove that a strong coupling NFL state is realized at the infrared

fixed point in two space dimensions.

Because we rely on RG to guide us to the properties of the critical points, our interpretations are based on scaling arguments. We deduce that the states realized at the fixed points are NFLs if quasiparticles are ill-defined. Two signatures that can independently invalidate the existence of quasiparticles are,

- the dynamical critical exponent, which measures the relative scaling of time with respect to a fixed spatial direction, being greater than one;
- the electron fields developing an anomalous scaling dimension.

In both cases, the electron propagator contains branch cuts, which implies the absence of quasiparticle poles on the complex frequency plane. For concreteness, let us consider a general

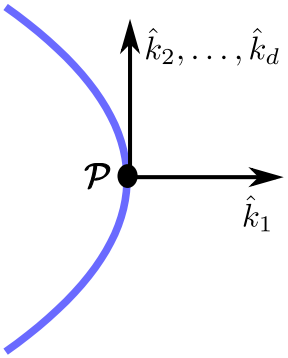

Figure 1.4: The setup for the local coordinates at a point $\mathscr{P}$ (filled circle) on the Fermi surface. The blue curve is the Fermi surface, and the arrows represent the coordinate system. The tangent plane at point $\mathscr{P}$ is spanned by $\{\hat{k}_2, \ldots, \hat{k}_d\}$, while $\hat{k}_1$ points along the normal at $\mathscr{P}$.

scaling form of an electron propagator in a d dimensional metal,

$$G(k_0, k_1, \ldots, k_d) = \frac{1}{k_1^{1-2\widetilde{\eta}_\psi}} \mathscr{G}\left(\frac{k_0^{1/z_0}}{k_1}, \frac{k_2^{1/z_2}}{k_1}, \ldots, \frac{k_d^{1/z_d}}{k_1} \right), \tag{1.3}$$

where k_0 is Euclidean frequency, and $k_1, \ldots, k_d$ are the d components of momentum measured from a point $\mathscr{P}$ on the Fermi surface (see Fig. 1.4). Here k_1 points along the normal to the Fermi surface, while $k_2, \ldots, k_d$ lie on the tangent plane to the Fermi surface at $\mathscr{P}$, as shown in Fig.

1.4. The exponent $\widetilde{\eta}_\psi$ is the anomalous scaling dimension of the electrons, $\mathscr{G}(y_0, y_2, \ldots, y_{d-1})$ is a universal function, z_0 is the dynamical critical exponent, and $z_2, \ldots, z_d$ encapsulate spatial anisotropy. Here we have elected to measure the scaling dimension of various quantities with respect to k_1.

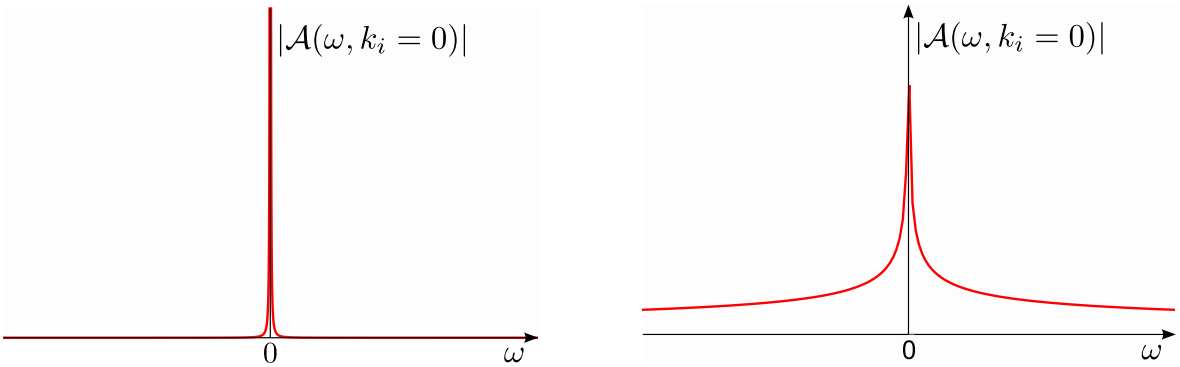

Figure 1.5: Spectral function on the Fermi surface. (a) Fermi liquid with $0^+ \equiv 10^{-12}$ and (b) NFL in Eq. (1.8).

For Fermi liquids with a $d-1$ dimensional Fermi surface, $\widetilde{\eta}_\psi = 0$, $z_0 = 1$, and $z_i = 1/2$. At low energy, $\varepsilon(k) \equiv k_1 + \sum_{i>1} k_i^2$ is the energy of the single-particle excitations. Therefore, the simplest possible expression of G in this case is,

$$G(k_0, k_1, \ldots, k_d) = \frac{1}{ik_0 - \varepsilon(k)}, \tag{1.4}$$

which leads to the well known expression for the spectral function

$$\mathscr{A}(\omega, \vec{k}) \equiv -\frac{1}{\pi} \operatorname{Im}\left[G(k_0 \mapsto -i\omega + 0^+, k_1, \ldots, k_d)\right] \tag{1.5}$$

$$= \delta(\omega - \varepsilon(k)), \tag{1.6}$$

implying particle like excitations whenever the frequency $\omega = \varepsilon(k)$. In contrast, for a NFL with $\widetilde{\eta}_\psi = 0$, $z_0 > 1$, and $z_i = 1/2$,

$$G(k_0, k_1, \ldots, k_d) = \frac{1}{i\operatorname{sgn}(k_0)\,|k_0|^{1/z_0} - \varepsilon(k)}, \tag{1.7}$$

which leads to (using Eq. (1.5))

$$\mathscr{A}(\omega,\vec{k}) = \frac{1}{\pi}\,\frac{\lambda_2\ \mathrm{sgn}\,(\omega)\,|\omega|^{1/z_0}}{\left(\lambda_1 \mathrm{sgn}\,(\omega)\,|\omega|^{1/z_0} - \varepsilon(k)\right)^2 + \lambda_2^2 |\omega|^{2/z_0}}, \tag{1.8}$$

where

$$\lambda_1 = \cos\left(\frac{\pi(z_0-1)}{2z_0}\right), \quad \text{and} \quad \lambda_2 = \sin\left(\frac{\pi(z_0-1)}{2z_0}\right). \tag{1.9}$$

$\mathscr{A}(\omega,\vec{k})$ in Eq. (1.8) has a power law singularity as a function of ω on the Fermi surface ($k_i = 0$), which implies an absence of particle-like excitations. Therefore, the well defined quasiparticles are absent when the dynamical critical exponent $z_0 > 1$. In Fig. 1.5 we show the contrasting behavior of the spectral function for a Fermi liquid and the NFL in Eq. (1.7).

CHAPTER 2

ANTIFERROMAGNETIC CRITICAL POINT IN ISOTROPIC METALS

Certain metallic compounds can be turned into an antiferromagnet by changing pressure or the density of electrons. In order to described the physics near the phase transition, it is important to identify whether the antiferromagnetic state is due to local moments as in a Mott insulator state [49, 60, 61], or it arises from the modulation of the spin polarization of the itinerant electrons, i.e. spin density waves [62]. Here we study the latter scenario and describe the QCP of a Fermi liquid to spin density wave transition through a perturbative RG analysis.

2.1 (Co)Dimensional Regularization

In the works presented in this chapter and the next, we use a novel regularization scheme that was developed by Dalidovich and Lee in the context of nematic QCP [58]. Because of the importance of this technique to the rest of the thesis, we outline its key properties in this section.

This perturbative RG scheme is motivated by the need to develop a controlled effective

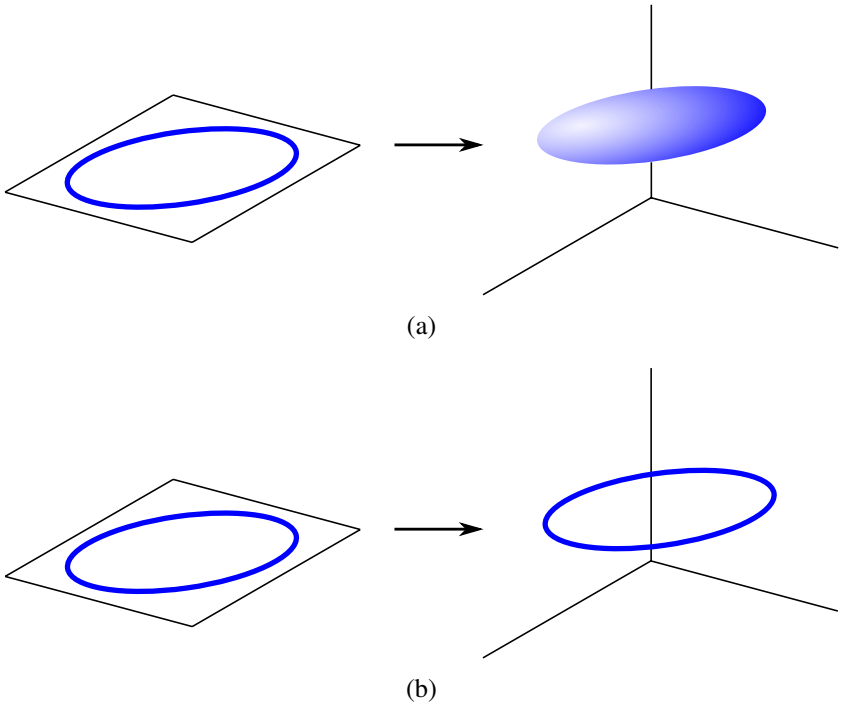

Figure 2.1: Two ways of increasing the spatial dimension of a two dimensional system with a one dimensional Fermi surface. (a) Increasing the dimension of the Fermi surface. (b) Increasing the codimension of the Fermi surface.

theory for theories with Fermi surfaces in the presence of a critical bosonic mode. Perturbative control of quantum fluctuations is achieved by increasing the space dimensions in which the theory is defined. In the presence of a Fermi surface this can be achieved in two ways (also see Fig. 2.1),

- increasing the dimension of the Fermi surface [63, 64], or
- increasing the dimensions orthogonal (codimensions) to the Fermi surface [65].

We take the latter path for two reasons,

1. increasing the codimensions reduces the electronic density of states, which suppresses intervening instabilities like superconductivity, thereby providing perturbative control at lowest energy;

(a) (b)

Figure 2.2: Comparison between the sets of 'hot' electrons that strongly couples to the critical fluctuations of a density wave order parameter. The broken line ending in arrows represents the momentum carried by the order parameter. (a) A Fermi line coupled to the critical fluctuations. The red (blue) dots (ellipse) represent(s) the hotspots (Fermi surface). (b) A Fermi surface coupled to the critical fluctuations. The red (blue) ellipses (ellipsoid) represent(s) the hot manifolds (Fermi surface).

2. Fermi surfaces with dimensions greater than one contain extended submanifolds that remain strongly coupled with the critical fluctuations (see Fig. 2.2). This introduces a new energy scale, which qualitatively modifies the low energy properties compared to those in two space dimensions.

The codimensions of the Fermi surface is extended in the following way starting from the two dimensional theory,

1. Construct Dirac spinors out of antipodal points on the Fermi surface and rewrite the two dimensional theory in the spinor basis[1].

2. Generalize the theory to d dimensions by adding $d-2$ codimensions.

3. Apply dimensional regularization to derive the beta functions and the critical exponents within the minimal subtraction scheme near the upper critical dimension.

Here the deviation from the upper critical dimension plays the role of the small parameter, in terms of which the perturbation theory is organized.

[1]Changing the representation aids in maintaining locality. This is a crucial step that distinguishes the current construction from earlier attempt by Senthil and Shankar [65].

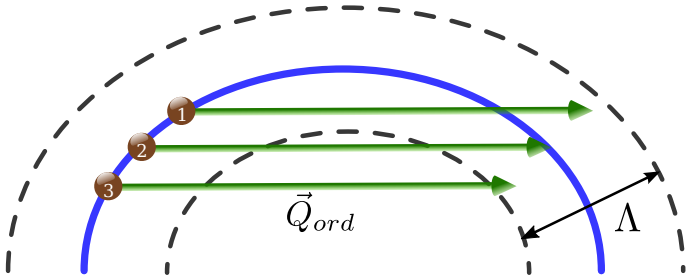

Figure 2.3: Prominence of hotspots at low energy. The solid curve is a segment of a Fermi surface, the broken curves are UV cutoff contours for the electrons, the (green) arrow represents the momentum of the order parameter ($\vec{Q}_{ord}$), and the (brown) filled circles represent distinct points on the Fermi surface. For large enough Λ, the order parameter fluctuations can scatter electrons from all three points 1, 2, and 3. However, as $\Lambda \to 0$ only electrons in a small neighborhood of point 2 can be scattered by the order parameter. Thus, point 2 becomes a hotspot at low energy.

2.2 Preface

Since the spin density wave (SDW) order parameter carries a finite momentum ($\vec{Q}_{ord} \neq 0$) in the ordered phase, its critical fluctuations scatter electrons whose momenta differ by $\vec{Q}_{ord}$. At high energy the order parameter fluctuations scatter electrons, both, on and away from the Fermi surface as shown in Fig. 2.3. However, as energy is reduced, scatterings of electrons away from the Fermi surface are suppressed, such that in the low energy limit, for Fermi surfaces without nested segments, only a few points on the Fermi surface remain coupled through the fluctuations of the order parameter. These points are called *hotspots*, as they are most strongly affected by the critical fluctuations at low energy.

The *spin-fermion model* is a minimal model that describes the interactions between the electrons at the hotspots and the critical fluctuations of the SDW order parameter [66, 67]. In spite of its simplicity, the low energy properties of the two dimensional spin-fermion model remains ill-understood owing to the absence of a well defined perturbative limit. In this work we develop a systematic expansion in $\varepsilon = 3 - d$ within the dimensional regularization scheme discussed earlier. By deriving the one-loop beta functions, we show that below three dimensions a *quasilocal* NFL state is realized at the critical point, where the fluctuations of the

order parameter become localized on the plane of the Fermi surface, and the Fermi surface gets nested at the hotspots. The one-loop fixed point becomes exact in three dimensions, where the quasilocal NFL gives way to a quasilocal marginal Fermi liquid state.

Because of depleted density of states near the Fermi surface, superconductivity is suppressed at the fixed point. However, we do obtain enhancements of a number of pairing and density wave susceptibilities, pointing towards the possibility of competing instabilities of the NFL close to two dimensions.

Quasilocal strange metal

Shouvik Sur[1] and Sung-Sik Lee[1,2]
[1]*Department of Physics & Astronomy, McMaster University, 1280 Main St. W., Hamilton ON L8S 4M1, Canada*
[2]*Perimeter Institute for Theoretical Physics, 31 Caroline St. N., Waterloo ON N2L 2Y5, Canada*
(Received 31 August 2014; revised manuscript received 26 January 2015; published 23 March 2015)

One of the key factors that determine the fates of quantum many-body systems in the zero temperature limit is the competition between kinetic energy that delocalizes particles in space and interaction that promotes localization. While one dominates over the other in conventional metals and insulators, exotic states can arise at quantum critical points where none of them clearly wins. Here we present a class of metallic states that emerge at an antiferromagnetic (AF) quantum critical point in the presence of one-dimensional Fermi surfaces embedded in space dimensions three and below. At the critical point, interactions between particles are screened to zero in the low-energy limit and at the same time the kinetic energy is suppressed in certain spatial directions to the leading order in a perturbative expansion that becomes asymptotically exact in three dimensions. The resulting *dispersionless* and *interactionless* state exhibits distinct quasilocal strange metallic behaviors due to a subtle dynamical balance between screening and infrared singularity caused by spontaneous reduction of effective dimensionality. The strange metal, which is stable near three dimensions, shows enhanced fluctuations of bond density waves, *d*-wave pairing, and pair density waves.

DOI: 10.1103/PhysRevB.91.125136 PACS number(s): 71.10.Hf, 74.40.Kb, 11.10.Gh

I. INTRODUCTION

The richness of exotic zero-temperature states in condensed matter systems [1,2] can be attributed to quantum fluctuations driven by kinetic energy and interaction, which can not be simultaneously minimized due to the uncertainty principle. In conventional metals, the kinetic energy plays the dominant role, and interactions only dress electrons into quasiparticles which survive as coherent excitations in the absence of instabilities [3,4]. The existence of well defined quasiparticle excitations is the cornerstone of Landau Fermi liquid theory [5], which successfully explains a large class of metals. However, the Fermi liquid theory breaks down at the verge of spontaneous formation of order in metals [6–8]. Near continuous quantum phase transitions, new metallic states can arise as quantum fluctuations of the order parameter destroy the coherence of quasiparticles through interactions that persist down to the zero-energy limit [9,10]. A systematic understanding of the resulting strange metallic states is still lacking, although there exist some examples whose universal behaviors in the low-energy limit can be understood within controlled theoretical frameworks [11–15].

Antiferromagnetic (AF) quantum phase transition commonly arises in strongly correlated systems including electron doped cuprates [16], iron pnictides [17], and heavy fermion compounds [18]. In two space dimensions, it has been shown that the interactions between the AF mode and itinerant electrons qualitatively modify the dynamics of the system at the critical point [19,20]. A recent numerical simulation shows a strong enhancement of superconducting correlations near the AF critical point [21]. However, the precise nature of the putative strange metallic state has not been understood yet due to a lack of theoretical control over the strongly coupled theory that governs the critical point [22].

In this paper, based on a controlled expansion, we show that a novel quantum state arises at the AF quantum critical point in metals that support a one-dimensional Fermi surface through a nontrivial interplay between kinetic energy and interactions. To the lowest order in the perturbative expansion that becomes asymptotically exact at low energies in three dimensions, we find that quasiparticles are destroyed even though the interaction between electrons and the AF mode is screened to zero in the low-energy limit. This unusual behavior is possible as the system develops an infinite sensitivity to the interaction through the kinetic energies that become dispersionless in certain spatial directions. The dynamical balance between vanishing kinetic energy and interactions results in a stable *quasilocal strange metal*, which supports incoherent single-particle excitations and enhanced correlations for various competing orders.

II. MODEL AND DIMENSIONAL REGULARIZATION

We first consider two space dimensions. Although the specific lattice is not crucial for the following discussion, we consider the square lattice with the nearest and next-nearest neighbor hoppings. For electron density close to half-filling (one electron per site), the system supports a Fermi surface, shown in Fig. 1. The minimal theory that describes the AF critical point in a two-dimensional metal includes the collective AF fluctuations that are coupled to electrons near the hot spots, which are the set of points on the Fermi surface connected by the AF wave vector [19,20,22]. In this paper, we consider the collinear AF order with a commensurate wave vector that is denoted as arrows in Fig. 1. If the AF order is incommensurate or noncollinear, the critical theory is modified from the one for the collinear AF order with a commensurate wave vector. As will be shown later, the simplest case we consider here already has quite intricate structures.

The action for the commensurate AF mode and the electrons near the hot spots reads

$$\mathcal{S} = \sum_{n=1}^{4}\sum_{m=\pm}\sum_{\sigma=\uparrow,\downarrow}\int \frac{d^3k}{(2\pi)^3}\psi^{(m)*}_{n,\sigma}(k)\big[ik_0 + e^m_n(\vec{k})\big]\psi^{(m)}_{n,\sigma}(k) + \frac{1}{2}\int \frac{d^3q}{(2\pi)^3}\big[q_0^2 + c^2|\vec{q}|^2\big]\vec{\phi}(-q)\cdot\vec{\phi}(q) + g_0\sum_{n=1}^{4}\sum_{\sigma,\sigma'=\uparrow,\downarrow}\int \frac{d^3k}{(2\pi)^3}$$
$$\times\frac{d^3q}{(2\pi)^3}[\vec{\phi}(q)\cdot\psi^{(+)*}_{n,\sigma}(k+q)\vec{\tau}_{\sigma,\sigma'}\psi^{(-)}_{n,\sigma'}(k) + \text{c.c.}] + \frac{u_0}{4!}\int \frac{d^3k_1}{(2\pi)^3}\frac{d^3k_2}{(2\pi)^3}\frac{d^3q}{(2\pi)^3}[\vec{\phi}(k_1+q)\cdot\vec{\phi}(k_2-q)][\vec{\phi}(k_1)\cdot\vec{\phi}(k_2)]. \quad (1)$$

Here, $k = (k_0,\vec{k})$ denotes frequency and the two-dimensional momentum $\vec{k} = (k_x,k_y)$. $\psi^{(\pm)}_{n,\sigma}$'s are fermionic fields, which represent electrons of spin $\sigma = \uparrow,\downarrow$ near the hot spots labeled by $n = 1,2,3,4$, $m = \pm$, as is shown in Fig. 1. The axis in momentum space has been chosen such that the AF wave vector becomes $\vec{Q}_{\rm AF} = \pm\sqrt{2}\pi\,\hat{y} = \pm\sqrt{2}\pi\,\hat{x}$ up to the reciprocal vectors $\sqrt{2}\pi(\hat{x}\pm\hat{y})$. In this coordinate, the energy dispersions of the fermions near the hot spots can be written as $e^{\pm}_1(\vec{k}) = -e^{\pm}_3(\vec{k}) = vk_x \pm k_y$, $e^{\pm}_2(\vec{k}) = -e^{\pm}_4(\vec{k}) = \mp k_x + vk_y$, where $\vec{k}$ represents deviation of momentum away from each hot spot. It is noted that the local curvature of the Fermi surface can be ignored because the k-linear terms dominate at low energies. The component of Fermi velocity parallel to $\vec{Q}_{\rm AF}$ at each hot spot is set to be unity up to the sign by rescaling $\vec{k}$. v measures the component of the Fermi velocity perpendicular to $\vec{Q}_{\rm AF}$. If v was zero, the hot spots connected by $\vec{Q}_{\rm AF}$ would be perfectly nested. $\vec{\phi}(q)$ represents the three components of the boson field, which describes the fluctuating AF order parameter carrying frequency q_0 and momentum $\vec{Q}_{\rm AF}+\vec{q}$. $\vec{\tau}$ represents the three generators of the SU(2) group. c is the velocity of the AF collective mode. g_0 is the Yukawa coupling between the collective mode and the electrons near the hot spots, and u_0 is the quartic coupling between the collective modes. v, c, g_0, and u_0 are genuine parameters of the theory, which can not be removed by a redefinition of the momentum or fields.

In two dimensions, the perturbative expansion in g_0, u_0 fails because the couplings grow rapidly as the length scale is increased under the renormalization group (RG) flow. Although the growth of the couplings is tamed by screening,

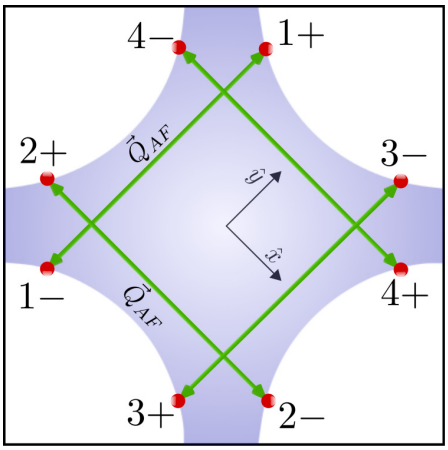

FIG. 1. (Color online) A two-dimensional Fermi surface where the shaded (unshaded) region represents occupied (unoccupied) states in momentum space. The hot spots on the Fermi surface are denoted as (red) dots. The (green) arrows represent the AF wave vector $\vec{Q}_{\rm AF}$.

it is hard to follow the RG flow because the flow will stop (if it does) outside the perturbative window. In higher dimensions, the growth of the couplings becomes slower. Therefore we aim to tune the space dimension such that the balance between the slow growth of the couplings and the screening stabilizes the interacting theory at weak coupling. Here, we increase the co-dimension of the Fermi surface while fixing its dimension to be one. A mere increase of co-dimension of the Fermi surface introduces a nonlocality in the kinetic energy [23]. In order to keep the locality of the theory, we introduce two-component spinors [14], by combining fermion fields on opposite sides of the Fermi surface, $\Psi_{1,\sigma} = (\psi^{(+)}_{1,\sigma},\psi^{(+)}_{3,\sigma})^T$, $\Psi_{2,\sigma} = (\psi^{(+)}_{2,\sigma},\psi^{(+)}_{4,\sigma})^T$, $\Psi_{3,\sigma} = (\psi^{(-)}_{1,\sigma},-\psi^{(-)}_{3,\sigma})^T$, $\Psi_{4,\sigma} = (\psi^{(-)}_{2,\sigma},-\psi^{(-)}_{4,\sigma})^T$ and writing the kinetic term of the fermions as $S_0 = \sum_{n=1}^{4}\sum_{\sigma=\uparrow,\downarrow}\int\frac{d^3k}{(2\pi)^3}\bar{\Psi}_{n,\sigma}(k)[i\gamma_0k_0 + i\gamma_1\varepsilon_n(\vec{k})]\Psi_{n,\sigma}(k)$, where $\gamma_0 = \sigma_y,\gamma_1 = \sigma_x$, $\bar{\Psi}_{n,\sigma} = \Psi^{\dagger}_{n,\sigma}\gamma_0$ with $\varepsilon_1(\vec{k}) = e^+_1(\vec{k})$, $\varepsilon_2(\vec{k}) = e^+_2(\vec{k})$, $\varepsilon_3(\vec{k}) = e^-_1(\vec{k})$, $\varepsilon_4(\vec{k}) = e^-_2(\vec{k})$. Now we add $(d-2)$ extra dimensions, which are perpendicular to the Fermi surface. We also generalize the SU(2) group to SU(N_c), and introduce N_f flavors of fermion to write a general theory,

$$\mathcal{S} = \sum_{n=1}^{4}\sum_{\sigma=1}^{N_c}\sum_{j=1}^{N_f}\int dk\bar{\Psi}_{n,\sigma,j}(k)[i\mathbf{\Gamma}\cdot\mathbf{K} + i\gamma_{d-1}\varepsilon_n(\vec{k})]$$
$$\times\Psi_{n,\sigma,j}(k) + \frac{1}{4}\int dq[|\mathbf{Q}|^2 + c^2|\vec{q}|^2]\text{Tr}[\Phi(-q)\Phi(q)]$$
$$+ i\frac{g\mu^{(3-d)/2}}{\sqrt{N_f}}\sum_{n=1}^{4}\sum_{\sigma,\sigma'=1}^{N_c}\sum_{j=1}^{N_f}\int dkdq[\bar{\Psi}_{\bar{n},\sigma,j}(k+q)$$
$$\times\Phi_{\sigma,\sigma'}(q)\gamma_{d-1}\Psi_{n,\sigma',j}(k)] + \frac{\mu^{3-d}}{4}\int dk_1dk_2dq$$
$$\times\{u_1\text{Tr}[\Phi(k_1+q)\Phi(k_2-q)]\text{Tr}[\Phi(k_1)\Phi(k_2)]$$
$$+ u_2\text{Tr}[\Phi(k_1+q)\Phi(k_2-q)\Phi(k_1)\Phi(k_2)]\}. \quad (2)$$

Here, $dk \equiv \frac{d^{d+1}k}{(2\pi)^{d+1}}$ and $k = (\mathbf{K},\vec{k})$ is $(d+1)$-dimensional vector. $\vec{k} = (k_x,k_y)$ represents the original two-dimensional momentum and $\mathbf{K} = (k_0,k_1,\ldots,k_{d-2})$ includes frequency and momentum components along the $(d-2)$ new directions present in $d > 2$. $(\mathbf{\Gamma},\gamma_{d-1})$ with $\mathbf{\Gamma} = (\gamma_0,\gamma_1,\ldots,\gamma_{d-2})$ represent $(d-1)$-dimensional gamma matrices that satisfy the Clifford algebra, $\{\gamma_\mu,\gamma_\nu\} = 2I\delta_{\mu\nu}$ with $\text{Tr}[I] = 2$. $\Psi_{n,\sigma,j}$ with $\sigma = 1,2,\ldots,N_c$ and $j = 1,2,\ldots,N_f$ is in the fundamental representation of SU(N_c) spin group and SU(N_f) flavor group. $\Phi(q) = \sum_{a=1}^{N_c^2-1}\phi^a(q)\tau^a$ is a matrix field where τ^a's are the SU(N_c) generators with $\text{Tr}[\tau^a\tau^b] = 2\delta^{ab}$. In the Yukawa interaction, $(n,\bar{n})$ represent pairs of hot spots connected by $\vec{Q}_{\rm AF}$: $\bar{1} = 3,\bar{2} = 4,\bar{3} = 1,\bar{4} = 2$. μ is an energy

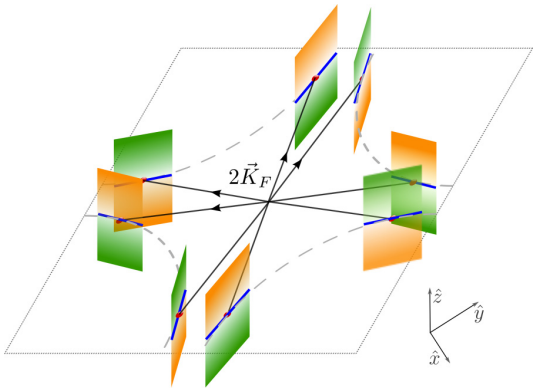

FIG. 2. (Color online) One-dimensional Fermi surfaces embedded in the three-dimensional momentum space. The locally flat patches of two-dimensional Fermi surface near the hot spots are gapped out by the p_z-wave charge density wave carrying momentum $2\vec{k}_F$ except for the line nodes at $k_z = 0$.

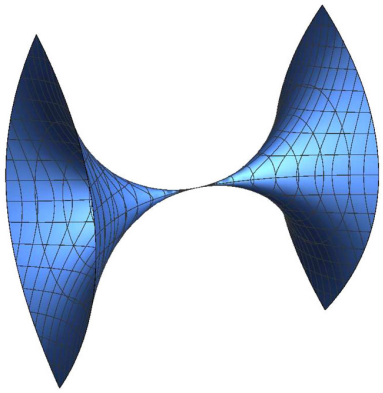

FIG. 3. (Color online) A patch of Fermi surface created by a p_z-wave CDW with momentum $2\vec{k}_F$. The center of the patch is pinched due to the CDW order that vanishes linearly in p_z. If the antiferromagnetic order parameter connects the pinched points, the low-energy effective theory for the critical point becomes Eq. (2) in three dimensions.

scale introduced for the Yukawa coupling and the quartic couplings, which have the scaling dimensions $(3-d)/2$ and $(3-d)$, respectively. For $N_c \leqslant 3$, $\mathrm{Tr}[\Phi^4] = \frac{1}{2}(\mathrm{Tr}[\Phi^2])^2$ and u_2 is not an independent coupling. In this case, it is convenient to set $u_2 = 0$ without loss of generality. For $N_c \geqslant 4$, however, u_1 and u_2 are independent, and one should keep both of them. It is straightforward to check that Eq. (1) is reproduced from Eq. (2) once we set $d = 2$, $N_c = 2$, and $N_f = 1$.

The action supports one-dimensional Fermi surfaces embedded in d-dimensional momentum space. The fermions have energy $E_n(k_1,\ldots,k_{d-2},\vec{k}) = \pm\sqrt{\sum_{i=1}^{d-2} k_i^2 + [\varepsilon_n(\vec{k})]^2}$, which disperses linearly in the $(d-1)$-dimensional space perpendicular to the line node defined by $k_i = 0$ for $1 \leqslant i \leqslant d-2$ and $\varepsilon_n(\vec{k}) = 0$. To understand the physical content of the dimensional regularization, it is useful to consider the theory at $d = 3$. With the choice of $(\gamma_0,\gamma_1,\gamma_2) = (\sigma_y,\sigma_z,\sigma_x)$ and identifying $k_1 = k_z$, the kinetic energy for $\Psi_{1,\sigma}$ and $\Psi_{3,\sigma}$ is written as $H_0 = (vk_x \pm k_y)[\psi^{(\pm)*}_{1,\sigma,j}\psi^{(\pm)}_{1,\sigma,j} - \psi^{(\pm)*}_{3,\sigma,j}\psi^{(\pm)}_{3,\sigma,j}] \mp k_z[\psi^{(\pm)*}_{1,\sigma,j}\psi^{(\pm)}_{3,\sigma,j} + h.c.]$. The kinetic energy for $\Psi_{2,\sigma}$ and $\Psi_{4,\sigma}$ can be obtained by 90° rotation. The first term gives patches of the locally flat two-dimensional Fermi surface. The second term describes a p_z-wave charge density wave (CDW) that gaps out the two-dimensional Fermi surface to leave line nodes at $k_z = 0$, as is shown in Fig. 2. The full action in Eq. (2) describes the AF transition driven by electrons near the hot spots on the line nodes.

We emphasize that Eq. (2) is not just a mathematical construction. The theory in three space dimensions can arise at the AF quantum critical point in the presence of p_z-wave CDW of momentum $2\vec{k}_F$. If local curvature of the underlying Fermi surface is included, the dispersion near a pair of points on the Fermi surface connected by the momentum $2\vec{k}_F$ can be written as $\epsilon_\pm(\vec{k}) = \pm k_x + \gamma_1 k_y^2 + \gamma_2 k_z^2$, where k_x is chosen to be perpendicular to the Fermi surface, and γ_i represent the local curvatures of the Fermi surface. The p_z-wave CDW leads to the spectrum $\mathcal{E}$, which is determined by $\begin{vmatrix} k_x + \gamma_1 k_y^2 + \gamma_2 k_z^2 - \mathcal{E} & k_z \\ k_z & -k_x + \gamma_1 k_y^2 + \gamma_2 k_z^2 - \mathcal{E} \end{vmatrix} = 0$. This results in a pinched Fermi surface located at $\gamma_1 k_y^2 + \gamma_2 k_z^2 = \sqrt{k_x^2 + k_z^2}$ as is shown in Fig. 3. If the antiferromagnetic ordering wave vector connects the pinched points, the low-energy effective theory for the phase transition is precisely described by Eq. (2) in three dimensions. Because the curvature is irrelevant at low energies, the pinched Fermi surfaces can be regarded as Fermi lines near the hot spots. A similar field theory can also arise at an orbital selective antiferromagnetic quantum critical point in a three-dimensional semimetal as is discussed in Appendix A.

The action in general dimensions respects the U(1) charge conservation, the SU(N_c) spin rotation, the SU(N_f) flavor rotation, the 90° space rotation in (k_x,k_y), the reflections, and the time-reversal symmetries. For $N_c = 2$, the pseudospin symmetry, which rotates $\Psi_{n,\sigma,j}(k)$ into $i\tau^{(y)}_{\sigma,\sigma'}\gamma_0\bar{\Psi}^T_{n,\sigma',j}(-k)$, is present [22]. The action in Eq. (2) is also invariant under the SO($d-1$) rotation in $\mathbf{K}$. In Appendix B, we provide further details on symmetry.

The theory in $2 \leqslant d \leqslant 3$ continuously interpolates the physical theories, which describe the AF critical points in $d = 2$ and 3. Because the couplings are marginal in three dimensions, we consider $d = 3-\epsilon$ and expand around three space dimensions using ϵ as a small parameter. We use the field theoretic renormalization group scheme to compute the beta functions, which govern the RG flow of the renormalized velocities and coupling constants.

By embedding the one-dimensional Fermi surface in higher dimensions, the density of state (DOS) is reduced to $\rho(E) \sim E^{d-2}$. As is the case for the usual dimensional regularization scheme for relativistic field theories, the reduced DOS tames quantum fluctuations at low energies and allows us to access low-energy physics in a controlled way. Of course, there is no guarantee that the physics obtained near $d = 3$ is continuously extrapolated all the way to $d = 2$ because of the possibility that some operators that are irrelevant near $d = 3$ become relevant to drive instability near $d = 2$. However, it is our very goal to systematically examine the potential instability as the dimension is lowered toward $d = 2$, for which we first need to establish the existence of a stable fixed point at $d = 3$, which can be realized on its own.

III. STRANGE METAL FIXED POINT

We include one-loop quantum corrections to obtain the beta functions for the velocities and couplings (see Appendices C and D for computational details),

$$\frac{dv}{dl} = -\frac{(N_c^2-1)}{2N_cN_f\pi^2}\frac{zvg^2}{c}h_2(v,c), \tag{3}$$

$$\frac{dc}{dl} = -\frac{zg^2}{8\pi^2}\left\{\pi\frac{c}{v} - \frac{2(N_c^2-1)}{N_cN_f}[h_1(v,c)-h_2(v,c)]\right\}, \tag{4}$$

$$\frac{dg}{dl} = \frac{z}{2}g\left\{\epsilon - \frac{g^2}{4\pi v} - \frac{g^2}{4\pi^3 N_cN_f c}\big[2(N_c^2-1)\pi h_2(v,c) - h_3(v,c)\big]\right\}, \tag{5}$$

$$\frac{du_1}{dl} = \frac{zu_1}{2c^2\pi^2}\left[c^2\pi\left(2\pi\epsilon - \frac{g^2}{v}\right) + \frac{(N_c^2-1)}{N_fN_c}cg^2(h_1(v,c) - h_2(v,c)) - (N_c^2+7)u_1 - \frac{2(2N_c^2-3)}{N_c}u_2 - 3\left(1+\frac{3}{N_c^2}\right)\frac{u_2^2}{u_1}\right], \tag{6}$$

$$\frac{du_2}{dl} = \frac{zu_2}{2c^2\pi^2}\left[c^2\pi\left(2\pi\epsilon - \frac{g^2}{v}\right) + \frac{(N_c^2-1)}{N_fN_c}cg^2(h_1(v,c) - h_2(v,c)) - 12u_1 - \frac{2(N_c^2-9)}{N_c}u_2\right]. \tag{7}$$

Here, l is the logarithmic length scale. $z = [1 - \frac{(N_c^2-1)}{4N_cN_f\pi^2}\frac{g^2}{c}(h_1(v,c)-h_2(v,c))]^{-1}$ is the dynamical critical exponent that determines the scaling dimension of $\mathbf{K}$ relative to $\vec{k}$. $h_i(v,c)$ are given by $h_1(v,c) = \int_0^1 dx\sqrt{\frac{1-x}{c^2+(1+v^2-c^2)x}}$, $h_2(v,c) = c^2\int_0^1 dx\sqrt{\frac{1-x}{[c^2+(1+v^2-c^2)x]^3}}$, and $h_3(v,c) = \int_0^1 dx_1\int_0^{1-x_1}dx_2\int_0^{2\pi}d\theta[\frac{1}{\zeta(v,c,x_1,x_2,\theta)} - \frac{v}{c}\frac{\sin 2\theta}{\zeta^2(v,c,x_1,x_2,\theta)}]$ with

$$\zeta(v,c,x_1,x_2,\theta) = \frac{2v}{c}(x_1\cos^2\theta + x_2\sin^2\theta) + (1-x_1-x_2)\times\left[vc\cos^2(\theta+\pi/4) + \frac{c}{v}\sin^2(\theta+\pi/4)\right].$$

The RG flow of the couplings and the velocities is shown in Fig. 4(a). We first examine the RG flow in the subspace of $g = 0$. At the Gaussian fixed points ($u_i = g = 0$ with $v,c \neq 0$), the theory is free. With $u_1 \neq 0$ and $u_2 = 0$, the theory flows to the $O(N_c^2-1)$ Wilson-Fisher (WF) fixed points at $u_1^* = \frac{2\pi^2c^2\epsilon}{N_c^2+7}$ with dynamical critical exponent $z = 1$. For $N_c \geqslant 4$, one also needs to consider u_2. As u_2 is turned on, the $O(N_c^2-1)$ WF fixed points become unstable and it shows a run-away flow [24], which suggests a first-order phase transition.

In the presence of Yukawa coupling, a stable low-energy fixed point arises. If some components of the velocities were not allowed to flow, the theory could flow to a fixed point with finite couplings [25]. However, the full RG flow is more complicated because of running velocities. As g is turned on, it initially grows as is expected from the fact that it is relevant below $d = 3$. As g grows, the fermions at different hot spots are mixed with each other through quantum fluctuations. As a result, the hot spots become increasingly nested at low energies: v flows to zero as $1/l$ for $\epsilon > 0$ and as $1/\ln(l)$ for $\epsilon = 0$ in the low-energy limit. The dynamical nesting of the fermionic band, in turn, modifies the AF mode in two important ways. First, the boson becomes increasingly slow in the q_x, q_y directions because the collective mode can decay into dispersionless particle-hole pairs near the nested hot spots. As a result, c decreases toward zero, leading to emergent locality in the (x,y) space. Second, quantum fluctuations become more and more efficient in screening the interactions due to the abundant low-energy density of states supported by the nested Fermi surface and the dispersionless boson. In summary of the

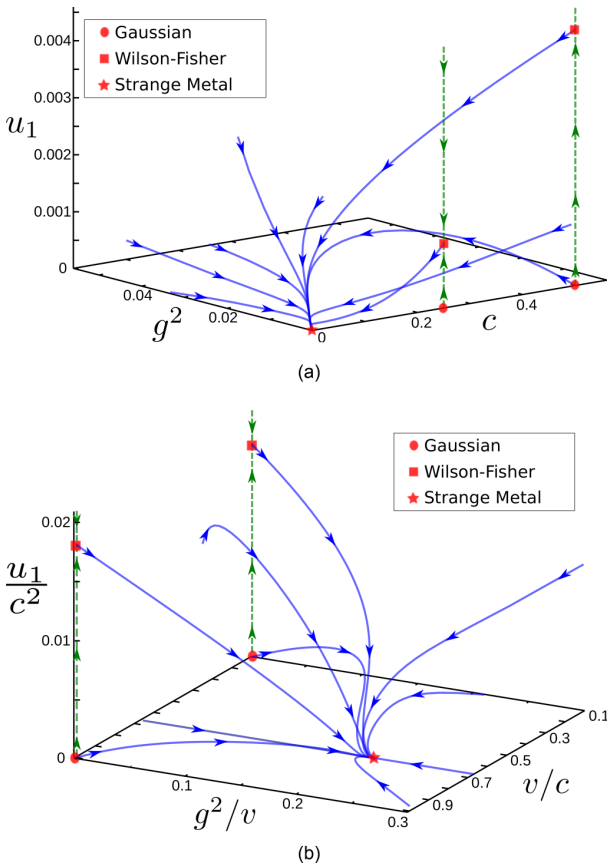

FIG. 4. (Color online) One-loop RG flow of the couplings and velocities for $N_c = 2$, $N_f = 1$, and $\epsilon = 0.01$. We set $u_2 = 0$, which can be done without loss of generality for $N_c < 4$. The solid lines denote flows in the three-dimensional space of the parameters shown in the figure. The dashed lines represent flows within the subspace of $g = 0$. (a) The whole manifold of $g = u_1 = 0$ represents the noninteracting (Gaussian) fixed points parameterized by (v,c). Once u_1 is turned on at the Gaussian fixed points (denoted by circles), the theory flows to the Wilson-Fisher fixed points (squares). As the Yukawa coupling is introduced, couplings and velocities flow to the stable fixed point at $g^* = u_i^* = v^* = c^* = 0$. (b) RG flow of the ratios of the parameters for the same values of N_c, N_f, and ϵ as in (a). The Yukawa coupling measured in the unit of $\sqrt{v}$ and the ratio of the two velocities remain nonzero at the stable fixed point.

RG flow, (i) g induces dynamical nesting, renormalizing v,c to smaller values, and (ii) smaller v,c make screening more efficient, making g,u_i smaller. This cycle of negative feedback leaves no room for a coexistence of the kinetic terms (v,c) and the interactions (g,u_i). It has only one fate down the road of RG flow: mutual destruction. To the one-loop order, all of v,c,g,u_i eventually flow to zero in the low-energy limit at and below three dimensions if initial values of u_i's are not too large in magnitude.

The new interactionless and quasidispersionless fixed point is distinct from the Gaussian fixed point, which is dominated by the kinetic energy. Unlike at the Gaussian fixed point, the kinetic energy and the interactions maintain "a balance of power" along the path to their demise. This can be seen from the fact that the ratios defined by

$$w \equiv \frac{v}{c}, \quad \lambda \equiv \frac{g^2}{v}, \quad \kappa_i \equiv \frac{u_i}{c^2} \tag{8}$$

flow to a stable fixed point,

$$w^* = \frac{N_c N_f}{N_c^2 - 1}, \quad \lambda^* = \frac{4\pi\left(N_c^2 + N_c N_f - 1\right)}{N_c^2 + N_c N_f - 3}\epsilon, \quad \kappa_i^* = 0, \tag{9}$$

in the $c \to 0$ limit as is shown in Fig. 4(b). At the fixed point, the dynamical critical exponent is renormalized to $z = 1 + \frac{\lambda^*}{8\pi}$ to the leading order in λ. The nontrivial quantum correction to z implies that the effect of interaction is not gone even though g,u_i vanish in the low-energy limit. This is due to the emergent locality associated with the dynamical nesting of the Fermi surface and the dispersionless bosonic spectrum. The IR singularity supported by the locality makes the system infinitely susceptible to interaction, leading to finite quantum corrections even with vanishing interactions. The fixed point is stable for general N_c and N_f, and small perturbations of w, λ, κ_i away from Eq. (9) die out in the low-energy limit. In particular, the ϕ^4 vertices acquire an anomalous dimension and become irrelevant at the new fixed point. The one-loop fixed point is exact at $d = 3$ because higher order terms are systematically suppressed by λ and κ_i, which flow to zero in the low-energy limit. For $d < 3$, κ_i, c, and v can receive higher-loop corrections to become nonzero at the fixed point. The details on higher-loop contributions can be found in Appendix E.

If the initial value of κ_1 is sufficiently large and negative, κ_1 runs away to $-\infty$, potentially driving a first-order transition. The stable fixed point in Eq. (9) and the run-away flow is separated by an unstable fixed point at $\kappa_1^* = -\frac{4\pi^2\epsilon}{(N_c^2+7)(N_c^2+N_c N_f-3)}, \kappa_2^* = 0$ with the same values of w^* and λ^* as in Eq. (9). The unstable fixed point, which can be realized at a multicritical point, describes a state distinct from the state described by the stable fixed point in Eq. (9). The two fixed points are distinguished by the different ways the couplings and velocities approach the origin.

IV. PHYSICAL PROPERTIES

The existence of the stable low-energy fixed point implies scale invariance of the Green's function in the limit when k_x,k_y, and $|\mathbf{K}|$ go to zero with $\frac{k_y}{k_x}$ and $\frac{\mathbf{K}}{|k_x|^z}$ fixed at the second order phase transition. Here, we focus on the Green's function near the hot spot 1+ in Fig. 1. The Green's function near other hot spots can be obtained by applying reflection or 90° rotation. In the scaling limit, the fermion Green's function takes the form

$$\mathcal{G}(k) = \frac{1}{|k_y|^{1-2\tilde{\eta}_\psi}} \tilde{G}\left(\frac{\mathbf{K}}{|k_y|^z}\right), \tag{10}$$

where $\tilde{\eta}_\psi \sim O(\epsilon^2)$ is the net anomalous dimension, which vanishes to the linear order in ϵ and $\tilde{G}(x)$ is a universal function. Because v flows to zero logarithmically in the low-energy limit, the dependence on k_x is suppressed as $\frac{k_x}{\ln(1/k_x)}$ for $d < 3$ and as $\frac{k_x}{\ln(\ln(1/k_x))}$ at $d = 3$ in the scaling limit. The dynamical critical exponent is nontrivial even to the linear order in ϵ for $d < 3$. As a result, the spectral function shows a power-law distribution in energy instead of a delta function peak, exhibiting a non-Fermi liquid behavior. At $d = 3$, we have $z = 1$ as in Fermi liquid. However, the Green's function is modified by logarithmic corrections compared to that of the Fermi liquid due to λ, which flows to zero logarithmically. This is a marginal Fermi liquid [26]. Since the boson velocity also flows to zero in the same fashion, v flows to zero, the boson Green's function becomes independent of k_x,k_y in the scaling limit up to corrections that are logarithmically suppressed,

$$\mathcal{D}(k) = \frac{C}{|\mathbf{K}|^{\frac{2-2\tilde{\eta}_\phi}{z}}}, \tag{11}$$

where C is a constant and $\tilde{\eta}_\phi \sim O(\epsilon^2)$. This *quasilocal strange metal* supports nonquasiparticle excitations, which are dispersionless along x,y directions in the scaling limit. Here, the effective space dimension becomes dynamically reduced as a result of quantum fluctuations. The quasilocal behaviors associated with extreme velocity anisotropies were reported in nodal semimetals [27,28]. Local critical behaviors with $z = \infty$ also arise in the dynamical mean-field approximation for the Kondo lattice model [29] and from gravitational constructions [30–32]. The present quasilocal state is distinct from the earlier examples in that it is a stable zero temperature state that supports an extended Fermi surface with a finite z.

The quasilocal strange metal is stable at the one-loop order, which becomes exact in the $d \to 3$ limit. As one approaches $d = 2$, higher order corrections become important. The theory at $d = 2$ remains strongly coupled even in the large N_c and/or large N_f limit. One possibility is that the quasilocal strange metal becomes unstable towards an ordered state below a critical dimension. To identify the channels that may become unstable at $d = 2$, we examine charge density wave (CDW) and superconducting (SC) correlations that are enhanced by quantum fluctuations [21,22]. In principle, particle-hole or particle-particle fluctuations between un-nested patches of Fermi surface may drive an instability if the coupling is strong at the lattice scale [33]. However, those operators that connect nested patches receive the strongest quantum corrections.

In the spin-singlet CDW channel, the set of operators

$$O_{\mathrm{CDW}}^{\pm} = \int dk[(\bar{\Psi}_{1,\sigma,j}\Psi_{1,\sigma,j} + \bar{\Psi}_{3,\sigma,j}\Psi_{3,\sigma,j}) \pm (\bar{\Psi}_{2,\sigma,j}\Psi_{2,\sigma,j} + \bar{\Psi}_{4,\sigma,j}\Psi_{4,\sigma,j})],$$

which describes a p_y-wave and a p_x-wave CDW, respectively, with momentum $2\vec{k}_F$ is most strongly enhanced. These CDW operators, which are pseudospin singlets for $N_c = 2$, break the reflection symmetry and represent bond density waves without on-site modulation of charge. This is different from the bond density wave order which forms a pseudospin doublet with the d-wave pairing order [34]. In the SC channel, we focus on the representation that is symmetric in SU(N_f) and antisymmetric in SU(N_c), which reduces to the spin-singlet SC order for $N_c = 2, N_f = 1$. There are two sets of equally strong SC fluctuations. The first set of operators describes the $d_{x^2-y^2}$-wave and g-wave pairings with zero momentum [35,36], while the second set of operators describes s-wave and d_{xy}-wave pairings with a finite momentum $2\vec{k}_F$ [37,38]. The attractive interaction for the pairing is mediated by the commensurate spin fluctuations that scatter a pair of electrons from one hot spot to another hot spot. Due to the nesting, the finite momentum pairing is as strong as the conventional zero momentum pairing to the one-loop order. The propensity for finite momentum pairing may lead to exotic superconducting states in two dimensions [39,40]. If the quasilocal strange metal is unstable toward a competing order at low temperature in two dimensions, the strange metallic behaviors predicted in Eqs. (10) and (11) can show up within a finite temperature window whose range can be made parametrically large by tuning N_c and N_f [41]. For more details on the computation of the anomalous dimensions for the CDW and SC orders, please see Appendix F.

Within the perturbative regime that we explore in this paper, the anomalous dimensions for various susceptibilities associated with "hot" electrons near the hot spots remain small. Because hot spots are only points in momentum space, thermodynamic and transport properties are dominated by cold electrons, which exhibit Fermi liquid behaviors. For example, the specific heat will be proportional to $T^{2-\epsilon}$ to the leading order of temperature T, and the conductivity is expected to be dominated by cold electrons [42]. As one approaches $d = 2$, the contribution from hot electrons may, in principle, dominate over the contribution from the cold electrons as the anomalous dimensions become larger. Moreover, the behavior of cold electrons may also deviate from those of a Fermi liquid far away from three dimensions, as the coupling between cold electrons and collective modes, which is irrelevant in the perturbative regime, becomes strong near $d = 2$ [42]. In this case, non-Fermi liquid behavior may show up even for the thermodynamic and transport properties of cold electrons. However, we can not address this issue in a controlled manner because it requires strong coupling, which lies outside the perturbative window.

V. CONCLUSION

We show that a strange metallic state emerges at the AF quantum critical point in a metal that supports a one-dimensional Fermi surface based on a perturbative expansion that gives the exact low-energy fixed point in three dimensions. Even though the interaction is screened to zero in the low-energy limit, dynamical reduction of the effective dimensionality drives the system into a strange metallic state, which supports partially dispersionless incoherent single-particle excitations along with enhanced superconducting and charge density wave fluctuations. The present theory continuously interpolates between the three-dimensional theory for one-dimensional Fermi surfaces and two-dimensional metals. The three-dimensional theory can arise at the AF quantum critical point in the presence of p_z-wave CDW, which is described by a stable quasilocal marginal Fermi liquid. Our formalism also provides a way to access potential instabilities of the non-Fermi liquids that arise at the AF quantum critical points below three dimensions as ϵ increases.

ACKNOWLEDGMENTS

We thank Andrey Chubukov, Catherine Pepin, Patrick Lee, Max Metlitski, Subir Sachdev, T. Senthil and Yong Baek Kim for helpful discussions. The research was supported in part by the Natural Sciences and Engineering Research Council of Canada (Canada), the Early Research Award from the Ontario Ministry of Research and Innovation, and the Templeton Foundation. Research at the Perimeter Institute is supported in part by the Government of Canada (Canada) through Industry Canada, and by the Province of Ontario through the Ministry of Research and Information.

APPENDIX A: A THREE-DIMENSIONAL LATTICE MODEL FOR A RELATED FIELD THEORY

In this appendix, we construct a three-dimensional lattice model in which a field theory similar to the one considered in the main text can be realized. We consider a tetragonal lattice where staggered fluxes pierce through unit plaquettes. A gauge is chosen such that the hopping t_z along the z direction is real. The nearest neighbor hoppings in the XY plane are written as $\{t_1 e^{i\phi}, t_2 e^{i\phi}\}(\{t_1 e^{-i\phi}, t_2 e^{-i\phi}\})$ in the two orthogonal directions along (against) the arrows, as is shown in Figs. 5(a) and 5(b). Here, the magnitudes of staggered flux per plaquette are $(4\phi, 2\phi, 2\phi)$ in the three planes. In the coordinate system shown in Figs. 5(a) and 5(b), the lattice vectors become $\vec{a}_1 = (1,0,0)$, $\vec{a}_2 = (0,1,0)$, $\vec{a}_3 = \frac{1}{2}(1,1,1)$, where the distance between nearest neighbor A sites in the XY plane is chosen to be 1. The reciprocal vectors are given by $\vec{b}_1 = 2\pi(1,0,-1)$, $\vec{b}_2 = 2\pi(0,1,-1)$, $\vec{b}_3 = 4\pi(0,0,1)$.

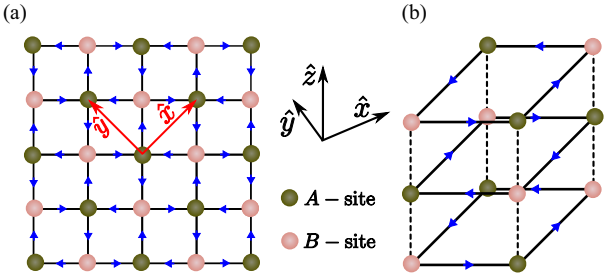

FIG. 5. (Color online) (a) Flux lattice in the XY plane. The green (dark) and the red (light) disks represent sites A and B, respectively. (b) Three-dimensional arrangement of the A and B sites.

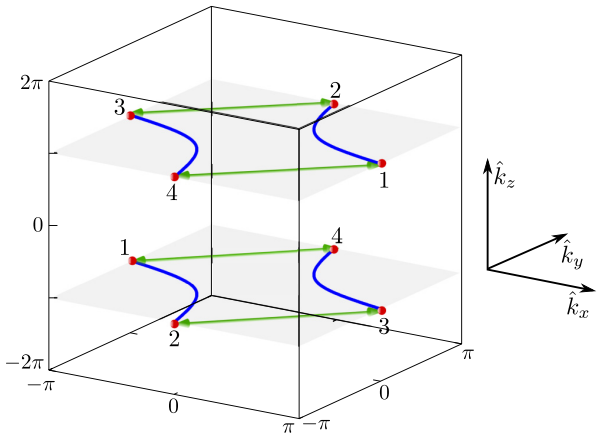

FIG. 6. (Color online) The (blue) curves represent the Fermi lines embedded in the three-dimensional momentum space for Eq. (A3) with $t_1 = 0.6t_2$. The (green) arrows represent the antiferromagnetic ordering vector with $\vec{Q} = (\pi,\pi,0)$. The shaded regions represent the $k_z = \pm\pi$ planes. There are four distinct hot spots connected by $\vec{Q}$ denoted by $n = 1,2,3,4$.

The tight-binding Hamiltonian with the nearest-neighbor hoppings becomes

$$H = -\sum_{\vec{k}} [\mathcal{D}(\vec{k}) c_A^\dagger(\vec{k}) c_B(\vec{k}) + \text{H.c.}], \tag{A1}$$

where $c_{A(B)}$ is the destruction operator for electrons at A (B) sites, and

$$\begin{aligned}\mathcal{D}(\vec{k}) = 2\Bigg\{ &\cos(\phi)\Bigg[t_+ \cos\left(\frac{k_x}{2}\right)\cos\left(\frac{k_y}{2}\right) + t_- \sin\left(\frac{k_x}{2}\right) \\ &\times \sin\left(\frac{k_y}{2}\right)\Bigg] + t_z \cos\left(\frac{k_z}{2}\right)\Bigg\} \\ &+ 2i\sin(\phi)\Bigg[t_+ \sin\left(\frac{k_x}{2}\right)\sin\left(\frac{k_y}{2}\right) \\ &+ t_- \cos\left(\frac{k_x}{2}\right)\cos\left(\frac{k_y}{2}\right)\Bigg],\end{aligned} \tag{A2}$$

with $t_\pm = t_1 \pm t_2$. The Hamiltonian is diagonal in spin indices, and we have suppressed the spin indices in the electron operators. The 2×2 Hamiltonian supports a particle-hole symmetric band with the dispersion $E(\vec{k}) = \pm|\mathcal{D}(\vec{k})|$ at half-filling. With the choice of $0 < t_1 < t_2$ and $\phi = \frac{\pi}{2}$, one obtains one-dimensional Fermi surfaces (or *Fermi lines*) located at

$$\begin{aligned} &k_z = \pm\pi, \\ &\sin\left(\tfrac{k_x}{2}\right)\sin\left(\tfrac{k_y}{2}\right) + \tfrac{t_-}{t_+}\cos\left(\tfrac{k_x}{2}\right)\cos\left(\tfrac{k_y}{2}\right) = 0. \end{aligned} \tag{A3}$$

The Fermi lines embedded in the three-dimensional momentum space are shown in Fig. 6.

We assume that there exists an electron-electron interaction, which drives the semimetal into an antiferromagnetic state. In particular, we consider an orbital selective antiferromagnetic order, where electrons in the bonding and antibonding states within a unit cell have opposite spins, which then modulate

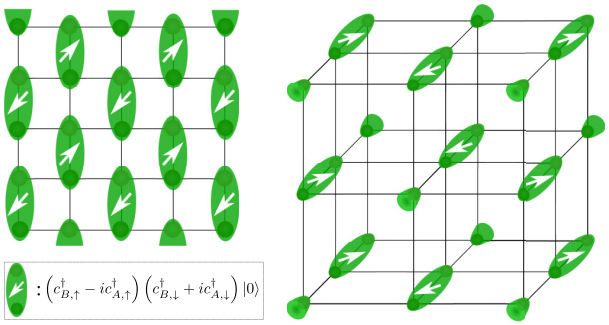

FIG. 7. (Color online) A real space pattern for the orbital selective antiferromagnetic order (a) on the XY plane and (b) in the full three-dimensional lattice.

with momentum $(\pi,\pi,0)$ in space. This is illustrated in Fig. 7. If the phase transition is continuous, the critical spin fluctuations associated with the order strongly interact with electrons on the Fermi lines connected by the ordering vector $\vec{Q} = (\pi,\pi,0)$ as is shown in Fig. 6. In this case, there exist four distinct hot spots connected by the ordering vector. As is considered in the main text, the minimal theory that describes the quantum critical point includes the electronic excitations near the hot spots and the critical antiferromagnetic mode that is coupled with electrons through the Yukawa coupling,

$$\begin{aligned}\mathcal{S}_{\text{eff}} = &\int \frac{d^4k}{(2\pi)^4}\sum_n \bar{\Psi}_n(k)[ik_0\gamma_0 + i\gamma_1 k_z + i\gamma_2\varepsilon_n(\vec{k})]\Psi_n(\vec{k}) \\ &+ ig_0\int \frac{d^4k}{(2\pi)^4}\frac{d^4q}{(2\pi)^4}\vec{\Phi}(q)\cdot[\bar{\Psi}_{1;s}(k+q)\gamma_2\vec{\tau}_{s,s'}\Psi_{4;s'}(k) \\ &+ \bar{\Psi}_{2;s}(k+q)\gamma_2\vec{\tau}_{s,s'}\Psi_{3;s'}(k)] + \text{H.c.} \\ &+ \frac{1}{2}\int \frac{d^4q}{(2\pi)^4}\left[q_0^2 + c_z^2 q_z^2 + c_x^2 q_x^2 + c_y^2 q_y^2\right]\vec{\Phi}(-q)\cdot\vec{\Phi}(q) \\ &+ \frac{u_0}{4!}\int \frac{d^4q_1}{(2\pi)^4}\frac{d^4q_2}{(2\pi)^4}\frac{d^4q_3}{(2\pi)^4}[\vec{\Phi}(q_1+q_2)\cdot\vec{\Phi}(q_2)] \\ &\times[\vec{\Phi}(q_3-q_2)\cdot\vec{\Phi}(q_3)].\end{aligned} \tag{A4}$$

Here, $\Psi_n(\vec{k}) \equiv \begin{pmatrix} c_A(\vec{K}_n+\vec{k}) \\ c_B(\vec{K}_n+\vec{k})\end{pmatrix}$ with $n = 1,2,3,4$ denotes electrons near the nth hot spot with

$$\begin{aligned} &\vec{K}_1 = (\pm\pi,0,\pm\pi), \quad \vec{K}_2 = (0,\pm\pi,\pm\pi), \\ &\vec{K}_3 = (\mp\pi,0,\pm\pi), \quad \vec{K}_4 = (0,\mp\pi,\pm\pi), \end{aligned} \tag{A5}$$

and $\bar{\Psi}_n \equiv \Psi_n^\dagger\gamma_0$ with $\gamma_0 = \sigma_z$, $\gamma_1 = \sigma_y$, and $\gamma_2 = \sigma_x$. $\varepsilon_n(\vec{k})$ is the linearized dispersion around each hot spot,

$$\begin{aligned} &\varepsilon_1(\vec{k}) = t_-k_x - t_+k_y, \quad \varepsilon_2(\vec{k}) = -t_+k_x + t_-k_y, \\ &\varepsilon_3(\vec{k}) = -t_-k_x + t_+k_y, \quad \varepsilon_4(\vec{k}) = t_+k_x - t_-k_y. \end{aligned} \tag{A6}$$

We have scaled away t_z dependence by absorbing it in the $\hat{z}$ component of momentum. $\vec{\Phi}(q)$ represents the critical fluctuations of the SDW order parameter.

Unlike the action in Eq. (2), Eq. (A4) lacks the C_4 symmetry in the XY plane and the SO(2) rotation symmetry in the

TABLE I. Table of spinors obtained by applying the spatial $\pi/2$ rotation and reflections in the x and y directions accompanied by reflections in $k_1,k_2,\ldots,k_{d-2}$. Under the three space symmetries, the energy-momentum vector $k=(k_0,k_1,\ldots,k_{d-2},k_x,k_y)$ is transformed to $k_{R_{\pi/2}}=(k_0,k_1,\ldots,k_{d-2},-k_y,k_x)$, $k_{R_x}=(k_0,-k_1,\ldots,-k_{d-2},-k_x,k_y)$, and $k_{R_y}=(k_0,-k_1,\ldots,-k_{d-2},k_x,-k_y)$, respectively. The spin and flavor indices are suppressed.

	$R_{\pi/2}$	R_x	R_y
$\Psi_1(k)$	$\Psi_2(k_{R_{\pi/2}})$	$-i\gamma_0\Psi_3(k_{R_x})$	$i\gamma_0\gamma_{d-1}\Psi_3(k_{R_y})$
$\Psi_2(k)$	$\gamma_{d-1}\Psi_1(k_{R_{\pi/2}})$	$i\gamma_0\gamma_{d-1}\Psi_4(k_{R_x})$	$-i\gamma_0\Psi_4(k_{R_y})$
$\Psi_3(k)$	$\Psi_4(k_{R_{\pi/2}})$	$i\gamma_0\Psi_1(k_{R_x})$	$i\gamma_0\gamma_{d-1}\Psi_1(k_{R_y})$
$\Psi_4(k)$	$-\gamma_{d-1}\Psi_3(k_{R_{\pi/2}})$	$i\gamma_0\gamma_{d-1}\Psi_2(k_{R_x})$	$i\gamma_0\Psi_2(k_{R_y})$

k_0-k_z plane. This results in velocity anisotropy for the bosons. However, we expect that this theory also flows to a quasilocal fixed point similar to the one discussed in the main text [43].

APPENDIX B: SYMMETRY

In this appendix, we elaborate on the symmetries of the action in Eq. (2). The internal symmetry is $\mathrm{U}(1)^2\times\mathrm{SU}(N_c)\times\mathrm{SU}(N_f)^2$ associated with charge, spin, and flavor conservations. There are two U(1)'s and two SU(N_f)'s because the charge and flavor are conserved within the two sets of hot spots ({1,3} and {2,4}) separately. Besides the internal symmetry, the action has $\pi/2$ rotation and reflection symmetries under which the spinors transform as is shown in Table I. In $d>2$, the SO($d-1$) spacetime rotational symmetry is present. Under SO($d-1$) rotation, k_μ and $\bar\psi_{n,\sigma,j}\gamma_\mu\psi_{n,\sigma,j}$ form vectors for $\mu=0,1,\ldots,d-2$. For $N_c=2$, there also exists a pseudo-spin symmetry under which the superspinor $\chi_{n,\sigma,j}(k)=(\Psi_{n,\sigma,j}(k),i\tau^{(y)}_{\sigma,\sigma'}\gamma_0\bar\Psi^T_{n,\sigma',j}(-k))^T$ transforms as $\chi_{n,\sigma,j}\mapsto U\chi_{n,\sigma,j}$, where U represents SU(2) matrix that acts on the particle-hole space.

APPENDIX C: RENORMALIZATION GROUP ANALYSIS

In this appendix, we describe the method that is used to compute the beta functions for the velocities and couplings. In order to incorporate quantum corrections, we renormalize the theory by "tuning" the parameters in the action in Eq. (2) such that the physical observables become insensitive to the UV cutoff scale. This amounts to adding counter terms that remove UV divergences in the quantum effective action order by order in the couplings. The internal and spacetime symmetries guarantee that the counter terms take the following form:

$$\begin{aligned}\mathcal{S}_{\rm CT}=&\sum_{n=1}^{4}\sum_{\sigma=1}^{N_c}\sum_{j=1}^{N_f}\int\frac{d^{d+1}k}{(2\pi)^{d+1}}\bar\Psi_{n,\sigma,j}(k)\left[i\mathcal{A}_1\boldsymbol{\Gamma}\cdot\mathbf{K}+i\mathcal{A}_3\gamma_{d-1}\varepsilon_n\left(\vec k;\frac{\mathcal{A}_2}{\mathcal{A}_3}v\right)\right]\Psi_{n,\sigma,j}(k)+\frac14\int\frac{d^{d+1}q}{(2\pi)^{d+1}}[\mathcal{A}_4|\mathbf{Q}|^2+\mathcal{A}_5c^2|\vec q|^2]\\
&\times\mathrm{Tr}[\Phi(-q)\Phi(q)]+i\mathcal{A}_6\frac{g\mu^{(3-d)/2}}{\sqrt{N_f}}\sum_{n=1}^{4}\sum_{\sigma,\sigma'=1}^{N_c}\sum_{j=1}^{N_f}\int\frac{d^{d+1}k}{(2\pi)^{d+1}}\frac{d^{d+1}q}{(2\pi)^{d+1}}[\bar\Psi_{\bar n,\sigma,j}(k+q)\Phi_{\sigma,\sigma'}(q)\gamma_{d-1}\Psi_{n,\sigma',j}(k)]\\
&+\frac{\mu^{3-d}}{4}\int\frac{d^{d+1}k_1}{(2\pi)^{d+1}}\frac{d^{d+1}k_2}{(2\pi)^{d+1}}\frac{d^{d+1}q}{(2\pi)^{d+1}}\{\mathcal{A}_7u_1\mathrm{Tr}[\Phi(k_1+q)\Phi(k_2-q)]\mathrm{Tr}[\Phi(k_1)\Phi(k_2)]\\
&+\mathcal{A}_8u_2\mathrm{Tr}[\Phi(k_1+q)\Phi(k_2-q)\Phi(k_1)\Phi(k_2)]\},\end{aligned}\tag{C1}$$

where $\varepsilon_1(\vec k;v)=vk_x+k_y$, $\varepsilon_2(\vec k;v)=-k_x+vk_y$, $\varepsilon_3(\vec k;v)=vk_x-k_y$, and $\varepsilon_4(\vec k;v)=k_x+vk_y$. In the minimal subtraction scheme, the counter terms only include contributions that are divergent in the $\epsilon\to0$ limit,

$$\mathcal{A}_n\equiv\mathcal{A}_n(v,c,g,u;\epsilon)=\sum_{m=1}^{\infty}\frac{Z_{n,m}(v,c,g,u)}{\epsilon^m},\tag{C2}$$

where $Z_{n,m}(v,c,g,u)$ are finite functions of the couplings in the $\epsilon\to0$ limit. The renormalized action is given by the sum of the original action and the counter terms, which can be expressed in terms of bare fields and bare couplings,

$$\begin{aligned}\mathcal{S}_{\rm ren}=&\sum_{n=1}^{4}\sum_{\sigma=1}^{N_c}\sum_{j=1}^{N_f}\int\frac{d^{d+1}k_B}{(2\pi)^{d+1}}\bar\Psi_{B;n,\sigma,j}(k_B)[i\boldsymbol{\Gamma}\cdot\mathbf{K}_B+i\gamma_{d-1}\varepsilon_n(\vec k_B;v_B)]\Psi_{B;n,\sigma,j}(k)\\
&+\frac14\int\frac{d^{d+1}q_B}{(2\pi)^{d+1}}\left[|\mathbf{Q}_B|^2+c_B^2|\vec q_B|^2\right]\mathrm{Tr}[\Phi_B(-q_B)\Phi_B(q_B)]\\
&+i\frac{g_B}{\sqrt{N_f}}\sum_{n=1}^{4}\sum_{\sigma,\sigma'=1}^{N_c}\sum_{j=1}^{N_f}\int\frac{d^{d+1}k_B}{(2\pi)^{d+1}}\frac{d^{d+1}q_B}{(2\pi)^{d+1}}[\bar\Psi_{B;\bar n,\sigma,j}(k_B+q_B)\Phi_{B;\sigma,\sigma'}(q_B)\gamma_{d-1}\Psi_{B;n,\sigma',j}(k_B)]\\
&+\frac14\int\frac{d^{d+1}k_{1B}}{(2\pi)^{d+1}}\frac{d^{d+1}k_{2B}}{(2\pi)^{d+1}}\frac{d^{d+1}q_B}{(2\pi)^{d+1}}\{u_{1B}\mathrm{Tr}[\Phi_B(k_{1B}+q_B)\Phi_B(k_{2B}-q_B)]\mathrm{Tr}[\Phi_B(k_{1B})\Phi_B(k_{2B})]\\
&+u_{2B}\mathrm{Tr}[\Phi_B(k_{1B}+q_B)\Phi_B(k_{2B}-q_B)\Phi_B(k_{1B})\Phi_B(k_{2B})]\}.\end{aligned}\tag{C3}$$

Here, the renormalized quantities are related to the bare ones through

$$\begin{aligned}
\mathbf{K} &= \mathcal{Z}_\tau^{-1}\mathbf{K}_B, \quad \vec{k} = \vec{k}_B,\\
\Psi_{n,\sigma,j}(k) &= \mathcal{Z}_\psi^{-\frac{1}{2}}\Psi_{B;n,\sigma,j}(k_B), \quad \Phi(q) = \mathcal{Z}_\phi^{-\frac{1}{2}}\Phi_B(q_B),\\
v &= \frac{\mathcal{Z}_3}{\mathcal{Z}_2}v_B, \quad c = \left(\frac{\mathcal{Z}_\phi\mathcal{Z}_\tau^{d-1}}{\mathcal{Z}_5}\right)^{\frac{1}{2}}c_B,\\
g &= \frac{\mathcal{Z}_\psi\mathcal{Z}_\phi^{\frac{1}{2}}\mathcal{Z}_\tau^{2(d-1)}}{\mathcal{Z}_6}\mu^{-\frac{3-d}{2}}g_B,\\
u_1 &= \frac{\mathcal{Z}_\phi^2\mathcal{Z}_\tau^{3(d-1)}}{\mathcal{Z}_7}\mu^{-(3-d)}u_{1B},\\
u_2 &= \frac{\mathcal{Z}_\phi^2\mathcal{Z}_\tau^{3(d-1)}}{\mathcal{Z}_8}\mu^{-(3-d)}u_{2B},
\end{aligned} \tag{C4}$$

where $\mathcal{Z}_\tau = \frac{\mathcal{Z}_1}{\mathcal{Z}_3}$, $\mathcal{Z}_\psi = \mathcal{Z}_1\mathcal{Z}_\tau^{-d}$, and $\mathcal{Z}_\phi = \mathcal{Z}_4\mathcal{Z}_\tau^{-(d+1)}$ with $\mathcal{Z}_n = 1 + \mathcal{A}_n$. We use the freedom of choosing an overall scale to fix the scaling dimension of $\vec{k}$ to be 1. The renormalized Green's function defined through

$$\begin{aligned}
&\langle\Psi(k_1)\dots\Psi(k_f)\bar{\Psi}(k_{f+1})\dots\bar{\Psi}(k_{2f})\Phi(q_1)\dots\Phi(q_b)\rangle\\
&= G^{(2f,b)}(k_i,q_j;v,c,g,u_i,\mu)\delta^{(d+1)}\\
&\quad\times\left(\sum_{i=1}^{f}(k_i - k_{i+f}) + \sum_{j=1}^{b}q_j\right)
\end{aligned} \tag{C5}$$

satisfies the renormalization group equation:

$$\begin{aligned}
&\Big[z\big(\mathbf{K}_i\cdot\nabla_{\mathbf{K}_i} + \mathbf{Q}_j\cdot\nabla_{\mathbf{Q}_j}\big) + \big(\vec{k}_i\cdot\vec{\nabla}_{\vec{k}_i} + \vec{q}_j\cdot\vec{\nabla}_{\vec{q}_j}\big) - \beta_v\frac{\partial}{\partial v}\\
&\quad - \beta_c\frac{\partial}{\partial c} - \beta_g\frac{\partial}{\partial g} - \beta_{u_i}\frac{\partial}{\partial u_i} + 2f\left(\frac{d+2}{2} - \eta_\psi\right)\\
&\quad + b\left(\frac{d+3}{2} - \eta_\phi\right) - (z(d-1)+2)\Big]\\
&\quad\times G^{(2f,b)}(k_i,q_i;v,c,g,u_i,\mu) = 0.
\end{aligned} \tag{C6}$$

Here, the dynamical critical exponent and the anomalous dimensions of the fields are given by $z = 1 + \frac{\partial\ln\mathcal{Z}_\tau}{\partial\ln\mu}$, $\eta_\psi = \frac{1}{2}\frac{\partial\ln\mathcal{Z}_\psi}{\partial\ln\mu}$, $\eta_\phi = \frac{1}{2}\frac{\partial\ln\mathcal{Z}_\phi}{\partial\ln\mu}$, and the beta functions that describe the flow of the parameters with increasing energy scale are given by $\beta_v = \frac{\partial v}{\partial\ln\mu}$, $\beta_c = \frac{\partial c}{\partial\ln\mu}$, $\beta_g = \frac{\partial g}{\partial\ln\mu}$, $\beta_{u_i} = \frac{\partial u_i}{\partial\ln\mu}$. The set of coupled equations for the critical exponents and the beta functions can be rewritten as

$$\begin{aligned}
&\mathcal{Z}_3[(d-1)(z-1) + 2\eta_\psi] - \mathcal{Z}_3' = 0,\\
&\mathcal{Z}_1[d(z-1) + 2\eta_\psi] - \mathcal{Z}_1' = 0,\\
&\mathcal{Z}_4[(d+1)(z-1) + 2\eta_\phi] - \mathcal{Z}_4' = 0,\\
&\mathcal{Z}_2\{\beta_v - v[(d-1)(z-1) + 2\eta_\psi]\} + v\mathcal{Z}_2' = 0,\\
&\mathcal{Z}_5\{2\beta_c - c[(d-1)(z-1) + 2\eta_\phi]\} + c\mathcal{Z}_5' = 0,\\
&\mathcal{Z}_6\left\{\beta_g - g\left[-\frac{3-d}{2} + 2(d-1)(z-1) + 2\eta_\psi + \eta_\phi\right]\right\}\\
&\quad + g\mathcal{Z}_6' = 0,\\
&\mathcal{Z}_7\big\{\beta_{u_1} - u_1[-(3-d) + 3(d-1)(z-1) + 4\eta_\phi]\big\}\\
&\quad + u_1\mathcal{Z}_7' = 0,\\
&\mathcal{Z}_8\big\{\beta_{u_2} - u_2[-(3-d) + 3(d-1)(z-1) + 4\eta_\phi]\big\}\\
&\quad + u_2\mathcal{Z}_8' = 0,
\end{aligned} \tag{C7}$$

which solve to give

$$z = \big[1 + \big(\tfrac{1}{2}g\partial_g + u_i\partial_{u_i}\big)(Z_{1,1} - Z_{3,1})\big]^{-1}, \tag{C8}$$

$$\begin{aligned}
\eta_\psi &= -\frac{\epsilon}{2}z\left(\frac{1}{2}g\partial_g + u_i\partial_{u_i}\right)(Z_{1,1} - Z_{3,1})\\
&\quad + \frac{1}{2}z\left(\frac{1}{2}g\partial_g + u_i\partial_{u_i}\right)(2Z_{1,1} - 3Z_{3,1}),
\end{aligned} \tag{C9}$$

$$\begin{aligned}
\eta_\phi &= -\frac{\epsilon}{2}z\left(\frac{1}{2}g\partial_g + u_i\partial_{u_i}\right)(Z_{1,1} - Z_{3,1})\\
&\quad + \frac{1}{2}z\left(\frac{1}{2}g\partial_g + u_i\partial_{u_i}\right)(4Z_{1,1} - 4Z_{3,1} - Z_{4,1}),
\end{aligned} \tag{C10}$$

$$\beta_v = zv\big(\tfrac{1}{2}g\partial_g + u_i\partial_{u_i}\big)(Z_{2,1} - Z_{3,1}), \tag{C11}$$

$$\beta_c = \tfrac{1}{2}zc\big(\tfrac{1}{2}g\partial_g + u_i\partial_{u_i}\big)(2Z_{1,1} - 2Z_{3,1} - Z_{4,1} + Z_{5,1}), \tag{C12}$$

$$\beta_g = -zg\left[\frac{\epsilon}{2} + \frac{1}{2}\left(\frac{1}{2}g\partial_g + u_i\partial_{u_i}\right)(2Z_{3,1} + Z_{4,1} - 2Z_{6,1})\right], \tag{C13}$$

$$\begin{aligned}
\beta_{u_1} &= -zu_1\big[\epsilon - \big(\tfrac{1}{2}g\partial_g + u_i\partial_{u_i}\big)(2Z_{1,1} - 2Z_{3,1}\\
&\quad - 2Z_{4,1} + Z_{7,1})\big],
\end{aligned} \tag{C14}$$

$$\begin{aligned}
\beta_{u_2} &= -zu_2\big[\epsilon - \big(\tfrac{1}{2}g\partial_g + u_i\partial_{u_i}\big)(2Z_{1,1} - 2Z_{3,1}\\
&\quad - 2Z_{4,1} + Z_{8,1})\big].
\end{aligned} \tag{C15}$$

The counter terms can be computed order by order in the loop expansion. We include the contributions from the one-loop diagrams shown in Fig. 8. The computations of the diagrams are discussed in the next appendix. Here we summarize the final results:

$$\begin{aligned}
Z_{1,1} &= -\frac{\big(N_c^2-1\big)}{4\pi^2N_cN_f}\frac{g^2}{c}h_1(v,c),\\
Z_{2,1} &= \frac{\big(N_c^2-1\big)}{4\pi^2N_cN_f}\frac{g^2}{c}h_2(v,c),\\
Z_{3,1} &= -Z_{2,1},\\
Z_{4,1} &= -\frac{1}{4\pi}\frac{g^2}{v},\\
Z_{5,1} &= 0,\\
Z_{6,1} &= -\frac{1}{8\pi^3N_cN_f}\frac{g^2}{c}h_3(v,c),
\end{aligned}$$

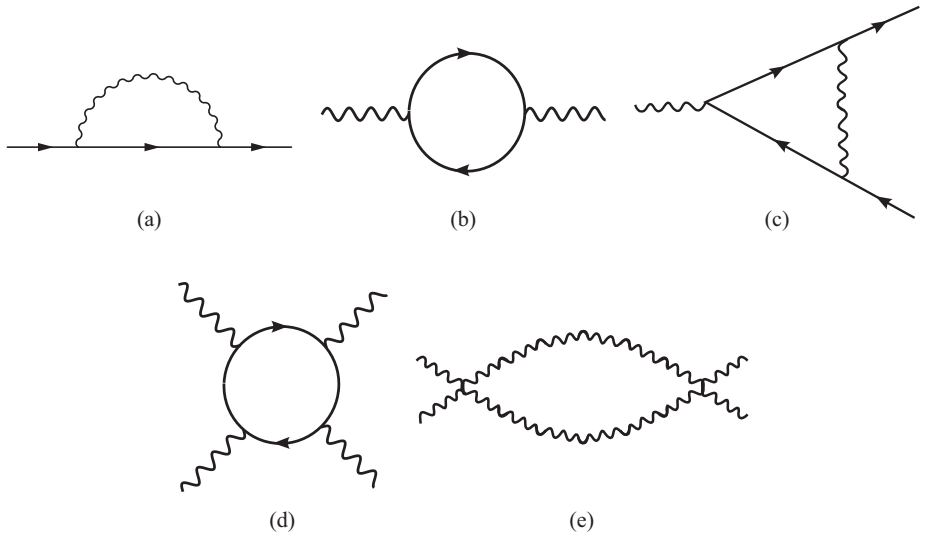

FIG. 8. One-loop Feynman diagrams that contribute to the quantum effective action. Solid (wiggly) lines represent the fermion (boson) propagator. Cubic vertices represent the Yukawa coupling, g. In (e), each quartic vertex can be either u_1 or u_2.

$$Z_{7,1} = \frac{1}{2\pi^2 c^2}\Bigg[\left(N_c^2+7\right)u_1 + 2\left(2N_c - \frac{3}{N_c}\right)u_2 + 3\left(1+\frac{3}{N_c^2}\right)\frac{u_2^2}{u_1}\Bigg],$$
$$Z_{8,1} = \frac{1}{2\pi^2 c^2}\left[12u_1 + 2\left(N_c - \frac{9}{N_c}\right)u_2\right], \tag{C16}$$

where $h_i(v,c)$ are defined in the main text. This gives the beta functions and the dynamical critical exponent shown in Eqs. (3)–(7) and below. The anomalous dimensions of the fields are given by

$$\eta_\psi = z\frac{\left(N_c^2-1\right)}{8\pi^2 N_c N_f}\frac{g^2}{c}\{\epsilon[h_1(v,c)-h_2(v,c)] - [2h_1(v,c)-3h_2(v,c)]\}, \tag{C17}$$
$$\eta_\phi = \frac{z}{8\pi}\frac{g^2}{c}\left\{\frac{c}{v} - (4-\epsilon)\frac{\left(N_c^2-1\right)}{\pi N_c N_f}[h_1(v,c)-h_2(v,c)]\right\}. \tag{C18}$$

It is noted that the beta functions used in the main text describe the flow of the couplings with increasing length scale, which is defined to be $\frac{\partial g}{\partial l} \equiv -\beta_g$.

Because all v,c,g,u_i flow to zero in the low-energy limit as discussed in the main text, it is more convenient to consider the ratios of the couplings, $w = \frac{v}{c}$, $\lambda = \frac{g^2}{v}$, and $\kappa_i = \frac{u_i}{c^2}$. The beta functions for the ratios are given by

$$\frac{\partial w}{\partial l} = \frac{zw\lambda}{8\pi}\left\{1 - \frac{2w\left(N_c^2-1\right)}{\pi N_c N_f}[h_1(wc,c)+h_2(wc,c)]\right\}, \tag{C19}$$
$$\frac{\partial \lambda}{\partial l} = z\lambda\left\{\epsilon - \frac{\lambda}{4\pi}\left[1 - \frac{w}{\pi^2 N_c N_f}h_3(wc,w)\right]\right\}, \tag{C20}$$
$$\frac{\partial \kappa_1}{\partial l} = z\kappa_1\Bigg[\left(\epsilon - \frac{\lambda}{4\pi}\right) - \frac{\left(N_c^2+7\right)}{2\pi^2}\kappa_1 - \frac{\left(2N_c^2-3\right)}{\pi^2 N_c}\kappa_2 - \frac{3\left(N_c^2+3\right)}{2\pi^2 N_c^2}\frac{\kappa_2^2}{\kappa_1}\Bigg], \tag{C21}$$
$$\frac{\partial \kappa_2}{\partial l} = z\kappa_2\left[\left(\epsilon - \frac{\lambda}{4\pi}\right) - \frac{6}{\pi^2}\kappa_1 - \frac{N_c^2-9}{\pi^2 N_c}\kappa_2\right]. \tag{C22}$$

By using $\lim_{c\to 0} h_1(wc,c) = \frac{\pi}{2}$, $\lim_{c\to 0} h_2(wc,c) = 0$, and $\lim_{c\to 0} h_3(wc,c) = \frac{2\pi^2}{1+w}$, it can be shown that the beta functions for c, w, λ, and κ_i simultaneously vanish at the attractive fixed point given in Eq. (9). At the fixed point, the dynamical critical exponent and the anomalous dimensions are given by

$$z = 1 + \frac{N_c^2 + N_c N_f - 1}{2\left(N_c^2 + N_c N_f - 3\right)}\epsilon,$$
$$\eta_\psi = \eta_\phi = -\frac{N_c^2 + N_c N_f - 1}{2\left(N_c^2 + N_c N_f - 3\right)}\epsilon \tag{C23}$$

to the leading order in ϵ. Both the dynamical critical exponent and the anomalous dimensions modify the scaling of the renormalized Green's function as can be checked from Eq. (C6). As a result, the two-point functions in Eqs. (10) and (11) are controlled by the net anomalous dimensions defined by $\tilde{\eta}_\psi = \eta_\psi + \frac{(z-1)(2-\epsilon)}{2}$, $\tilde{\eta}_\phi = \eta_\phi + \frac{(z-1)(2-\epsilon)}{2}$, which vanish to the linear order in ϵ. It is expected that there will be nontrivial anomalous dimensions for the two-point functions beyond the one-loop level [14]. Higher-point correlation functions exhibit nontrivial anomalous dimensions even to the linear order in ϵ because the quantum corrections are not canceled in Eq. (C6) for $2f + b > 2$.

APPENDIX D: COMPUTATION OF ONE-LOOP DIAGRAMS

In this section, we outline the computations of the one-loop Feynman diagrams that result in Eq. (C16). We will use δS to denote the contributions to the quantum effective action, and $S_{\rm CT}$ to denote the counter terms that are needed to cancel the UV divergent pieces in δS in the $\epsilon \to 0$ limit.

1. Fermion self-energy

The quantum correction to the fermion self-energy from the diagram in Fig. 8(a) is

$$\delta\mathcal{S}^{(2,0)} = \frac{2g^2\mu^{3-d}}{N_f}\left(N_c - \frac{1}{N_c}\right)\sum_{n=1}^{4}\sum_{\sigma=1}^{N_c}\sum_{j=1}^{N_f}\int\frac{d^{d+1}k}{(2\pi)^{d+1}}\bar{\Psi}_{n,\sigma,j}(k)\Upsilon^{(n)}_{(2,0)}(k)\Psi_{n,\sigma,j}(k), \tag{D1}$$

where

$$\Upsilon^{(n)}_{(2,0)}(k) = \int\frac{d^{d-1}\mathbf{Q}}{(2\pi)^{d-1}}\frac{d^2\vec{q}}{(2\pi)^2}\gamma_{d-1}G_{\bar{n}}(k+q)\gamma_{d-1}D(q), \tag{D2}$$

and the bare Green's functions are given by

$$G_n(k) = -i\frac{\mathbf{\Gamma}\cdot\mathbf{K} + \gamma_{d-1}\varepsilon_n(\vec{k})}{|\mathbf{K}|^2 + \varepsilon_n^2(\vec{k})}, \tag{D3}$$

$$D(q) = \frac{1}{|\mathbf{Q}|^2 + c^2|\vec{q}|^2}. \tag{D4}$$

After the integrations over $\vec{q}$ and $\mathbf{Q}$, Eq. (D2) can be expressed in terms of a Feynman parameter,

$$\Upsilon^{(n)}_{(2,0)}(k) = \frac{i}{(4\pi)^{(d+1)/2}c}\Gamma\left(\frac{3-d}{2}\right)\int_0^1 dx\sqrt{\frac{1-x}{c^2+x(1+v^2-c^2)}}\left\{x(1-x)\left[|\mathbf{K}|^2 + \frac{c^2\varepsilon_{\bar{n}}^2(\vec{k})}{c^2+x(1+v^2-c^2)}\right]\right\}^{-\frac{3-d}{2}}$$
$$\times\left[\mathbf{K}\cdot\mathbf{\Gamma} - \frac{c^2\varepsilon_{\bar{n}}(\vec{k})\gamma_{d-1}}{c^2+x(1+v^2-c^2)}\right]. \tag{D5}$$

The UV divergent part in the $\epsilon \to 0$ limit is given by

$$\Upsilon^{(n)}_{(2,0)}(k) = \frac{i}{8\pi^2 c\epsilon}[h_1(v,c)\mathbf{K}\cdot\mathbf{\Gamma} - h_2(v,c)\varepsilon_{\bar{n}}(\vec{k})\gamma_{d-1}],$$

where $h_1(v,c) = \int_0^1 dx\sqrt{\frac{1-x}{c^2+(1+v^2-c^2)x}}$, $h_2(v,c) = c^2\int_0^1 dx\sqrt{\frac{1-x}{(c^2+(1+v^2-c^2)x)^3}}$. This leads to the one-loop counter term for the fermion self-energy:

$$\mathcal{S}^{(2,0)}_{\rm CT} = -i\frac{g^2}{4\pi^2 c\epsilon}\frac{N_c^2-1}{N_f N_c}\sum_{n=1}^{4}\sum_{\sigma=1}^{N_c}\sum_{j=1}^{N_f}\int\frac{d^{d+1}k}{(2\pi)^{d+1}}\bar{\Psi}_{n,\sigma,j}(k)[h_1(v,c)\mathbf{K}\cdot\mathbf{\Gamma} - h_2(v,c)\varepsilon_{\bar{n}}(\vec{k})\gamma_{d-1}]\Psi_{n,\sigma,j}(k). \tag{D6}$$

2. Boson self-energy

The boson self-energy in Fig. 8(b) is given by

$$\delta\mathcal{S}^{(0,2)} = -2g^2\mu^{3-d}\sum_a\int\frac{d^{d+1}q}{(2\pi)^{d+1}}\Upsilon_{(0,2)}(q)\phi^a(-q)\phi^a(q), \tag{D7}$$

where

$$\Upsilon_{(0,2)}(q) = \frac{1}{2}\sum_n\int\frac{d^{d-1}\mathbf{K}}{(2\pi)^{d-1}}\frac{d^2\vec{k}}{(2\pi)^2}\mathrm{Tr}[\gamma_{d-1}G_{\bar{n}}(k+q)\gamma_{d-1}G_n(k)]. \tag{D8}$$

We first integrate over $\vec{k}$. Using the Feynman parametrization, we write the resulting expression as

$$\Upsilon_{(0,2)}(q) = \frac{1}{2\pi v}\int_0^1 dx\int\frac{d^{d-1}\mathbf{K}}{(2\pi)^{d-1}}\frac{[x(1-x)]^{-\frac{1}{2}}\,\mathbf{K}\cdot(\mathbf{K}+\mathbf{Q})}{x|\mathbf{K}+\mathbf{Q}|^2 + (1-x)|\mathbf{K}|^2}. \tag{D9}$$

The quadratically divergent term is the mass renormalization, which is automatically tuned away at the critical point in the present scheme. The remaining correction to the kinetic energy of the boson becomes $\Upsilon_{(0,2)}(q) = -\frac{|\mathbf{Q}|^2}{16\pi v\epsilon}$ up to finite terms. Accordingly,

we add the following counter term:

$$\mathcal{S}_{\rm CT}^{(0,2)} = -\sum_a \frac{g^2}{8\pi v\epsilon}\int \frac{d^{d+1}q}{(2\pi)^{d+1}}|\mathbf{Q}|^2\phi^a(-q)\phi^a(q). \tag{D10}$$

3. Yukawa vertex correction

The diagram in Fig. 8(c) gives rise to the vertex correction in the quantum effective action,

$$\delta\mathcal{S}^{(2,1)} = i\frac{2g^3\mu^{\frac{3}{2}(3-d)}}{N_c N_f^{3/2}}\sum_{a,n}\sum_{j,\sigma,\sigma'}\int\frac{d^{d+1}k}{(2\pi)^{d+1}}\frac{d^{d+1}q}{(2\pi)^{d+1}}\phi^a(q)\bar{\Psi}_{n,\sigma,j}(k+q)\tau^a_{\sigma,\sigma'}\Upsilon^{(n)}_{(2,1)}(k,q)\Psi_{\bar{n},\sigma',j}(k), \tag{D11}$$

where

$$\Upsilon^{(n)}_{(2,1)}(k,q) = \int\frac{d^{d-1}\mathbf{P}}{(2\pi)^{d-1}}\frac{d^2\vec{p}}{(2\pi)^2}\gamma_{d-1}G_{\bar{n}}(p+q+k)\gamma_{d-1}G_n(p+k)\gamma_{d-1}D(p). \tag{D12}$$

Here, we use the identity for the SU(N_c) generators, $\sum_{a=1}^{N_c^2-1}\tau^a\tau^b\tau^a = -\frac{2}{N_c}\tau^b$. The UV divergent part in the $\epsilon\to 0$ limit, which can be extracted by setting all external frequency and momenta to zero except $\mathbf{K}$, is given by

$$\Upsilon^{(n)}_{(2,1)}(\mathbf{K}) = \gamma_{d-1}\int\frac{d^{d-1}\mathbf{P}}{(2\pi)^{d-1}}\frac{d^2\vec{p}}{(2\pi)^2}\frac{|\mathbf{P}|^2-\varepsilon_{\bar{n}}(\vec{p})\varepsilon_n(\vec{p})}{[|\mathbf{P}|^2+c^2|\vec{p}|^2]\big[|\mathbf{K}+\mathbf{P}|^2+\varepsilon_n^2(\vec{p})\big]\big[|\mathbf{K}+\mathbf{P}|^2+\varepsilon_{\bar{n}}^2(\vec{p})\big]}. \tag{D13}$$

We introduce two Feynman parameters to combine the denominators in the above expression. In new coordinates (R,θ) defined by $\varepsilon_n(\vec{p}) = \sqrt{2v}R\cos\theta$ and $\varepsilon_{\bar{n}}(\vec{p}) = \sqrt{2v}R\sin\theta$, Eq. (D13) is rewritten as

$$\Upsilon^{(n)}_{(2,1)}(\mathbf{K}) = \gamma_{d-1}\frac{\Gamma(3)}{4\pi^2}\int_0^1 dx_1\int_0^{1-x_1}dx_2\int_0^{2\pi}d\theta\int_0^\infty dRR\int\frac{d^{d-1}\mathbf{P}}{(2\pi)^{d-1}}\frac{|\mathbf{P}|^2-vR^2\sin(2\theta)}{[|\mathbf{P}|^2+2(x_1+x_2)\mathbf{K}\cdot\mathbf{P}+M^2(v,c,x_1,x_2,\mathbf{K},R,\theta)]^3}, \tag{D14}$$

where $M^2(v,c,x_1,x_2,\mathbf{K},R,\theta) = (x_1+x_2)|\mathbf{K}|^2 + R^2c\zeta(v,c,x_1,x_2,\theta)$ with $\zeta(v,c,x_1,x_2,\theta) = \frac{2v}{c}(x_1\cos^2\theta + x_2\sin^2\theta) + (1-x_1-x_2)(vc\cos^2(\theta+\pi/4) + \frac{c}{v}\sin^2(\theta+\pi/4))$. Integrating over $\mathbf{P}$ and R, we obtain $\Upsilon^{(n)}_{(2,1)}(\mathbf{K}) = \frac{\gamma_{d-1}}{16\pi^3\epsilon c}h_3(v,c) + \mathcal{O}(\epsilon^0)$, where

$$h_3(v,c) = \int_0^1 dx_1\int_0^{1-x_1}dx_2\int_0^{2\pi}d\theta\left[\frac{1}{\zeta(v,c,x_1,x_2,\theta)} - \frac{v\sin 2\theta}{c\zeta^2(v,c,x_1,x_2,\theta)}\right].$$

It is noted that the UV divergent part of $\Upsilon^{(n)}_{(2,1)}$ is independent of n. From this, we identify the counter term for the Yukawa vertex,

$$\mathcal{S}_{\rm CT}^{(2,1)} = -i\frac{g^3\mu^{(3-d)/2}}{8\pi^3 N_c N_f^{3/2}\epsilon c}h_3(v,c)\sum_{a,n}\sum_{j,\sigma,\sigma'}\int\frac{d^{d+1}k}{(2\pi)^{d+1}}\frac{d^{d+1}q}{(2\pi)^{d+1}}\phi^a(q)\cdot[\bar{\Psi}_{\bar{n},\sigma,j}(k+q)\tau^a_{\sigma,\sigma'}\gamma_{d-1}\Psi_{n,\sigma',j}(k)]. \tag{D15}$$

4. ϕ^4 vertex corrections

There are two one-loop diagrams for the quartic vertex. The quantum correction from Fig. 8(d) is given by

$$\begin{aligned}\delta\mathcal{S}_1^{(0,4)} = \frac{1}{4}\frac{g^4\mu^{2(3-d)}}{N_f^2}\sum_{a_1,a_2,a_3,a_4=1}^{N_c^2-1}\int\frac{d^{d+1}q_1}{(2\pi)^{d+1}}\frac{d^{d+1}q_2}{(2\pi)^{d+1}}\frac{d^{d+1}q_3}{(2\pi)^{d+1}}\frac{d^{d+1}q_4}{(2\pi)^{d+1}}\delta(q_1+q_2+q_3+q_4)\\ \times\Upsilon_{(0,4);1}(q_1,q_2,q_3)\mathrm{Tr}[\tau^{a_1}\tau^{a_2}\tau^{a_3}\tau^{a_4}]\phi^{a_1}(q_1)\phi^{a_2}(q_2)\phi^{a_3}(q_3)\phi^{a_4}(q_4),\end{aligned} \tag{D16}$$

where

$$\Upsilon_{(0,4);1}(q_1,q_2,q_3) = \sum_n\int\frac{d^{d+1}k}{(2\pi)^{d+1}}\mathrm{Tr}[\gamma_{d-1}G_n(q_1+k)\gamma_{d-1}G_{\bar{n}}(q_1+q_2+k)\gamma_{d-1}G_n(q_1+q_2+q_3+k)\gamma_{d-1}G_{\bar{n}}(k)]. \tag{D17}$$

When $\mathbf{Q}_i = 0$, the above expression becomes

$$\begin{aligned}\Upsilon_{(0,4);1}(q_1,q_2,q_3) = \sum_n\int\frac{d^{d+1}k}{(2\pi)^{d+1}}\mathrm{tr}\Big[\frac{1}{\varepsilon_n(\vec{q}_1+\vec{k})+\gamma_{d-1}\mathbf{K}\cdot\mathbf{\Gamma}}\frac{1}{\varepsilon_{\bar{n}}(\vec{q}_1+\vec{q}_2+\vec{k})+\gamma_{d-1}\mathbf{K}\cdot\mathbf{\Gamma}}\\ \times\frac{1}{\varepsilon_n(\vec{q}_1+\vec{q}_2+\vec{q}_3+\vec{k})+\gamma_{d-1}\mathbf{K}\cdot\mathbf{\Gamma}}\frac{1}{\varepsilon_{\bar{n}}(\vec{k})+\gamma_{d-1}\mathbf{K}\cdot\mathbf{\Gamma}}\Big].\end{aligned} \tag{D18}$$

The matrix $\gamma_{d-1}\mathbf{K}\cdot\mathbf{\Gamma}$ has an eigenvalue $i|\mathbf{K}|$ or $-i|\mathbf{K}|$. Since the Green's functions in the trace involve the common matrix, they always have poles on one side in the complex plane of k_x (k_y) for $n = 1,3$ ($n = 2,4$). This is because $\varepsilon_n(\vec{k})$ and $\varepsilon_{\bar{n}}(\vec{k})$ have the

same velocity in the k_x (k_y) direction for $n = 1,3$ ($n = 2,4$). As a result, the integration over $\vec{k}$ vanishes when the external $\mathbf{Q}_i$'s are zero. Therefore no counter term is generated from Fig. 8(d).

The diagram in Fig. 8(e) represents three different terms which are proportional to u_1^2, u_1u_2 and u_2^2. It is straightforward to compute the counter terms to obtain

$$\begin{aligned}\mathcal{S}_{\rm CT}^{(0,4)} = \frac{\mu^{3-d}}{8\pi^2c^2\epsilon}\int \frac{d^{d+1}q_1}{(2\pi)^{d+1}}\frac{d^{d+1}q_2}{(2\pi)^{d+1}}\frac{d^{d+1}q_3}{(2\pi)^{d+1}}\frac{d^{d+1}q_4}{(2\pi)^{d+1}}\delta(q_1+q_2+q_3+q_4)\\ \times\Bigg\{\Bigg[\Big(N_c^2+7\Big)u_1^2+2\Big(2N_c-\frac{3}{N_c}\Big)u_1u_2+3\Big(1+\frac{3}{N_c^2}\Big)u_2^2\Bigg]\mathrm{Tr}[\Phi(q_1)\Phi(q_2)]\mathrm{Tr}[\Phi(q_3)\Phi(q_4)]\\ +\Bigg[12u_1u_2+2\Big(N_c-\frac{9}{N_c}\Big)u_2^2\Bigg]\mathrm{Tr}[\Phi(q_1)\Phi(q_2)\Phi(q_3)\Phi(q_4)]\Bigg\}.\end{aligned} \tag{D19}$$

APPENDIX E: BEYOND ONE-LOOP

The stability of the quasilocal strange metallic fixed point has been established to the one-loop order. To examine higher-loop effects, one has to understand how general diagrams depend on the couplings and velocities. In the limit v,c are small, the largest contributions come from the diagrams where only nested hot spots are involved. Therefore we focus on the diagrams which have only $\Psi_{n,\sigma}$ and $\Psi_{\bar{n},\sigma}$ for a fixed n. Consider a general L-loop diagram that involves hot spots $n = 1,3$ with V_g Yukawa vertices and V_u quartic vertices,

$$\begin{aligned}I \sim g^{V_g}u_i^{V_u}\int\Big[\prod_{i=1}^{L}dp_i\Big]\prod_{l=1}^{I_f}\\ \times\Bigg\{\frac{1}{\mathbf{\Gamma}\cdot\mathbf{K}_l+\gamma_{d-1}\big[vk_{l,x}+(-1)^{\frac{n_l-1}{2}}k_{l,y}\big]}\Bigg\}\\ \times\prod_{m=1}^{I_b}\Big(\frac{1}{|\mathbf{Q}_m|^2+c^2|\vec{q}_m|^2}\Big).\end{aligned} \tag{E1}$$

Here, both u_1 and u_2 are loosely denoted as u_i because the power counting is equivalent for the two. $k_l = (\mathbf{K}_l,\vec{k}_l)$ and $q_m = (\mathbf{Q}_m,\vec{q}_m)$ represent the momenta that go through the fermion and boson propagators, respectively. They are linear superpositions of the internal momenta p_i and external momenta. n_l is either 1 or 3. Once x components of all momenta are scaled by $1/v$, one has

$$\begin{aligned}I \sim \frac{g^{V_g}u_i^{V_u}}{v^L}\int\Big[\prod_{i=1}^{L}dp_i\Big]\prod_{l=1}^{I_f}\\ \times\Bigg\{\frac{1}{\mathbf{\Gamma}\cdot\mathbf{K}_l+\gamma_{d-1}\big[k_{l,x}+(-1)^{\frac{n_l-1}{2}}k_{l,y}\big]}\Bigg\}\\ \times\prod_{m=1}^{I_b}\Bigg(\frac{1}{|\mathbf{Q}_m|^2+\frac{q_{m,x}^2}{w^2}+c^2q_{m,y}^2)}\Bigg).\end{aligned} \tag{E2}$$

The integrations of the internal momenta are well defined in the $v,c\to 0$ limit with fixed w as far as each loop contains at least one fermion propagator. The exceptions are the loops that are solely made of the boson propagators for which the y-momentum integration is UV divergent for $c = 0$. The UV divergence is cut off at $q_{m,y}\sim 1/c$ for each boson loop. If there are L_b boson loops, the entire diagram goes as

$$I \sim \frac{g^{V_g}u_i^{V_u}}{v^Lc^{L_b}} = \lambda^{\frac{V_g+2-E}{2}}\kappa_i^{V_u}w^{-V_u}g^{(E-2)}c^{\delta}, \tag{E3}$$

where E is the number of external lines and $\delta = V_u - L_b \geqslant 0$. Here we used the identity $L = \frac{V_g+2V_u+2-E}{2}$.

Equation (E3) implies that the multiplicative renormalizations for the kinetic energy ($E = 2$), the Yukawa coupling ($E = 3$), and the quartic vertices ($E = 4$) defined in Eq. (C2) go as

$$\begin{aligned}\mathcal{A}_1,..,\mathcal{A}_5 &\sim \lambda^{\frac{V_g}{2}}\kappa_i^{V_u}w^{-V_u}c^{\delta},\\ \mathcal{A}_6 &\sim \lambda^{\frac{V_g-1}{2}}\kappa_i^{V_u}w^{-V_u}c^{\delta},\\ \mathcal{A}_7 &\sim \lambda^{\frac{V_g-2}{2}}\kappa_i^{V_u}w^{-V_u}c^{\delta}\frac{g^2}{u_7},\\ \mathcal{A}_8 &\sim \lambda^{\frac{V_g-2}{2}}\kappa_i^{V_u}w^{-V_u}c^{\delta}\frac{g^2}{u_8}.\end{aligned} \tag{E4}$$

$\mathcal{A}_1,..,\mathcal{A}_6$ remain finite in the limit v,c,g,u_i go to zero with fixed λ,w,κ_i. Therefore higher-loop corrections in $\mathcal{A}_1,..,\mathcal{A}_6$ are systematically suppressed by powers of λ,κ_i. On the other hand, $\mathcal{A}_7$ and $\mathcal{A}_8$ are proportional to $\lambda^{\frac{V_g}{2}}\kappa_i^{V_u-1}w^{-V_u+1}c^{\delta-1}$. Since the higher-loop quantum corrections with $\delta\geqslant 1$ are obviously suppressed, we will focus on the contributions with $\delta = 0$ in $\mathcal{A}_7$ and $\mathcal{A}_8$, which go as $1/c$ in the $c\to 0$ limit. The only diagrams with $\delta = 0$ are the ones that do not contain u_i. At the one-loop order, there is one such diagram for the ϕ^4 vertices, Fig. 8(d). Due to a chiral structure that is present in the one-loop diagram, it vanishes as is shown in Sec. D 4. Higher-loop diagrams with $\delta = 0$ do not vanish in general. For example, the two-loop diagrams in Fig. 9 generate quantum corrections for κ_i that are order of $\frac{\lambda^3}{c}$. At $d = 3$, these higher-loop corrections are still vanishingly small in the low-energy limit. This is because λ vanishes as $1/l$ while c vanishes only as $1/\ln(l)$ in the $l\to\infty$ limit, where l is the logarithmic length scale. Since all higher-loop corrections are suppressed at $d = 3$, the one-loop beta functions become asymptotically exact in the low-energy limit where λ, κ_i vanish along with v, c. For $d < 3$, the higher-loop quantum corrections to κ_i grow as c becomes small with $\lambda\neq 0$. This suggests that c should be stabilized at a nonzero value once higher-loop corrections are included. In particular, κ_i enters into the beta function of c at the three-loop and higher orders. It is expected that the feedback of κ_i will stabilize c at a

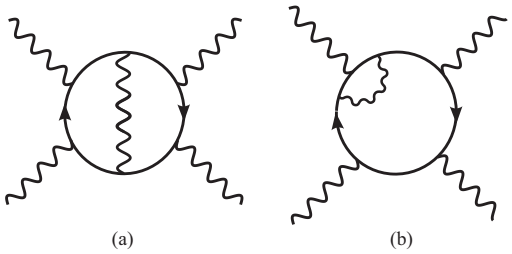

FIG. 9. Nonvanishing two-loop corrections to the ϕ^4 vertex that do not contain u_1 or u_2.

nonzero value in the low-energy limit. Once the velocity becomes nonzero, κ_i will flow to a nonzero and finite value at the fixed point. Because of the continuity from the exact $d = 3$ fixed point, not only c, v, κ_i, λ but also $\frac{\lambda^n}{c}$ with $n \geqslant 3$ at the fixed point in $d = 3 - \epsilon$ should go to zero in the $\epsilon \to 0$ limit. Therefore higher-order corrections including the corrections to κ_i with $\delta = 0$ are systematically suppressed, and the expansion is controlled for small ϵ.

APPENDIX F: ENHANCEMENT OF SUPERCONDUCTING AND CHARGE DENSITY WAVE FLUCTUATIONS

In this appendix, we compute the anomalous dimensions of the superconducting (SC) and charge density wave (CDW) operators that are enhanced at the strange metallic fixed point.

1. Anomalous dimension

We consider an insertion of a fermion bilinear,

$$\mathcal{S}_\rho = \rho\mu \int \frac{d^{d+1}k}{(2\pi)^{d+1}} \widetilde{\Psi}_{n,\sigma,j}(k)\Omega_{n,\sigma,j;n',\sigma',j'}\Psi_{n',\sigma',j'}(k). \quad \text{(F1)}$$

Here, ρ is a dimensionless source. $\widetilde{\Psi}_{n,\sigma,j}(k)$ is either $\bar{\Psi}_{n,\sigma,j}(k)$ or $\Psi^T_{n,\sigma,j}(-k)$ depending on whether the operator creates particle-hole or particle-particle excitations. $\Omega_{n,\sigma,j;n',\sigma',j'}$ is a matrix that specifies the momentum, spin, and flavor quantum numbers of the insertion. The UV divergence in the quantum effective action coming from the insertion is canceled by a counter term of the same form, $\mathcal{S}_{\rho;\mathrm{CT}} = \rho\mu\mathcal{A}_\rho \int \frac{d^{d+1}k}{(2\pi)^{d+1}} \widetilde{\Psi}_{n,\sigma,j}(k)\Omega_{n,\sigma,j;n',\sigma',j'}\Psi_{n',\sigma',j'}(k)$ with $\mathcal{A}_\rho = \sum_m \frac{Z_{\rho,m}}{\epsilon^m}$. The renormalized insertion can be written as

$$\mathcal{S}_{\rho;\mathrm{ren}} = \rho_B \int \frac{d^{d+1}k_B}{(2\pi)^{d+1}} \widetilde{\Psi}_{B;n,\sigma,j}(k)\Omega_{n,\sigma,j;n',\sigma',j'}\Psi_{B;n',\sigma',j'}(k), \quad \text{(F2)}$$

where the renormalized source ρ is related to the bare source ρ_B as $\rho = \mu^{-1}\frac{\mathcal{Z}_\psi \mathcal{Z}_\tau^{d-1}}{\mathcal{Z}_\rho}\rho_B$ with $\mathcal{Z}_\rho = 1 + \mathcal{A}_\rho$. From this, one can obtain the beta function for the source,

$$\frac{d\rho}{dl} = \rho(1 + \gamma_\rho), \quad \text{(F3)}$$

where $\gamma_\rho = z(\frac{g}{2}\partial_g + u_i\partial_{u_i})(Z_{3,1} - Z_{\rho,1})$ is the anomalous dimension of the source. The larger the anomalous dimension of the source is, the stronger the enhancement is.

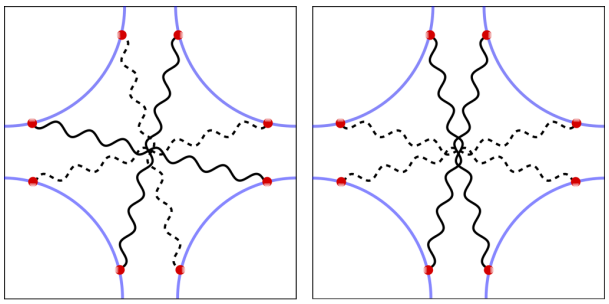

(a) (b)

FIG. 10. (Color online) Cooper pair wave functions represented by the vertices (a) $\mathcal{S}^{(+)}_{A,\gamma_{d-1}}$ and (b) $\mathcal{S}^{(-)}_{A,\gamma_{d-1}}$. A wiggly line connecting two momenta k_1 and k_2 represents a Cooper pair made of electrons at those momenta. The dashed wiggly lines are intended to represent the relative minus sign in the Cooper pair wave function relative to the ones connected by the solid lines. The Cooper pair created by $\mathcal{S}^{(+)}_{A,\gamma_{d-1}}(\mathcal{S}^{(-)}_{A,\gamma_{d-1}})$ undergoes four (two) phase winding under 2π rotation, which correspond to g ($d_{x^2-y^2}$) wave pairing.

2. Superconducting channel

Here, we examine the superconducting channels described by the pairing vertices of the form

$$\mathcal{S}^{(\pm)}_{A,\widehat{\Omega}} = \mu V \sum_{j,\sigma,\sigma'} \int \frac{d^{d+1}k}{(2\pi)^{d+1}} \{[\Psi^T_{1,\sigma,j}(-k)A_{\sigma,\sigma'}\widehat{\Omega}\Psi_{1,\sigma',j}(k) + \Psi^T_{3,\sigma,j}(-k)A_{\sigma,\sigma'}\widehat{\Omega}\Psi_{3,\sigma',j}(k)] \pm [\Psi^T_{2,\sigma,j}(-k)A_{\sigma,\sigma'} \times \widehat{\Omega}\Psi_{2,\sigma',j}(k) + \Psi^T_{4,\sigma,j}(-k)A_{\sigma,\sigma'}\widehat{\Omega}\Psi_{4,\sigma',j}(k)]\}. \quad \text{(F4)}$$

Here, V is a source for the pairing operator. $A_{\sigma,\sigma'}$ is an antisymmetric matrix that represents the spin-singlet pairing for the case of $N_c = 2$. $\widehat{\Omega}$ is a 2×2 matrix that acts on the Dirac indices. Among all possible $\widehat{\Omega}$, we find the channels with $\widehat{\Omega} = \gamma_{d-1}$ and I are most strongly enhanced. Therefore we will focus on these channels in the rest of the section. $\mathcal{S}^{(+)}_{A,\gamma_{d-1}}(\mathcal{S}^{(-)}_{A,\gamma_{d-1}})$ describes the g-wave ($d_{x^2-y^2}$-wave) pairing with zero net momentum of Cooper pairs as is illustrated in Fig. 10. $\mathcal{S}^{(+)}_{A,I}(\mathcal{S}^{(-)}_{A,I})$

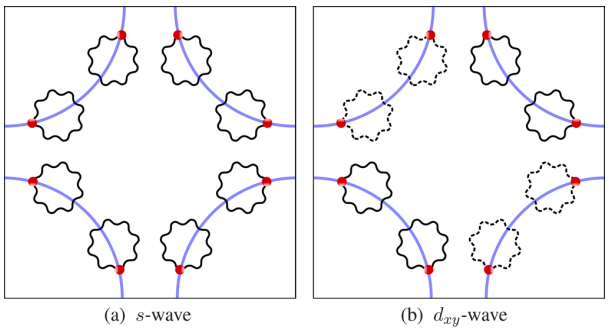

(a) s-wave (b) d_{xy}-wave

FIG. 11. (Color online) Cooper pair wave functions represented by the vertices (a) $\mathcal{S}^{(+)}_{A,I}$ and (b) $\mathcal{S}^{(-)}_{A,I}$. A wiggly line that ends on a hot spot represents a Cooper pair made of electrons from that hot spot. Therefore the Cooper pair carries nonzero momenta, $2\vec{k}_F$. The Cooper pair created by $\mathcal{S}^{(+)}_{A,I}(\mathcal{S}^{(-)}_{A,I})$ undergoes zero (two) phase winding under 2π rotation, which correspond to s (d_{xy}) wave pairing.

describes the Cooper pairs with nonzero net momentum $2\vec{k}_F$ in the s-wave (d_{xy}-wave) channel as is shown in Fig. 11.

The one-loop quantum correction to the SC insertion is given by

$$\delta\mathcal{S}^{(\pm)}_{A,\widehat{\Omega}} = N_V \mu^{4-d} V g^2 \sum_{j,\sigma,\sigma'} \int \frac{d^{d+1}k}{(2\pi)^{d+1}} \Big\{ \Big[\Psi^T_{1,\sigma,j}(-k) A_{\sigma,\sigma'} \Upsilon^{(1)}_{\widehat{\Omega}}(k) \Psi_{1,\sigma',j}(k) + \Psi^T_{3,\sigma,j}(-k) A_{\sigma,\sigma'} \Upsilon^{(3)}_{\widehat{\Omega}}(k) \Psi_{3,\sigma',j}(k) \Big] \pm \Big[\Psi^T_{2,\sigma,j}(-k) A_{\sigma,\sigma'} \Upsilon^{(2)}_{\widehat{\Omega}}(k) \Psi_{2,\sigma',j}(k) + \Psi^T_{4,\sigma,j}(-k) A_{\sigma,\sigma'} \Upsilon^{(4)}_{\widehat{\Omega}}(k) \Psi_{4,\sigma',j}(k) \Big] \Big\}, \tag{F5}$$

where

$$\Upsilon^{(n)}_{\widehat{\Omega}}(k) = \int \frac{d^{d+1}q}{(2\pi)^{d+1}} D(q) \gamma^T_{d-1} G^T_{\bar{n}}(-k-q) \widehat{\Omega} G_{\bar{n}}(k+q) \gamma_{d-1} \tag{F6}$$

and $N_V = \frac{2(N_c+1)}{N_c N_f}$. Using $\gamma_0^T = -\gamma_0$ and $\gamma_i^T = \gamma_i$, for $i = 1,2,\ldots,(d-1)$, we obtain

$$\Upsilon^{(n)}_{\widehat{\Omega}}(\mathbf{K}) = \int \frac{d^{d+1}q}{(2\pi)^{d+1}} \frac{\big[(K_0+Q_0)\gamma_0 - \sum_{\nu=1}^{d-2}(K_\nu+Q_\nu)\gamma_\nu + \varepsilon_{\bar{n}}(\vec{q})\gamma_{d-1}\big]\gamma_{d-1}\widehat{\Omega}\gamma_{d-1}[-(\mathbf{K}+\mathbf{Q})\cdot\mathbf{\Gamma} + \varepsilon_{\bar{n}}(\vec{q})\gamma_{d-1}]}{[|\mathbf{Q}|^2 + c^2|\vec{q}|^2]\big[|\mathbf{K}+\mathbf{Q}|^2 + \varepsilon^2_{\bar{n}}(\vec{q})\big]^2}, \tag{F7}$$

when $\vec{k} = 0$. Changing coordinates from (q_x, q_y) to (R,θ) with $\varepsilon_{\bar{n}}(\vec{q}) = \sqrt{2v}R\cos\theta$ and $\varepsilon_n(\vec{q}) = \sqrt{2v}R\sin\theta$, one can perform the integrations over R and $\mathbf{Q}$ using the Feynman parametrization to obtain

$$\Upsilon^{(n)}_{\widehat{\Omega}}(\mathbf{K}) = \frac{1}{16\pi^3 c\epsilon}\widehat{\Omega} h_{\rm SC}(v,c) + \mathcal{O}(\epsilon^0),$$

where $h_{\rm SC}(v,c) = \frac{2v}{c}\int_0^1 dx \int_0^{2\pi} d\theta \frac{x\cos^2\theta}{\zeta_1^2(v,c,x,\theta)}$ with

$$\zeta_1(v,c,x,\theta) = \frac{2vx}{c}\cos^2\theta + (1-x)\left[\frac{c}{v}\sin^2\left(\theta+\frac{\pi}{4}\right) + vc\cos^2\left(\theta+\frac{\pi}{4}\right)\right].$$

Note that $h_{\rm SC}(v,c)$ is same for $\widehat{\Omega} = \gamma_{d-1}, I$. Therefore we add the counter term

$$\mathcal{S}^{(\pm)}_{A,\widehat{\Omega};\rm CT} = -\mu V \frac{N_V}{16\pi^3\epsilon}\frac{g^2}{c} h_{\rm SC}(v,c) \sum_{\sigma,\sigma'} \int \frac{d^{d+1}k}{(2\pi)^{d+1}} \Big\{ \Big[\Psi^T_{1,\sigma}(-k) \times A_{\sigma,\sigma'}\widehat{\Omega}\Psi_{1,\sigma'}(k) + \Psi^T_{3,\sigma}(-k) A_{\sigma,\sigma'}\widehat{\Omega}\Psi_{3,\sigma'}(k) \Big] \pm \Big[\Psi^T_{2,\sigma}(-k) A_{\sigma,\sigma'}\widehat{\Omega}\Psi_{2,\sigma'}(k) + \Psi^T_{4,\sigma}(-k) A_{\sigma,\sigma'}\widehat{\Omega}\Psi_{4,\sigma'}(k) \Big] \Big\}, \tag{F8}$$

which gives the anomalous dimension of the source, $\gamma_V = \frac{N_V}{8\pi^2}\frac{zg^2}{c}[\frac{1}{2\pi}h_{\rm SC}(v,c) - (N_c-1)h_2(v,c)]$ for the four vertices, $\mathcal{S}^{(\pm)}_{A,\gamma_{d-1}}$ and $\mathcal{S}^{(\pm)}_{A,I}$. At the quasilocal strange metal fixed point, we have $\lim_{c\to 0} h_2(w^*c,c) = 0$ and $\lim_{c\to 0} h_{\rm SC}(w^*c,c) = \pi^2$, and the anomalous dimension becomes $\gamma_V = \frac{\lambda^*}{8\pi(N_c-1)}$.

It is interesting that the finite momentum pairing is as strong as the zero=momentum pairing. This is a consequence of the nesting, which allows a pair of electrons to stay on the Fermi surface as they are scattered from one hot spot to another. The attractive interaction is mediated by the commensurate spin fluctuations which scatter a pair of electrons in one hot spot to another hot spot, e.g., from 1+ to 1−. Because one electron in the Cooper pair with momentum $2\vec{k}_F$ is above the Fermi surface and the other is below the Fermi surface, the matrix element for the scattering is negative at low frequencies. As a result, the interaction is attractive in the symmetric combination.

3. Charge density wave channel

Here, we compute anomalous dimensions for CDW operators of the form

$$\mathcal{S}^{(\pm)}_{\rho} = \rho^{(\pm)}\mu \sum_{j,\sigma}\int \frac{d^{d+1}k}{(2\pi)^{d+1}} \times \{[\bar{\Psi}_{1,\sigma,j}(k)\Psi_{1,\sigma,j}(k) + \bar{\Psi}_{3,\sigma,j}(k)\Psi_{3,\sigma,j}(k)] \pm [\bar{\Psi}_{4,\sigma,j}(k)\Psi_{4,\sigma,j}(k) + \bar{\Psi}_{2,\sigma,j}(k)\Psi_{2,\sigma,j}(k)]\}. \tag{F9}$$

$\mathcal{S}^{(+)}_{\rho}$ ($\mathcal{S}^{(-)}_{\rho}$) describes a p_y-wave (p_x-wave) CDW that carries momentum $2\vec{k}_F$ as is shown in Fig. 12. These operators are pseudospin singlets for $N_c = 2$ and have no SC counterpart connected by the pseudospin transformation. The one-loop

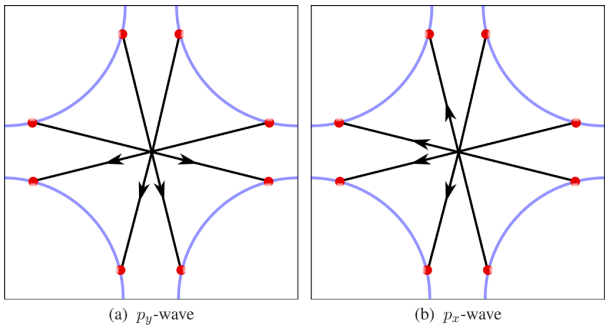

(a) p_y-wave (b) p_x-wave

FIG. 12. (Color online) Wave functions of the particle-hole pairs created by the vertices (a) $\mathcal{S}^{(+)}_{\rho}$ and (b) $\mathcal{S}^{(-)}_{\rho}$. An arrow from k_2 to k_1 represents a particle-hole pair created by $i(c^*_{k_1}c_{k_2} - c^*_{k_2}c_{k_1})$, where c_k is the electron field at momentum k with spin and flavor indices suppressed. $\mathcal{S}^{(+)}_{\rho}$ ($\mathcal{S}^{(-)}_{\rho}$) is odd under the y (x) reflection, while both of them preserve time reversal.

quantum correction is given by

$$\delta\mathcal{S}_{\rho}^{(\pm)} = -N_{\rho}\rho^{(\pm)}\mu^{4-d}g^2\sum_{j,\sigma}\int\frac{d^{d+1}k}{(2\pi)^{d+1}}\Big\{\big[\bar{\Psi}_{1,\sigma,j}(k)\Upsilon_{\rho}^{(1)}(k)\Psi_{1,\sigma,j}(k)+\bar{\Psi}_{3,\sigma,j}(k)\Upsilon_{\rho}^{(3)}(k)\Psi_{3,\sigma,j}(k)\big]$$
$$\pm\big[\bar{\Psi}_{2,\sigma,j}(k)\Upsilon_{\rho}^{(2)}(k)\Psi_{2,\sigma,j}(k)+\bar{\Psi}_{4,\sigma,j}(k)\Upsilon_{\rho}^{(4)}(k)\Psi_{4,\sigma,j}(k)\big]\Big\}, \tag{F10}$$

where

$$\Upsilon_{\rho}^{(n)}(k) = \int\frac{d^{d+1}q}{(2\pi)^{d+1}}D(q)\gamma_{d-1}G_{\bar{n}}(k+q)G_{\bar{n}}(k+q)\gamma_{d-1} \tag{F11}$$

and $N_{\rho} = \frac{2}{N_f}(N_c - \frac{1}{N_c})$. From a straightforward calculation, we identify the counter term

$$\mathcal{S}_{\rho;\mathrm{CT}}^{(\pm)} = -\rho^{(\pm)}\mu\frac{N_{\rho}}{16\pi^3\epsilon}\frac{g^2}{c}h_{\mathrm{CDW}}(v,c)\sum_{j,\sigma}\int\frac{d^{d+1}k}{(2\pi)^{d+1}}\{[\bar{\Psi}_{1,\sigma,j}(k)\Psi_{1,\sigma,j}(k)+\bar{\Psi}_{3,\sigma,j}(k)\Psi_{3,\sigma,j}(k)]$$
$$\pm[\bar{\Psi}_{4,\sigma,j}(k)\Psi_{4,\sigma,j}(k)+\bar{\Psi}_{2,\sigma,j}(k)\Psi_{2,\sigma,j}(k)]\}, \tag{F12}$$

where $h_{\mathrm{CDW}}(v,c) = \int_0^1 dx\int_0^{2\pi}d\theta x[\frac{1}{\zeta_1(v,c,x,\theta)} + \frac{2v}{c}\frac{\cos^2\theta}{\zeta_1^2(v,c,x,\theta)}]$. From this we find the anomalous dimension of the CDW source, $\gamma_{\mathrm{CDW}}^{(\pm)} = \frac{N_{\rho}}{16\pi^3}\frac{zg^2}{c}[h_{\mathrm{CDW}}(v,c) - 2\pi h_2(v,c)]$. At the fixed point, we have $\lim_{c\to 0}h_{\mathrm{CDW}}(w^*c,c) = 2\pi^2$ and the anomalous dimension becomes $\gamma_{\mathrm{CDW}}^{(\pm)} = \frac{\lambda^*}{4\pi}$.

[1] X.-G. Wen, *Quantum Field Theory of Many-Body Systems*, Oxford Graduate Texts (Oxford University Press, New York, 2007).
[2] S. Sachdev, *Quantum Phase Transitions* (Cambridge University Press, Cambridge, 2011).
[3] R. Shankar, Rev. Mod. Phys. **66**, 129 (1994).
[4] J. Polchinski, *Proceedings of the 1992 TASI*, edited by J. Harvey and J. Polchinski (World Scientific, Singapore, 1993).
[5] L. Landau, Sov. Phys. JETP **3**, 920 (1957).
[6] J. A. Hertz, Phys. Rev. B **14**, 1165 (1976).
[7] A. J. Millis, Phys. Rev. B **48**, 7183 (1993).
[8] H. v. Löhneysen, A. Rosch, M. Vojta, and P. Wölfle, Rev. Mod. Phys. **79**, 1015 (2007).
[9] G. R. Stewart, Rev. Mod. Phys. **73**, 797 (2001).
[10] T. Senthil, Phys. Rev. B **78**, 035103 (2008).
[11] C. Nayak and F. Wilczek, Nucl. Phys. B **417**, 359 (1994).
[12] D. F. Mross, J. McGreevy, H. Liu, and T. Senthil, Phys. Rev. B **82**, 045121 (2010).
[13] H.-C. Jiang, M. S. Block, R. V. Mishmash, J. R. Garrison, D. Sheng, O. I. Motrunich, and M. P. Fisher, Nature (London) **493**, 39 (2013).
[14] D. Dalidovich and S.-S. Lee, Phys. Rev. B **88**, 245106 (2013).
[15] S. Sur and S.-S. Lee, Phys. Rev. B **90**, 045121 (2014).
[16] T. Helm, M. V. Kartsovnik, I. Sheikin, M. Bartkowiak, F. Wolff-Fabris, N. Bittner, W. Biberacher, M. Lambacher, A. Erb, J. Wosnitza, and R. Gross, Phys. Rev. Lett. **105**, 247002 (2010).
[17] K. Hashimoto, K. Cho, T. Shibauchi, S. Kasahara, Y. Mizukami, R. Katsumata, Y. Tsuruhara, T. Terashima, H. Ikeda, M. A. Tanatar, H. Kitano, N. Salovich, R. W. Giannetta, P. Walmsley, A. Carrington, R. Prozorov, and Y. Matsuda, Science **336**, 1554 (2012).
[18] T. Park, F. Ronning, H. Yuan, M. Salamon, R. Movshovich, J. Sarrao, and J. Thompson, Nature (London) **440**, 65 (2006).
[19] A. Abanov and A. V. Chubukov, Phys. Rev. Lett. **84**, 5608 (2000).
[20] A. Abanov and A. Chubukov, Phys. Rev. Lett. **93**, 255702 (2004).
[21] E. Berg, M. A. Metlitski, and S. Sachdev, Science **338**, 1606 (2012).
[22] M. A. Metlitski and S. Sachdev, Phys. Rev. B **82**, 075128 (2010).
[23] T. Senthil and R. Shankar, Phys. Rev. Lett. **102**, 046406 (2009).
[24] A. L. Fitzpatrick, S. Kachru, J. Kaplan, and S. Raghu, Phys. Rev. B **88**, 125116 (2013).
[25] J. Lee, P. Strack, and S. Sachdev, Phys. Rev. B **87**, 045104 (2013).
[26] C. M. Varma, P. B. Littlewood, S. Schmitt-Rink, E. Abrahams, and A. E. Ruckenstein, Phys. Rev. Lett. **63**, 1996 (1989).
[27] Y. Huh and S. Sachdev, Phys. Rev. B **78**, 064512 (2008).
[28] L. Savary, E.-G. Moon, and L. Balents, Phys. Rev. X **4**, 041027 (2014).
[29] Q. Si, S. Rabello, K. Ingersent, and J. L. Smith, Nature (London) **413**, 804 (2001).
[30] S.-S. Lee, Phys. Rev. D **79**, 086006 (2009).
[31] M. Čubrović, J. Zaanen, and K. Schalm, Science **325**, 439 (2009).
[32] T. Faulkner, H. Liu, J. McGreevy, and D. Vegh, Phys. Rev. D **83**, 125002 (2011).
[33] K. Efetov, H. Meier, and C. Pépin, Nat. Phys. **9**, 442 (2013).
[34] S. Sachdev and R. La Placa, Phys. Rev. Lett. **111**, 027202 (2013).
[35] D. J. Scalapino, E. Loh, Jr., and J. E. Hirsch, Phys. Rev. B **34**, 8190 (1986).
[36] K. Miyake, S. Schmitt-Rink, and C. M. Varma, Phys. Rev. B **34**, 6554 (1986).
[37] P. Fulde and R. A. Ferrell, Phys. Rev. **135**, A550 (1964).
[38] A. I. Larkin and Y. N. Ovchinnikov, Sov. Phys. JETP **20**, 762 (1965).
[39] E. Berg, E. Fradkin, and S. A. Kivelson, Nat. Phys. **5**, 830 (2009).
[40] P. A. Lee, Phys. Rev. X **4**, 031017 (2014).
[41] A. L. Fitzpatrick, S. Kachru, J. Kaplan, and S. Raghu, Phys. Rev. B **89**, 165114 (2014).
[42] S. A. Hartnoll, D. M. Hofman, M. A. Metlitski, and S. Sachdev, Phys. Rev. B **84**, 125115 (2011).
[43] S. Sur and S.-S. Lee (unpublished).

CHAPTER 3

DENSITY WAVE CRITICALITIES IN ANISOTROPIC METALS

In the previous chapter, we considered the spin density wave (SDW) transition in a fourfold rotation (C_4) symmetric metal. In this chapter we study the critical points at both spin and charge density wave transitions in a metal with two fold rotational (C_2) symmetry [68].

3.1 Preface

The motivation for the work presented in this chapter is threefold:

1. The presence of C_4 symmetry forces x and y components of momenta to scale identically. Therefore, by relaxing the C_4 symmetry to C_2, it is in principle possible to obtain an *anisotropic* fixed point, where x and y components of momenta have distinct scaling dimensions.

2. In the last chapter we presented a one-loop analysis of the SDW critical point in C_4-symmetric systems. Although we obtained a stable fixed point below three dimensions,

the correct expansion parameter was unclear because of the IR enhancements brought about by the quasilocality. Further, the extent of the quasilocality itself may not be robust against higher-loop quantum corrections, since they can potentially renormalize some of the hitherto vanishing velocity components to non-zero values. The presence of C_4 symmetry reduces the number of ways the system can adjust in response to quantum fluctuations. Thus, it is interesting to inquire whether relaxing such constrains enables the system to adopt a different strategy while it seeks to stabilize itself.

3. Within the framework of the hotspot based spin-fermion model it is possible to describe not only SDW transitions, but also charge density wave (CDW) transitions. While the CDW vertex commutes with itself, the SDW vertex does not, which is expected to lead to contrasting low energy behavior. The contrast is apparent at one-loop order, where the vertex correction at the SDW (CDW) critical point anti-screens (screens) the electron-boson interaction vertex. As we shall see in the enclosed article, the sign of the vertex correction ultimately determines the fate of a continuous phase transition between a Fermi liquid and the proposed ordered state. Thus, elucidation of the contrast between the two density wave instabilities provides an additional insight.

We use the dimensional regularization scheme discussed in the last chapter to control quantum fluctuations near the upper critical dimensions. Although some degree of quasilocality is still present at the one-loop order, inclusion of a two-loop contribution removes the quasilocality. The stable fixed point, thus obtained, reveals a new kind of NFL state, where a universal Fermi surface curvature emerges at the hotspots due to spatial anisotropy, and the ratios of the boson and electron velocity components flow to universal values at the fixed point.

The CDW critical point is likely to be unstable below three dimensions to either a discontinuous transition, or formation of other kinds of CDW states that are not accounted for in the current formalism. However, in three dimensions, there is a stable fixed point with a finite basin of attraction, which is described by a quasilocal marginal Fermi liquid state.

Anisotropic Non-Fermi Liquids

Shouvik Sur[1] and Sung-Sik Lee[1,2]

[1]Department of Physics & Astronomy, McMaster University,
1280 Main St. W., Hamilton ON L8S 4M1, Canada

[2]Perimeter Institute for Theoretical Physics,
31 Caroline St. N., Waterloo ON N2L 2Y5, Canada

We study non-Fermi liquids that arise at the quantum critical points associated with the spin and charge density wave transitions in metals with the C_2 symmetry. We use the dimensional regularization scheme, where one-dimensional Fermi surface is embedded in $3-\epsilon$ dimensional momentum space. In three dimensions, quasilocal marginal Fermi liquids arise at the spin and charge density wave critical points. The speed of order parameter fluctuations along the ordering wavevector is logarithmically renormalized to zero compared to that of Fermi velocity. Below three dimensions, a perturbative anisotropic non-Fermi liquid is realized at the spin density wave critical point, where not only time but also different spatial coordinates develop distinct anomalous dimensions. The stable non-Fermi liquid exhibits an emergent algebraic nesting as the patches of Fermi surface are deformed into a universal power-law shape near the hot spots. Due to the anisotropic scaling, the energy of spin fluctuations disperse with different power laws in different momentum directions. At the charge density wave critical point, on the other hand, the perturbative expansion breaks down immediately below three dimensions as the interaction renormalizes the speed of charge fluctuations to zero within a finite renormalization group scale through a two-loop effect.

I. INTRODUCTION

Continuous quantum phase transitions are believed to play important roles in several classes of strongly correlated metals such as high T_c cuprates, iron pnictides, and heavy fermion compounds [1–7]. Proximity of metals to symmetry broken phases generates intriguing non-Fermi liquid behaviors near quantum critical points through the coupling between soft particle-hole excitations and the order parameter fluctuations. At the critical point, the low-energy excitations near the Fermi surface strongly damp the order parameter fluctuations which, in turn, feed back to affect the dynamics of low energy fermions [8–19]. In two space dimensions, the metallic quantum critical points remain largely ill-understood due to strong coupling between the itinerant electrons and the collective modes.

In chiral non-Fermi liquids, strong kinematic constraints protect critical exponents from quantum corrections beyond one-loop, although it is a strongly coupled theory in two space dimensions[20]. However, such non-perturbative constraints are not available for non-chiral cases. In the absence of general non-perturbative tools, it is of interest to find perturbative non-Fermi liquids which can be understood in a controlled way. Different deformations have been considered to find controlled non-Fermi liquids. An introduction of a large number of flavors fails to tame strong quantum fluctuations in the presence of a Fermi surface [21–24]. To tame quantum fluctuations, one can use a dimensional regularization scheme where the dimension of space is increased with the co-dimension of the Fermi surface fixed to be one [25–27]. This scheme preserves a non-vanishing density of states at the Fermi surface. However, the increase in the dimension of Fermi surface beyond one results in an UV/IR mixing[28], which leads to a loss of emergent locality in the momentum space[29]. In the presence of UV/IR mixing, the size of Fermi surface enters in the low-energy scaling of all physical quantities unlike in two space dimensions. An alternative strategy is to reduce the density of states for the collective boson [30, 31] or the fermions [32–34]. This can be achieved either by modifying the dispersion to a non-local form or embedding the one-dimensional Fermi surface in a higher dimensional space. In the latter 'co-dimensional' regularization scheme, one can preserve locality and avoid UV/IR mixing by introducing a nodal gap generated by breaking certain symmetry, which leaves behind a one-dimensional Fermi surface embedded in general dimensions[32, 34]. Perturbative non-Fermi liquids become accessible near the upper critical dimension, where the deviation from the upper critical dimension becomes a small parameter.

In a recent work [34], a spin-density wave critical point was studied in a metal with the C_4 symmetry based on the co-dimensional regularization scheme. From one-loop renormalization group (RG) analysis, a stable quasilocal non-Fermi liquid state was found at the infrared (IR) fixed point below three dimensions. Although interactions are renormalized to zero in the low energy limit, an emergent nesting enhances quantum fluctuations. A balance between the vanishing coupling and the IR singularity caused by the dynamical nesting results in a stable non-Fermi liquid.

The emergent nesting is a consequence of interaction which tends to localize particles in certain directions in the real space. However, the effect of the interactions is rather limited in the presence of the C_4 symmetry, which constrains the x and y components of momentum to scale identically. Because the deviation from perfect nesting flows to zero only logarithmically in length scale, the Fermi surface nesting becomes noticeable only when the momentum is exponentially close to the hot spot. The situation is different when the C_4 symmetry is explicitly or spontaneously broken to the two-fold rotational symmetry[35–42]. If the system undergoes a

continuous density wave transition in metals with the C_2 symmetry [43, 44], a new type of non-Fermi can emerge at the quantum critical point. Because different components of momentum receive different quantum corrections, the system can exhibit a stronger dynamical nesting. In this paper, we study the scaling properties of the quantum critical points associated with spin density wave (SDW) and charge density wave (CDW) transitions in metals with the C_2 symmetry.

The paper is organized as follows. In section II, we introduce the low energy effective theory that describes the density wave critical points in two space dimensions with the C_2 symmetry. We take advantage of the formal similarities between the SDW and the CDW critical points to formulate a unified approach to both cases. Here we employ the dimensional regularization scheme, where the one-dimensional Fermi surface is embedded in $3-\epsilon$ space dimensions. In section III, we outline the RG procedure, and derive the general expressions for the critical exponents and the beta functions. In section IV, we show that the SDW critical point is described by a non-Fermi liquid fixed point below three dimensions. In the low energy limit, not only frequency but also different momentum components acquire anomalous dimensions, resulting in an anisotropic non-Fermi liquid. We compute the critical exponents that govern the anisotropy and other critical exponents to the leading order in ϵ. In the low energy limit, the energy of the collective mode disperses with different powers in different momentum directions. Furthermore, the Fermi surface near the hot spots connected by the SDW vector is deformed to a universal power-law shape. The algebraic nesting is much stronger compared to the C_4 symmetric case where the Fermi surface is deformed only logarithmically. It is also shown that a component of the boson velocity, which flows to zero at the one-loop order, flows to a nonzero value which is order of $\epsilon^{1/3}$ due to a two-loop correction. The non-zero but small velocity enhances some of the higher-loop diagrams. Despite the enhancement, higher loop corrections are systematically suppressed in the small ϵ limit. Section V is devoted to the CDW critical point. Although the system flows to a stable marginal Fermi liquid in three dimensions, it flows out of the perturbative window in the low energy limit for any nonzero ϵ. In section VI, we conclude with a summary.

II. THE MODEL

In this section we introduce the minimal model for the quantum critical point associated with the spin and charge density wave transitions in a two-dimensional metal with the C_2 symmetry. A rectangular lattice with anisotropic hoppings in the $\hat{x}$ and $\hat{y}$ directions gives an anisotropic Fermi surface as is shown in Fig. 1a. At a generic filling, the Fermi surface is not nested. Without nesting, weak interactions do not produce density wave instabilities. Here we assume that there exists a microscopic Hamiltonian with a finite strength of interaction that drives a spin or charge density wave transition in the C_2 symmetric metal. We consider a commensurate density wave with wave vector $\vec{Q}_{ord}$ which satisfies $2\vec{Q}_{ord} = 0$ modulo the reciprocal vectors. The specific choice of the wave vector and the shape of the Fermi surface is unimportant for the low energy description of the quantum critical point. This is because the order parameter fluctuations are strongly coupled with electrons near a finite number of hot spots which are connected to each other through the primary wave vector $\vec{Q}_{ord}$. The hot spots are represented as (red) dots in Fig. 1b. In the ordered state, the Fermi surface is reconstructed (see Fig. 1c) due to a gap that opens up in the single particle excitation spectrum at the hot spots.

We study the universal properties of the critical points within the framework of low energy effective field theory that is independent of the microscopic details. A spin-fermion model is the minimal theory that describes the interaction between the collective mode and the itinerant electrons [45, 46]. In the minimal model, we focus on the vicinity of the hot spots and consider interactions of the electrons near the hot spots with long wavelength fluctuations of the order parameter. At low energies, we can ignore the Fermi surface curvature and use linearized electronic dispersions around the hot spots. We emphasize that linearizing the dispersion is not equivalent to taking the one-dimensional limit because the collective modes scatter electrons across the hot spots whose Fermi velocities are not parallel to each other. Due to the similarities between the SDW and CDW critical points, we introduce a general action which is applicable to both cases,

$$
\begin{aligned}
S = & \sum_{j=1}^{N_f} \sum_{s=1}^{N_c} \sum_{l=1}^{2} \sum_{m=\pm} \int \frac{d^3k}{(2\pi)^3}\, \psi^*_{l,m,j,s}(k) \left(ik_0 + \vec{v}_{l,m} \cdot \vec{k} \right) \psi_{l,m,j,s}(k) \\
& + \frac{1}{4} \int \frac{d^3q}{(2\pi)^3}\, \left(q_0^2 + c_x^2 q_x^2 + c_y^2 q_y^2 \right) \mathrm{Tr}\left(\Phi(-q)\Phi(q) \right) \\
& + \frac{\widetilde{g}}{\sqrt{N_f}} \sum_{j=1}^{N_f} \sum_{l=1}^{2} \sum_{s,s'=1}^{N_c} \int \frac{d^3k}{(2\pi)^3} \frac{d^3q}{(2\pi)^3} \left[\psi^*_{l,+,j,s}(k+q)\, \Phi_{s,s'}(q)\, \psi_{l,-,j,s'}(k) + \text{h.c.} \right] \\
& + \frac{1}{4} \int \frac{d^3q_1}{(2\pi)^3} \frac{d^3q_3}{(2\pi)^3} \frac{d^3q_3}{(2\pi)^3} \Big[\widetilde{u}_1\, \mathrm{Tr}\left(\Phi(-q_1+q_2)\Phi(q_1) \right)\, \mathrm{Tr}\left(\Phi(-q_3-q_2)\Phi(q_3) \right) \\
& + \widetilde{u}_2\, \mathrm{Tr}\left(\Phi(-q_1+q_2)\Phi(q_1)\Phi(-q_3-q_2)\Phi(q_3) \right) \Big].
\end{aligned}
\tag{1}
$$

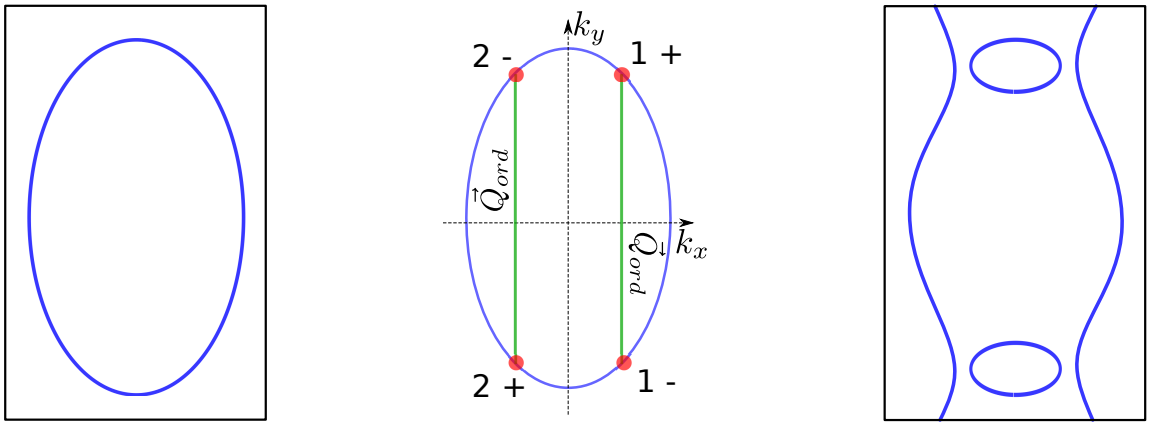

(a) (b) (c)

FIG. 1: (a) Anisotropic Fermi surface in two space dimensions. (b) At the critical point, density wave fluctuations induce strong scatterings between electrons near the hot spot denoted by the (red) dots. (c) Reconstructed Fermi surface in the ordered phase.

Here $\psi_{l,m,j,s}(k)$ describe electrons near the hot spots, where (l,m) with $l=1,2$ and $m=\pm$ labels the four hot spots as shown in Fig. 1b. $j=1,2,..,N_f$ and $s=1,2,..,N_c$ represent a flavor index and the spin, respectively. The $SU(2)$ spin is generalized to $SU(N_c)$. The parameter N_f is an extra flavor which can arise from degenerate bands with the $SU(N_f)$ symmetry. $\vec{k}$ is the two-dimensional momentum that measures a deviation from the hot spots. $\vec{v}_{l,m}$ is the Fermi velocity at each hot spot : $\vec{v}_{1,+} \equiv (v_x, v_y) = -\vec{v}_{2,+}$, $\vec{v}_{1,-} \equiv (v_x, -v_y) = -\vec{v}_{2,-}$, with $v_x, v_y > 0$. The $N_c \times N_c$ matrix field $\Phi(q)$ represents the density wave mode of frequency q_0 and momentum $\vec{Q}_{ord}+\vec{q}$. The boson field satisfies $\Phi^\dagger(q) = \Phi(-q)$ because $2\vec{Q}_{ord} = 0$ [47]. The matrix field can be written as

$$\Phi(q) = \begin{cases} \vec{\phi}(q)\cdot\vec{\tau} & \text{for SDW} \\ \sqrt{\frac{2}{N_c}}\,\phi(q)\,\mathcal{I}_{N_c} & \text{for CDW} \end{cases} \tag{2}$$

where $\tau^{(\alpha)}$ is the α-th generator of $SU(N_c)$ in the fundamental representation, and $\mathcal{I}_{N_c}$ is the $N_c \times N_c$ identity matrix. $\tau^{(\alpha)}$ and $\mathcal{I}_{N_c}$ represent the spin and charge vertices, respectively. We choose the normalization $\mathrm{Tr}\left(\tau^{(\alpha)}\tau^{(\beta)}\right) = 2\delta^{\alpha\beta}$ for the τ-matrices. For $N_c = 2$ and 3 in the SDW case and for any N_c in the CDW case, $\widetilde{u}_1$ and $\widetilde{u}_2$ are equivalent, and we can set $\widetilde{u}_2 = 0$ without loss of generality. For the CDW critical point, both N_f and N_c play the same role, and the physics depends only on the total number of electron species, $\widetilde{N}_f = N_c N_f$.

Some parameters in Eq. (1) can be absorbed into scales of momentum and fields. We scale $(k_x, k_y) \mapsto \left(\frac{k_x}{c_x}, \frac{k_y}{v_y}\right)$ and $(\Phi, \psi) \mapsto \sqrt{c_x v_y}(\Phi, \psi)$ to rewrite the action as

$$\begin{aligned} S = &\sum_{j=1}^{N_f}\sum_{s=1}^{N_c}\sum_{l=1}^{2}\sum_{m=\pm}\int \frac{d^3k}{(2\pi)^3}\,\psi^*_{l,m,j,s}(k)\left(ik_0 + \mathcal{E}_{l,m}(\vec{k})\right)\psi_{l,m,j,s}(k) \\ &+ \frac{1}{4}\int \frac{d^3q}{(2\pi)^3}\,\left(q_0^2 + q_x^2 + c^2 q_y^2\right)\mathrm{Tr}\left(\Phi(-q)\Phi(q)\right) \\ &+ \frac{g_0}{\sqrt{N_f}}\sum_{j=1}^{N_f}\sum_{l=1}^{2}\sum_{s,s'=1}^{N_c}\int \frac{d^3k}{(2\pi)^3}\frac{d^3q}{(2\pi)^3}\left[\psi^*_{l,+,j,s}(k+q)\,\Phi_{s,s'}(q)\,\psi_{l,-,j,s'}(k) + \text{h.c.}\right] \\ &+ \frac{1}{4}\int \frac{d^3q_1}{(2\pi)^3}\frac{d^3q_2}{(2\pi)^3}\frac{d^3q_3}{(2\pi)^3}\Big[u_{1;0}\,\mathrm{Tr}\left(\Phi(-q_1+q_2)\Phi(q_1)\right)\,\mathrm{Tr}\left(\Phi(-q_3-q_2)\Phi(q_3)\right) \\ &+ u_{2;0}\,\mathrm{Tr}\left(\Phi(-q_1+q_2)\Phi(q_1)\Phi(-q_3-q_2)\Phi(q_3)\right)\Big]. \end{aligned} \tag{3}$$

The rescaled dispersions are $\mathcal{E}_{1,+}(\vec{k}) = -\mathcal{E}_{2,+}(\vec{k}) = vk_x + k_y$, and $\mathcal{E}_{1,-}(\vec{k}) = -\mathcal{E}_{2,-}(\vec{k}) = vk_x - k_y$, where $v \equiv \frac{v_x}{c_x}$ and

$c \equiv \frac{c_y}{v_y}$ represent the relative velocities between electron and boson in the two directions. The couplings are also rescaled to $g_0 \equiv \frac{\widetilde{g}}{\sqrt{c_x v_y}}$ and $u_{i;0} \equiv \frac{\widetilde{u}_i}{c_x v_y}$.

The $(2+1)$-dimensional theory is now generalized to a $(d+1)$-dimensional theory which describes the one-dimensional Fermi surface embedded in d-dimensional momentum space. Following the formalism in Ref. [34], we express Eq. (3) in the basis of spinors $\Psi_{+,j,s}(k) = (\psi_{1,+,j,s}(k), \quad \psi_{2,+,j,s}(k))^T$ and $\Psi_{-;j;s}(k) = (\psi_{1,-;j;s}(k), \quad -\psi_{2,-;j;s}(k))^T$, and add $(d-2)$ extra co-dimensions to the Fermi surface,

$$
\begin{aligned}
S = & \sum_{j=1}^{N_f} \sum_{s=1}^{N_c} \sum_{n=\pm} \int dk \; \bar{\Psi}_{n,j,s}(k) \left(i\mathbf{K}\cdot\mathbf{\Gamma} + i\varepsilon_n(\vec{k})\, \gamma_{d-1} \right) \Psi_{n,j,s}(k) \\
& + \frac{1}{4} \int dq \; \left(|\mathbf{Q}|^2 + q_x^2 + c^2 q_y^2 \right) \; \mathrm{Tr}\left(\Phi(-q)\Phi(q) \right) \\
& + i \, \frac{g_0}{\sqrt{N_f}} \sum_{j=1}^{N_f} \sum_{s,s'=1}^{N_c} \int dk \; dq \; \left[\bar{\Psi}_{+,j,s}(k+q) \; \gamma_{d-1} \; \Phi_{s,s'}(q) \; \Psi_{-,j,s'}(k) - \text{h.c.} \right] \\
& + \frac{1}{4} \int dq_1 \; dq_2 \; dq_3 \; \Big[u_{1;0} \; \mathrm{Tr}\left(\Phi(-q_1+q_2)\Phi(q_1) \right) \; \mathrm{Tr}\left(\Phi(-q_3-q_2)\Phi(q_3) \right) \\
& + u_{2;0} \; \mathrm{Tr}\left(\Phi(-q_1+q_2)\Phi(q_1)\Phi(-q_3-q_2)\Phi(q_3) \right) \Big],
\end{aligned}
\tag{4}
$$

where $k \equiv (\mathbf{K}, \vec{k})$ and $dk \equiv \frac{d^{d+1}k}{(2\pi)^{d+1}}$. The two dimensional vectors on the plane of the Fermi surface are denoted as $\vec{k} = (k_x, k_y)$, while $\mathbf{K} = (k_0, k_1, \ldots, k_{d-2})$ denotes $(d-1)$ dimensional vectors with $k_1, \ldots, k_{d-2}$ being the newly added co-dimensions. We collect the first $(d-1)$ γ-matrices in $\mathbf{\Gamma} = (\gamma_0, \gamma_1, \ldots, \gamma_{d-2})$. The conjugate spinor is defined by $\bar{\Psi}_{n,j,s} = \Psi^\dagger_{n,j,s}\gamma_0$. The dispersions of the spinors along the $\vec{k}$ direction are inherited from the two dimensional dispersion, $\varepsilon_\pm(\vec{k}) = vk_x \pm k_y$. It is easy to check that we recover Eq. (3) in $d=2$ with $\gamma_0 = \sigma_y$ and $\gamma_1 = \sigma_x$, where σ_i are Pauli matrices. The theory in general dimensions interpolate between the two-dimensional metal and a semi-metal with a line node in three dimensions. The action is invariant under $U(1) \times SU(N_c) \times SU(N_f)$, which are associated with the particle number, spin and flavor conservations, respectively. The theory is also invariant under time reversal, inversion, and $SO(d-1)$ rotations in $\mathbf{K}$.

The engineering scaling dimensions of the $(d+1)$-momentum, the fields and the couplings are

$$
\begin{aligned}
& [\mathbf{K}] = 1, \quad [k_x] = 1, \quad [k_y] = 1, \\
& [\Psi_{n,j,s}] = -\frac{1}{2}(d+2), \quad [\Phi] = -\frac{1}{2}(d+3), \quad [v] = 0
\end{aligned}
$$

$$
[c] = 0, \quad [g_0] = \frac{1}{2}(3-d), \quad \text{and} \quad [u_0] = 3-d. \tag{5}
$$

Classically, frequency and all momentum components have the same scaling dimension. The upper critical dimension is $d=3$ at which all the couplings in the theory are dimensionless at the Gaussian fixed point. We apply the field theoretic renormalization group (RG) based on a perturbative expansion in $\epsilon \equiv 3-d$.

III. RENORMALIZATION GROUP

In this section we outline our RG scheme, and derive the general expressions for the beta functions and the critical exponents. The readers who wish to skip the details can jump to Eqs. (17) - (27) which are the main results of this section.

Starting with the action in Eq. (4), we define dimensionless couplings

$$
g = \mu^{-(3-d)/2} \, g_0, \qquad u_i = \mu^{-(3-d)} \, u_{i;0}, \tag{6}
$$

where μ is a scale at which the renormalized couplings are to be defined. From the action in Eq. (4), the quantum effective action is computed perturbatively in the couplings. The logarithmic divergences that arise at the upper critical dimension manifest themselves as poles in ϵ. Requiring the renormalized quantum effective action to be analytic in ϵ, we add counter terms of the form,

$$
\begin{aligned}
S_{CT} = & \sum_{j=1}^{N_f} \sum_{s=1}^{N_c} \sum_{n=\pm} \int dk\ \bar{\Psi}_{n,j,s}(k) \left(i\mathcal{A}_1 \mathbf{K}\cdot\mathbf{\Gamma} + i(\mathcal{A}_2 v k_x + n\mathcal{A}_3 k_y)\,\gamma_{d-1}\right) \Psi_{n,j,s}(k) \\
& + \frac{1}{4}\int dq\ \left(\mathcal{A}_4 |\mathbf{Q}|^2 + \mathcal{A}_5 q_x^2 + \mathcal{A}_6 c^2 q_y^2\right) \mathrm{Tr}\left(\Phi(-q)\Phi(q)\right) \\
& + \mathcal{A}_7 \mu^{(3-d)/2} \frac{ig}{\sqrt{N_f}} \sum_{j=1}^{N_f} \sum_{s,s'=1}^{N_c} \int dk\ dq\ \left[\bar{\Psi}_{+,j,s}(k+q)\ \gamma_{d-1}\ \Phi_{s,s'}(q)\ \Psi_{-,j,s'}(k) - \text{h.c.}\right] \\
& + \frac{\mu^{(3-d)}}{4} \int dq_1\ dq_2\ dq_3 \Big[\mathcal{A}_8 u_1\ \mathrm{Tr}\left(\Phi(-q_1+q_2)\Phi(q_1)\right)\ \mathrm{Tr}\left(\Phi(-q_3-q_2)\Phi(q_3)\right) \\
& \qquad + \mathcal{A}_9 u_2\ \mathrm{Tr}\left(\Phi(-q_1+q_2)\Phi(q_1)\Phi(-q_3-q_2)\Phi(q_3)\right)\Big], \qquad (7)
\end{aligned}
$$

with $\mathcal{A}_i \equiv \mathcal{A}_i(v,c,g,u,\epsilon) = \sum_{m=1}^{\infty} Z_{i,m}(v,c,g,u)\ \epsilon^{-m}$. The counter terms are chosen to cancel the poles in ϵ based on the minimal subtraction scheme. Due to the lack of full rotational symmetry in the $(\mathbf{K},\vec{k})$-space and the C_4 symmetry in the (k_x,k_y)-plane, the kinetic terms are renormalized differently in the $\mathbf{K}$, k_x, and k_y directions, respectively. Therefore, $\mathbf{K}$, k_x and k_y can have different quantum scaling dimensions. The sum of the original action and the counter terms gives the bare action,

$$
\begin{aligned}
S_B = & \sum_{j=1}^{N_f} \sum_{s=1}^{N_c} \sum_{n=\pm} \int dk_B\ \bar{\Psi}_{B;n,j,s}(k_B) \left(i\mathbf{K}_B\cdot\mathbf{\Gamma} + i(v_B k_{B;x} + n k_{B;y})\,\gamma_{d-1}\right) \Psi_{B;n,j,s}(k_B) \\
& + \frac{1}{4}\int dq_B\ \left(|\mathbf{Q}_B|^2 + q_{B;x}^2 + c_B^2 q_{B;y}^2\right) \mathrm{Tr}\left(\Phi_B(-q_B)\Phi_B(q_B)\right) \\
& + i\,\frac{g_B}{\sqrt{N_f}} \sum_{j=1}^{N_f} \sum_{s,s'=1}^{N_c} \int dk_B\ dq_B\ \left[\bar{\Psi}_{B;+,j,s}(k_B+q_B)\ \gamma_{d-1}\ \Phi_{B;s,s'}(q_B)\ \Psi_{B;-,j,s'}(k_B) - \text{h.c.}\right] \\
& + \frac{1}{4}\int dq_{1;B}\ dq_{2;B}\ dq_{3;B} \Big[u_{1;B}\ \mathrm{Tr}\left(\Phi_B(-q_{1;B}+q_{2;B})\Phi_B(q_{1;B})\right)\ \mathrm{Tr}\left(\Phi_B(-q_{3;B}-q_{2;B})\Phi_B(q_{3;B})\right) \\
& \qquad + u_{2;B}\ \mathrm{Tr}\left(\Phi_B(-q_{1;B}+q_{2;B})\Phi_B(q_{1;B})\Phi_B(-q_{3;B}-q_{2;B})\Phi_B(q_{3;B})\right)\Big]. \qquad (8)
\end{aligned}
$$

Here the bare quantities are related to their renormalized counterparts through the multiplicative factors,

$$
\begin{aligned}
& \mathbf{K} = \mathcal{Z}_\tau^{-1}\,\mathbf{K}_B, \qquad k_x = \mathcal{Z}_x^{-1}\,k_{B;x}, \\
& k_y = k_{B;y}, \qquad \Psi_{n,j,s} = \mathcal{Z}_\psi^{-\frac{1}{2}}\,\Psi_{B;n,j,s}, \\
& \Phi = \mathcal{Z}_\phi^{-\frac{1}{2}}\,\Phi_B, \qquad v = \frac{\mathcal{Z}_x^2\,\mathcal{Z}_\tau^{d-1}\,\mathcal{Z}_\psi}{\mathcal{Z}_2}\,v_B, \\
& c = \left[\frac{\mathcal{Z}_x\,\mathcal{Z}_\phi\,\mathcal{Z}_\tau^{d-1}}{\mathcal{Z}_6}\right]^{\frac{1}{2}} c_B, \\
& g = \mu^{-(3-d)/2}\,\frac{\mathcal{Z}_x^2\,\mathcal{Z}_\tau^{2(d-1)}\,\mathcal{Z}_\psi\,\mathcal{Z}_\phi^{\frac{1}{2}}}{\mathcal{Z}_7}\,g_B, \\
& u_1 = \mu^{-(3-d)}\,\frac{\mathcal{Z}_x^3\,\mathcal{Z}_\tau^{3(d-1)}\,\mathcal{Z}_\phi^2}{\mathcal{Z}_8}\,u_{1;B},
\end{aligned}
$$

$$
u_2 = \mu^{-(3-d)}\,\frac{\mathcal{Z}_x^3\,\mathcal{Z}_\tau^{3(d-1)}\,\mathcal{Z}_\phi^2}{\mathcal{Z}_9}\,u_{2;B}, \qquad (9)
$$

where

$$
\begin{aligned}
& \mathcal{Z}_\tau = \frac{\mathcal{Z}_1}{\mathcal{Z}_3}, \quad \mathcal{Z}_x = \mathcal{Z}_\tau\,\left[\frac{\mathcal{Z}_5}{\mathcal{Z}_4}\right]^{1/2}, \\
& \mathcal{Z}_\psi = \frac{\mathcal{Z}_3}{\mathcal{Z}_x\,\mathcal{Z}_\tau^{(d-1)}}, \quad \mathcal{Z}_\phi = \frac{\mathcal{Z}_4}{\mathcal{Z}_x\,\mathcal{Z}_\tau^{(d+1)}}, \qquad (10)
\end{aligned}
$$

with $\mathcal{Z}_i \equiv \mathcal{Z}_i(v,c,g,u,\epsilon) = 1 + \mathcal{A}_i(v,c,g,u,\epsilon)$. Here we made the choice $k_y = k_{B;y}$, which fixes the scaling dimension of k_y to be 1. This choice can be always made, even at the quantum level, because one can measure scaling dimensions of other quantities with respect to that of k_y. $\mathcal{Z}_\tau$ and $\mathcal{Z}_x$ encode the anisotropic quantum corrections, which lead to anomalous dimensions for $\mathbf{K}$ and k_x.

The renormalization group equation is obtained by requiring that the bare Green's function is invariant under the change of the scale μ at which the renormalized vertex functions are defined. The renormalized Green's function,

$$\begin{aligned}&\langle\Phi(q_1)\dots\Phi(q_b)\Psi(k_1)\dots\Psi(k_f)\bar{\Psi}(k_{f+1})\dots\bar{\Psi}(k_{2f})\rangle\\&\equiv G^{(2f,b)}(q_i,k_j;v,c,g,u;\mu)\end{aligned}$$

$$\times\,\delta^{(d+1)}\left(\sum_{i=1}^{b}q_i+\sum_{j=1}^{f}(k_j-k_{f+j})\right), \tag{11}$$

obeys the renormalization group equation,

$$\begin{aligned}&\Big[z_\tau\,\left(\mathbf{K}_j\cdot\nabla_{\mathbf{K}_j}+\mathbf{Q}_i\cdot\nabla_{\mathbf{Q}_i}\right)+z_x\,\left(k_{j;x}\partial_{k_{j;x}}+q_{i;x}\partial_{q_{i;x}}\right)+\left(k_{j;y}\partial_{k_{j;y}}+q_{i;y}\partial_{q_{i;y}}\right)\\&-\beta_v\frac{\partial}{\partial v}-\beta_c\frac{\partial}{\partial c}-\beta_g\frac{\partial}{\partial g}-\beta_{u_1}\frac{\partial}{\partial u_1}-\beta_{u_2}\frac{\partial}{\partial u_2}\\&+2f\left(\frac{d+2}{2}-\eta_\psi\right)+b\left(\frac{d+3}{2}-\eta_\phi\right)-\left(z_\tau\,(d-1)+z_x+1\right)\Big]G^{(2f,b)}(q_i,k_j;v,c,g,u;\mu)=0.\end{aligned} \tag{12}$$

Here z_τ and z_x are the quantum scaling dimensions for $\mathbf{K}$ and k_x given by

$$z_\tau=1+\frac{\partial\ln\mathcal{Z}_\tau}{\partial\ln\mu},\qquad z_x=1+\frac{\partial\ln\mathcal{Z}_x}{\partial\ln\mu}, \tag{13}$$

and η_ψ and η_ϕ are the anomalous dimensions of the fields,

$$\eta_\psi=\frac{1}{2}\frac{\partial\ln\mathcal{Z}_\psi}{\partial\ln\mu},\qquad \eta_\phi=\frac{1}{2}\frac{\partial\ln\mathcal{Z}_\phi}{\partial\ln\mu}. \tag{14}$$

The beta functions, which describe the change of couplings with an increasing energy scale, are defined as

$$\begin{aligned}\beta_v&=\frac{\partial v}{\partial\ln\mu},\qquad \beta_c=\frac{\partial c}{\partial\ln\mu},\\ \beta_g&=\frac{\partial g}{\partial\ln\mu},\qquad \beta_{u_i}=\frac{\partial u_i}{\partial\ln\mu}.\end{aligned} \tag{15}$$

We use the relationship between the bare and renormalized quantities defined in Eq. (9) to obtain a set of coupled differential equations,

$$\begin{aligned}&\mathcal{Z}_1\Big[d(z_\tau-1)+(z_x-1)+2\eta_\psi\Big]-\frac{\partial\mathcal{Z}_1}{\partial\ln\mu}=0,\\&\mathcal{Z}_2\Big[\beta_v-v\left\{(d-1)(z_\tau-1)+2(z_x-1)+2\eta_\psi\right\}\Big]+v\,\frac{\partial\mathcal{Z}_2}{\partial\ln\mu}=0,\\&\mathcal{Z}_3\Big[(d-1)(z_\tau-1)+(z_x-1)+2\eta_\psi\Big]-\frac{\partial\mathcal{Z}_3}{\partial\ln\mu}=0,\\&\mathcal{Z}_4\Big[(d+1)(z_\tau-1)+(z_x-1)+2\eta_\phi\Big]-\frac{\partial\mathcal{Z}_4}{\partial\ln\mu}=0,\\&\mathcal{Z}_5\Big[(d-1)(z_\tau-1)+3(z_x-1)+2\eta_\phi\Big]-\frac{\partial\mathcal{Z}_5}{\partial\ln\mu}=0,\\&\mathcal{Z}_6\Big[2\beta_c-c\left\{(d-1)(z_\tau-1)+(z_x-1)+2\eta_\phi\right\}\Big]+c\,\frac{\partial\mathcal{Z}_6}{\partial\ln\mu}=0,\\&\mathcal{Z}_7\Big[\beta_g-g\left\{-\frac{3-d}{2}+2(d-1)(z_\tau-1)+2(z_x-1)+2\eta_\psi+\eta_\phi\right\}\Big]+g\,\frac{\partial\mathcal{Z}_7}{\partial\ln\mu}=0,\\&\mathcal{Z}_8\Big[\beta_{u_1}-u_1\left\{-(3-d)+3(d-1)(z_\tau-1)+3(z_x-1)+4\eta_\phi\right\}\Big]+u_1\,\frac{\partial\mathcal{Z}_8}{\partial\ln\mu}=0,\\&\mathcal{Z}_9\Big[\beta_{u_2}-u_2\left\{-(3-d)+3(d-1)(z_\tau-1)+3(z_x-1)+4\eta_\phi\right\}\Big]+u_2\,\frac{\partial\mathcal{Z}_9}{\partial\ln\mu}=0,\end{aligned} \tag{16}$$

which are solved to obtain the expressions for the critical exponents and the beta functions,

$$z_\tau = \left[1 + \left(\frac{1}{2} g\partial_g + \sum_i u_i \partial_{u_i}\right)(Z_{1,1} - Z_{3,1})\right]^{-1}, \tag{17}$$

$$z_x = 1 - \frac{1}{2} z_\tau \left(\frac{1}{2} g\partial_g + \sum_i u_i \partial_{u_i}\right)(2Z_{1,1} - 2Z_{3,1} - Z_{4,1} + Z_{5,1}), \tag{18}$$

$$\eta_\psi = \frac{\epsilon}{2}(z_\tau - 1) - \frac{1}{2}\left[2(z_\tau - 1) + (z_x - 1) + z_\tau \left(\frac{1}{2} g\partial_g + \sum_i u_i \partial_{u_i}\right) Z_{3,1}\right], \tag{19}$$

$$\eta_\phi = \frac{\epsilon}{2}(z_\tau - 1) - \frac{1}{2}\left[4(z_\tau - 1) + (z_x - 1) + z_\tau \left(\frac{1}{2} g\partial_g + \sum_i u_i \partial_{u_i}\right) Z_{4,1}\right], \tag{20}$$

$$\partial_\ell v = \frac{1}{2} z_\tau v \left(\frac{1}{2} g\partial_g + \sum_i u_i \partial_{u_i}\right)(2Z_{1,1} - 2Z_{2,1} - Z_{4,1} + Z_{5,1}), \tag{21}$$

$$\partial_\ell c = -\frac{1}{2} z_\tau c \left(\frac{1}{2} g\partial_g + \sum_i u_i \partial_{u_i}\right)(2Z_{1,1} - 2Z_{3,1} - Z_{4,1} + Z_{6,1}), \tag{22}$$

$$\partial_\ell g = \frac{1}{4} z_\tau g \left[2\epsilon + \left(\frac{1}{2} g\partial_g + \sum_i u_i \partial_{u_i}\right)(2Z_{1,1} + 2Z_{3,1} + Z_{4,1} + Z_{5,1} - 4Z_{7,1})\right], \tag{23}$$

$$\partial_\ell u_1 = \frac{1}{2} z_\tau u_1 \left[2\epsilon - \left(\frac{1}{2} g\partial_g + \sum_i u_i \partial_{u_i}\right)(2Z_{1,1} - 2Z_{3,1} - 3Z_{4,1} - Z_{5,1} + 2Z_{8,1})\right], \tag{24}$$

$$\partial_\ell u_2 = \frac{1}{2} z_\tau u_2 \left[2\epsilon - \left(\frac{1}{2} g\partial_g + \sum_i u_i \partial_{u_i}\right)(2Z_{1,1} - 2Z_{3,1} - 3Z_{4,1} - Z_{5,1} + 2Z_{9,1})\right], \tag{25}$$

where we introduced the IR beta function, $\partial_\ell \lambda = -\beta_\lambda$ which describes the RG flow with an increase of the logarithmic *length* scale ℓ.

In the absence of the Yukawa coupling, every quartic coupling u_i is accompanied by $1/c$ in the perturbative series. This reflects the IR singularity for the flat bosonic band in the $c \to 0$ limit. Since the actual perturbative expansion is organized in terms of u_i/c, it is convenient to introduce $\chi_i = u_i/c$. The beta functions for χ_i can be readily obtained from those of u_i and c,

$$\partial_\ell \chi_1 = \frac{1}{2} z_\tau \chi_1 \left[2\epsilon + \left(\frac{1}{2} g\partial_g + \sum_i u_i \partial_{u_i}\right)(2Z_{4,1} + Z_{5,1} + Z_{6,1} - 2Z_{8,1})\right], \tag{26}$$

$$\partial_\ell \chi_2 = \frac{1}{2} z_\tau \chi_2 \left[2\epsilon + \left(\frac{1}{2} g\partial_g + \sum_i u_i \partial_{u_i}\right)(2Z_{4,1} + Z_{5,1} + Z_{6,1} - 2Z_{9,1})\right]. \tag{27}$$

IV. SPIN DENSITY WAVE CRITICALITY

We have introduced the minimal theories for the SDW and CDW critical points. Despite the similarities between the two theories, the behaviors of the two are quite different. The difference originates from the non-abelian and abelian nature of the Yukawa vertex in Eq. (2) for the SDW and CDW theories, respectively. In this section, we will focus on the SDW case, and return to the CDW case in section V.

A. One Loop

In this subsection we present the one-loop analysis for the SDW critical point. From the one-loop diagrams shown in Fig. 2, we obtain the following counter terms (see Appendix A for details of the calculation),

$$Z_{1,1} = -\frac{(N_c^2 - 1)}{4\pi^2 N_c N_f}\, g^2\, h_1(v, c),$$

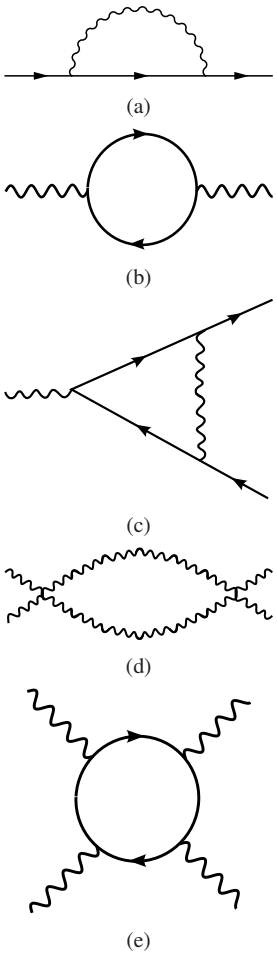

FIG. 2: The one-loop Feynman diagrams. The solid (wiggly) line represents the electron (boson) propagator.

$$
\begin{aligned}
Z_{2,1} &= \frac{(N_c^2-1)}{4\pi^2 N_c N_f}\, g^2\, h_2(v,c)\\
Z_{3,1} &= -\frac{(N_c^2-1)}{4\pi^2 N_c N_f}\, g^2\, h_2(v,c)\\
Z_{4,1} &= -\frac{1}{8\pi}\,\frac{g^2}{v},\\
Z_{5,1},\ \ Z_{6,1} &= 0,\\
Z_{7,1} &= -\frac{1}{8\pi^3 N_c N_f}\, g^2\, v\, h_3(v,c),\\
Z_{8,1} &= \frac{N_c^2+7}{2\pi^2}\chi_1 + \frac{2N_c^2-3}{\pi^2 N_c}\chi_2 + \frac{3(N_c^2+3)}{2\pi^2 N_c^2}\frac{\chi_2^2}{\chi_1},\\
Z_{9,1} &= \frac{6}{\pi^2}\chi_1 + \frac{2(N_c^2-9)}{2\pi^2 N_c}\chi_2,
\end{aligned}
\tag{28}
$$

where

$$
\begin{aligned}
h_1(v,c) &= \int_0^1 dx\, \sqrt{\frac{1-x}{c^2+x(1-(1-v^2)c^2)}},\\
h_2(v,c) &= c^2\int_0^1 dx\, \sqrt{\frac{1-x}{[c^2+x(1-(1-v^2)c^2)]^3}}.\\
h_3(v,c) &= \int_0^{2\pi} d\theta \int_0^1 dx_1 \int_0^{1-x_1} dx_2\, \left[\frac{1}{\zeta(\theta,x_1,x_2,v,c)}\right.\\
&\qquad \left. - \frac{v^2\,\sin(2\theta)}{\zeta^2(\theta,x_1,x_2,v,c)}\right]
\end{aligned}
\tag{29}
$$

with

$$
\begin{aligned}
\zeta(\theta,x_1,x_2,v,c) &= 2v^2[x_1\sin^2(\theta)+x_2\cos^2(\theta)]\\
&+ (1-x_1-x_2)\left[\sin^2\left(\theta+\frac{\pi}{4}\right)+c^2v^2\cos^2\left(\theta+\frac{\pi}{4}\right)\right].
\end{aligned}
\tag{30}
$$

From Eqs. (17) - (27), and Eq. (28), we obtain the one-loop beta functions for the SDW critical point,

$$\partial_\ell v = \frac{z_\tau\, g^2}{16\pi}\left[1-\frac{4(N_c^2-1)}{\pi N_c N_f}\, v\,(h_1(v,c)+h_2(v,c))\right], \tag{31}$$

$$\partial_\ell c = -\frac{z_\tau g^2 c}{16\pi v}\left[1-\frac{4(N_c^2-1)}{\pi N_c N_f}\, v\,(h_1(v,c)-h_2(v,c))\right], \tag{32}$$

$$\partial_\ell g = z_\tau\, g\left[\frac{\epsilon}{2}-\frac{g^2}{32\pi v}\left(1+\frac{4(N_c^2-1)}{\pi N_c N_f}\, v\,(h_1(v,c)+h_2(v,c))\right)+\frac{N_c^2-1}{8\pi^3 N_c N_f}\, g^2 v\, h_3(v,c)\right], \tag{33}$$

$$\partial_\ell \chi_1 = z_\tau\,\chi_1\left[\left(\epsilon-\frac{g^2}{8\pi v}\right)-\left(\frac{N_c^2+7}{2\pi^2}\chi_1+\frac{2N_c^2-3}{\pi^2 N_c}\chi_2+\frac{3(N_c^2+3)}{2\pi^2 N_c^2}\frac{\chi_2^2}{\chi_1}\right)\right], \tag{34}$$

$$\partial_\ell \chi_2 = z_\tau\,\chi_2\left[\left(\epsilon-\frac{g^2}{8\pi v}\right)-\left(\frac{6}{\pi^2}\chi_1+\frac{N_c^2-9}{\pi^2 N_c}\chi_2\right)\right]. \tag{35}$$

Now we explain the physical origin of each term in the beta functions based on the results obtained in Appendix A. The boson self energy in Fig. 2b is proportional to $|\mathbf{Q}|^2$ and inde-

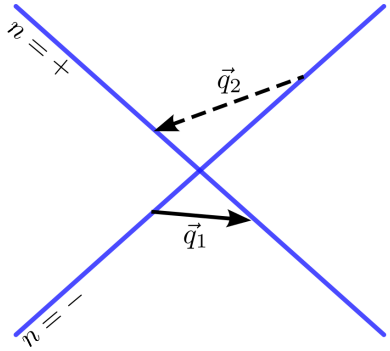

FIG. 3: For any momentum $\vec{q} = (q_x, q_y)$ on the xy-plane, one can always find particle-hole pairs with zero energy across two patches of Fermi surface near hot spots. Since the fermionic energy dispersion is linear, the spectrum of particle-hole pair is independent of $\vec{q}$.

pendent of $\vec{q} = (q_x, q_y)$. This is because a boson with any $\vec{q}$ can be absorbed by a particle-hole pair on the Fermi surface (see Fig. 3), and the energy spectrum of particle-hole excitations is independent of $\vec{q}$. Vanishing $Z_{5,1}$ and $Z_{6,1}$ at the one-loop order leads to a weakened dependence of the dressed boson propagator on q_x, q_y relative to that of $\mathbf{Q}$. As a result, c_x and c_y are renormalized to smaller values. Because $v = v_x/c_x$ and $c = c_y/v_y$, as defined in Eqs. (1) and (3), the suppression of c_x and c_y enhances v and suppresses c. This is shown in the first terms on the right hand side of Eqs. (31) and (32). The $\mathbf{K}$ dependent term ($Z_{1,1}$) in the fermion self energy in Fig. 2a similarly reduces v_x and v_y. This reduces v and enhance c as is shown in the second terms on the right hand side of Eqs. (31) and (32). Fig. 2a also directly renormalizes the Fermi velocity through $Z_{2,1}$, $Z_{3,1}$. The spin fluctuations mix electrons from different hot spots. This reduces the angle between the Fermi velocities at the hot spots connected by $\vec{Q}_{ord}$, thereby improving the nesting between the hot spots. As v_x and v_y are renormalized to smaller and larger values respectively, v and c are suppressed. This is embodied in the third terms in the expressions for $\partial_\ell v$ and $\partial_\ell c$.

The beta function for the Yukawa vertex includes two different contributions. The second, third and fourth terms on the right hand side of Eq. (33) are the contributions from the boson and fermion self energies which alter the scaling dimensions of spacetime and the fields. The contributions from the self-energies weaken the interaction at low energies because the virtual excitations in Figs. 2a, 2b screens the interaction. This is reflected in the negative contributions to the beta function. The last term in Eq. (33) is the vertex correction ($Z_{7,1}$) shown in Fig. 2c. Unlike the contributions from the self-energies, the vertex correction anti-screens the interaction, which tends to make the interaction stronger. The anti-screeening is attributed to the fact that the SDW vertices anti-commute on average in the sense,

$$\sum_{a=1}^{N_c^2-1} \tau^a \tau^b \tau^a = -\frac{2}{N_c}\,\tau^b. \tag{36}$$

This is analogous to the anti-screening effect which results in the asymptotic freedom in non-abelian gauge theories. The anti-screening effect also has a significant impact at the two-loop order as will be discussed in Sec. IV B.

The beta functions for χ_i can be understood similarly. The second terms in the Eqs. (34) and (35) are the contributions from the boson self-energy. Rest of the terms in these equations are the standard vertex corrections ($Z_{8,1}$, $Z_{9,1}$) from Fig. 2d. We note that Fig. 2e does not contribute to the beta functions, because it is UV finite at $d = 3$[34].

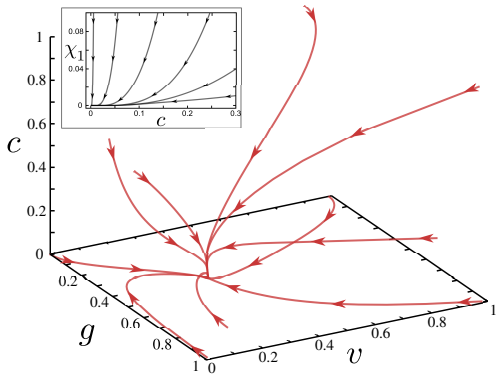

FIG. 4: Projection of the RG flow in the space of (g, v, c) for $N_c = 2$, $N_f = 1$ and $\epsilon = 0.01$. The arrows point towards decreasing energy. An IR fixed point given by Eq. (43) exists on the (g, v) plane with $c = 0$. (Inset) Projection of the RG flow in the (χ_1, c) plane. c (χ_1) flows to zero logarithmically (algebraically).

In Fig. 4 we plot the one-loop RG flow of the four parameters, $(g, v, c, \chi_1 = u_1/c)$ for $N_c = 2$ and $N_f = 1$. Here we set $u_2 = 0$. The RG flow shows the presence of a stable IR fixed point with vanishing c and χ_1. In order to find the analytic expression of the couplings at the fixed point for general N_c and N_f, we expand $h_i(v, c)$ to the linear order in c with $v \sim 1$,

$$h_1(v,c) = \frac{\pi}{2} - 2c + \mathcal{O}\left(c^2\right), \quad h_2(v,c) = 2c + \mathcal{O}\left(c^2\right),$$
$$h_3(v,c) = \frac{2\pi^2}{v(1+v)} - \frac{4\pi}{v}c + \mathcal{O}\left(c^2\right). \tag{37}$$

In the small c limit, the beta functions become

$$\partial_\ell v = \frac{z_\tau}{16\pi}\, g^2 \left[1 - \frac{2(N_c^2-1)}{N_c N_f}\, v\right], \tag{38}$$

$$\partial_\ell c = -\frac{z_\tau}{16\pi}\frac{g^2 c}{v}\left[\left(1-\frac{2(N_c^2-1)}{N_c N_f}\,v\right)+\frac{16(N_c^2-1)}{\pi N_c N_f}\,v\,c\right], \tag{39}$$

$$\partial_\ell g = \frac{1}{2}z_\tau\, g\left[\epsilon-\frac{g^2}{16\pi v}\left\{1+\frac{2(N_c^2-1)}{N_c N_f}\,v-\frac{8v}{N_c N_f(1+v)}\right\}\right], \tag{40}$$

$$\partial_\ell \chi_1 = z_\tau\,\chi_1\left[\left(\epsilon-\frac{g^2}{8\pi v}\right)-\left(\frac{N_c^2+7}{2\pi^2}\chi_1+\frac{2N_c^2-3}{\pi^2 N_c}\chi_2+\frac{3(N_c^2+3)}{2\pi^2 N_c^2}\frac{\chi_2^2}{\chi_1}\right)\right], \tag{41}$$

$$\partial_\ell \chi_2 = z_\tau\,\chi_2\left[\left(\epsilon-\frac{g^2}{8\pi v}\right)-\left(\frac{6}{\pi^2}\chi_1+\frac{N_c^2-9}{\pi^2 N_c}\chi_2\right)\right]. \tag{42}$$

Although the anti-screening vertex correction (the last term in Eq. (40)) tends to enhance the coupling, the screening from the self-energies is dominant for any $N_c \geq 2$. As a result, g is stabilized at a finite value below three dimensions. The stable one-loop fixed point is given by

$$\begin{aligned} v_* &= \frac{N_c N_f}{2(N_c^2-1)},\\ g_*^2 &= \frac{4\pi N_c N_f}{(N_c^2-1)}\,\aleph(N_c,N_f)\,\epsilon,\\ c_* &= 0,\\ \chi_{1*} &= \chi_{2*} = 0, \end{aligned} \tag{43}$$

where

$$\aleph(N_c,N_f) = \frac{2(N_c^2-1)+N_c N_f}{2(N_c^2-3)+N_c N_f}. \tag{44}$$

At the one-loop order, the dynamical critical exponent $z_\tau = 1+\frac{\aleph(N_c,N_f)}{2}\epsilon$ becomes greater than one while z_x retains its classical value. However, z_x deviates from one at the two-loop order as will be shown later. It is remarkable that the quantum scaling dimensions of the quartic vertices $\left(\epsilon - g^2/8\pi v\right)$ become negative at the fixed point, resulting in their irrelevance even below three dimensions. This is due to the effective increase of the total spacetime dimension arising from $z_\tau > 1$. In a sense, the upper critical dimension for the quartic vertices is pushed down below $3-\epsilon$ at the interacting fixed point[9, 10].

We note that Eq. (43) is the fixed point of the full beta functions in Eqs. (31) - (35), because the truncation of higher order terms in Eq. (37) becomes exact in the small c limit. Besides the stable fixed point and the Gaussian fixed point, there exist two unstable interacting fixed points. One is the Wilson-Fisher fixed point with $g = 0$. The other is an unstable fixed point with the same values of g, c, v as in Eq. (43), but with a non-vanishing quartic coupling, $(\chi_1,\chi_2) = \left(-\frac{2\pi^2(1+\aleph(N_c,N_f))\,\epsilon}{N_c^2+7}, 0\right)$. The full RG flow in the subspace of χ_1, χ_2 at fixed g and v is shown in Fig. 5.

We now focus on the stable fixed point with $\chi_i = 0$ which is realized at the critical point without further fine tuning. The presence of the fixed point implies that the electron and boson propagators satisfy the scaling forms,

$$G_{l,m}(k) = \frac{1}{|k_y|^{1-2\widetilde{\eta}_\psi}}\,\mathcal{G}_{l,m}\left(\frac{k_x}{|k_y|^{z_x}}, \frac{\mathbf{K}}{|k_y|^{z_\tau}}\right), \tag{45}$$

$$D(q) = \frac{1}{|q_y|^{2-2\widetilde{\eta}_\phi}}\,\mathcal{D}\left(\frac{q_x}{|q_y|^{z_x}}, \frac{\mathbf{Q}}{|q_y|^{z_\tau}}\right). \tag{46}$$

The anomalous dimensions that dictate the scaling of the two-point functions are given by combinations of η_ψ, η_ϕ, z_τ and z_x.

$$\begin{aligned} \widetilde{\eta}_\psi &= \frac{2z_\tau + z_x - 3}{2} + \eta_\psi,\\ \widetilde{\eta}_\phi &= \frac{2z_\tau + z_x - 3}{2} + \eta_\phi. \end{aligned} \tag{47}$$

At the one-loop order, $\widetilde{\eta}_\psi = 0$ and $\widetilde{\eta}_\phi = 0$. $\mathcal{G}_{l,m}(x,y)$ and $\mathcal{D}(x,y)$ are universal functions of the dimensionless ratios of momentum and frequency. Due to the non-trivial dynamical critical exponent, the single-particle excitations are not well-defined, and the electrons near the hot spots become non-Fermi liquid below three dimensions.

The velocity c which measures the boson velocity along the direction of the ordering vector with respect to the Fermi velocity flows to zero logarithmically. The vanishing velocity leads to enhanced fluctuations of the collective mode at low energies, which can make higher-loop corrections bigger than naively expected. This can, in principle, pose a serious threat to a controlled expansion. In order to see whether the perturbative expansion is controlled beyond one-loop, one first needs to understand how higher-loop corrections change the flow of c. In the following two sub-sections, we show that c flows to a non-zero value which is order of $\epsilon^{1/3}$ due to a two-loop correction, and the perturbative expansion is controlled.

B. Beyond One Loop

The vanishing boson velocity at the one-loop fixed point can enhance higher order diagrams which are nominally suppressed by the small coupling $g^2 \sim \epsilon$. An L-loop diagram with V_g Yukawa vertices and V_u quartic vertices takes the form of

$$\begin{aligned} F(p_i; v, c, g, \chi; \epsilon, V_g, V_u, L) &\propto g^{V_g}\chi^{V_u}c^{V_u}\\ &\times \int\left[\prod_{i=1}^{L} dp_i'\right]\prod_{l=1}^{I_f}\left(\frac{1}{\mathbf{\Gamma}\cdot\mathbf{K}_l + \gamma_{d-1}\left[v k_{l,x} + n_l k_{l,y}\right]}\right)\\ &\times \prod_{m=1}^{I_b}\left(\frac{1}{|\mathbf{Q}_m|^2 + q_{m,x}^2 + c^2 q_{m,y}^2}\right). \end{aligned} \tag{48}$$

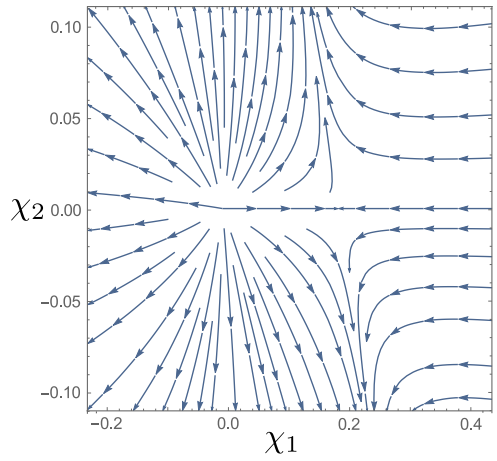

(a)

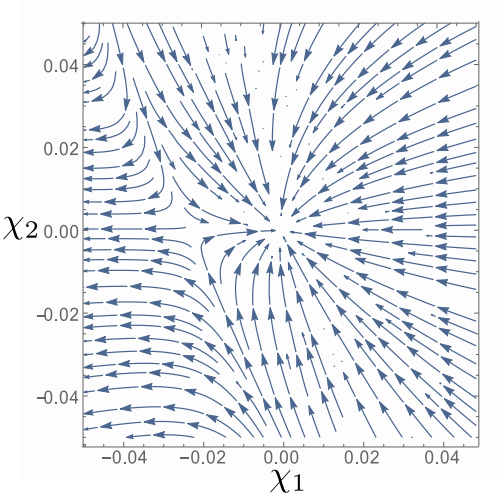

(b)

FIG. 5: RG Flow in the $\chi_1 - \chi_2$ plane with $N_c = 4, N_f = 1$, and $\epsilon = 0.2$. (a) In the subspace of $g = 0$, there are two unstable fixed points at $\chi_1 = 0$ and $\chi_1 \sim \epsilon$ with $\chi_2 = 0$. The former is the Gaussian fixed point, while the latter is the Wilson-Fisher fixed point. (b) In the subspace of $g = g_*$ and $v = v_*$, there exist an unstable non-Fermi liquid at $\chi_1 \sim -\epsilon$, and a stable non-Fermi liquid at $\chi_1 = 0$ with $\chi_2 = 0$. The arrows in both plots point towards increasing length scale.

Here p_i (p_i') are external (internal) momenta, and k_i and q_i are linear combinations of p_i and p_i'. χ represents either χ_1 or χ_2, whose difference is not important for the current purpose. I_f and I_b are the numbers of the internal electron and boson propagators, respectively. n_l is either $+$ or $-$ depending on the hot spot index carried by the l-th electron propagator.

When c is zero, some loop integrations can diverge as the dependence on q_y drops out in the boson propagator. This happens in the bosonic loops which are solely made of boson propagators. For example, y-component of the internal momentum in Fig. 2d is unbounded at $c = 0$. For a small but nonzero c, the UV divergence is cut-off at a scale proportional to $1/c$. As a result, the diagram is enhanced by $1/c$.

Such enhancement *can* also arise if bosonic loops are formed out of dressed propagators and dressed vertices. For example, the diagram in Fig. 6a is proportional to $1/c$ although it superficially does not contain pure boson loops. Because the boson self-energy made of the fermion bubble in Fig. 6a is independent of q_y, the integration over an internal y-momentum diverges as $1/c$ in the small c limit. Such enhancement may also arise in diagrams where fermion loops dress boson vertices. For example, the fermion loop in Fig. 6b can be viewed as a correction to the quartic vertex. Once the fermion bubble is replaced with a quartic vertex, the resulting diagram contains two bosonic loops. As a result, the diagram can be enhanced by upto $1/c^2$. In Fig. 7, we list some higher-loop diagrams which can be enhanced by upto $1/c^2$ for the same reasoning.

For non-bosonic loops such as the one in Fig. 7a, there exists a fermion propagator which can not be absorbed into boson self-energy or vertex corrections. For those loops, the loop integrations are not singular in the small c limit because the large internal momentum is cut-off by the energy of electrons. Thus, a general diagram can be enhanced *at most* by a factor of c^{-L_b}, where L_b is the number of loops solely made of bosonic propagators once fermion loops are replaced by boson self energy or vertex corrections. Therefore, we estimate the upper bound for the magnitude of general higher-loop diagrams to be

$$F(p_i; v, c, g, \chi; \epsilon, V_g, V_u, L) = \left(\frac{g^2}{c}\right)^{V_g/2} \chi^{V_u}\, c^{(E-2)/2+(L-L_b)}\, f(p_i; v, c; \epsilon, L), \tag{49}$$

where we have used the relation $L = (V_g + 2V_u + 2 - E)/2$ with E being the number of external legs. The function $f(p_i; v, c; \epsilon, L)$ is regular in the small c limit. We emphasize that Eq. (49) is an upper bound in the small c limit. The actual magnitudes may well be smaller by positive powers of c. For example, Fig. 8a is nominally order of g^4/c in the small c limit according to Eq. (49). However, an explicit computation shows that it is order of g^4. Currently, we do not have

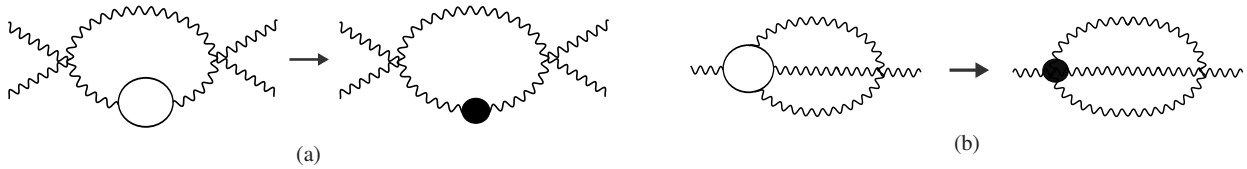

FIG. 6: (a) A two-loop diagram which is enhanced by $1/c$. (b) A three-loop diagram which may be enhanced by upto $1/c^2$. These diagrams do not include any bosonic loop that is solely made of boson propagators. Nonetheless, these can exhibit enhancements in powers of $1/c$ if the boson self energy and the quartic vertex correction (represented by shaded circles) are not suppressed at large momentum.

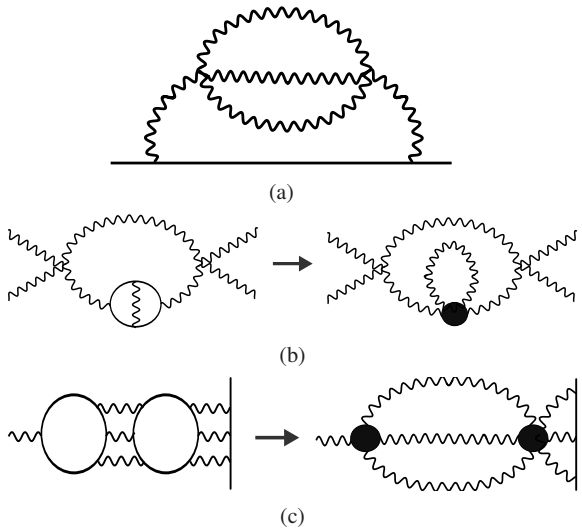

FIG. 7: Three examples with two bosonic loops made of dressed propagators and vertices.

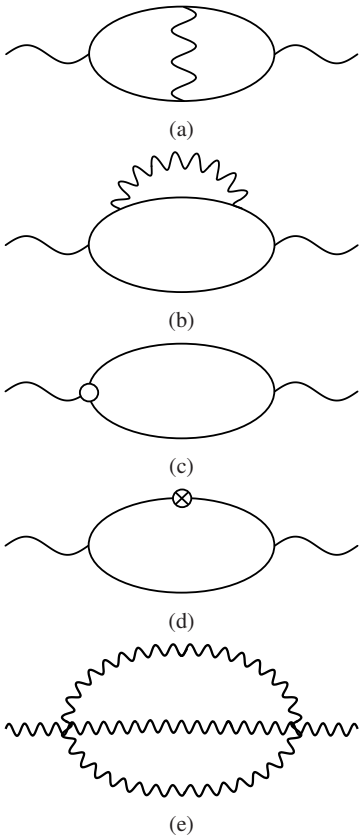

FIG. 8: The diagrams for the two-loop boson self energy. The small circles in (c) and (d) denote the one-loop counter terms.

a systematic way to estimate the actual magnitudes of general diagrams. Our strategy here is to use the upper bound which is enough to show that the perturbative expansion is controlled.

The ratio g^2/c which diverges at the one-loop fixed point may spoil the control of the perturbative expansion. However, such a conclusion is premature because higher-loop diagrams that are divergent at the one-loop fixed point can feed back to the flow of c and stabilize c at a nonzero value. As long as c is not too small, higher-loop diagrams can be still suppressed.

In order to include the leading quantum correction to c, we focus on the two-loop diagrams for the boson self-energy shown in Fig. 8. An explicit calculation in Appendix A 2 shows that only Fig. 8a renormalizes c in the small c limit. Other two-loop diagrams are suppressed by additional factors of c, g, or χ_i compared to Figs. 8a. Because stabilization of c at a non-zero value can occur only through two or higher loop effect, the non-zero value of c must be order of ϵ^b with $b > 0$. The two-loop diagram in Fig. 8a is proportional to $g^4 q_y^2$, which is strictly smaller than the upper bound in Eq. (49) by a factor of c. Its contribution to $Z_{6,1}$ is given by

$$Z_{6,1} = -\frac{8}{N_c N_f}\frac{g^4}{v^2 c^2}\left(h_6(v) + \mathcal{O}(c)\right), \tag{50}$$

where $h_6(v)$ is defined in Eq. (A35). The extra factor of $1/c^2$ in Eq. (50) originates from the fact that $Z_{6,1}$ is the multiplicative renormalization to the boson kinetic term, $c^2 q_y^2$. Since the quantum correction from the two-loop diagram does not vanish in the small c limit, it is relatively large compared to the vanishingly small classical action $c^2 q_y^2$. Because Fig. 8a generates a positive kinetic term at low energy (the counter term

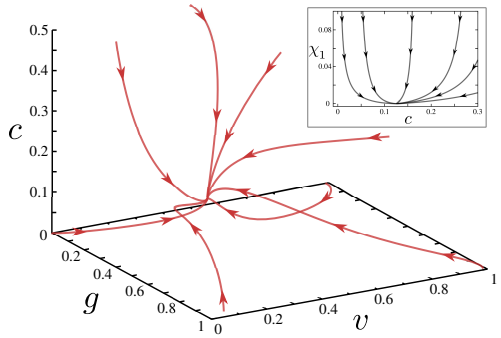

FIG. 9: Projection of the RG flow in the (g, v, c) space for $N_c = 2$, $N_f = 1$ and $\epsilon = 0.01$. The fixed point in Fig. 4 is modified by the two-loop correction (Fig. 8a) such that c flows to a non-zero value as shown in Eq. (57). (Inset) Projection of the RG flow in the (χ_1, c) plane. Although χ_1 still flows to zero, c does not.

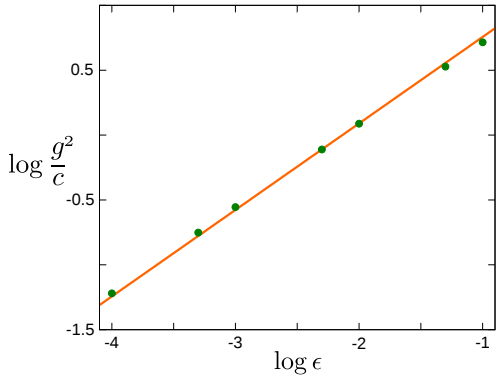

FIG. 10: The ratio g^2/c as a function of ϵ obtained from the numerical solution of the full beta functions in the low energy limit for $N_f = 1$ and $N_c = 2$. The filled circles are from the numerical solution of the beta functions, and the straight line is a fit, $g^2/c = 26.5\,\epsilon^{2/3}$.

in Eq. (50) is opposite to the logarithmic quantum correction generated at low energy from the Wilsonian RG), it stabilizes c at a nonzero value. For this, the anti-screening effect for the vertex correction in Eq. (36) is crucial. Without the anti-screening, Eq. (50) would come with the opposite sign, and c would flow to zero even faster by the two-loop effect.

The RG flow which includes the two-loop effect is shown in Fig. 9 for $N_c = 2$ and $N_f = 1$. c flows to a small but non-zero value in the low energy limit, while the other three parameters flow to values that are similar to those obtained at the one-loop order. g^2/c remains order of $\epsilon^{2/3}$ at the fixed point as is shown in Fig. 10. To find the fixed point for general N_c and N_f analytically, we analyze the beta functions in the region where $v \sim 1$ and $0 < c \ll 1$. The beta functions can be written as an expansion in g^2/c, χ_i and c as suggested by Eq. (49),

$$\partial_\ell \lambda = \lambda \sum_{l,m,n=0}^{\infty} J^{(\lambda)}_{l,m,n}(v,\epsilon) \left(\frac{g^2}{c}\right)^l \chi_i^{m-1} c^{n-1}, \qquad (51)$$

where λ represents a velocity or a coupling, and $J^{(\lambda)}_{l,m,n}(v,\epsilon)$ are functions of v and ϵ. Negative powers of χ_i and c can appear in Eq. (51) for $\lambda = \chi_i$ or c. This is because the Yukawa coupling alone can generate bosonic quartic vertices as in Fig. 11, and the quantum correction to the boson velocity can be independent of c as is reflected in Eq. (50). However, some $J^{(\lambda)}_{l,m,n}(v,\epsilon)$ are zero. According to Eq. (49), we have $J^{(\lambda)}_{l,0,n}(v,\epsilon) = 0$ for $\lambda = v, c, g$, and $J^{(\lambda)}_{l,m,n<2}(v,\epsilon) = 0$ for $\lambda = v, g$. Because v can be renormalized only in the presence of g, one also has $J^{(v)}_{0,m,n}(v,\epsilon) = 0$. Furthermore, the full $(d+1)$-dimensional rotational invariance in the bosonic subsector implies $J^{(c)}_{0,m,n}(v,\epsilon) = 0$. To $\mathcal{O}\left((g^2/c)\,c^2, \chi, (g^2/c)^2\right)$ in the small $g^2/c, \chi, c$ limit, the beta functions are given by

$$\partial_\ell v = \frac{z_\tau}{16\pi}\, v \left[\frac{g^2}{v} - \frac{2(N_c^2-1)}{N_c N_f}\, g^2\right], \qquad (52)$$

$$\partial_\ell c = -\frac{z_\tau}{16\pi}\, \frac{g^2 c}{v} \left[\left(1 - \frac{2(N_c^2-1)}{N_c N_f}\, v\right) + \frac{16(N_c^2-1)v}{\pi N_c N_f} \left(c - \frac{8\pi^2}{(N_c^2-1)} \frac{g^2\, h_6(v)}{v^2 c^2}\right)\right], \qquad (53)$$

$$\partial_\ell g = \frac{1}{2} z_\tau\, g \left[\epsilon - \frac{g^2}{16\pi v}\left\{1 + \frac{2(N_c^2-1)}{N_c N_f}\, v - \frac{8v}{N_c N_f (1+v)}\left(1 - \frac{2}{\pi}(1+v)c\right)\right\}\right], \qquad (54)$$

$$\partial_\ell \chi_1 = z_\tau\, \chi_1 \left[\left(\epsilon - \frac{g^2}{8\pi v} - \frac{8}{N_c N_f} \frac{g^4\, h_6(v)}{v^2 c^2}\right) - \left(\frac{N_c^2+7}{2\pi^2}\chi_1 + \frac{2N_c^2-3}{\pi^2 N_c}\chi_2 + \frac{3(N_c^2+3)}{2\pi^2 N_c^2}\frac{\chi_2^2}{\chi_1}\right)\right], \qquad (55)$$

$$\partial_\ell \chi_2 = z_\tau\, \chi_2 \left[\left(\epsilon - \frac{g^2}{8\pi v} - \frac{8}{N_c N_f} \frac{g^4\, h_6(v)}{v^2 c^2}\right) - \left(\frac{6}{\pi^2}\chi_1 + \frac{N_c^2-9}{\pi^2 N_c}\chi_2\right)\right]. \qquad (56)$$

It is noted that $J^{(c)}_{1,1,1}(v,\epsilon), J^{(c)}_{2,1,0}(v,\epsilon) = 0$ in Eq. (53). This underscores the fact that the actual magnitudes of the dia-

grams can be smaller than Eq. (49) which is only the upper bound.

In the small c limit, only the flows of c and χ_i are affected by the two-loop diagram through the fourth term in Eq. (53) and the third terms in Eqs. (55) and (56), respectively. While c tends to decrease under the one-loop effect, the two-loop correction enhances c due to the anti-screening produced by the vertex correction. These opposite tendencies eventually balance each other to yield a stable fixed point for c. At the fixed point of $v_* \sim O(1)$ and $g_*^2 \sim O(\epsilon)$, the beta function for c is proportional to $-c + r\epsilon/c^2$ with a constant $r > 0$, such that c flows to $O(\epsilon^{1/3})$ in the low energy limit. This confirms that g^2/c is $\mathcal{O}\left(\epsilon^{2/3}\right)$ at the fixed point.

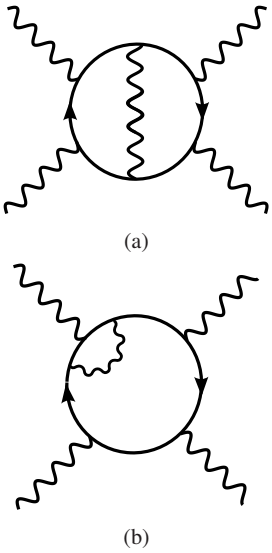

(a) (b)

FIG. 11: The leading two-loop diagrams that generate bosonic quartic interaction.

The RG flow in the $\chi_1 - \chi_2$ plane resembles Fig. 5 for small ϵ, and the χ_i's remain irrelevant at the fixed point. The two-loop diagrams in Fig. 11 will generate non-zero quartic couplings which are at most order of $O(g^6/c^2)$ in the beta function for χ_i. This is no longer singular because $g \sim \epsilon$ and $c \sim \epsilon^{1/3}$ at the fixed point. If the leading order term of $O(g^6/c^2)$ survives, the beta functions for χ_i has the form of $-\epsilon\chi_i + r' g^6/c^2$ with a constant r'. This suggests that χ_i is at most $\mathcal{O}\left(\epsilon^{4/3}\right)$ at the fixed point. Other two-loop diagrams and higher-loop diagrams are suppressed by additional powers of $\epsilon^{1/3}$ compared to the one-loop diagrams and the two-loop diagram in Fig. 8a, which are already included. Therefore, the two-loop effect modifies the fixed point as

$$
\begin{aligned}
v_* &= \frac{N_c N_f}{2(N_c^2-1)} + \mathcal{O}\left(\epsilon^{1/3}\right), \\
g_*^2 &= \frac{4\pi\, N_c N_f}{(N_c^2-1)}\, \aleph(N_c, N_f) \Bigg[\epsilon \\
&\quad - \frac{16}{N_c^2-1} \left(\frac{2\,\aleph^4(N_c, N_f)\, h_6(v_*)}{N_c N_f} \right)^{1/3} \epsilon^{4/3} \Bigg] + \mathcal{O}\left(\epsilon^{5/3}\right), \\
c_* &= 4\pi \left[\frac{2\aleph(N_c, N_f)}{N_c N_f}\, h_6(v_*) \right]^{1/3} \epsilon^{1/3} + \mathcal{O}\left(\epsilon^{2/3}\right), \\
\chi_{i;*} &= \mathcal{O}\left(\epsilon^{4/3}\right).
\end{aligned}
\tag{57}
$$

It is noted that $\mathcal{O}(\epsilon^\alpha)$ in the above equations represent the upper bounds of the sub-leading terms. The actual sub-leading terms may be smaller than the upper bound. For example, the actual sub-leading correction to v_* is $\mathcal{O}\left(\epsilon^{2/3}\right)$ because the $\mathcal{O}(c)$ term in $h_1(v,c)+h_2(v,c)$ is exactly zero (see Eq. (37)).

Eqs. (17)-(20) along with Eq. (49) implies that the anomalous dimensions at the fixed point can be expressed as

$$
\Delta = \sum_{l,m,n=0} A_{l,m,n} \left(\frac{g_*^2}{c_*} \right)^l \chi_*^m\, c_*^n, \tag{58}
$$

where Δ represents either $z_\tau - 1$, $z_x - 1$, η_ψ or η_ϕ, and $A_{l,m,n}$ are constants with $A_{0,0,n} = 0$. Using the expressions of the parameters at the fixed point (Eq. (57)), we compute the critical exponents up to order $\epsilon^{4/3}$,

$$
\begin{aligned}
z_\tau &= 1 + \frac{\aleph(N_c, N_f)}{2}\, \epsilon \\
&\quad - 8 \left(2 + \frac{\aleph(N_c, N_f)}{N_c^2 - 1} \right) \left(\frac{2\aleph^4(N_c, N_f)}{N_c N_f}\, h_6(v_*) \right)^{1/3} \epsilon^{4/3}, \\
z_x &= 1 - 16 \left(\frac{2\aleph^4(N_c, N_f)}{N_c N_f}\, h_6(v_*) \right)^{1/3} \epsilon^{4/3}, \\
\widetilde{\eta}_\psi &= 4 \left(\frac{2\aleph^4(N_c, N_f)}{N_c N_f}\, h_6(v_*) \right)^{1/3} \epsilon^{4/3}, \\
\widetilde{\eta}_\phi &= 16 \left(\frac{2\aleph^4(N_c, N_f)}{N_c N_f}\, h_6(v_*) \right)^{1/3} \epsilon^{4/3}.
\end{aligned}
\tag{59}
$$

We note that $\mathcal{O}\left(\epsilon^{2/3}\right)$ terms are absent in Eq. (59), since the one-loop diagrams are not singular in the $c \to 0$ limit. The fixed point value of $\chi_{i;*}$ does not affect the critical exponents up to $\mathcal{O}\left(\epsilon^{4/3}\right)$ because a single ϕ^4 vertex does not contribute to any of the nine counter terms. Because z_x differs from one at the fixed point, the system develops an anisotropy in the (k_x, k_y) plane. It is noted that the effective dimension of spacetime is modified from $4 - \epsilon$ to $z_\tau(2-\epsilon) + 1 + z_x$.

C. Control of the perturbative expansion

In the previous section, we incorporated one particular two-loop diagram which stabilizes the boson velocity at a non-zero value in order to compute the critical exponents to the order of $\epsilon^{4/3}$. A natural question is whether it is safe to ignore other two-loop diagrams, and more generally whether the perturbative expansion is under control for small ϵ. Eq. (49) along with Eq. (57) implies that quantum corrections are systematically suppressed by powers of $g^2/c \sim \epsilon^{2/3}$, $\chi \lesssim \epsilon^{4/3}$ as the number of loops increases, and there exist only a finite number of diagrams at each order. Here we confirm that other two-loop diagrams and higher-loop diagrams are indeed sub-leading, and they do not modify the critical exponents in Eq. (59) up to the order of $\epsilon^{4/3}$.

Sub-leading terms come in two ways. The first is from the c-expansions of $h_i(v,c)$ defined in Eq. (37). The second is from higher-loop diagrams. For $Z_{n,1}$ with $n = 1, 2, 3, 7$, two-loop diagrams are suppressed at least by $\epsilon^{5/3}$ according to Eq. (49) because $(L - L_b) \geq 1$ for the fermion self energy and the Yukawa vertex correction. $\mathcal{O}\left(c^2\right)$ terms in the expansion of $h_i(v,c)$ from the one-loop diagrams are also at most order of $\epsilon^{5/3}$. For $Z_{4,1}$, the one-loop diagram does not contain any sub-leading term in c. According to Eq. (49), higher-loop contributions to $Z_{4,1}$ are at most order of $g^4/c \sim \epsilon^{5/3}$ again because $L - L_b \geq 1$ for the diagrams that includes fermion loops. As noted earlier, the first non-vanishing contributions to $Z_{5,1}$ and $Z_{6,1}$ arise at the two-loop order. In Appendix A 2, we show that the leading order term in $Z_{5,1}$ is at most order of $g^4 c \sim \epsilon^{7/3}$. In contrast, Eq. (50) shows that the leading order term in $Z_{6,1}$ is $g^4/c^2 \sim \epsilon^{4/3}$ which is already included. The sub-leading terms are suppressed by $c, g^2/c^2 \sim \epsilon^{1/3}$. As discussed below Eq. (56), χ_i are at most $\mathcal{O}\left(\epsilon^{4/3}\right)$ from two-loop contributions. However, $\chi_i \sim \epsilon^{4/3}$ can not affect the critical exponents up to $\mathcal{O}\left(\epsilon^{4/3}\right)$ because a single quartic vertex only renormalizes boson mass. Thus the critical exponents in Eq. (59) are accurate up to $\mathcal{O}\left(\epsilon^{4/3}\right)$.

It is interesting to note that the perturbative expansion is not simply organized by the number of loops. Instead, one has to perform an expansion in terms of the couplings and the boson velocity together. There are notable consequence of this unconventional expansion. First, the perturbative expansion is in power series of $\epsilon^{1/3}$. Second, not all diagrams at a given loop play the same role; only one two-loop diagram (Fig. 8a) is important for the critical exponents to the order of $\epsilon^{4/3}$.

D. Physical Properties

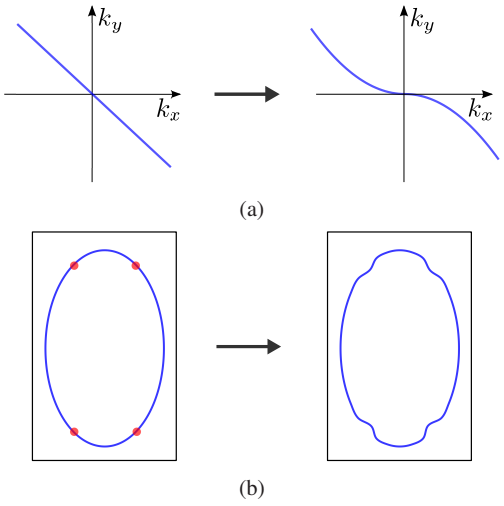

FIG. 12: (a) The patches of Fermi surface near the hot spots are deformed into a universal non-analytic curve. (b) The hot spots become algebraically nested near the hot spots.

In this section we discuss the physical properties of the non-Fermi liquid state that is realized at the SDW critical point. The anomalous dimension of k_x implies that the Fermi surface near the hot spots are deformed into a universal curve,

$$k_y \sim \text{sgn}\,(k_x)\,|k_x|^{1/z_x} \tag{60}$$

as is illustrated in Fig. 12. As ϵ increases, z_x decreases in accordance to Eq. (59), which leads to a stronger algebraic nesting of the Fermi surface near the hot spots. This is in contrast to the C_4-symmetric case, where the emergent nesting is only logarithmic[23, 34, 46]. The electronic spectral function at the hot spot scales with frequency as

$$\mathcal{A}_{l,m}(\omega) \sim \frac{1}{\omega^{(1-2\widetilde{\eta}_\psi)/z_\tau}}, \tag{61}$$

and the dynamical spin structure factor at momentum $\vec{Q}_{ord}$,

$$\mathcal{S}(\omega) \sim \frac{1}{\omega^{(2-2\widetilde{\eta}_\phi)/z_\tau}}. \tag{62}$$

As one moves away from the hot spots or the ordering vector in the x (y) directions, the electron spectral function and the spin structure factor will exhibit peak at frequency $\omega \sim |k_x|^{z_\tau/z_x}$ and $\omega \sim |k_y|^{z_\tau}$ depending on the direction of momentum. In principle, all exponents $z_\tau, z_x, \widetilde{\eta}_\psi, \widetilde{\eta}_\phi$ can be determined from the angle resolved photoemission and inelastic neutron scattering experiments.

We also estimate the contribution of electrons near the hot spots to the optical conductivity following a recent work by Patel *et al.* for the C_4-symmetric model [49]. The scaling dimension of free energy density $\mathcal{F}$ is

$$[\mathcal{F}] = z_\tau(d-1) + 1 + z_x. \tag{63}$$

The current density $\mathcal{J}_\mu$ has the dimension of $[\mathcal{J}_\mu] = [\mathcal{F}] - [k_\mu]$. Because k_x and k_y have different scaling dimensions, the two diagonal elements of the optical conductivity have different scaling dimensions,

$$\begin{aligned}[\sigma_{xx}] &= z_\tau(1-\epsilon) + 1 - z_x, \\ [\sigma_{yy}] &= z_\tau(1-\epsilon) + z_x - 1,\end{aligned} \tag{64}$$

at $d = 3 - \epsilon$. The contribution of the hot spot electrons to the optical conductivity obeys the hyperscaling [49] and scales with frequency as

$$\begin{aligned}\sigma^{hot}_{xx}(\omega) &\sim \omega^{1-\epsilon+(1-z_x)/z_\tau}, \\ \sigma^{hot}_{yy}(\omega) &\sim \omega^{1-\epsilon-(1-z_x)/z_\tau}.\end{aligned} \tag{65}$$

Because $z_x < 1$, the hot spot contribution to the optical conductivity is greater along the ordering vector than the perpendicular direction at low frequency [50, 51]. We emphasize that the anisotropy in Eq. (65) arises from anisotropic spatial scaling, rather than anisotropic carrier velocity [52, 53]. Electrons away from the hot spots are expected to violate the hyperscaling, and contribute to the optical conductivity as $\sigma \sim k_F \omega^{-\epsilon}$ with different coefficients in x and y directions, where k_F is the scale associated with the size of Fermi surface. For small ϵ, the contributions from cold electrons will dominate the hot spot contributions. However, the hot spot contribution can be dominant for σ_{yy} if $z_\tau + z_x < 1$.

V. CHARGE DENSITY WAVE CRITICALITY

In this section, we discuss the low energy properties of the CDW critical point. Since many aspects are similar to the SDW case, we will highlight the differences between the two critical points. The main differences arise from the commuting versus non-commuting nature of the respective interaction vertices as is shown in Eqs. (1) and (2). It is analogous to the difference between the nematic and ferromagnetic critical points [48].

Since the CDW order parameter couples to the global $U(1)$ charge, the interaction vertex is diagonal in both the spin and flavor space. One can also set $\chi_2 = 0$ for any N_f and N_c since the two quartic vertices are equivalent. As derived in Appendix A, the counter terms resulting from the one-loop diagrams in Fig. 2 are

$$\begin{aligned} Z_{1,1} &= -\frac{1}{4\pi^2 \widetilde{N}_f}\, g^2\, h_1(v,c), & Z_{2,1} &= \frac{1}{4\pi^2 \widetilde{N}_f}\, g^2\, h_2(v,c) \\ Z_{3,1} &= -\frac{1}{4\pi^2 \widetilde{N}_f}\, g^2\, h_2(v,c) & Z_{4,1} &= -\frac{1}{8\pi}\,\frac{g^2}{v}, \\ Z_{5,1} &= 0, & Z_{6,1} &= 0, \\ Z_{7,1} &= \frac{1}{8\pi^3 \widetilde{N}_f}\, g^2\, v\, h_3(v,c), & Z_{8,1} &= \frac{9}{2\pi^2}\,\chi_1, \end{aligned} \tag{66}$$

where $\widetilde{N}_f = N_c N_f$. Using the general expressions of the beta functions in section III, we obtain the one loop beta-functions for the CDW critical point. As in the SDW case, the boson velocity flows to zero in the low energy limit at the one-loop order. Therefore, we focus on the regime with small c where the one-loop beta functions take the form,

$$\partial_\ell v = \frac{z_\tau}{16\pi}\, g^2 \left[1 - \frac{2v}{\widetilde{N}_f}\right], \tag{67}$$

$$\partial_\ell c = -\frac{z_\tau}{16\pi}\,\frac{c}{v}\, g^2 \left[\left(1 - \frac{2v}{\widetilde{N}_f}\right) + \frac{16\, v\, c}{\pi \widetilde{N}_f}\right], \tag{68}$$

$$\partial_\ell g = \frac{z_\tau}{2}\, g \left[\epsilon - \frac{g^2}{16\pi v}\left\{\left(1 + \frac{2v}{\widetilde{N}_f}\right) + \frac{8v}{\widetilde{N}_f(1+v)}\left(1 - \frac{2}{\pi}(1+v)c\right)\right\}\right], \tag{69}$$

$$\partial_\ell \chi_1 = z_\tau\, \chi_1 \left[\left(\epsilon - \frac{g^2}{8\pi v}\right) - \frac{9}{2\pi^2}\,\chi_1\right]. \tag{70}$$

We note that the sign of $Z_{7,1}$ for the CDW critical point is opposite to that of the SDW critical point. This is due to the fact that the three CDW vertices (identity matrix) that appear in Fig. 2c are mutually commuting, while the SDW vertices ($SU(N_c)$ generators) are mutually anti-commuting as shown in Eq. (36). Consequently, the vertex correction screens the interaction at the CDW critical point in contrast to the SDW case. A stable one-loop fixed point arises at

$$\begin{aligned} v_* &= \frac{\widetilde{N}_f}{2}, \\ g_*^2 &= 4\pi \widetilde{N}_f \frac{\widetilde{N}_f + 2}{\widetilde{N}_f + 6}\,\epsilon, \\ c_* &= 0, \\ \chi_{1;*} &= \frac{8\pi^2\,\epsilon}{9(\widetilde{N}_f + 6)}. \end{aligned} \tag{71}$$

To the leading order in ϵ, the critical exponents become

$$z_\tau = 1 + \frac{\widetilde{N}_f + 2}{2(\widetilde{N}_f + 6)}\,\epsilon, \quad z_x = 1, \quad \widetilde{\eta}_\psi = 0 \quad \text{and} \quad \widetilde{\eta}_\phi = 0. \tag{72}$$

Since the one-loop vertex correction screens the Yukawa interaction in Eq. (69), the Yukawa coupling is not strong enough to push the upper critical dimension for χ_1 below $3 - \epsilon$ in contrast to the SDW case. As a result, χ_1 remains non-zero at the one-loop fixed point below three dimensions. It is interesting to note that the weaker (better screened) Yukawa coupling makes it possible for the quartic coupling to be stronger at the CDW critical point as compared to the SDW case.

We now investigate how the two-loop correction modifies the flow of c. The two-loop diagram in Fig. 8 leads to

$$Z_{5,1} = 0, \qquad Z_{6,1} = \frac{8}{\widetilde{N}_f}\,\frac{g^4}{v^2 c^2}\, h_6(v) \tag{73}$$

to the leading order in c. The modified beta functions for c and χ_1 are given by

$$\partial_\ell c = -\frac{z_\tau}{16\pi}\,\frac{c}{v}\, g^2 \left[\left(1 - \frac{2v}{\widetilde{N}_f}\right) + \frac{16\, v}{\pi \widetilde{N}_f}\left(c + \frac{8\pi^2 g^2 h_6(v)}{v^2 c^2}\right)\right], \tag{74}$$

$$\partial_\ell \chi_1 = z_\tau\, \chi_1 \left[\left(\epsilon - \frac{g^2}{8\pi v} + \frac{8}{\widetilde{N}_f}\,\frac{g^4}{v^2 c^2}\, h_6(v)\right) - \frac{9}{2\pi^2}\,\chi_1\right]. \tag{75}$$

It is noted that the sign of $Z_{6,1}$ in Eq. (73), which contributes the fourth term in Eq. (74) and the third term in Eq. (75), is opposite to that of $Z_{6,1}$ for the SDW case in Eq. (50). This is again due to the commuting CDW vertices in contrast to the anti-commuting SDW vertices in Eq. (36). Therefore the two-loop diagram further reduces c for the CDW case while it stops c from flowing to zero for the SDW case. Since Eq. (67) is not modified by the two-loop diagram, v flows to $v_* = \widetilde{N}_f/2$, irrespective of how the other parameters flow, as long as c remains small. To understand the fate of the system in the low energy limit, it is useful to examine the flow of g, c, χ_1 with fixed $v = v_*$,

$$\partial_\ell g = \frac{z_\tau}{2}\, g \left[\epsilon - \frac{g^2}{4\pi \widetilde{N}_f}\left\{1 + \frac{4}{\widetilde{N}_f + 2}\left(1 - \frac{\widetilde{N}_f + 2}{\pi}\, c\right)\right\}\right], \tag{76}$$

$$\partial_\ell c = -\frac{32 z_\tau}{\widetilde{N}_f^3}\, h_6(\widetilde{N}_f/2)\, g^2\, c^2 \left(\frac{\widetilde{N}_f^2}{32\pi^2 h_6(\widetilde{N}_f/2)} + \frac{g^2}{c^3}\right), \tag{77}$$

$$\partial_\ell \chi_1 = z_\tau\, \chi_1 \left[\left(\epsilon - \frac{g^2}{4\pi \widetilde{N}_f} + \frac{32}{\widetilde{N}_f^3} \frac{g^4}{c^2}\, h_6(\widetilde{N}_f/2) \right) - \frac{9}{2\pi^2}\, \chi_1 \right]. \tag{78}$$

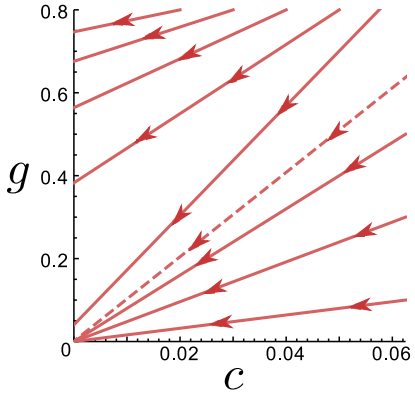

(a)

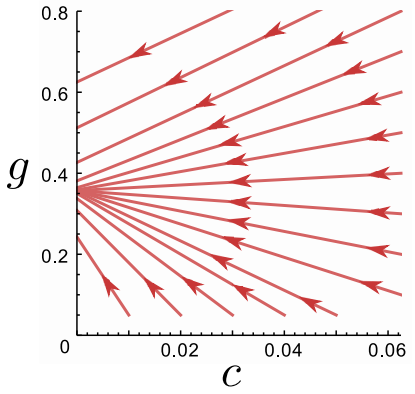

(b)

FIG. 13: RG flow of g and c at the CDW critical point with $\widetilde{N} = 2$ and $v = v_* = 1$. (a) In $d = 3$ there is a fixed point at the origin with a finite basin of attraction; for flows originating outside the basin, c flows to zero after a finite RG time. The dashed line in (a) denotes the separatrix which divides the flows to the stable quasilocal marginal Fermi liquid (below the separatrix) from the flow toward the non-perturbative regime (above the separatrix). (b) In $d = 3 - \epsilon$, c flows to zero after a finite RG time with a finite g. For the plot we have chosen $\epsilon = 0.01$.

Let us first analyze the flow in $d = 3$ (Fig. 13a). According to Eq. (77), $c(\ell)$ always decreases with increasing length scale. If the initial value of c is sufficiently small such that $c_0 \ll \pi/(\widetilde{N}_f + 2)$, the inequality will be always satisfied at lower energies. In this case, one can ignore the last term in Eq. (76) to obtain a logarithmically decreasing Yukawa coupling,

$$g^2(\ell) = \frac{g_0^2}{1 + \alpha_g(\widetilde{N}_f)\, g_0^2\, \ell}, \tag{79}$$

where $g_0 \equiv g(\ell = 0)$ and $\alpha_g(\widetilde{N}_f) = \dfrac{1}{8\pi \widetilde{N}_f} \left(1 + \dfrac{4}{\widetilde{N}_f + 2} \right)$.

The RG flow of c is relatively more complicated due to the important role of the two-loop correction. When $g^2 \ll \dfrac{c^3}{\pi^2 \widetilde{N}_f \alpha_c(\widetilde{N}_f)}$, where $\alpha_c(\widetilde{N}_f) = \dfrac{32}{\widetilde{N}_f^3}\, h_6(\widetilde{N}_f/2)$, the second term on the right hand side of Eq. (77) is negligible. In this case, the beta function for c gives

$$c(\ell) = c_0 \left[1 + \frac{c_0}{\pi^2 \widetilde{N}_f\, \alpha_g(\widetilde{N}_f)} \ln\left(1 + \alpha_g(\widetilde{N}_f)\, g_0^2\, \ell \right) \right]^{-1}, \tag{80}$$

where we have utilized the expression for $g(\ell)$ in Eq. (79). Since $g^2(\ell) \sim \ell^{-1}$ and $c(\ell) \sim (\ln \ell)^{-1}$ in the $\ell \to \infty$ limit, the second term on the right hand side of Eq. (77) becomes even smaller compared to the first term as ℓ increases, which justifies Eq. (80) at all $l > 0$. The quartic coupling flows to zero as $\chi_1(\ell) \sim \ell^{-1/(4\pi \widetilde{N}_f \alpha_g(\widetilde{N}_f))}$. Therefore, all the parameters, except for v, flow to zero in the low energy limit. Although c flows to zero, the critical point remains perturbatively controlled because g flows to zero much faster, such that $g^2/c \ll 1$. This is a stable quasilocal marginal Fermi liquid (MFL) [54].

In contrast, the first term on the right hand side of Eq. (77) is negligible if $g^2 \gg \dfrac{c^3}{\pi^2 \widetilde{N}_f \alpha_c(\widetilde{N}_f)}$, in which case we obtain

$$c(\ell) = \sqrt{\frac{c_0^2 - (2\alpha_c(\widetilde{N}_f)\, g_0^2 - \alpha_g(\widetilde{N}_f)\, c_0^2)\, g_0^2\, \ell}{1 + \alpha_g(\widetilde{N}_f)\, g_0^2\, \ell}}. \tag{81}$$

We note that the coefficient of ℓ in the numerator in Eq. (81) depends on the initial values of g and c. If $g_0^2 > \dfrac{\alpha_g(\widetilde{N}_f)\, c_0^2}{2\alpha_c(\widetilde{N}_f)}$, which automatically implies $g^2 \gg \dfrac{c^3}{\pi^2 \widetilde{N}_f \alpha_c(\widetilde{N}_f)}$ for small c, the boson velocity becomes zero at a *finite* RG time

$$\ell_0 = \frac{c_0^2/g_0^2}{2\alpha_c(\widetilde{N}_f)\, g_0^2 - \alpha_g(\widetilde{N}_f)\, c_0^2}. \tag{82}$$

This is different from the first case where c vanishes only asymptotically while the ratio g^2/c remains small. In the current case, the ratio g^2/c blows up, resulting in a loss of control over the perturbative expansion. For example, as $\ell \to \ell_0$, χ_1 diverges as $(\ell_0 - \ell)^{-a(c_0, g_0, \widetilde{N}_f)}$ with $a(c_0, g_0, \widetilde{N}_f) = \dfrac{32 h_6(\widetilde{N}_f/2)}{\widetilde{N}_f^3} \dfrac{g_0^4\, \ell_0}{c_0^2 (1 + \alpha_g(\widetilde{N}_f) g_0^2 \ell_0)}$, which results in the theory becoming non-perturbative.

Finally, let us consider the case where $\dfrac{c_0^3}{\pi^2 \widetilde{N}_f \alpha_c(\widetilde{N}_f)} \ll g_0^2 < \dfrac{\alpha_g(\widetilde{N}_f)\, c_0^2}{2\alpha_c(\widetilde{N}_f)}$. In this case, c initially approaches a nonzero constant dictated by Eq. (81). However, the system

eventually enters into the regime with $g^2 \ll \frac{c^3}{\pi^2 \widetilde{N}_f \alpha_c(\widetilde{N}_f)}$ at sufficiently large length scale. This is because g decreases much faster than c in this regime. Therefore the system again flows to the quasilocal marginal Fermi liquid.

Having understood the fate of the critical point in three dimensions, we consider the case below three dimensions (Fig. 13b). For $\epsilon > 0$, $g^2 \sim \epsilon$ as long as c is initially small. On the other hand, c flows to zero in a finite RG time, and the system becomes strongly coupled in the low energy limit.

The system flows to strong coupling regime when initial Yukawa coupling is large in $d = 3$ and for any nonzero Yukawa coupling in $d < 3$. In this case, there are various possibilities. First, the system may still flow to a strongly interacting non-Fermi liquid fixed point, which is beyond the regime of applicability of the current perturbative approach. Second, c^2 may become negative at low energies, which results in a shift of the ordering vector. In this case, the commensurate CDW can not occur without a further fine tuning. Third, the system may develop an instability toward other competing order, such as superconductivity[55]. Finally, a first order transition is a possibility.

The difference between the SDW and CDW critical points is summarized in Table I. The differences arise from the fact that the vertex correction screens (anti-screens) the interaction for the CDW (SDW) critical point. Within the present framework, it is also possible to consider a SDW critical point where the $SU(N_c)$ spin rotational symmetry is explicitly broken down to a subgroup. In the Ising case where only one mode becomes critical at the critical point, the Yukawa vertex is commuting as in the CDW case. Therefore, we expect that the Ising SDW critical point will be similar to the CDW critical point.

VI. SUMMARY AND DISCUSSION

In this work, we studied the spin and charge density wave critical point in metals with the C_2 symmetry, where a one dimensional Fermi surface is embedded in space dimensions three and below. Within one-loop RG analysis augmented by a two-loop diagram, we obtained an anisotropic non-Fermi liquid below three dimensions at the SDW critical point. The Green's function near the hot spots and the spin-spin correlation function obey the anisotropic scaling, where not only frequency but also different components of momentum acquire non-trivial anomalous dimensions. Consequently, the Fermi surface develops an algebraic nesting near the hot spots with a universal shape. The stable non-Fermi liquid fixed point turns into a quasilocal marginal Fermi liquid in three dimensions, which is characterized by vanishing interactions and an emergent flat direction in the bosonic dispersion. In contrast to the SDW criticality, the CDW critical point flows to a non-perturbative regime below three dimensions, while there is a finite parameter regime where the marginal Fermi liquid is still stable in three dimensions.

At the SDW critical point, it is expected that superconducting, pair density wave and charge density wave fluctuations are enhanced[23, 34, 56]. At the one-loop order, the pattern of enhancement is expected to be similar to the case with the C_4 symmetry. However, it will be of interest to examine the effects of anisotropic scaling through a comparative study. In particular, the stronger nesting in the C_2 case will increase the phase space for the zero-energy particle-particle excitations with momentum $2k_F$. This will help enhance the pair density wave fluctuations, which was found to be as strong as the d-wave superconducting fluctuations at the one-loop order in the C_4 case[34].

VII. ACKNOWLEDGMENT

We thank Luis Balicas, Peter Lunts and Subir Sachdev for helpful discussions. The research was supported in part by the Natural Sciences and Engineering Research Council of Canada (Canada) and the Early Research Award from the Ontario Ministry of Research and Innovation. Research at the Perimeter Institute is supported in part by the Government of Canada (Canada) through Industry Canada, and by the Province of Ontario through the Ministry of Research and Information.

Appendix A: Computation of Feynman diagrams

In this appendix we show the key steps for computing the Feynman diagrams.

1. One loop diagrams

a. *Electron self energy*

The quantum correction to the electron self-energy from the diagram in Fig. 2a is

$$\delta S^{(2,0)} = \mu^{3-d}\, 2\mathcal{B}^{(1L)}_{(2,0)}\, g^2 \sum_{n=\pm} \sum_{s=1}^{N_c} \sum_{j=1}^{N_f} \int dk\; \bar{\Psi}_{n,s,j}(k)\; \Upsilon^{(n)}_{(2,0)}(k)\; \Psi_{n,s,j}(k), \tag{A1}$$

	SDW	CDW
$d=3$	Quasilocal MFL $v_* \sim 1, \quad c(\ell) \sim \frac{1}{\ln \ell}$, $g^2(\ell), \chi_i \sim \frac{1}{\ell}$.	• Non-perturbative $\left(g_0^2 > \frac{\alpha_g(\widetilde{N}_f)\, c_0^2}{2\alpha_c(\widetilde{N}_f)} \right)$ $v_* \sim 1, \quad g^2(\ell) \sim \frac{1}{\ell}, \quad c(\ell = \ell_0 < \infty) = 0,$ $\chi_1(\ell) \sim (l_0 - l)^{-a(c_0, g_0, \widetilde{N}_f)}$. • Quasilocal MFL $\left(g_0^2 < \frac{\alpha_g(\widetilde{N}_f)\, c_0^2}{2\alpha_c(\widetilde{N}_f)} \right)$ $v_* \sim 1, \quad g^2(\ell) \sim \frac{1}{\ell}, \quad c(\ell) \sim \frac{1}{\ln \ell}$, $\chi_1(\ell) \sim \ell^{-1/(4\pi \widetilde{N}_f \alpha_g(\widetilde{N}_f))}$.
$d = 3 - \epsilon$	Anisotropic NFL $v_* \sim 1, \;\; g_*^2 \sim \epsilon$ $c_* \sim \epsilon^{1/3}, \;\; \chi_{i;*} \sim \epsilon^{4/3}$	Non-perturbative

TABLE I: Behaviors of the renormalized couplings and velocities with increasing logarithmic length scale ℓ at the SDW and CDW critical points. The universal (non-universal) constants $\alpha_g(\widetilde{N}_f)$ and $\alpha_c(\widetilde{N}_f)$ (ℓ_0 and $a(c_0, g_0, \widetilde{N}_f)$) are defined in the main text. Here NFL and MFL represents non-Fermi liquid and marginal Fermi liquid, respectively.

where

$$\mathcal{B}^{(1L)}_{(2,0)} = \begin{cases} \dfrac{N_c^2 - 1}{N_f N_c} & \text{for SDW} \\ \dfrac{1}{N_f N_c} & \text{for CDW} \end{cases} \tag{A2}$$

and

$$\Upsilon^{(n)}_{(2,0)}(k) = \int \frac{d^{d-1}\mathbf{Q}}{(2\pi)^{d-1}} \frac{d^2\vec{q}}{(2\pi)^2}\, \gamma_{d-1} G_{\bar{n}}(k+q) \gamma_{d-1}\, D(q). \tag{A3}$$

The bare Green's functions are given by

$$G_n(k) = -i\, \frac{\mathbf{\Gamma}\cdot\mathbf{K} + \gamma_{d-1}\varepsilon_n(\vec{k})}{|\mathbf{K}|^2 + \varepsilon_n^2(\vec{k})}, \tag{A4}$$

$$D(q) = \frac{1}{|\mathbf{Q}|^2 + q_x^2 + c^2 q_y^2}. \tag{A5}$$

After the integrations over $\vec{q}$ and $\mathbf{Q}$, Eq. (A3) can be expressed in terms of a Feynman parameter,

$$\Upsilon^{(n)}_{(2,0)}(k) = \frac{i}{(4\pi)^{(d+1)/2}} \Gamma\left(\frac{3-d}{2}\right) \int_0^1 dx \sqrt{\frac{1-x}{c^2 + x(1-(1-v^2)c^2)}} \\ \times \left[x(1-x) \left\{ |\mathbf{K}|^2 + \frac{c^2\, \varepsilon_{\bar{n}}^2(\vec{k})}{c^2 + x(1-(1-v^2)c^2)} \right\} \right]^{-\frac{3-d}{2}} \left[\mathbf{K}\cdot\mathbf{\Gamma} - \frac{c^2\, \varepsilon_{\bar{n}}(\vec{k})\, \gamma_{d-1}}{c^2 + x(1-(1-v^2)c^2)} \right]. \tag{A6}$$

The UV divergent part in the $d \to 3$ limit is given by

$$\Upsilon^{(n)}_{(2,0)}(k) = \frac{i}{8\pi^2\, \epsilon} \left[h_1(v,c)\, \mathbf{K}\cdot\mathbf{\Gamma} - h_2(v,c)\, \varepsilon_{\bar{n}}(\vec{k}) \gamma_{d-1} \right], \tag{A7}$$

where

$$h_1(v,c) = \int_0^1 dx \sqrt{\frac{1-x}{c^2 + x(1-(1-v^2)c^2)}}, \quad h_2(v,c) = c^2 \int_0^1 dx \sqrt{\frac{1-x}{[c^2 + x(1-(1-v^2)c^2)]^3}}. \tag{A8}$$

This leads to the one-loop counter term for the electron self-energy,

$$S_{CT}^{(2,0)} = -\frac{\mathcal{B}_{(2,0)}^{(1L)}}{4\pi^2\epsilon}\, g^2 \sum_{n=\pm}\sum_{s=1}^{N_c}\sum_{j=1}^{N_f}\int dk \times \bar{\Psi}_{n,s,j}(k)\left[ih_1(v,c)\,\mathbf{K}\cdot\mathbf{\Gamma} - ih_2(v,c)\,\varepsilon_{\bar{n}}(\vec{k})\gamma_{d-1}\right]\Psi_{n,s,j}(k). \tag{A9}$$

b. Boson self energy

The boson self energy in Fig. 2b is given by

$$\delta S^{(0,2)} = -\mu^{3-d}\,\frac{g^2}{2}\int dq\;\Upsilon_{(0,2)}(q)\;\mathrm{Tr}\left(\Phi(-q)\Phi(q)\right), \tag{A10}$$

where

$$\Upsilon_{(0,2)}(q) = \sum_{n=\pm}\int dk\;\mathrm{Tr}\left[\gamma_{d-1}G_n(k+q)\gamma_{d-1}G_{\bar{n}}(k)\right]. \tag{A11}$$

We first integrate over $\vec{k}$. Because $\vec{q}$ can be absorbed into the internal momentum $\vec{k}$, $\Upsilon_{(0,2)}(q)$ is independent of $\vec{q}$. Using the Feynman parameterization, we write the resulting expression as

$$\Upsilon_{(0,2)}(q) = \frac{1}{2\pi v}\int_0^1 dx\int\frac{d^{d-1}\mathbf{K}}{(2\pi)^{d-1}}\,\frac{[x(1-x)]^{-\frac{1}{2}}\;\mathbf{K}\cdot(\mathbf{K}+\mathbf{Q})}{x\,|\mathbf{K}+\mathbf{Q}|^2+(1-x)\,|\mathbf{K}|^2}. \tag{A12}$$

The quadratically divergent term is the mass renormalization, which is automatically tuned away at the critical point in the present scheme. The remaining correction to the kinetic energy of the boson becomes

$$\Upsilon_{(0,2)}(q) = -\frac{|\mathbf{Q}|^2}{16\pi v\epsilon} \tag{A13}$$

up to finite terms. Accordingly we add the following counter term,

$$S_{CT}^{(0,2)} = -\frac{1}{4}\,\frac{1}{8\pi\,\epsilon}\,\frac{g^2}{v}\int dq\;\;|\mathbf{Q}|^2\;\;\mathrm{Tr}\left(\Phi(-q)\Phi(q)\right). \tag{A14}$$

c. Yukawa vertex correction

The diagram in Fig. 2c gives rise to the vertex correction in the quantum effective action,

$$\delta S^{(2,1)} = i\frac{g}{\sqrt{N_f}}\,\mu^{\frac{3(3-d)}{2}}\,2\mathcal{B}_{(2,1)}^{(1L)}\,g^2\sum_{j=1}^{N_f}\sum_{s,s'=1}^{N_c} \times\int dk\;dq\;\left[\bar{\Psi}_{+,j,s}(k+q)\;\Upsilon_{(2,1)}^{(+,-)}(k,q)\;\Phi_{s,s'}(q)\;\Psi_{-,j,s'}(k) - \text{h.c.}\right], \tag{A15}$$

where

$$\Upsilon_{(2,1)}^{(n,\bar{n})}(k,q) = \int dp\;\gamma_{d-1}G_{\bar{n}}(p+q+k)\gamma_{d-1}G_n(p+k)\gamma_{d-1}\;D(p) \tag{A16}$$

and

$$\mathcal{B}_{(2,1)}^{(1L)} = \begin{cases}\dfrac{1}{N_cN_f} & \text{for SDW}\\[2ex] -\dfrac{1}{N_cN_f} & \text{for CDW}\end{cases}. \tag{A17}$$

The minus sign in $\mathcal{B}^{(1L)}_{(2,1)}$ for the SDW case is due to the anti-commuting nature of the $SU(N_c)$ generators, $\sum_{a=1}^{N_c^2-1} \tau^a \tau^b \tau^a = -\frac{2}{N_c}\,\tau^b$. The UV divergent part in the $\epsilon \to 0$ limit can be extracted by setting all external frequency and momenta to zero except $\mathbf{Q}$,

$$\Upsilon^{(n,\bar{n})}_{(2,1)}(\mathbf{Q}) = \gamma_{d-1} \int dp\, \frac{|\mathbf{P}|^2 - \varepsilon_{\bar{n}}(\vec{p})\varepsilon_n(\vec{p})}{\left[|\mathbf{P}|^2 + p_x^2 + c^2 p_y^2\right]\left[|\mathbf{Q}+\mathbf{P}|^2 + \varepsilon^2_{\bar{n}}(\vec{p})\right]\left[|\mathbf{P}|^2 + \varepsilon^2_{n}(\vec{p})\right]}. \tag{A18}$$

Eq. (A18) is evaluated following the computation in Ref. [34] to obtain

$$\Upsilon^{(n,\bar{n})}_{(2,1)}(\mathbf{K}) = \frac{\gamma_{d-1}\, v}{16\pi^3\, \epsilon}\, h_3(v,c) + \mathcal{O}\left(\epsilon^0\right), \tag{A19}$$

where

$$h_3(v,c) = \int_0^{2\pi} d\theta \int_0^1 dx_1 \int_0^{1-x_1} dx_2 \left[\frac{1}{\zeta(\theta,x_1,x_2,v,c)} - \frac{v^2\, \sin(2\theta)}{\zeta^2(\theta,x_1,x_2,v,c)}\right], \tag{A20}$$

with

$$\begin{aligned}\zeta(\theta,x_1,x_2,v,c) &= 2v^2[x_1 \sin^2(\theta) + x_2 \cos^2(\theta)] \\ &\quad + (1-x_1-x_2)\left[\sin^2\left(\theta+\frac{\pi}{4}\right) + c^2v^2\cos^2\left(\theta+\frac{\pi}{4}\right)\right].\end{aligned} \tag{A21}$$

Note that the UV divergent part of $\Upsilon^{(n,\bar{n})}_{(2,1)}$ is independent of $(n,\bar{n})$. From this, we identify the counter term for the Yukawa vertex,

$$\begin{aligned}S^{(2,1)}_{CT} = -i\frac{g}{\sqrt{N_f}}\,\frac{\mathcal{B}^{(1L)}_{(2,1)}}{8\pi^3\epsilon}\, g^2 v\, h_3(v,c) \sum_{j=1}^{N_f}\sum_{s,s'=1}^{N_c} \\ \times \int dk\, dq\, \left[\bar{\Psi}_{+,j,s}(k+q)\, \gamma_{d-1}\, \Phi_{s,s'}(q)\, \Psi_{-,j,s'}(k) - \text{h.c.}\right].\end{aligned} \tag{A22}$$

d. ϕ^4 vertex corrections

There are two types of one-loop diagrams that can potentially contribute to the renormalization of the quartic vertex as is shown in Fig. 2d and Fig. 2e. The diagram in Fig. 2e is UV finite at $d = 3$ [34], which implies that it does not contain an ϵ^{-1} pole in $d = 3-\epsilon$. The second type of diagrams are produced by the boson vertices only. They lead to non-zero counter terms,

$$\begin{aligned}S^{(0,4)}_{CT} = \frac{1}{8\pi^2 c\,\epsilon}\int dq_1 dq_2 dq_3 dq_4\, \delta(q_1+q_2+q_3+q_4) \\ \times\Big\{\left[\mathcal{B}^{(1L;1a)}_{(0,4)} u_1^2 + \mathcal{B}^{(1L;1b)}_{(0,4)} u_1 u_2 + \mathcal{B}^{(1L;1c)}_{(0,4)} u_2^2\right] \text{Tr}\left(\Phi(q_1)\Phi(q_2)\right) \text{Tr}\left(\Phi(q_3)\Phi(q_4)\right) \\ + \left[\mathcal{B}^{(1L;2a)}_{(0,4)} u_1 u_2 + \mathcal{B}^{(1L;2b)}_{(0,4)} u_2^2\right] \text{Tr}\left(\Phi(q_1)\Phi(q_2)\Phi(q_3)\Phi(q_4)\right)\Big\}.\end{aligned} \tag{A23}$$

Here

$$\begin{aligned}\mathcal{B}^{(1L;1a)}_{(0,4)} = N_c^2+7,\;\; \mathcal{B}^{(1L;1b)}_{(0,4)} = \frac{2(2N_c^2-3)}{N_c},\;\; \mathcal{B}^{(1L;1c)}_{(0,4)} = \frac{3(N_c^2+3)}{N_c^2}, \\ \mathcal{B}^{(1L;2a)}_{(0,4)} = 12,\;\; \mathcal{B}^{(1L;2b)}_{(0,4)} = \frac{2(N_c^2-9)}{N_c}\end{aligned} \tag{A24}$$

for the SDW case. For the CDW case, one can set $u_2 = 0$ and $\mathcal{B}^{(1L;1a)}_{(0,4)} = 9$.

2. Two loops boson self-energy

There are five diagrams, shown in Fig. 8, that contribute to the boson self energy at the two-loop order. We will first show that only Fig. 8a contributes to the renormalization of c to the leading order in c. We will also outline the key steps for an explicit computation of Fig. 8a.

Let us denote the loop integrations in figures 8b - 8d for fixed electron flavor n as $\Upsilon^{2L;b}_{(0,2)}(q)$, $\Upsilon^{2L;c}_{(0,2)}(q)$ and $\Upsilon^{2L;d}_{(0,2)}(q)$, respectively, with q being the external frequency-momentum. At $c=0$ the loop integrations in Fig. 8b is given by

$$\Upsilon^{2L;b}_{(0,2)}(q) = \int \frac{d^4p}{(2\pi)^4}\frac{d^4k}{(2\pi)^4}\frac{\text{Tr}\left(\gamma_{d-1}G_{\bar{n}}(k)\gamma_{d-1}G_n(k+p)\gamma_{d-1}G_{\bar{n}}(k)\gamma_{d-1}G_n(k+q)\right)}{|\mathbf{P}|^2+p_x^2}. \tag{A25}$$

The integrand depends on p_y only through

$$G_n(k+p) = \left[i(\mathbf{K}+\mathbf{P})\cdot\mathbf{\Gamma} + (\varepsilon_n(k)+vp_x+np_y)\gamma_{d-1}\right]^{-1}. \tag{A26}$$

Changing coordinate as $p_y \mapsto p_y - n((\varepsilon_n(k)+vp_x)$, $G_n(k+p)$ becomes independent of $\vec{k}$. Since $\varepsilon_n(\vec{k})$ and $\varepsilon_{\bar{n}}(\vec{k})$ are linearly independent, we can change coordinates as $(k_x,k_y)\mapsto(\varepsilon_n(\vec{k}),\varepsilon_{\bar{n}}(\vec{k}))$ and shift $\varepsilon_n(\vec{k})\mapsto\varepsilon_n(\vec{k})-\varepsilon_n(\vec{q})$ to make $\Upsilon^{2L;b}_{(0,2)}(q)$ independent of $\vec{q}$. This shows that Fig. 8b does not depend on $\vec{q}$ in the small c limit. Note that such dependence may arise at order g^4c or higher, but these contributions are subdominant to that of Fig. 8a.

$\Upsilon^{2L;c}_{(0,2)}(q)$ and $\Upsilon^{2L;d}_{(0,2)}(q)$ closely resemble $\Upsilon_{(0,2)}(q)$. Because the one-loop counter terms are independent of the x and y components of momentum, it is straightforward to shift the internal integration variable to show that $\Gamma^{2L;c}_{(0,2)}(q)$ and $\Gamma^{2L;d}_{(0,2)}(q)$ are independent of $\vec{q}$, irrespective of the value of c. Therefore, diagrams in Figs. 8c and 8d do not contribute to $Z_{5,1}$ and $Z_{6,1}$. 8e is also sub-leading because $\chi_i=0$ at the one-loop fixed point.

The quantum correction due to Fig. 8a is

$$\delta S^{2L;a}_{(0,2)} = \mu^{2(3-d)}\,\frac{8\mathcal{B}^{(2L)}_{(0,2)}}{4}\,g^4\int dq\;\Upsilon^{2L;a}_{(0,2)}(q)\;\text{Tr}\left(\Phi(-q)\Phi(q)\right) \tag{A27}$$

where

$$\Upsilon^{2L;a}_{(0,2)}(q) = -\int dp\,dk\;\frac{\text{Tr}\left(\gamma_{d-1}G_+(k+q)\gamma_{d-1}G_-(p+q)\gamma_{d-1}G_+(p)\gamma_{d-1}G_-(k)\right)}{|\mathbf{P}-\mathbf{K}|^2+(p_x-k_x)^2+c^2(p_y-k_y)^2} \tag{A28}$$

and $\mathcal{B}^{(2L)}_{(0,2)} = \mathcal{B}^{(1L)}_{(2,1)}$ as defined in Eq. (A17). In order to extract the leading order term that depends on $\vec{k}$ in the small c limit, we set $c=0$ and $\mathbf{Q}=0$ in $\Upsilon^{2L;a}_{(0,2)}(q)$ to write

$$\Upsilon^{2L;a}_{(0,2)}(\vec{q}) = -\int dp\,dk\;\frac{\text{Tr}\left(\gamma_{d-1}G_+(\mathbf{K},\vec{k}+\vec{q})\gamma_{d-1}G_-(\mathbf{P},\vec{p}+\vec{q})\gamma_{d-1}G_+(p)\gamma_{d-1}G_-(k)\right)}{|\mathbf{P}-\mathbf{K}|^2+(p_x-k_x)^2}. \tag{A29}$$

Using $\text{Tr}\left(\gamma_\mu\gamma_\nu\right) = 2\delta_{\mu,\nu}\mathcal{I}_2$, we evaluate the trace in the numerator to obtain

$$\begin{aligned}\Upsilon^{2L;a}_{(0,2)}(\vec{q}) &= -2\int dp\,dk\\ &\times\frac{[|\mathbf{K}|^2-\varepsilon_+(\vec{k}+\vec{q})\varepsilon_-(\vec{k})][|\mathbf{P}|^2-\varepsilon_-(\vec{p}+\vec{q})\varepsilon_+(\vec{p})]-\mathbf{K}\cdot\mathbf{P}[\varepsilon_+(\vec{k}+\vec{q})+\varepsilon_-(\vec{k})][\varepsilon_-(\vec{p}+\vec{q})+\varepsilon_+(\vec{p})]}{[|\mathbf{K}|^2+\varepsilon_+^2(\vec{k}+\vec{q})][|\mathbf{K}|^2+\varepsilon_-^2(\vec{k})][|\mathbf{P}|^2+\varepsilon_-^2(\vec{p}+\vec{q})][|\mathbf{P}|^2+\varepsilon_+^2(\vec{p})][|\mathbf{P}-\mathbf{K}|^2+(p_x-k_x)^2]}.\end{aligned} \tag{A30}$$

We change coordinates for both $\vec{p}$ and $\vec{k}$ as $(k_x,k_y)\mapsto(k_+,k_-)$ with $k_\pm=\varepsilon_\pm(\vec{k})$, and shift $k_+\mapsto k_+-\varepsilon_+(\vec{q})$ and $p_-\mapsto p_--\varepsilon_-(\vec{q})$ to rewrite the expression as

$$\begin{aligned}\Upsilon^{2L;a}_{(0,2)}(\vec{q}) &= -\frac{1}{2v^2}\int dp'\,dk'\\ &\times\frac{[|\mathbf{K}|^2-k_+k_-][|\mathbf{P}|^2-p_+p_-]-\mathbf{K}\cdot\mathbf{P}[k_++k_-][p_++p_-]}{[|\mathbf{K}|^2+k_+^2][|\mathbf{K}|^2+k_-^2][|\mathbf{P}|^2+p_-^2][|\mathbf{P}|^2+p_+^2][|\mathbf{P}-\mathbf{K}|^2+\frac{1}{4v^2}(p_++p_--k_+-k_-+2q_y)^2]},\end{aligned} \tag{A31}$$

where $dk' \equiv \frac{d^{d-1}\mathbf{K}dk_+dk_-}{(2\pi)^{d+1}}$. It is noted that $\Upsilon^{2L;a}_{(0,2)}(\vec{q})$ has become *independent* of q_x in the small c limit. This implies that $Z_{5,1}$ is at most order of g^4c which is negligible. From now on, we will focus on $Z_{6,1}$.

We integrate over $\mathbf{P}$ and $\mathbf{K}$ after introducing Feynman parameters, x, y and u, w. Employing a Schwinger parameter, α, we have

$$\begin{aligned}\Upsilon^{2L;a}_{(0,2)}(\vec{q}) = &-\frac{1}{2\pi^2(4\pi)^{d+1}v^2}\int_0^1 dx\,du\int_0^{1-x}dy\int_0^{1-u}dw\,\frac{(1-u-w)^{(3-d)/2}}{A^{(d-1)/2}}\int_0^\infty d\alpha\,e^{-\alpha M^2}\\
&\times\int_{-\infty}^{\infty}dp_+dp_-dk_+dk_-\Big[\Big\{\frac{(d-1)^2}{4A}+\frac{d^2-1}{4A^2}\,(1-u-w)(1-x-y)^2\Big\}\alpha^{3-d}\\
&-\frac{(d-1)(1-u-w)}{2A}\Big\{p_+p_-+\Big((1-x-y)^2+\frac{A}{1-u-w}\Big)\,k_+k_-\\
&+(1-x-y)(k_++k_-)(p_++p_-)\Big\}\alpha^{4-d}+(1-u-w)\,p_+p_-k_+k_-\,\alpha^{5-d}\Big],\end{aligned}\tag{A32}$$

where

$$\begin{aligned}&A\equiv A(x,y,u,w)=(u+w)+(x+y)(1-x-y)(1-u-w),\quad\text{and}\\
&M^2\equiv M^2(k_\pm,p_\pm;x,y,u,w;v,q_y)=uk_+^2+wk_-^2+x(1-u-w)p_+^2+y(1-u-w)p_-^2\\
&\qquad+\frac{(1-u-w)(1-x-y)}{4v^2}(p_++p_--k_+-k_-+2q_y)^2.\end{aligned}\tag{A33}$$

At this stage, we substract the mass renormalization from $\Upsilon^{2L;a}_{(0,2)}(\vec{q})$ and proceed with the computation of $\Delta\Upsilon^{2L;a}_{(0,2)}(\vec{q}) = \Upsilon^{2L;a}_{(0,2)}(\vec{q}) - \Upsilon^{2L;a}_{(0,2)}(0)$. After integrating over $p_\pm$, $k_\pm$ and α, we extract the pole in ϵ as

$$\Delta\Upsilon^{2L;a}_{(0,2)}(\vec{q}) = \frac{q_y^2\,h_6(v)}{\epsilon\,v^2}.\tag{A34}$$

Here the function $h_6(v)$ is defined as

$$\begin{aligned}h_6(v) = &\frac{2}{(4\pi)^4}\int_0^1 dx\,du\int_0^{1-x}dy\int_0^{1-u}dw\,\frac{1}{A}\Big[\Big\{1+\frac{2}{A}(1-u-w)(1-x-y)^2\Big\}\,\frac{J_1}{A}\\
&-\Big\{1+\frac{1}{A}(1-u-w)(1-x-y)^2\Big\}\,J_2-\frac{1-u-w}{A}\Big\{J_3+(1-x-y)J_4\Big\}+(1-u-w)J_5\Big],\end{aligned}\tag{A35}$$

where

$$\begin{aligned}&J_1\equiv J_1(\eta_i)=\frac{\eta_5}{\sqrt{\eta_1\eta_2\eta_3\eta_4}},\\
&J_2\equiv J_2(\eta_i,f_i)=\frac{f_3}{\sqrt{\eta_1\eta_2\eta_3\eta_4}}\Big[\frac{\eta_5}{2\eta_4}-f_4(1+f_4)\Big],\\
&J_3\equiv J_3(\eta_i,f_i)=\frac{f_1}{\sqrt{\eta_1\eta_2\eta_3\eta_4}}\Big[\frac{\eta_5}{2}\Big\{f_2(1-f_2)\Big(\frac{1}{\eta_3}+\frac{(1+f_3)^2}{\eta_4}\Big)-\frac{1}{\eta_2}\Big\}\\
&\quad-f_2(1-f_2)(1+f_3)^2(1+f_4)^2\Big],\\
&J_4\equiv J_4(\eta_i,f_i)=\frac{f_1+f_2(1-f_1)}{\sqrt{\eta_1\eta_2\eta_3\eta_4}}\Big[\frac{\eta_5}{2}\Big(\frac{1}{\eta_3}+\frac{(1+f_3)^2}{\eta_4}\Big)-(1+f_3)(1+f_4)(f_3+f_4(1+f_3))\Big],\\
&J_5\equiv J_5(\eta_i,f_i)=\frac{f_1}{2\sqrt{\eta_1\eta_2\eta_3\eta_4}}\Big[\frac{\eta_5}{2\eta_4}\Big(\frac{3f_2f_3(1-f_2)(1+f_3)^2}{\eta_4}+\frac{f_2(1-f_2)(2+3f_3)}{\eta_3}-\frac{f_3}{\eta_2}\Big)\\
&\quad-(1+f_4)\Big(\frac{3f_2f_3(1-f_2)(1+f_3)^2(1+2f_4)}{\eta_4}+\frac{f_2f_4(1-f_2)(2+3f_3)}{\eta_3}-\frac{f_3f_4}{\eta_2}\Big)\Big],\end{aligned}\tag{A36}$$

with

$$\begin{aligned}&\eta_1\equiv\eta_1(a_1,F)=a_1+F,\\
&\eta_2\equiv\eta_2(a_i,F)=\frac{a_2F+a_1(a_2+F)}{a_1+F},\\
&\eta_3\equiv\eta_3(a_i,u,F)=\frac{a_2uF+a_1(a_2(u+F)+uF)}{a_2F+a_1(a_2+F)},\end{aligned}$$

$$\eta_4 \equiv \eta_4(a_i,u,w,F) = \frac{a_2uwF + a_1(a_2(w(u+F)+uF)+uwF)}{a_2uF + a_1(a_2(u+F)+uF)},$$
$$\eta_5 \equiv \eta_5(a_i,u,w,F) = \frac{a_1a_2uwF}{a_2uwF + a_1(a_2(w(u+F)+uF)+uwF)}, \tag{A37}$$

$$f_1 \equiv f_1(a_1,F) = \frac{F}{a_1+F},$$
$$f_2 \equiv f_2(a_i,F) = \frac{a_1F}{a_2F + a_1(a_2+F)},$$
$$f_3 \equiv f_3(a_i,u,F) = -\frac{a_1a_2F}{a_2uF + a_1(a_2(u+F)+uF)},$$
$$f_4 \equiv f_4(a_i,u,w,F) = -\frac{a_1a_2uF}{a_2uwF + a_1(a_2(uF+w(u+F))+uwF)}. \tag{A38}$$

The functions a_i and F are defined as,

$$a_1 \equiv a_1(x,u,w) = x(1-u-w), \qquad a_2 \equiv a_2(y,u,w) = y(1-u-w),$$
$$F \equiv F(x,y,u,w;v) = \frac{(1-x-y)(1-u-w)}{4v^2}. \tag{A39}$$

Therefore, the counter term to $\vec{q}$ dependent part of the bosonic kinetic energy is given by

$$\begin{aligned} S^{(2L)}_{(0,2);CT} &= -\delta S^{2L;a}_{(0,2)} \\ &= -\frac{\mathcal{B}^{(2L)}_{(0,2)}}{4\epsilon}\,\frac{8g^4h_6(v)}{v^2}\int dq\; q_y^2\,\mathrm{Tr}\left(\Phi(-q)\Phi(q)\right), \end{aligned} \tag{A40}$$

which gives

$$Z_{5,1} = 0, \tag{A41}$$
$$Z_{6,1} = -8\mathcal{B}^{(2L)}_{(0,2)}\,\frac{g^4\,h_6(v)}{v^2c^2} \tag{A42}$$

to the leading order in c.

[1] G. R. Stewart, Rev. Mod. Phys. **73**, 797 (2001).
[2] H. v. Löhneysen, A. Rosch, M. Vojta, and P. Wölfle, Rev. Mod. Phys. **79**, 1015 (2007).
[3] P. Gegenwart, Q. Si, and F. Steglich, Nature Physics **4**, 186 - 197 (2008).
[4] N. P. Armitage, P. Fournier, and R. L. Greene, Rev. Mod. Phys. **82**, 2421 (2010).
[5] T. Helm, M. V. Kartsovnik, I. Sheikin, M. Bartkowiak, F. Wolff-Fabris, N. Bittner,W. Biberacher,M. Lambacher, A. Erb, J.Wosnitza, and R. Gross, Phys. Rev. Lett. **105**, 247002 (2010).
[6] K. Hashimoto, K. Cho, T. Shibauchi, S. Kasahara, Y. Mizukami, R. Katsumata, Y. Tsuruhara, T. Terashima, H. Ikeda, M. A. Tanatar, H. Kitano, N. Salovich, R. W. Giannetta, P. Walmsley, A. Carrington, R. Prozorov, and Y. Matsuda, Science **336**, 1554 (2012).
[7] T. Park, F. Ronning, H. Yuan, M. Salamon, R. Movshovich, J. Sarrao, and J. Thompson, Nature (London) **440**, 65 (2006).
[8] T. Moriya and J. Kawabata, J. Phys. Soc. Jpn. **34**, 639 (1973); J. Phys. Soc. Jpn. **35** , 669 (1973).
[9] J. A. Hertz, Phys. Rev. B **14**, 1165 (1976).
[10] A. J. Millis, Phys. Rev. B 48, 7183 (1993).
[11] T. Holstein, R. E. Norton, and P. Pincus, Phys. Rev. B **8**, 2649 (1973).
[12] M. Y. Reizer, Phys. Rev. B **40**, 11571 (1989).
[13] P. A. Lee, Phys. Rev. Lett. **63**, 680 (1989).
[14] P. A. Lee and N. Nagaosa, Phys. Rev. B **46**, 5621 (1992).
[15] B. L. Altshuler, L. B. Ioffe, and A. J. Millis, Phys. Rev. B **50**, 14048 (1994).
[16] J. Polchinski, Nucl. Phys. B **422**, 617 (1994).
[17] Y. B. Kim, A. Furusaki, X.-G. Wen, and P. A. Lee, Phys. Rev. B **50**, 17917 (1994).
[18] B. I. Halperin, P. A. Lee, and N. Read, Phys. Rev. B **47**, 7312 (1993).
[19] Ar. Abanov, A. V. Chubukov, and J. Schmalian, Adv. in Phys. **52**, 119 - 218 (2003).
[20] S. Sur & S.-S. Lee, Phys. Rev. B **90**, 045121 (2014).
[21] S.-S. Lee, Phys. Rev. B **80**, 165102 (2009).
[22] M. A. Metlitski and S. Sachdev, Phys. Rev. B **82**, 075127 (2010).
[23] M. A. Metlitski and S. Sachdev, Phys. Rev. B **82**, 075128 (2010).
[24] T. Holder and W. Metzner, arxiv: 1503.05089 (2015)

[25] S. Chakravarty, R. E. Norton, and O. F. Syljuåsen, Phys. Rev. Lett., **74**, 1423 (1995).
[26] A. L. Fitzpatrick, S. Kachru, J. Kaplan, and S. Raghu, Phys. Rev. B **88**, 125116 (2013).
[27] A. L. Fitzpatrick, S. Kachru, J. Kaplan, and S. Raghu, Phys. Rev. B **89**, 165114 (2014).
[28] I. Mandal and S.-S. Lee, Phys. Rev. B , (2015).
[29] S.-S. Lee, Phys. Rev. B **78**, 085129 (2008).
[30] C. Nayak and F. Wilczek, Nucl. Phys. B **417**, 359 (1994); Nucl. Phys. B **430**, 534 (1994).
[31] D. F. Mross, J. McGreevy, H. Liu, and T. Senthil, Phys. Rev. B **82**, 045121 (2010).
[32] D. Dalidovich & S.-S. Lee, Phys. Rev. B **88**, 245106 (2013).
[33] T. Senthil and R. Shankar, Phys. Rev. Lett. **102**, 046406 (2009).
[34] S. Sur & S.-S. Lee, Phys. Rev. B **91**, 125136 (2015).
[35] N. D.-Leyraud and L. Taillefer, Physica C **481**, 161 (2012).
[36] J.-H. Chu, J. G. Analytis, K. De Greve, P. L. McMahon, Z. Islam, Y. Yamamoto, and I. R. Fisher, Science **329**, 824 (2010).
[37] T.-M. Chuang, M. P. Allan, Jinho Lee, Yang Xie, Ni Ni, S. L. Budko, G. S. Boebinger, P. C. Canfield, and J. C. Davis, Science **327**, 181 (2010).
[38] M. J. Lawler, K. Fujita, Jhinhwan Lee, A. R. Schmidt, Y. Kohsaka, Chung Koo Kim, H. Eisaki, S. Uchida, J. C. Davis, J. P. Sethna, and Eun-Ah Kim, Nature **466**, 347 (2010).
[39] Y. Ando, K. Segawa, S. Komiya, and A. N. Lavrov, Phys. Rev. Lett. **88**, 137005 (2002).
[40] J. Fink, V. Soltwisch, J. Geck, E. Schierle, E. Weschke, and B. Büchner, Phys. Rev. B **83**, 092503 (2011).
[41] V. Hinkov, D. Haug, B. Fauqu, P. Bourges, Y. Sidis, A. Ivanov, C. Bernhard, C. T. Lin, B. Keimer, Science **319**, 597 (2008).
[42] S. A. Kivelson, E. Fradkin, and V. J. Emery, Nature **393**, 550 (1998).
[43] R. Zhou, Z. Li, J. Yang, D.L. Sun, C. T. Lin and G.-Q. Zheng, Nature Comm. **4**, 2265 (2013).
[44] X. Lu, J. T. Park, R. Zhang, H. Luo, A. H. Nevidomskyy, Q. Si, P. Dai, Science **345**, 657(2014).
[45] A. V. Chubukov, Europhys. Lett. **44**, 655 (1998).
[46] Ar. Abanov and A. V. Chubukov, Phys. Rev. Lett. **84**, 5608 (2000).
[47] C. Nayak, Phys. Rev. B **62**, 4880 (2000).
[48] J. Rech, C. Pépin, and A. V. Chubukov, Phys. Rev. B **74**, 195126 (2006).
[49] A. A. Patel, P. Strack, and S. Sachdev, arxiv: 1507.05962 (2015).
[50] M. Nakajima, T. Lianga, S. Ishidaa, Y. Tomiokab, K. Kihoub, C. H. Leeb, A. Iyob, H. Eisakib, T. Kakeshitaa, T. Itob, and S. Uchida, PNAS **108**, 12238 (2011).
[51] A. Dusza, A. Lucarelli, F. Pfuner, J.-H. Chu, I. R. Fisher, and L. Degiorgi, Europhys. Lett. **93**, 37002 (2011).
[52] M. A. Tanatar, E. C. Blomberg, A. Kreyssig, M. G. Kim, N. Ni, A. Thaler, S. L. Budko, P. C. Canfield, A. I. Goldman, I. I. Mazin, and R. Prozorov, Phys. Rev. B **81**, 184508 (2010).
[53] B. Valenzuela, E. Bascones, and M. J. Caldern, Phys. Rev. Lett. **105**, 207202 (2010).
[54] C. M. Varma, P. B. Littlewood, S. Schmitt-Rink, E. Abrahams, and A. E. Ruckenstein, Phys. Rev. Lett. **63**, 1996 (1989).
[55] Y. Wang and A. V. Chubukov, arXiv:1507.03583.
[56] E. Berg, M. A. Metlitski and S. Sachdev, Science **338**, 1606 (2012).

CHAPTER 4

CHIRAL NON-FERMI LIQUIDS

In the first two chapters of the thesis we have established two perturbative NFL states near three dimensions. Here we provide a non-perturbative proof for the existence of a stable NFL state in two dimensions at a $\vec{Q}_{ord} = 0$ critical point. Before highlighting the key elements of the enclosed article, we discuss an important aspect of the formalism used in deriving our results.

4.1 The Patch Approximation

In this section we define and justify the *patch approximation*, within which we study the aforementioned QCP. At the QPT, the critical fluctuations of the order parameter (henceforth referred to as the 'boson') couples to the entire Fermi surface. Coarse graining for the boson involves reduction of the UV cutoff towards the origin in the momentum space, while that for the electrons (at finite density) requires sending the UV cutoff contours towards the Fermi surface. This immediately gives rise to an incompatibility of scaling transformations, even at the Gaussian fixed point, since under coarse graining, the momentum, $\vec{q}$, carried by the boson

transforms as

$$q_x \mapsto e^{-\ell} q_x, \quad \text{and} \quad q_y \mapsto e^{-\ell} q_y, \tag{4.1}$$

while the momentum $\vec{K}$ carried by an electron transforms as

$$k_1 \mapsto e^{-\ell} k_1, \quad \text{and} \quad k_2 \mapsto k_2, \tag{4.2}$$

where ℓ is the logarithmic RG length scale, and $\vec{k} = \vec{K} - \vec{K}_F$ with 1 and 2 in the subscript, respectively, referring to directions perpendicular and parallel to the Fermi surface at a point on the Fermi surface with wavevector $\vec{K}_F$.

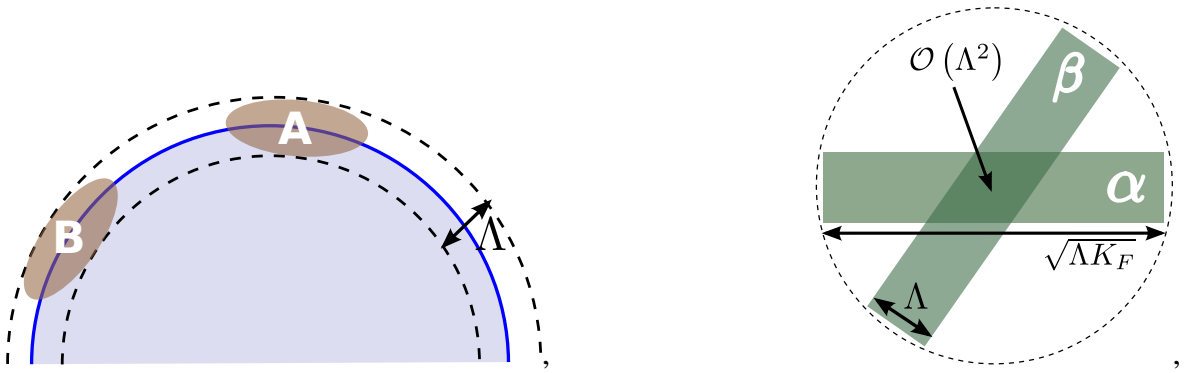

Figure 4.1: Justification of the patch approximation. (a) A part of the Fermi surface with two generic patches A and B. The solid (broken) line represents the Fermi surface (UV cutoff). (b) The dashed circle represents the momentum space of the boson with UV cutoff $\sim \frac{1}{2}\sqrt{\Lambda|\vec{K}_F|}$ (in the figure $K_F \equiv |\vec{K}_F|$). However, not all bosonic modes can couple with electrons in a given patch: the bosonic modes within the strip α (β) couples with the electrons in patch A (B).

Presently, there are two known ways to reconcile the discordant scaling transformations in Eqs. (4.1) and (4.2). One prescription, which we do not use in this thesis, involves letting the Fermi momentum $\vec{K}_F$ to flow under RG [69]. Here we use an alternative prescription, which involves breaking the Fermi surface into patches, and then focusing on only those patches that are strongly coupled to each other in the low energy limit. In order to justify this patch approximation to the Fermi surface [70], let us consider the electron-boson scatterings in two

non-overlapping Fermi surface patches A and B, as shown in Fig. 4.1(a). The bosonic modes that are coupled to the electrons in patch A (B) lie within the strip α (β) in the momentum space of the boson as shown in Fig. 4.1(b). Because the widths of A and B are restricted by Λ, the widths of α and β are restricted accordingly (see Fig. 4.1(b)). However, the lengths of α and β are controlled by the largest magnitude of momentum $\sim \sqrt{\Lambda|\vec{K}_F|}$ that the bosonic modes can carry along a tangent to the Fermi surface. The bosonic modes that can couple with electrons in both A and B lie at the intersection of α and β, which is order of Λ^2. Therefore, as $\Lambda|\vec{K}_F|^{-1} \to 0$ the coupling between A and B is suppressed by a factor of $\sqrt{\Lambda|\vec{K}_F|^{-1}} \ll 1$. This implies that, in the low energy limit, any two generic patches are effectively decoupled from each other. However, if the patches are antipodal, α and β coincide, resulting in strong inter-patch coupling [1]. Further, from Fig. 4.1(b), we note that bosonic modes in a given patch carry momentum predominantly along the Fermi surface. Therefore, it is sufficient to include the antipodal patches in the low energy theory.

According to the patch approximation, the electronic and bosonic dispersions in a particular patch is given by, respectively,

$$\varepsilon(\vec{k}) = vk_1 + \gamma k_2^2, \quad \text{and} \quad \chi^{-1}(q) = c^2 q_2^2, \tag{4.3}$$

where the momenta are measured from the center of the patch, v is the Fermi velocity at the patch center, γ is the local curvature of the patch, and c is velocity of the boson along the Fermi surface. The dispersions $\varepsilon(k)$ and $\chi^{-1}(q)$ allow for a common scaling for bosonic and electronic momenta,

$$k_1 \mapsto e^{-\ell} k_1, \quad \text{and} \quad k_2 \mapsto e^{-\ell/2}\, k_2. \tag{4.4}$$

This is the patch scaling that we will use in the paper for the RG analysis.

[1] A similar situation arises if the Fermi surface is such that Fermi velocities at distinct points are parallel to each other. However, such 'parallel patches' can be combined into a single patch with a suitably enlarged representation of the electron field.

4.2 Preface

In order to meet the goal set at the beginning of this chapter, we choose a model that describes the simplest two dimensional metal, where the electron transport along the x (y) direction is *chiral* (non-chiral) [71]. This leads to an electronic dispersion $E(\vec{K}) = K_x - \cos(K_y)$, where the momentum components are measured in units of inverse lattice spacing. The chirality implies an absence of electronic modes whose velocity is along $-\hat{K}_x$ direction. This is a two dimensional analogue of chiral TLL [72]; so we refer to the two dimensional metal as a chiral Fermi liquid, and the Fermi surface defined by $E(\vec{K}) = 0$ as the chiral Fermi surface. For a patch on a chiral Fermi surface antipodal patches do not exist by construction. Therefore, individual patches can be studied in isolation. This is the basis of the one patch approach used in the paper.

Here we consider a continuous QPT from the chiral Fermi liquid to a symmetry broken state with $\vec{Q}_{ord} = 0$. As discussed in the introductory chapter, even the critical theory containing a single patch of Fermi surface is not amenable to any known local perturbative technique in two dimensions [52]. However, the chiral dynamics imposes strong phase space constraints on the various scattering channels. Here we show how these constraints can be exploited to systematically extract the scaling properties of the IR fixed point, using a novel real space RG scheme that is suitable for theories with Fermi surfaces.

Chiral non-Fermi liquids

Shouvik Sur[1] and Sung-Sik Lee[1,2]
[1]*Department of Physics & Astronomy, McMaster University, 1280 Main Street West, Hamilton, Ontario, Canada L8S 4M1*
[2]*Perimeter Institute for Theoretical Physics, 31 Caroline Street North, Waterloo, Ontario, Canada N2L 2Y5*
(Received 7 December 2013; revised manuscript received 4 June 2014; published 17 July 2014)

A non-Fermi liquid state without time-reversal and parity symmetries arises when a chiral Fermi surface is coupled with a soft collective mode in two space dimensions. The full Fermi surface is described by a direct sum of chiral patch theories, which are decoupled from each other in the low-energy limit. Each patch includes low-energy excitations near a set of points on the Fermi surface with a common tangent vector. General patch theories are classified by the local shape of the Fermi surface, the dispersion of the critical boson, and the symmetry group, which form the data for distinct universality classes. We prove that a large class of chiral non-Fermi liquid states exists as stable critical states of matter. For this, we use a renormalization group scheme where low-energy excitations of the Fermi surface are interpreted as a collection of $(1+1)$-dimensional chiral fermions with a continuous flavor labeling the momentum along the Fermi surface. Due to chirality, the Wilsonian effective action is strictly UV finite. This allows one to extract the exact scaling exponents although the theories flow to strongly interacting field theories at low energies. In general, the low-energy effective theory of the full Fermi surface includes patch theories of more than one universality classes. As a result, physical responses include multiple universal components at low temperatures. We also point out that, in quantum field theories with extended Fermi surface, a noncommutative structure naturally emerges between a coordinate and a momentum which are orthogonal to each other. We show that the invalidity of patch description for Fermi liquid states is tied with the presence of UV/IR mixing associated with the emergent noncommutativity. On the other hand, UV/IR mixing is suppressed in non-Fermi liquid states due to UV insensitivity, and the patch description is valid.

DOI: 10.1103/PhysRevB.90.045121 PACS number(s): 71.10.Hf, 74.40.Kb, 11.10.Gh

I. INTRODUCTION

Landau Fermi liquid theory is the low-energy effective theory for conventional metals [1]. In Fermi liquids, kinematic constraints suppress nonforward scatterings caused by short-range interactions except for the pairing channel [2,3]. In the absence of both time-reversal and parity symmetries, even the pairing interactions are suppressed, and Fermi liquid states can exist as a stable phase of matter at zero temperature. In Fermi liquid states, the shape of the Fermi surface is a good "quantum number" at low energies, and many-body eigenstates can be constructed by filling single-particle states even in the presence of interactions.

The Fermi liquid theory breaks down in metals where a soft collective excitation mediates a singular interaction between fermions at quantum critical points or in quantum critical phases [4–39]. As a result of strong mixing between particle-hole excitations of the Fermi surface and the critical collective mode, quantum fluctuations of Fermi surface remain important at low energies, and the many-body ground state is no longer described by a serene Fermi sea.

Recently, different perturbative schemes have been developed in order to tame quantum fluctuations of Fermi sea and gain a controlled access to non-Fermi liquid states. One can continuously tune the energy dispersion of the soft collective mode [40,41] or the codimension of the Fermi surface [42] to obtain perturbative non-Fermi liquid fixed points. Non-Fermi liquid behaviors in an intermediate scale are also obtained from an alternative scheme [43]. Having established that there exist perturbative non-Fermi liquid fixed points, it is of interest to find examples of strongly interacting non-Fermi liquid states that can be understood beyond the perturbative limits.

It is an outstanding theoretical problem to understand the nonperturbative nature of wildly fluctuating Fermi surfaces in non-Fermi liquid states, especially in two space dimensions where strong quantum fluctuations persist down to arbitrarily low energies. Compared to the critical systems which have only discrete gapless points in momentum space, field theories for Fermi surface are more challenging due to the extra softness of the Fermi surface associated with the presence of an infinitely many gapless modes [37,38].

In this paper, we study a class of $(2+1)$-dimensional chiral non-Fermi liquid states without time-reversal and parity invariances. The metallic state in two space dimensions is chiral in the sense that one of the components of the Fermi velocity has a fixed sign. Although there are indications that the chiral non-Fermi liquid states are stable, so far there has been no rigorous proof of the stability due to a lack of control over the strongly interacting field theories [37]. In this work, we systematically exploit extra kinematic constraints imposed by the chiral nature of the theory to show that a large class of chiral non-Fermi liquid states indeed do exist as stable critical states of matter. For this we use the patch description where the full Fermi surface is decomposed into local patches in momentum space. General chiral patch theories are characterized by the geometric data of the local Fermi surface and the dispersion of the critical boson. Thanks to chirality, exact critical exponents can be obtained.

The chiral non-Fermi liquids are the two-dimensional analogs of the chiral Luttinger liquids [44]. In both cases, the stability is guaranteed by the absence of backscatterings. Furthermore, critical exponents are protected by chirality and can be computed exactly based on kinematic considerations.

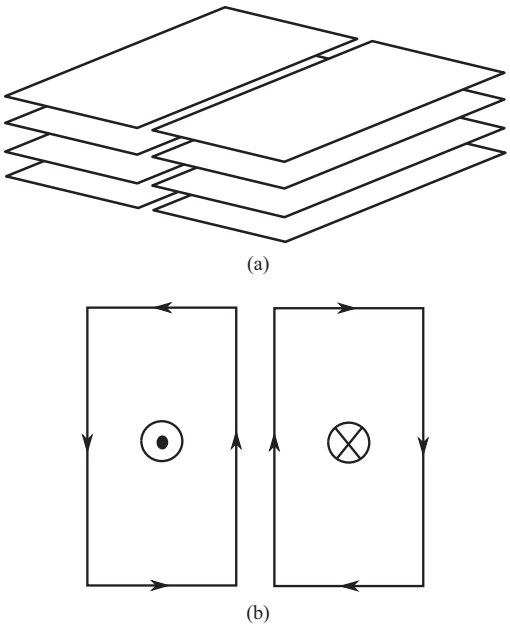

FIG. 1. (a) Two stacks of integer quantum Hall layers with $\nu = 1$. (b) When the directions of magnetic field are opposite in the two stacks, the edge modes have same chirality near the region where two stacks are close to each other. The interface of the two stacks is described by a two-dimensional chiral metal with two flavors.

The paper is organized in the following way. In Sec. II, we motivate the low-energy effective theory for chiral non-Fermi liquids from a setup that can be potentially realized in experiments. It is based on the chiral metal [45], where a two-dimensional chiral Fermi surface arises on the surface of a stack of quantum Hall layers in the presence of interlayer tunnelings. A flavor degree of freedom is introduced by bringing two such stacks with opposite magnetic fields close to each other as shown in Fig. 1(a). In the absence of tunneling between the two stacks, there is a flavor symmetry associated with a rotation in the space of flavor. The flavor symmetry can be spontaneously broken by an interaction between electrons. The quantum critical point associated with the symmetry breaking is described by a chiral non-Fermi liquid state. In Sec. III, we construct a low-energy effective theory for chiral non-Fermi liquid states using the local patch description. First, we focus on the most generic patches with nonzero quadratic curvatures of the Fermi surface. Near one of the generic points, the local dispersion of fermion is given by $\epsilon_k = k_x + \gamma_2 k_y^2$, where $\vec{k} = (k_x, k_y)$ is the momentum away from a point on the Fermi surface. Higher-order curvatures become important at isolated points on the Fermi surface where the quadratic curvature γ_2 vanishes as shown in Fig. 20. Theories for more general shapes of Fermi surface with the dispersion of the form, $\epsilon_k = k_x + \gamma_u k_y^u$ with $u > 2$ are discussed in Sec. VIII. After the patch theory is introduced, the two-dimensional Fermi surface is mapped into a collection of one-dimensional chiral fermions carrying a continuous flavor which corresponds to the momentum along the Fermi surface. In the following sections, we develop a renormalization group scheme based on the one-dimensional picture. Although the theory is superficially written as a one-dimensional theory, it remembers the two-dimensional nature of the underlying theory through a kinematic constraint between the two momentum components. In particular, the momentum along the Fermi surface (the continuous flavor) and the coordinate perpendicular to the Fermi surface obey an emergent noncommutative relation. The physical origin of the noncommutativity and its consequences are discussed in Sec. IV and Appendix A. In Sec. V, the regularization scheme and the renormalization group (RG) prescription for the field theory are introduced. Because the dynamical critical exponent is not known *a priori*, we choose a prescription which is compatible with any dynamical critical exponent. Namely, a cutoff is imposed only along the spatial direction perpendicular to the Fermi surface, but not in time. Because of this rather unusual choice of regularization scheme, the Wilsonian effective action obtained by integrating out short-distance (in space but not in time) modes includes terms that are nonlocal in time, although locality is maintained along the spatial direction. In Sec. VI, which constitutes the central part of the paper, we show the stability of the chiral path theories. In Sec. VI A, we consider the general form of the Wilsonian effective action allowed by scaling analysis. In the scaling under which the interaction remains invariant, a part of the kinetic term is irrelevant, and it introduces a UV cutoff scale to the theory. If the Wilsonian effective action were dependent on the UV cutoff scales in a singular way, the scaling dimensions would deviate from the "bare" ones. It turns out that the present theory is UV finite thanks to the chiral nature of the theory as is proved in Sec. VI B. As a result, one can take the limit of infinite UV cutoff scales. The UV finiteness and the absence of IR scale at the critical point implies that the theory should remain critical at low energies provided that the theory is IR finite as is explained in Sec. VI C. In Sec. VI D, it is shown that the theory is indeed IR finite through an explicit computation of the Wilsonian effective action. As a result, one can show that the exact scaling dimension is given by the bare scaling under which the interaction is kept invariant. In Sec. VI E, we emphasize the difference between the Wilsonian effective action and the full quantum effective action, which allows one to compute the Wilsonian effective action of the chiral patch theory perturbatively in the limit where the external momenta are smaller than the running cutoff scale while the full quantum effective action cannot be computed perturbatively [37]. In Sec. VII, the exact β functions are derived, from which the dynamical critical exponent and the scaling dimension of the fermionic field are obtained, which coincide with the ones obtained from the general scaling analysis in Sec. VI A. In Sec. VIII, we turn to general patch theories with cubic or higher-order local curvatures of the Fermi surface. In particular, inflection points on the Fermi surface are described by the patch theory with the local dispersion, $\epsilon_k = k_x + \gamma_3 k_y^3$. The results obtained in Secs. V–VII are extended to the general cases. From this, it is shown that the general chiral patch theories are also stable, and the exact dynamical critical exponents are obtained. In Sec. IX, we discuss the thermodynamic response of the system. The full Fermi surface is composed of local patch theories, some of which belong to different universality classes. As a result, physical response functions of the system possess multiple

universal components. In Sec. X, we close with a summary and discussions.

II. A POTENTIAL EXPERIMENTAL REALIZATION

To motivate the field theory for chiral non-Fermi liquids, we consider two stacks of $\nu = 1$ integer quantum Hall layers as shown in Fig. 1(a). Each layer supports a one-dimensional chiral edge mode. If magnetic field is applied in opposite directions in the two stacks, the edge modes have the same chirality in the region where the two stacks face each other as shown in Fig. 1(b).

In the presence of tunneling between the layers within each stack, the chiral edge modes disperse along the direction perpendicular to the quantum Hall layers and form a two-dimensional chiral Fermi surface [45]. The low-energy modes near the chiral Fermi surface can be described by two fermionic fields ψ_i, where the flavor $i = 1,2$ labels different stacks. We assume that electron spin is fully polarized and consider spinless fermions. In the absence of tunneling between the two stacks, the quadratic action has SU(2) flavor symmetry. Suppose that there is a short-range density-density interaction that respects the flavor symmetry,

$$H_{\text{int}} = V(c_1^* c_1 + c_2^* c_2)^2, \tag{1}$$

with $V > 0$. Here c_i represents the microscopic electron operator in the ith stack. It can be written as a superposition of low-energy fields which include not only the gapless chiral mode but also other gapped nonchiral modes which reside near the edge. By using the identity $\vec{\sigma}_{ij} \cdot \vec{\sigma}_{kl} = 2(\delta_{il}\delta_{jk} - \frac{1}{2}\delta_{ij}\delta_{kl})$ the interaction can be expressed as

$$H_{\text{int}} = -\frac{V}{3}(c_i^* \vec{\sigma}_{ij} c_j) \cdot (c_k^* \vec{\sigma}_{kl} c_l). \tag{2}$$

When V is large enough, H_{int} can lead to a condensation in the particle-hole channel, $\vec{\phi} \sim \langle c_i^* \vec{\sigma}_{ij} c_j \rangle$. The exciton condensation spontaneously breaks the flavor symmetry, inducing a charge imbalance (coherent tunneling) between the stacks when $\vec{\phi}$ points along (perpendicular to) the $\hat{z}$ direction. Once $\langle \vec{\phi} \rangle$ becomes nonzero, the system becomes a chiral Fermi liquid with a reduced symmetry. If the phase transition is continuous, the corresponding quantum critical point is described by a chiral metal which is coupled with a critical boson. If the SU(2) symmetry is explicitly broken by a small energy scale, there will be no sharp phase transition. Nonetheless, critical behaviors will show up at temperatures larger than the energy scale.

III. PATCH DESCRIPTION FOR CHIRAL NON-FERMI LIQUIDS

In this section, we construct a minimal theory for the quantum phase transition described in the previous section. If there is only nearest-neighbor hopping between chiral edge modes within each stack, the kinetic energy of the chiral metal in each stack can be written as

$$\varepsilon_K = K_x - 2t\cos(K_y d), \tag{3}$$

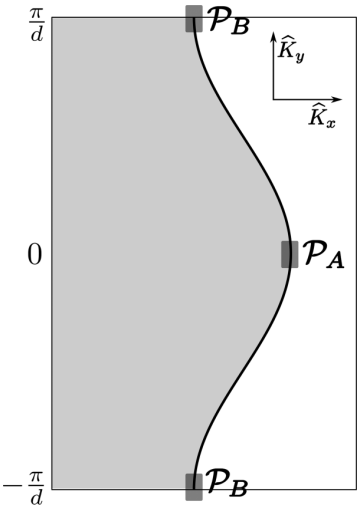

FIG. 2. The chiral Fermi sea. Generically, there are two points on the Fermi surface which have a common tangent vector. For example, the points $\mathcal{P}_A$ and $\mathcal{P}_B$ have the same tangent vectors and they remain strongly coupled to each other in the low-energy limit. A minimal patch theory should include all the points with the common tangent vector.

where K_x is the momentum along the edge, K_y is the momentum perpendicular to quantum Hall layers, and t (d) is the hopping matrix element (distance) between nearest layers within each stack. The velocity along the edge is normalized to be 1. At low energies, regions near the Fermi surface with different tangent vectors are decoupled from each other because of the kinematic separation [10]. As a result, one can focus on patches with a common tangent vector at low energies. Except for the inflection points at $(K_x = 0, K_y = \pm\pi/2d)$, there are two points at which the tangent vectors of the Fermi surface are parallel to each other. Here we focus on the generic patches away from the inflection points. Patch theories for the inflection points are discussed in Sec. VIII.

At the generic points, the local Fermi surface is parabolic. As a concrete example for patches with quadratic curvatures, we consider the low-energy modes near $\mathcal{P}_A \equiv (K_x = 2t, K_y = 0)$ and $\mathcal{P}_B \equiv (K_x = -2t, K_y = \pi/d)$, which have parallel tangent vectors, as shown in Fig. 2. They are described by the quadratic action,

$$S_2 = \sum_{j=1}^{2} \sum_{s=\pm} \int \frac{d\omega d^2\vec{k}}{(2\pi)^3} \left(i\omega + k_x + s\gamma k_y^2\right) \tilde{\psi}_{s,j}^*(\omega,\vec{k}) \tilde{\psi}_{s,j}(\omega,\vec{k}), \tag{4}$$

where $\tilde{\psi}_{+,j}$ ($\tilde{\psi}_{-,j}$) represents the low-energy excitations near $\mathcal{P}_A$ ($\mathcal{P}_B$) in the jth stack and $j = 1,2$, (k_x,k_y) refers to the deviation of the momentum of $\tilde{\psi}_{+,j}$ ($\tilde{\psi}_{-,j}$) from $\mathcal{P}_A$ ($\mathcal{P}_B$) and $\gamma = td^2$ is the absolute value of the local curvature. It is noted that the curvatures at the two points are equal in magnitude but opposite in sign.

Now, we consider a general theory where the fermions with N flavors are coupled with a boson:

$$\begin{aligned} S = &\int \frac{d\omega d^2\vec{k}}{(2\pi)^3}\left(i\eta\omega + k_x + s\gamma k_y^2\right)\tilde{\psi}^*_{s,j}(\omega,\vec{k})\tilde{\psi}_{s,j}(\omega,\vec{k}) \\ &+ \frac{1}{2}\int \frac{d\nu d^2\vec{q}}{(2\pi)^3}(\nu^2 + |\vec{q}|^2 + \mu^2)\phi_\alpha(-\nu,-\vec{q})\phi_\alpha(\nu,\vec{q}) \\ &+ g\int \frac{d\omega d^2\vec{k}}{(2\pi)^3}\frac{d\nu d^2\vec{q}}{(2\pi)^3} \\ &\times \phi_\alpha(\nu,\vec{q})\tilde{\psi}^*_{s,i}(\omega+\nu,\vec{k}+\vec{q})\tilde{T}^\alpha_{ij}\tilde{\psi}_{s,j}(\omega,\vec{k}). \end{aligned} \tag{5}$$

The summation over $s = \pm$ and $i,j = 1,2,\ldots,N$ are assumed in the expression. The example discussed in the previous section corresponds to the case with $N = 2$. In the following, we assume general N which are not necessarily large. In general, the low-energy physics can be governed by an effective theory with a dynamical critical exponent $z > 1$, in which case the term that is linear in frequency in the fermion kinetic term is irrelevant. Therefore, we keep a "coupling" η for the dynamical term. ϕ_α is a boson field, and $\tilde{T}^\alpha_{ij}$ is a matrix that characterizes the flavor quantum number carried by the boson. Here we consider the SU(N) flavor group, where $\tilde{T}^\alpha_{ij}$'s are traceless Hermitian matrices with $\alpha = 1,2,\ldots,N^2-1$. μ^2 is the mass of the boson which drives a quantum phase transition. For $\mu^2 > 0$ the system is described by the Fermi liquid with the unbroken symmetry. For $\mu^2 < 0$ a condensation of ϕ_α breaks the flavor symmetry spontaneously. We later focus on the critical point at which $\mu = 0$. However, it is helpful to keep a nonzero positive mass temporarily in order to avoid spurious IR singularities that may show up in intermediate steps of the RG analysis. It is noted that the boson is nonchiral because a chiral boson cannot be gapped even away from the critical point. The nonchiral kinetic energy for the boson is generated once the gapped nonchiral modes near the edge are integrated out. In the absence of time-reversal or parity invariance, one may add local terms that are linear in ν or q_x in the boson action. However, $\phi_\alpha\partial_\mu\phi_\alpha$ are total derivative terms and do not affect dynamics. Terms of the form $\phi_\alpha\partial_\mu\phi_\beta$ with $\alpha \neq \beta$ are prohibited by flavor symmetry. While $(\partial_\tau\phi^\alpha)(\partial_x\phi^\alpha)$ is allowed by symmetry, it is irrelevant compared to $(\partial_y\phi^\alpha)(\partial_y\phi^\alpha)$.

Although the minimal theory has two patches, one can reinterpret the two-patch theory as a one-patch theory with a larger representation of the flavor group. In order to see this, we define a fermion field ψ_j with doubled flavor indices $j = 1,2,\ldots,2N$ as

$$\begin{aligned} &\psi_j(\omega,\vec{k}) \equiv \tilde{\psi}_{+,j}(\omega,\vec{k}) \quad \text{for} \quad 1 \leqslant j \leqslant N, \\ &\psi_j(\omega,\vec{k}) \equiv \tilde{\psi}^*_{-,j-N}(-\omega,-\vec{k}) \quad \text{for} \quad N+1 \leqslant j \leqslant 2N. \end{aligned} \tag{6}$$

In terms of the $2N$-component fermion field, the action is written as

$$\begin{aligned} S = &\int \frac{d\omega d^2\vec{k}}{(2\pi)^3}\left(i\eta\omega + k_x + \gamma k_y^2\right)\psi^*_j(\omega,\vec{k})\psi_j(\omega,\vec{k}) \\ &+ \frac{1}{2}\int \frac{d\nu d^2\vec{q}}{(2\pi)^3}(\nu^2 + |\vec{q}|^2 + \mu^2)^{\theta/2}\phi_\alpha(-\nu,-\vec{q})\phi_\alpha(\nu,\vec{q}) \\ &+ g\int \frac{d\omega d^2\vec{k}}{(2\pi)^3}\frac{d\nu d^2\vec{q}}{(2\pi)^3} \\ &\times \phi_\alpha(\nu,\vec{q})\psi^*_i(\omega+\nu,\vec{k}+\vec{q})T^\alpha_{ij}\psi_j(\omega,\vec{k}). \end{aligned} \tag{7}$$

Here T^α is $2N \times 2N$ reducible representation of the SU(N) group given by

$$T^\alpha \equiv \begin{pmatrix} \tilde{T}^\alpha & 0 \\ 0 & -[\tilde{T}^\alpha]^T \end{pmatrix}. \tag{8}$$

We also consider a generalized boson action of the form $(\nu^2 + q_x^2 + q_y^2 + \mu^2)^{\theta/2}$, where θ is treated as a free parameter. The theory in Eq. (7) is nothing but a chiral one-patch theory where fermions transform in an enlarged reducible representation of the flavor group. In nonchiral two-patch theories, the transformation in Eq. (6) leads to a Dirac fermion with two components [42]. In this respect, the nature of the chiral two-patch theory is fundamentally different from the nonchiral two-patch theory. We choose the normalization of T^α such that $\mathrm{Tr}[(T^\alpha)^2] = 1$ for all α.

At the Gaussian fixed point, the scaling dimensions of momentum components, fields, and the coupling are given by

$$\begin{aligned} [\omega] &= 1, \\ [k_x] &= 1, \\ [k_y] &= \frac{1}{2}, \\ [\psi_i] &= -\frac{7}{4}, \\ [\phi_\alpha] &= -\frac{5+\theta}{4}, \\ [g] &= \frac{\theta-1}{4}, \\ [\mu] &= \frac{1}{2}. \end{aligned} \tag{9}$$

It is noted that ν^2, q_x^2 in the boson action is irrelevant compared to q_y^2. Therefore, we drop the dependencies on ν and q_x in the boson dispersion to consider the following boson propagator:

$$\chi_\theta(\vec{q}) = \frac{1}{\left|q_y^2 + \mu^2\right|^{\theta/2}}. \tag{10}$$

The fermion-boson coupling g is relevant (irrelevant) for $\theta > 1$ ($\theta < 1$) and marginal for $\theta = 1$. Consequently, the (2+1)-dimensional theory is at the upper critical dimension when $\theta = 1$, and below (above) the upper critical dimension when $\theta > 1$ ($\theta < 1$). The earlier works [40,41] developed a perturbative expansion for the critical point with $\mu = 0$ near $\theta = 1$. The most generic value for local theories, including the theory for the system discussed in the previous section, is $\theta = 2$. For a generic $\theta > 1$ not close to 1, the critical theory flows to a strongly interacting non-Fermi liquid state at low energies. However, we can obtain exact dynamical information of the theory thanks to the chiral nature of the theory. Note that we could have added a $\lambda\phi^4$ term to the action in Eq. (5). At the Gaussian fixed point the scaling dimension of the coupling

λ is $[\lambda] = \theta - 5/2$. Since it is irrelevant for $\theta < 5/2$, we drop it.

Upon integrating out the boson, we obtain a four-fermion interaction,

$$\int \frac{d\omega_1 d^2\vec{k}_1 d\omega_2 d^2\vec{k}_2 d\nu d^2\vec{q}}{(2\pi)^9} V_{ij;ln}\chi_\theta(q)\psi_i^*(\omega_2,\vec{k}_2) \times \psi_j(\omega_2+\nu,\vec{k}_2+\vec{q})\psi_l^*(\omega_1+\nu,\vec{k}_1+\vec{q})\psi_n(\omega_1,\vec{k}_1), \quad (11)$$

where $V_{ij;ln} = -\frac{g^2}{2}\sum_\alpha T^\alpha_{ij} T^\alpha_{ln}$. In this paper, we take the viewpoint that the Fermi surface is made of a collection of one-dimensional chiral fermions labeled by y momentum k_y. In order to simplify notation, henceforth, we use k without subscript to represent the y component of momentum. We go over to the $(1+1)$-dimensional real space which is conjugate to (ω,ϵ_k),

$$\psi_{j,k}(\tau,x) = \int \frac{d\omega}{2\pi}\frac{d\epsilon_k}{2\pi} e^{i\omega\tau + i\epsilon_k x}\psi_j(\omega,\epsilon_k - \gamma k^2,k). \quad (12)$$

Note that x is conjugate to $\epsilon_k = k_x + \gamma k^2$, but not to k_x. This implies that slowly varying modes in x carry momenta close to the Fermi surface, that is, $k_x \sim -\gamma k^2$. In this basis, the action takes the form of a *local* $(1+1)$-dimensional theory,

$$S = \int \frac{dk}{2\pi}\int d^2r\,\psi^*_{i,k}(r)[\eta\partial_\tau - i\partial_x]\psi_{i,k}(r) + \int \frac{dk_1}{2\pi}\frac{dk_2}{2\pi}\frac{dq}{2\pi}\int d^2r\; e^{i2\gamma(k_1-k_2)qx} V_{ij;ln}\chi_\theta(q) \times \psi^*_{i,k_2}(r)\psi_{j,k_2+q}(r)\psi^*_{l,k_1+q}(r)\psi_{n,k_1}(r). \quad (13)$$

Here $r = (\tau,x)$ and q, k, k_i represent y momenta, which are now interpreted as continuous flavors carried by the $1+1$D chiral fermions in addition to the discrete flavor. The long-range interaction mediated by the critical boson becomes a four-fermion vertex. In this representation, the sliding symmetry [38] is realized by a simple shift in y momentum, $\psi_{i,k} \to \psi_{i,k+\Delta k}$.

It is interesting to note that the curvature of Fermi surface completely drops out from the kinetic term. This is due to the fact that the kinetic energy is ultralocal in momentum space. Instead the curvature shows up in the phase factor of the four-fermion vertex. The phase factor plays a crucial role in describing the low-energy physics correctly. In particular, the phase factor is the only term that "remembers" the $(2+1)$-dimensional nature of the theory. Without the phase factor, the theory becomes a $(1+1)$-dimensional theory, which is fundamentally different from the $(2+1)$-dimensional theory. In other words, a nonzero curvature is a relevant perturbation to the $(1+1)$-dimensional theory which qualitatively modifies the low-energy behaviors. This feature can be checked from the fact that various expressions that characterize low-energy properties of the system become singular in the zero curvature limit, as shown later.

In Eq. (13), the translational symmetry appears to be explicitly broken by the phase factor. However, one can check that the symmetry is still intact once the fermion field $\psi(\tau,x)$ transforms projectively as

$$\psi_{i,k}(\tau,x) \to e^{-i\gamma k^2 x_0}\psi_{i,k}(\tau,x+x_0) \quad (14)$$

under a translation along the x direction. Before we delve into the RG analysis, we make a small digression in the next section to discuss the origin and implications of the phase factor in the four-fermion interaction.

IV. EMERGENT NONCOMMUTATIVITY

The phase factor in the four-fermion vertex is reminiscent of the Moyal product in noncommutative field theories [46], although it is not exactly of the same form. Indeed, it suggests that there is an emergent noncommutative structure between the x coordinate and the y momentum at low energies. In this section and Appendix A, we elaborate on this point. This section is rather orthogonal to the rest of the paper, and it may be skipped by the readers who want to reach the main conclusion of the paper quickly.

Physically, the phase factor represents a mismatch of x momenta between low-energy fermions which carry different y momenta. This is a consequence of the fact that x momentum is tied with y momentum at low energies due to the curvature of the Fermi surface. Suppose Λ_x is a UV cutoff in energy, which is equivalent to the largest x momentum a particle or hole can have away from the Fermi surface. Let us consider low-energy particle-hole pairs that can be created within the thin shell with width $2\Lambda_x$ near the Fermi surface. When $\Lambda_x = 0$, the x momentum is completely determined from the y momenta of the particle and hole: A particle-hole pair created by $\psi^*_{i,k+p}\psi_{j,k}$ carries x momentum, $-\gamma[(k+p)^2 - k^2]$. When $\Lambda_x \neq 0$, there is an uncertainty $2\Lambda_x$ in the x momentum of the particle-hole pair with fixed p and k as is illustrated in Fig. 3(a). Now we consider a second particle-hole pair created by $\psi^*_{i,k+\Delta k+p}\psi_{j,k+\Delta k}$, which carries the same net y momentum p but is made of different constituents. Due to the nonzero curvature of Fermi surface, the second pair has a different net x momentum. However, if Δk is too small, the x momentum of the second pair cannot be distinguished from that of the first pair within the uncertainty $2\Lambda_x$, as shown in Fig. 3(b). Therefore, Δk has to be large enough for the x momenta of the two particle-hole pairs to be resolved [see Fig. 3(c)]. In order for the difference in the x momenta of the two pairs to be greater than $2\Lambda_x$, Δk has to satisfy the inequality

$$|\gamma[(k+\Delta k+p)^2 - (k+\Delta k)^2] - \gamma[(k+p)^2 - k^2]| = |2\gamma p\Delta k| > 2\Lambda_x. \quad (15)$$

This implies

$$\Delta k\Delta x > \frac{1}{\gamma p}, \quad (16)$$

where we use the fact that the uncertainty in the real space is given by $\Delta x \sim \frac{1}{\Lambda_x}$. Without loss of generality, Δk, p, and Δx are assumed to be positive. Therefore, there is a nontrivial uncertainty relation between the x coordinate and the y momentum, which is inversely proportional to the curvature and the net y momentum of a particle-hole pair. This indicates that the zero curvature limit is singular. It is also interesting to note that the "Planck constant" in the uncertainty relation is dimensionful.

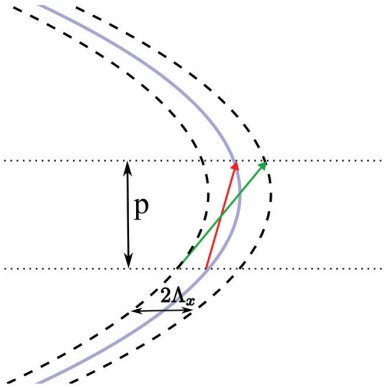

(a)

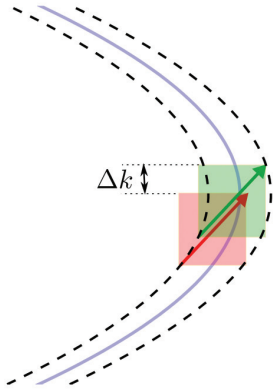

(b)

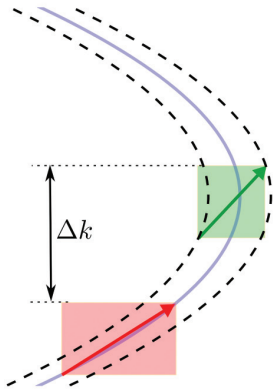

(c)

FIG. 3. (Color online) The solid curve is the Fermi surface, and the dashed curves represent the Fermi surface shifted by $\pm\Lambda_x$ along the k_x direction. (a) The two arrows represent the minimum and maximum x momenta a particle-hole pair $\psi^*_{i,k+p}\psi_{j,k}$ with fixed k and p can have within the thin shell of width $2\Lambda_x$. (b) The x momenta of two pairs of particle-hole excitations created by $\psi^*_{i,k+p}\psi_{j,k}$ and $\psi^*_{i,k+\Delta k+p}\psi_{j,k+\Delta k}$ cannot be resolved within the uncertainty $2\Lambda_x$ if Δk is too small. This is because the allowed x momenta for the first pair overlap with those for the second. (c) If Δk is large enough, the x momenta of the two pairs can be resolved because the largest possible x-momentum of the first particle-hole pair is smaller than the smallest possible momentum of the second pair.

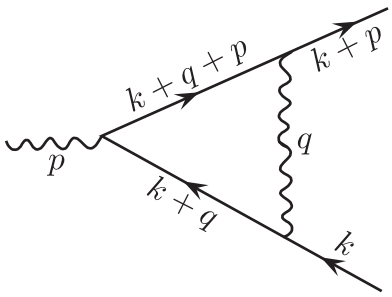

FIG. 4. One-loop vertex function.

This uncertainty relation implies that the theory has an IR scale which is inversely proportional to a UV scale. For example, we can construct an IR scale for the momentum of a particle-hole pair,

$$p^* \sim \frac{1}{\gamma \Delta k^{\max} \Delta x} \sim \frac{\Lambda_x}{\gamma \Lambda}, \tag{17}$$

from a UV scale Λ, where we use the fact that the largest uncertainty in k is given by the size of Fermi surface Λ. It is noted that Λ, which corresponds to the Fermi momentum, is, in general, much larger than Λ_x which is set by the low-energy scale, say temperature. Conversely, a small transverse momentum of a particle-hole pair p sets a UV momentum scale given by

$$\Lambda^* \sim \frac{\Lambda_x}{\gamma p}. \tag{18}$$

In order to appreciate the physical meaning of Eqs. (17) and (18), let us consider a one-loop vertex function shown in Fig. 4. Here a boson with three-momentum $(\omega_p, \vec{p})$ creates virtual particle-hole excitations with $(\omega_k + \omega_p + \nu, \vec{k} + \vec{p} + \vec{q})$ and $(\omega_k + \nu, \vec{k} + \vec{q})$ before the intermediate state settles at the final state with $(\omega_k + \omega_p, \vec{k} + \vec{p})$ and $(\omega_k, \vec{k})$. The virtual particle-hole excitations that contribute to this scattering amplitude are the ones whose net momentum is $\vec{p}$ with an energy cutoff $\Lambda_x \sim \omega_p$. In Fig. 5, the arrows represent the momentum $\vec{p}$ which is shifted along the Fermi surface to show possible particle-hole pairs that can be excited with the net momentum $\vec{p}$. Those with energy less than the cutoff, which fit inside the shell with width Λ_x, are denoted as solid arrows. Those with energy greater than the cutoff are drawn as dashed arrows. If p is large (relative to what we explain below), only a small region near the Fermi surface can accommodate the arrows within the shell as shown in Fig. 5(a). In this case, the largest momentum that the constituent particle/hole can have is cut off by Eq. (18), which is independent of Λ. Namely, the virtual particle-hole excitations do not sense the full extent of the Fermi surface. As p becomes smaller, more arrows can fit inside the shell. Eventually the largest momentum of the constituent particle/hole is set by the UV cutoff Λ as shown in Fig. 5(b). The momentum scale of p at which this crossover occurs is given by Eq. (17).

As a result of the interplay between IR and UV scales, IR behaviors of the theory can depend on UV scales in a nontrivial way [47]. This is particularly the case if there is UV divergence in the theory. Since the theories at and above the upper critical

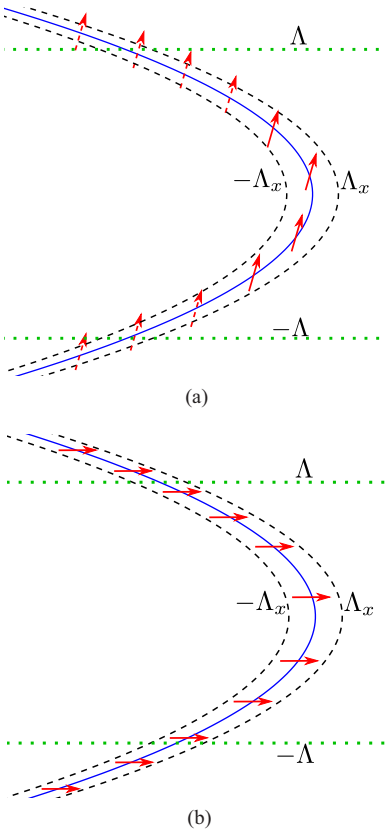

FIG. 5. (Color online) The solid curve is the Fermi surface, and the dashed curves represents the Fermi surface shifted by $\pm\Lambda_x$ along the k_x direction. The (red) arrows denote particle-hole pairs with momentum $\vec{p}$ created near the Fermi surface. The dotted horizontal lines represent the UV cutoff in the y momentum ($\pm\Lambda$), which is set by the size of the Fermi surface. (a) If the y momentum of a particle-hole pair, p, is large, then the phase space available to the pair within energy Λ_x is limited by $\frac{\Lambda_x}{\gamma p}$. Therefore, the arrows go outside the thin shell before they sense the full extension of the Fermi surface. (b) If p is small, then the available phase space of the particle-hole pairs is only limited by the size of Fermi surface.

dimension are sensitive to UV, we expect a nontrivial UV/IR mixing in Fermi liquids (marginal Fermi liquids) with $\theta < 1$ ($\theta = 1$). Let us ask how the scattering amplitude at a fixed $\vec{p}$ behaves as the UV cutoff Λ is increased. When p is small compared to p^* defined in Eq. (17), the phase space for the intermediate states increases as Λ increases. As a result, the scattering amplitude grows with a positive power of Λ in Fermi liquids with $\theta < 1$, as shown in Appendix A. For sufficiently large Λ, this UV divergence is eventually cut off by the scale given in Eq. (18), giving a singular dependence on p. We can also view this from a different perspective. For a fixed Λ, the scattering amplitude grows as p decreases as long as p is larger than p^*. When p becomes smaller than p^*, the putative IR singularity in p is eventually cut off by p^*. Therefore, the $\Lambda \to \infty$ limit and the $p \to 0$ limit do not commute.

In Fermi liquids, the UV and IR singularities of the amplitude are closely connected. This is not surprising because the modes that carry large momenta can have arbitrarily small energy. The UV/IR mixing is one way of understanding why "UV structures" of the theory should be specified in the low-energy effective theory for Fermi liquids. The shape of the entire Fermi surface and the Landau parameters which are nonlocal in momentum space are among the UV data without which even the properties that are local in momentum space cannot be determined in Fermi liquids. On the contrary, the UV/IR mixing is suppressed in non-Fermi liquid states with $\theta > 1$ because the theory is UV finite and insensitive to the UV cutoffs. As a result, properties that are local in momentum space, such as the vertex functions with small momentum transfers, can be obtained solely from the patch which is local in momentum space without invoking the knowledge of the entire Fermi surface. The suppression of UV/IR mixing is what makes the local-patch description possible in non-Fermi liquid states. We illustrate this difference between Fermi liquids and non-Fermi liquids in Appendix A through an explicit calculation of the vertex function.

V. REGULARIZATION AND RG PRESCRIPTION

In the following sections, we perform a RG analysis of the action in Eq. (13) to show that the theory flows to a stable interacting fixed point in the low-energy limit. As a first step, we regularize the theory. For this, we use the "mixed" space representation which consists of x coordinate and frequency. This representation is convenient because we adopt a RG prescription where the Wilsonian effective action is local in x but not in τ. In the mixed space, the bare action in Eq. (13) is written as

$$\begin{aligned} S = &\int \frac{dk}{2\pi}\frac{d\omega}{2\pi}\int dx\, \psi^*_{i,k}(\omega,x)[i\eta\omega - i\partial_x]\psi_{i,k}(\omega,x) \\ &+ \int \frac{dk_1}{2\pi}\frac{dk_2}{2\pi}\frac{dq}{2\pi}\frac{d\omega_1}{2\pi}\frac{d\omega_2}{2\pi}\frac{d\nu}{2\pi}\int dx\, e^{2i\gamma(k_1-k_2)qx} \\ &\times V_{ij;ln}\chi_\theta(q)\psi^*_{i,k_2}(\omega_2,x)\psi_{j,k_2+q}(\omega_2+\nu,x) \\ &\times \psi^*_{l,k_1+q}(\omega_1+\nu,x)\psi_{n,k_1}(\omega_1,x). \end{aligned} \tag{19}$$

Potential divergences present in the composite operators are removed by writing them in terms of normal ordered operators [48] defined by

$$\begin{aligned} \circ\,\mathcal{O}\,\circ = \exp\Bigg[-\sum_i \int dk d\omega \int dx_1 dx_2 \\ \times (2\pi)^2 G_0(\omega,x_{12})\frac{\delta}{\delta\psi^*_{i,k}(\omega,x_2)}\frac{\delta}{\delta\psi_{i,k}(\omega,x_1)}\Bigg]\mathcal{O}, \end{aligned} \tag{20}$$

where the bare Green's function is

$$\begin{aligned} G_0(\omega,x_{12}) &= \int_{-\infty}^{\infty}\frac{d\epsilon_k}{2\pi}e^{ix_{12}\epsilon_k}\frac{1}{i\eta\omega+\epsilon_k} \\ &= -i\,\mathrm{sgn}(\omega)\Theta(-x_{12}\omega)e^{-\eta|x_{12}||\omega|}, \end{aligned} \tag{21}$$

with $x_{12} \equiv x_1 - x_2$. The chiral nature is manifest in the fact that the fermion propagator vanishes for $x_{12}\omega > 0$: Particles (antiparticles) propagate only in one (the other) direction. This feature will play a crucial role in proving the stability of

(a) (b)

FIG. 6. Corrections to the quadratic vertex due to normal ordering of the quartic vertex.

the chiral non-Fermi liquid state later. It is convenient to use the diagrammatic representation to visualize various channels in which fields are contracted in the normal ordering and the operator product expansion (OPE). Two contracted fields are represented by an internal line. External lines represent uncontracted fields. Wiggly lines represent the four-fermion vertices or the propagator of the boson which has been integrated out. Upon normal ordering, the quartic vertex produces normal ordered quartic and quadratic vertices along with a constant. The quadratic vertex is generated from the quartic vertex as a pair of fermion fields are contracted as shown in Fig. 6. In order to contract two fermion fields within one composite operator without ambiguity, we introduce a point splitting in the four-fermion composite operator in Eq. (19) as

$$\psi^*_{i,k_2}(\omega_2,x+\epsilon)\psi_{j,k_2+q}(\omega_2+\nu,x+\epsilon) \times\psi^*_{l,k_1+q}(\omega_1+\nu,x)\psi_{n,k_1}(\omega_1,x). \tag{22}$$

The Hartree contribution from Fig. 6(a) vanishes due to the traceless condition of the interaction vertex, $\sum_{ij}\delta_{ij}V_{ij;nl}=0$. The Fock term in Fig. 6(b) is nonvanishing and given by

$$S_2' = \int \frac{dkd\omega}{(2\pi)^2}dx \,\circ\!\circ\, \psi^*_{i,k}(\omega,x)\psi_{i,k}(\omega,x) \,\circ\!\circ \times ig^2 v\,\mathrm{sgn}(\omega)\int\frac{dq}{2\pi}\int_0^{|\omega|}\frac{d\nu}{2\pi}\chi_\theta(q), \tag{23}$$

where the constant v is defined by

$$v=\frac{1}{N}\sum_\alpha \mathrm{Tr}[T^\alpha T^\alpha]. \tag{24}$$

Here the $\epsilon\to 0$ limit is taken before the UV cut off for frequency is taken to be infinite.

The partition function can be formally expanded as

$$Z=\int \mathcal{D}\psi e^{-S_2}\left[1-(S_2'+S_4)+\frac{1}{2}(S_2'+S_4)^2-\cdots\right], \tag{25}$$

where

$$S_2=\int\frac{dkd\omega}{(2\pi)^2}\int dx\psi^*_{i,k}(\omega,x)[i\eta\omega-i\partial_x]\psi_{i,k}(\omega,x), \tag{26}$$

$$S_2' = \int \frac{dkd\omega}{(2\pi)^2}\int dx \,\circ\!\circ\, \psi^*_{i,k}(\omega,x)\psi_{i,k}(\omega,x) \,\circ\!\circ \times ig^2 v\,\mathrm{sgn}(\omega)\int\frac{dq}{2\pi}\int_0^{|\omega|}\frac{d\nu}{2\pi}\chi_\theta(q),$$

$$S_4 = \int \frac{dk_1dk_2dqd\omega_1d\omega_2d\nu}{(2\pi)^6}\int dx\; e^{i2\gamma(k_1-k_2)qx} \times V_{ij;ln}\chi_\theta(q) \,\circ\!\circ\, \psi^*_{i,k_2}(\omega_2,x)\psi_{j,k_2+q}(\omega_2+\nu,x) \times\psi^*_{l,k_1+q}(\omega_1+\nu,x)\psi_{n,k_1}(\omega_1,x) \,\circ\!\circ\, . \tag{27}$$

We view this as a grand canonical ensemble for a gas of vertices $S_2'+S_4$ evaluated with respect to the quadratic action [49]. It is noted that the action is local in the one-dimensional space in x, and operators in the ensemble can be arbitrarily close to each other in the x direction. This can, in principle, give rise to UV divergences. However, we will see that UV divergence is absent in the present theory due to chirality for $\theta>1$. Therefore, we proceed without imposing a short-distance cutoff in the x direction.

Now we consider a Wilsonian effective action with a running cutoff length scale X_0. The Wilsonian effective action is constructed by fusing all operators whose relative distances in x-direction is smaller than X_0 in the ensemble of operators, $\int dx_1dx_2\cdots dx_n O(x_1)O(x_2)\cdots O(x_n)$. Here the frequencies and other indices are suppressed. For example, let us consider the n normal ordered operators $O(x_1),O(x_2),\ldots,O(x_n)$ in $(S_4)^n$ of Eq. (25) located at positions $x_1,x_2,\ldots,x_n$. If there is a group of operators $O_{i_1},O_{i_2},\ldots,O_{i_m}$ in $(S_4)^n$ such that for every operator in the group, say O_{i_p}, there exists another operator O_{i_q} in the group with $|x_{i_p}-x_{i_q}|<X_0$, then the cluster of the m operators is fused into a series of normal ordered operators according to the OPE,

$$\prod_{a=1}^m O_{i_a} = e^{\widehat{\mathcal{D}}_m}\,\circ\!\circ\prod_{a=1}^m O_{i_a}\,\circ\!\circ\,, \tag{28}$$

where

$$\widehat{\mathcal{D}}_m\equiv\sum_{c=2}^m\sum_{s=1}^{c-1}\widehat{d}_{c,s}, \tag{29}$$

with

$$\widehat{d}_{c,s}=\sum_j\int dkd\omega\int dx_1dx_2 \times\left[G_0(\omega,x_{12})\frac{\delta}{\delta\psi^{(c)*}_{j,k}(\omega,x_2)}\frac{\delta}{\delta\psi^{(s)}_{j,k}(\omega,x_1)}+\text{c.c.}\right]. \tag{30}$$

Here the role of $\widehat{d}_{c,s}$ is to contract a pair of fermion fields, one from O_{i_c} and the other from O_{i_s}. Fusion of operators is illustrated in Fig. 7. The Wilsonian effective action should include the vertices generated from the OPE. In particular, four-fermion vertices are generated from contracting $2(n-1)$ pairs of fermion fields in $(S_4)^n$,

$$\delta S_4=-\sum_{n=2}^\infty\frac{(-1)^n}{n!}\frac{(\widehat{\mathcal{D}}_n)^{2(n-1)}}{(2n-2)!}\,\circ\!\circ\,[(S_4)^n]_{X_0}\,\circ\!\circ\,, \tag{31}$$

where $[(S_4)^n]_{X_0}$ denotes the configurations for a group of n quartic vertices where the separation between nearest-neighbor vertices are less than X_0 in x direction.

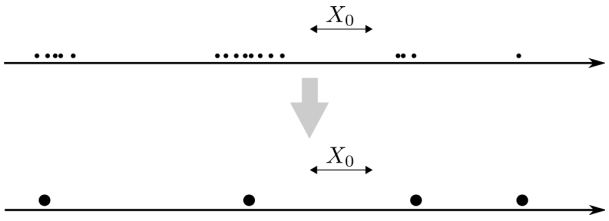

FIG. 7. Any group of operators, represented by small dots in the top panel, where separations between nearest neighbors are less than X_0 in x direction are fused into a composite operator which are denoted by big dots in the bottom panel.

For example,

$$\left[\left(\int dx\, O(x)\right)^2\right]_{X_0} = \int_{|x_1-x_2|<X_0} dx_1 dx_2 O(x_1)O(x_2). \quad (32)$$

Extension of Eq. (32) to $[(S_4)^n]_{X_0}$ with general n is straightforward, if more complicated. Similarly, quadratic vertices are generated by fusing $2n-1$ pairs of fermion fields,

$$\delta S_2 = -\sum_{n=2}^{\infty} \frac{(-1)^n}{n!} \frac{(\widehat{\mathcal{D}}_n)^{2n-1}}{(2n-1)!} \circ [(S_4)^n]_{X_0} \circ . \quad (33)$$

It is noted that we have employed an unconventional cutoff scheme. In the $(1+1)$-dimensional real space, two operators that are far from each other in the temporal direction are fused as far as their spatial separation is less than X_0, as shown in Fig. 8. The reason why we choose this unusual cutoff scheme is that the dynamical critical exponent z is not known *a priori*. Since z should be determined dynamically, we do not know yet how to rescale the temporal direction relative to the spatial direction under scale transformation. The present cutoff scheme is convenient because it is guaranteed to be invariant under the scale transformation with any z. The price we have to pay is that the fusion processes generate operators that are nonlocal in the temporal direction. For this reason, we have to explicitly compute the nonlocal terms that are generated from the fusion processes and add them to the effective action. This is different from the usual procedure for relativistic field theories where UV cutoff is imposed in all space-time directions and a fusion of operators generates only local operators that are already in the bare action.

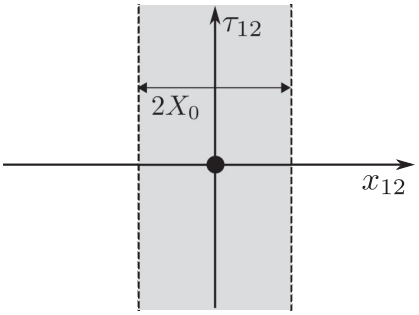

FIG. 8. The origin represents the position of one operator in the $(1+1)$-dimensional real space. If the second operator is within the shaded region in the space of the relative coordinate (x_{12}, τ_{12}), two operators are fused into one normal ordered operator.

VI. THE WILSONIAN EFFECTIVE ACTION

In this section, we prove the stability of the chiral patch theory. For this, we consider the Wilsonian effective action at scale X_0 constructed in the following way. When the separation between two operators along the x axis is larger than X_0 [see Fig. 9(a)], they are treated as independent operators. When their separation is less than X_0 [see Fig. 9(b)], they are fused through OPE. Different ways of contracting fields are represented by Feynman diagrams. Before we compute the Wilsonian effective action explicitly, we first discuss the general structure of the effective action inferred from scaling analysis. In particular, we show that the Wilsonian effective action is UV finite and has no scale except for the running cutoff scale X_0 in the low-energy limit. As a result, the exact scaling behavior of the theory can be obtained. After the general consideration, we compute the Wilsonian effective action explicitly and confirm the general conclusion obtained from the scaling analysis.

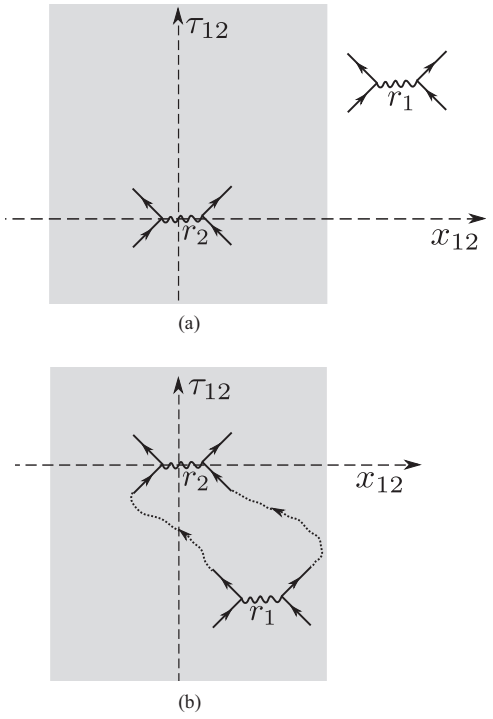

FIG. 9. The space of relative coordinates between two operators. Each quartic vertex is drawn as an extended object, although there is no spatial extension of the wiggly line in the x direction. The shaded region represents $|x_{12}| < X_0$ (see Fig. 8). (a) If the separation between two operators along the x axis is greater than X_0, the two operators are considered as independent operators. (b) If the separation between the two operators along the x axis is less than X_0, they are fused into one operator. Here we show a particular channel of fusion where two quartic operators are fused into one quartic operator. Each internal (dotted) line represents a pair of contracted fields, whereas external (solid) lines represent uncontracted fields.

A. UV finiteness and scale invariance

In general, the Wilsonian effective action at scale X_0 can be written as

$$\begin{aligned} S_{X_0} = &\sum_{m=1}^{\infty} \sum_{i_1,j_1,\ldots,i_m,j_m=1}^{N} \sum_{s_1,t_1,\ldots,s_m,t_m=0}^{\infty} \int dq_1 dk_1 \ldots dq_m dk_m \int d\omega_1 d\nu_1 \ldots d\omega_m d\nu_m \int dx \\ &\times S^{s_1,t_1,\ldots,s_m,t_m}_{i_1,j_1,\ldots,i_m,j_m}(x,q_1,k_1,\ldots,q_m,k_m,\omega_1,\nu_1,\ldots,\omega_m,\nu_m; X_0,\Lambda,\eta,V_{ij;ln},\mu)\, \delta\left(\sum_{a=1}^{m}(q_a-k_a)\right) \delta\left(\sum_{a=1}^{m}(\omega_a-\nu_a)\right) \\ &\times \left[\partial_x^{s_1}\psi^*_{i_1,q_1}(x,\omega_1)\right]\left[\partial_x^{t_1}\psi_{j_1,k_1}(x,\nu_1)\right]\cdots\left[\partial_x^{s_m}\psi^*_{i_m,q_m}(x,\omega_m)\right]\left[\partial_x^{t_m}\psi_{j_m,k_m}(x,\nu_m)\right]. \end{aligned} \tag{34}$$

Here Λ is the UV cutoff for y momentum. One can reduce the number of independent arguments of the effective action by one using scaling. It is straightforward to check that there exists no scaling under which all terms in Eq. (19) are invariant for $\theta > 1$. However, there are two natural choices of scaling. The first is the Gaussian scaling in Eq. (9) under which the quadratic term is scale invariant while the quartic vertex grows at low energies. Under the Gaussian scaling, $S^{s_1,t_1,\ldots,s_m,t_m}_{i_1,j_1,\ldots,i_m,j_m}$ has the scaling dimension $-(3m-5)/2-\sum_{i=1}^{m}(s_i+t_i)$, and it can be written as

$$\begin{aligned} &S^{s_1,t_1,\ldots,s_m,t_m}_{i_1,j_1,\ldots,i_m,j_m}(x,q,k,\omega,\nu; X_0,\Lambda,V,\eta,\mu) \\ &\quad = X_0^{(3m-5)/2+\sum_{a=1}^{m}(s_a+t_a)}\, \bar{S}^{s_1,t_1,\ldots,s_m,t_m}_{i_1,j_1,\ldots,i_m,j_m}\left(xX_0^{-1}, qX_0^{1/2}, kX_0^{1/2}, \omega X_0, \nu X_0; \Lambda X_0^{1/2}, VX_0^{(\theta-1)/2}, \eta, \mu X_0^{1/2}\right), \end{aligned} \tag{35}$$

where the subscripts in $q_a, k_a, \omega_a, \nu_a, V_{ij;ln}$ are omitted to avoid clutter in notation. In the long-distance limit with $X_0 \to \infty$, $\Lambda X_0^{1/2}$ and $VX_0^{(\theta-1)/2}$ diverge for $\theta > 1$. This is expected because the interaction is relevant at the Gaussian fixed point for $\theta > 1$. If the effective action has singular dependence on the divergent parameters, which is certainly the case for the effective action computed perturbatively in V, the scaling dimensions in Eq. (9) are modified by quantum corrections. However, the scaling form in Eq. (35) is not useful in extracting the low-energy behavior of strongly interacting theories unless the singular dependence of $\bar{S}^{s_1,t_1,\ldots,s_m,t_m}_{i_1,j_1,\ldots,i_m,j_m}$ on the divergent parameters are exactly known.

There exists an alternative scaling from which we can extract exact scaling behaviors in the chiral theory. This is the scaling where the interaction is kept invariant at the expense of making η irrelevant. The requirement that the quadratic term, $\psi^*\partial_x\psi$, and the quartic interaction in Eq. (19) remain invariant uniquely fixes the dimension of frequency to be $z = \frac{\theta+1}{2}$. Under this scaling, we assign the following scaling dimensions to momenta and fields:

$$\begin{aligned} [x] &= -1, \\ [k] &= \frac{1}{2}, \\ z \equiv [\omega] &= \frac{\theta+1}{2}, \\ [\psi_i] &= -\frac{\theta+2}{4}, \\ [V] &= 0, \\ [\eta] &= -\frac{\theta-1}{2}, \\ [\mu] &= \frac{1}{2}. \end{aligned} \tag{36}$$

Here $\psi_{i,k}(\omega,x)$ is in the mixed-space representation. It is noted that the dynamical critical exponent z is defined to be the scaling dimension of frequency measured in the unit of the scaling dimension of ϵ_k. The scaling in Eq. (36) allows one to write the coefficients of the effective action as

$$\begin{aligned} &S^{s_1,t_1,\ldots,s_m,t_m}_{i_1,j_1,\ldots,i_m,j_m}(x,q,k,\omega,\nu; X_0,\Lambda,V,\eta,\mu) \\ &\quad = X_0^{m(\theta+2)/2-(\theta+4)/2+\sum_{a=1}^{m}(s_a+t_a)}\, \tilde{S}^{s_1,t_1,\ldots,s_m,t_m}_{i_1,j_1,\ldots,i_m,j_m}\left(xX_0^{-1}, qX_0^{1/2}, kX_0^{1/2}, \omega X_0^{(\theta+1)/2}, \nu X_0^{(\theta+1)/2}; \Lambda X_0^{1/2}, V, \eta X_0^{-(\theta-1)/2}, \mu X_0^{1/2}\right). \end{aligned} \tag{37}$$

In this scaling, η enters as a scale in addition to Λ, while V is deemed dimensionless. In other words, Λ and η^{-1} play the role of UV cutoff scales, whereas μ is an IR cutoff, as shown in Fig. 10. If the effective action was singular in the limit of $\Lambda X_0^{1/2} \to \infty$, $\eta^{-1}X_0^{(\theta-1)/2} \to \infty$, and $\mu X_0^{1/2} \to 0$, anomalous dimensions would arise relative to the "bare" scaling dimensions shown in Eq. (36). However, it turns out that the chiral nature of the theory puts strict constraints on the way the effective action depends on Λ and η, and the effective action is finite in the $\Lambda X_0^{1/2}, \eta^{-1}X_0^{(\theta-1)/2} \to \infty$ limit. This brings us to the two key results of this paper.

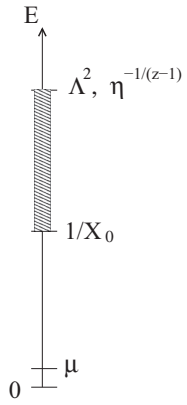

FIG. 10. In the Wilsonian effective action, "short-distance modes" between UV scales set by Λ^2, $\eta^{-2/(\theta-1)}$, and IR scale X_0^{-1} are integrated out. In the chiral theory, the resulting Wilsonian effective action is regular in the $\Lambda \to \infty$ and $\eta \to 0$ limit. As a result, only the running cutoff scale X_0 enters as a scale of the effective action in the $\mu X_0^{1/2} \to 0$ limit.

(i) The Wilsonian effective action is finite in the limit of $\Lambda X_0^{1/2} \to \infty$, $\eta^{-1} X_0^{(\theta-1)/2} \to \infty$, and $\mu X_0^{1/2} \to 0$ for $\theta > 1$. Since the UV and IR cutoff scales can be dropped, the Wilsonian effective action at the critical point with $\mu = 0$ is invariant under the coarse graining associated with an increase of X_0 and the rescaling dictated by Eq. (36), which gives the exact scaling dimensions.

(ii) The effective action is dominated by the RPA diagrams in the limit $qX_0^{1/2}, kX_0^{1/2}, \omega X_0^{(\theta+1)/2}, \nu X_0^{(\theta+1)/2} \to 0$, while other diagrams become important as well when $qX_0^{1/2}, kX_0^{1/2}, \omega X_0^{(\theta+1)/2}, \nu X_0^{(\theta+1)/2} \gtrsim 1$.

We prove these statements in generality and through explicit calculations in the following sections.

B. General proof of UV finiteness

In this section it is shown that all quantum corrections in the effective action are UV finite in the $\Lambda \to \infty$ and $\eta \to 0$ limit. In particular, integrations over internal frequencies and y momenta are separately UV finite for all diagrams.

1. UV finiteness of internal frequency integrations

Here we prove that frequency integrations are UV finite in the $\eta \to 0$ limit. In this limit, the fermion Green's function in Eq. (21) becomes $G(\omega, x) = -i\,\mathrm{sgn}(\omega)\Theta(-x\omega)$. At first, it appears dangerous to take the $\eta \to 0$ limit because the fermion propagator is not suppressed at large frequencies. It turns out that this does not cause any UV divergence because all internal frequencies in a given diagram are bounded by the external frequencies. To begin with the proof, we note that there are different ways to label internal frequencies for a given diagram. As an example, we show two different ways of assigning internal frequencies within a three-loop fermion self-energy diagram in Figs. 11(a) and 11(b). It turns out that there is a special choice which is more convenient for our proof. This is the choice where each loop [denoted by the dotted lines in Fig. 11(b)] associated with an internal frequency contains

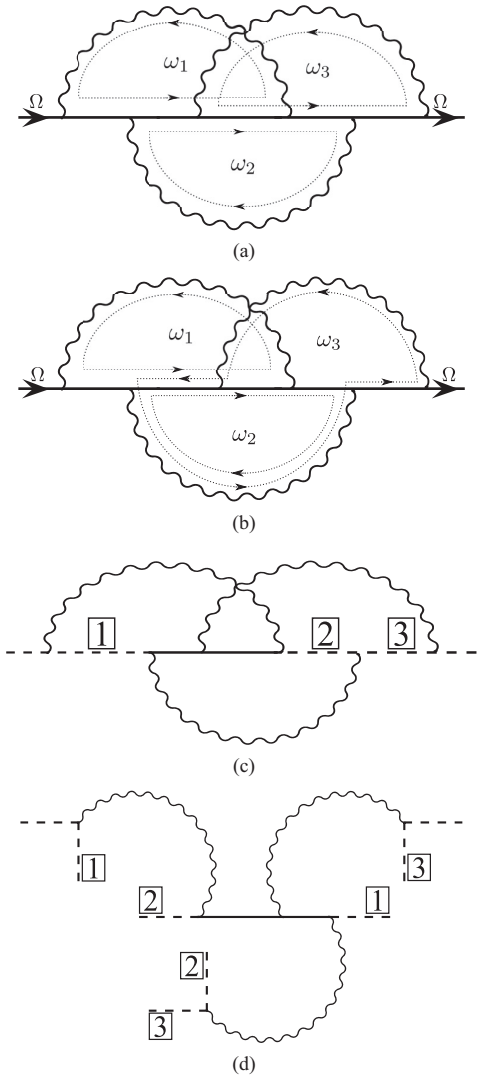

FIG. 11. A three-loop correction to the quadratic action. There are different ways of assigning internal frequencies, where internal frequencies are assigned to run along the dotted lines in (a) and (b). (a) All the fermion propagators in the loop of internal frequency ω_2 are shared with other loops associated with the internal frequencies, ω_1 and ω_3. (b) Each loop denoted by the dotted lines has an exclusive fermion propagator that is not shared with other loops. (c) The propagators that are exclusive to each loop in (b) are represented by dashed lines. The numbers in the boxes indicate the indices for the internal frequencies that run through the exclusive propagators. (d) A tree diagram whose legs are contracted to yield (b). The legs with matching numbers are contracted to give the corresponding dashed propagator in (c).

at least one fermion propagator which does not belong to other loops. We call this choice an "exclusive loop covering." Figure 11(a) is not an exclusive loop covering because the loop for ω_2 does not have any "exclusive" fermion propagator which carries only ω_2. On the other hand, Fig. 11(b) is an exclusive loop covering because for every ω_i there is at least

one exclusive fermion propagator which carries only ω_i. The exclusive fermion propagator for each internal frequency is denoted as dashed lines in Fig. 11(c).

Does an exclusive loop covering exist for every diagram? To show that the answer is yes, we note that any diagram can be constructed of a connected tree diagram by contracting some of its legs. This is always possible because one can keep cutting internal lines until all loops disappear without cutting the diagram into two disconnected ones. For example, the three-loop fermion self-energy diagram in Fig. 11(c) is constructed by joining three pairs of legs in the tree diagram shown in Fig. 11(d). In Fig. 11(c), we represent the internal lines of the parent tree diagram by solid lines and the new internal lines created through the joining procedure by dashed lines. A loop is formed by contracting a pair of legs, where an internal frequency is assigned to run through solid lines and the dashed line created from a new contraction. For each loop formed in this way, the solid propagators are, in general, shared by multiple loops while each of the dashed propagators, i.e., the ones formed by contracting external legs of the tree graph, are exclusive to one loop. Since this is true for all loops, we obtain an exclusive loop covering for the diagram.

Now we show that every internal frequency is bounded by the external frequency using the exclusive loop covering. As a simple example, let us examine the three-loop fermion self-energy diagram more closely. Each internal line carries a linear combination of the external frequency and internal frequencies as shown in Fig. 12. The key reason for the existence of an upper bound for internal frequencies is chirality. Since the fermions are chiral, the fermion propagator in Eq. (21) vanishes for positive (negative) frequency with $x > 0$ ($x < 0$). As a result, there is a set of constraints that internal frequencies have to satisfy for a given set of relative coordinates x_{ij} between vertices. For the three-loop self-energy diagram, the constraints read

$$\omega_1 x_{12} > 0, \tag{38}$$

$$\omega_2 x_{12} > 0, \tag{39}$$

$$\omega_3 x_{23} > 0, \tag{40}$$

$$(\omega_1 + \omega_2 - \omega_3) x_{23} > 0, \tag{41}$$

$$(\omega_1 + \omega_2 - \Omega) x_{31} > 0. \tag{42}$$

Here $x_{ij} \equiv x_i - x_j$ is the separation between the vertices i and j, which are labeled in Fig. 12. The constraints in Eqs. (38)–(40) are the constraints from the exclusive propagators, each of which carries only one internal frequency. Let $S(\{\omega_i\})$ be the set of internal frequencies that satisfy

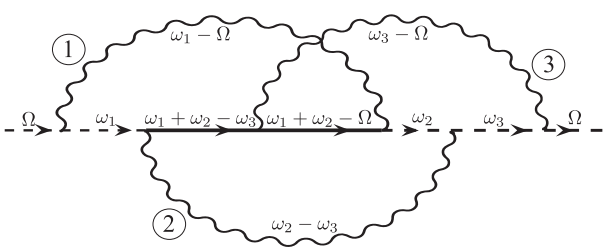

FIG. 12. A three-loop contribution to self-energy.

Eqs. (38)–(42). Once the signs of x_{ij}'s are fixed, the set does not depend on the magnitudes of x_{ij}'s. Our goal is to show that the set is bounded by the external frequency in all directions in the space of internal frequencies. To see this, we first add all nonexclusive constraints that contain ω_1. In this case, they are Eqs. (41) and (42). This leads to an inequality for ω_1,

$$(\omega_1 + \omega_2) x_{21} - \omega_3 x_{23} - \Omega x_{31} > 0. \tag{43}$$

Together with Eq. (38), Eq. (43) limits the range of ω_1 as

$$0 < \omega_1 x_{12} < \omega_3 x_{32} + \Omega x_{13} - \omega_2 x_{12}. \tag{44}$$

Equations (39) and (44) constrain the range of ω_2 as

$$0 < \omega_2 x_{12} < \omega_3 x_{32} + \Omega x_{13}. \tag{45}$$

Finally, Eq. (45), together with Eq. (40), leads to

$$0 < \omega_3 x_{23} < \Omega x_{13}. \tag{46}$$

This implies that for a fixed set of $\{x_{ij}\}$, ω_3 is bounded by Ω. Applying this to Eqs. (44) and (45), we find that ω_1 and ω_2 are also bounded by Ω.

Let $\tilde{S}(\{\omega_i\};\{x_{ij}\})$ be the set of internal frequencies that satisfy Eqs. (44)–(46). It is of note that $\tilde{S}(\{\omega_i\};\{x_{ij}\})$ not only depends on the signs of x_{ij}'s but also on their magnitudes unlike $S(\{\omega_i\})$. An important property of $\tilde{S}(\{\omega_i\};\{x_{ij}\})$ is that $\tilde{S}(\{\omega_i\};\{x_{ij}\}) \supseteq S(\{\omega_i\})$ for any $\{x_{ij}\}$. This is due to the fact that Eqs. (44)–(46) are necessary (not sufficient, in general) conditions of Eqs. (38)–(42). Since $\tilde{S}(\{\omega_i\};\{x_{ij}\})$ is bounded for any fixed set of $\{x_{ij}\}$, $S(\{\omega_i\})$ is also bounded by the external frequency in all directions in the space of internal frequencies. This proves that the integration over the internal frequencies is UV finite.

This argument can be easily generalized to all other diagrams. The rule is as follows. Consider a diagram with L loops with I internal fermion propagators and V vertices. For a fixed set of relative coordinates $\{x_{ij}\}$ of the vertices, there exist I constraints for L internal frequencies. Since vertices are normal ordered, fermion propagators can connect only distinct vertices. The existence of an exclusive loop covering implies that for every internal frequency ω_q there exists an exclusive constraint of the form

$$F_q(\omega_q) = x_{i_q j_q} \omega_q > 0, \tag{47}$$

where $q = 1,2,\ldots,L$ and $x_{i_q j_q}$ is the separation between the two vertices connected by the fermion propagator which carries only ω_q. Therefore, the I constraints can be divided into the L "exclusive" constraints and $I - L$ "nonexclusive" constraints. Nonexclusive constraints, in general, contain external frequencies and more than one internal frequency,

$$f_p(\{\omega_q\},\{\Omega_r\}) > 0, \tag{48}$$

where $\{\Omega_r\}$ is a set of external frequencies and $p = 1,2,\ldots,I-L$. Without loss of generality, we can assume that only the first k_1 nonexclusive constraints, $f_1, f_2, \ldots, f_{k_1}$, contain ω_1. We add them up to create a new constraint,

$$C_1 = f_1 + f_2 + \cdots + f_{k_1} > 0. \tag{49}$$

Since the first exclusive constraint is written as

$$F_1 = x_{i_1 j_1} \omega_1 > 0, \tag{50}$$

it is guaranteed that C_1 is of the form

$$C_1 = -x_{i_1 j_1}\omega_1 + C_1'(\omega_2,\omega_3,\ldots,\omega_L;\{\Omega_r\}) > 0. \quad (51)$$

This is due to the fact the relative coordinates of the vertices around a loop form a cyclic sum in $C_1 + F_1$, and it is independent of ω_1. With the aid of Eqs. (50) and (51), we see that ω_1 is bounded by other internal frequencies and the external frequencies,

$$0 < x_{i_1 j_1}\omega_1 < C_1'(\omega_2,\omega_3,\ldots,\omega_L;\{\Omega_r\}). \quad (52)$$

Next we construct a set of nonexclusive constraints for $\omega_2,\omega_3,\ldots,\omega_L$ made of

$$F_1 + C_1 = C_1'(\omega_2,\omega_3,\ldots,\omega_L;\{\Omega_r\}) > 0, \quad \text{and}$$
$$f_j > 0 \quad \text{with} \quad j = k_1+1, k_1+2,\ldots,L-I. \quad (53)$$

Using this set of nonexclusive constraints, we apply the same procedure for ω_2. Namely, we add all nonexclusive constraints that contain ω_2 to construct a new constraint $C_2 > 0$. Combined with $F_2 > 0$, one can obtain a bound for ω_2 of the form

$$0 < x_{i_2 j_2}\omega_2 < C_2'(\omega_3,\omega_4,\ldots,\omega_L;\{\Omega_r\}). \quad (54)$$

In this way, one can show that the range of ω_l is bounded by a linear combination of the external frequencies and the internal frequencies ω_m with $m > l$,

$$0 < x_{i_l j_l}\omega_l < C_l'(\omega_{l+1},\omega_{l+2},\ldots,\omega_L;\{\Omega_r\}). \quad (55)$$

The last internal frequency ω_L is bounded only by the external frequencies,

$$0 < x_{i_L j_L}\omega_L < C_L'(\{\Omega_r\}). \quad (56)$$

The set of L inequalities given by Eq. (55) implies that all the internal frequencies are bounded by the external frequencies. From the argument given below Eq. (46), the set of internal frequencies that satisfy the original constraints given by Eqs. (47) and (48) is also bounded by the external frequencies. Because all internal frequencies are bounded, all frequency integrations are UV finite even in the $\eta \to 0$ limit. This completes the proof that integrations over internal frequencies are UV finite for general diagrams. We emphasize that the UV finiteness is due to the chiral nature of the theory. For nonchiral theories, internal frequencies are not bounded by external ones.

2. *UV finiteness of y-momentum integrations*

It is easier to see that y-momentum integrations are UV finite. Let us first consider fermion loops which refer to loops that are solely made of fermion propagators. For example, a bubble in Fig. 13 leads to an integration of the form

$$\int_{-X_0}^{X_0} dx_{12} \int_{-\Lambda}^{\Lambda} dp\, e^{2i\gamma x_{12} q p}, \quad (57)$$

where x_{12} is the relative coordinate between the two quartic vertices, p is the y momentum that runs inside the loop, and q is the y-momentum transfer. It is noted that fermion propagators and the four-fermion vertices do not depend on the y momentum p that runs within the fermion loop except for the phase factor that results in Eq. (57). This

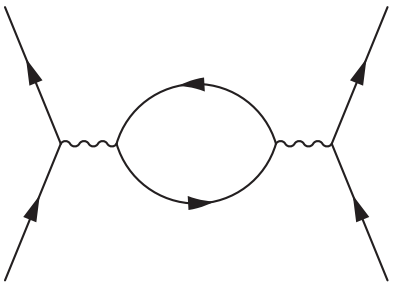

FIG. 13. A fusion of two quartic vertices which results in an operator which is independent of X_0.

leads to large fluctuations in the y momentum of the internal fermion. Due to the emergent uncertainty relation between the x coordinate and y momentum, as is manifest from the phase factor, wild fluctuations in p lead to a "confinement" of the relative coordinate of the two vertices x_{21}. In the $\Lambda \to \infty$ limit, the integration over p simply generates a δ function that puts a constraint on the positions of the vertices attached to the loop, which leads to $\frac{1}{\gamma|q|}$ after the integration over x_{12}. For a fermion loop with more than two external legs, the integration over the y momentum along the fermion loop fixes one of the coordinates of the vertices without UV divergence.

Now we consider mixed loops which refer to loops that contain at least one boson propagator. One can always assign internal momenta such that every mixed loop has at least one boson propagator which carries no other internal momenta except for the one associated with the loop. This can be easily understood from an argument that is similar to the one used in the previous section to show the existence of an exclusive loop covering for fermion propagator. This time we cut boson propagators to remove all mixed loops without creating disjoint diagrams. For each mixed loop removed from this procedure, the boson propagator that is cut is identified as the exclusive propagator. Therefore, each internal y-momentum integration of the original diagram goes as

$$\int_{-\Lambda}^{\Lambda} dq \frac{1}{|q^2+\mu^2|^{\theta/2}} \quad (58)$$

at most in the large q limit. For $\theta > 1$ this is UV convergent in the $\Lambda \to \infty$ limit.

C. IR finiteness

There are two reasons for the UV finiteness of the Wilsonian action. First, $(2+1)$ dimension is below the upper critical dimension for $\theta > 1$. As a result, only a finite number of diagrams are potentially UV divergent. Second, even the potentially divergent diagrams are finite due to chirality, which strictly limits the ranges of internal frequencies by the external ones.

On the other hand, the IR finiteness in the $\mu \to 0$ limit is less obvious. For example, the integration over the y momentum in Eq. (58) is IR divergent for $\mu = 0$ with $\theta > 1$. While the UV finiteness is controlled by kinematic constraints, the way IR finiteness is restored in the $\mu \to 0$ limit is through

dynamical mechanism. It turns out that the theory cures the IR singularity dynamically such that the theory flows to an IR fixed point governed by the scaling in Eq. (36). In the following section, we see that this is indeed the case through an explicit computation of the Wilsonian effective action.

D. An explicit computation of the Wilsonian effective action

Because the theory flows to a strongly interacting fixed point, it is not easy to compute the full Wilsonian effective action exactly. However, one can compute the effective action in the limit where the running cutoff length scale is small compared to the length scales associated with external momenta. The main outcome of the explicit calculation is that the operators that are generated from the RPA channels shown in Fig. 14 are the only ones that are $\mathcal{O}(1)$ in this limit. All other channels generate operators with extra factors of X_0 accompanied by additional factors of frequency or momentum. Therefore, those contributions are suppressed in the small momentum limit with fixed X_0 (equivalently small X_0 limit with fixed momenta). Once the $\mathcal{O}(1)$ corrections are consistently taken into account in the Wilsonian effective action, the IR singularity encountered in the $\mu \to 0$ limit is cured. We first illustrate the dominance of the RPA diagrams in the small X_0 limit by computing two representative diagrams, followed by a generalization to all diagrams.

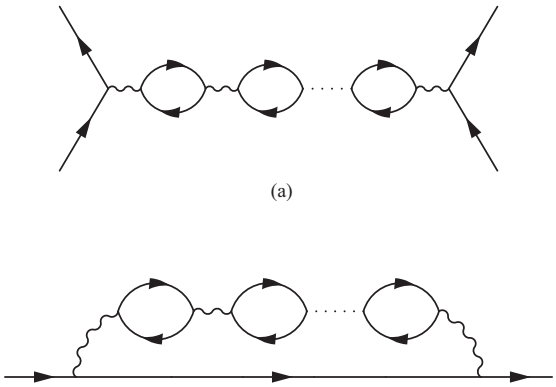

FIG. 14. Fusion channels that give rise to $O(1)$ corrections to the Wilsonian effective action in the small X_0 limit.

1. $(X_0)^0$ order

As a first example, let us consider the diagram shown in Fig. 13, where two quartic vertices are fused into one quartic vertex as two pairs of fermion fields are contracted. The one-loop contribution is given by

$$\begin{aligned}\delta S_4^{(\mathrm{RPA},1)} &= 2\int \frac{dk_1dk_2dqd\omega_1d\omega_2d\nu}{(2\pi)^6}dx_1 e^{i2\gamma(k_1-k_2)qx_1}V_{ij;ln}\chi_\theta(q)\\ &\times \frac{(-g^2)}{2}\chi_\theta(q)\int\frac{dk'}{2\pi}\frac{d\omega'}{2\pi}\int_{-X_0}^{X_0}dx_{21}e^{-2i\gamma k'qx_{21}}G_0(\omega'+\nu,x_{21})G_0(\omega',-x_{21})\\ &\times \circ\circ \psi^*_{i,k_2}(\omega_2,x_1)\psi_{j,k_2+q}(\omega_2+\nu,x_1)\psi^*_{l,k_1+q}(\omega_1+\nu,x_1+x_{21})\psi_{n,k_1}(\omega_1,x_1+x_{21})\circ\circ \qquad (59)\\ &= \int\frac{dk_1dk_2dqd\omega_1d\omega_2d\nu}{(2\pi)^6}dx_1e^{i2\gamma(k_1-k_2)qx_1}V_{ij;ln}\chi_\theta(q)\left[-c_B\chi_\theta(q)\frac{|\nu|}{|q|}\right]\\ &\times \circ\circ \psi^*_{i,k_2}(\omega_2,x_1)\psi_{j,k_2+q}(\omega_2+\nu,x_1)\psi^*_{l,k_1+q}(\omega_1+\nu,x_1)\psi_{n,k_1}(\omega_1,x_1)\circ\circ\,, \qquad (60)\end{aligned}$$

where $c_B = [g^2/(8\pi\gamma)]$ and $x_{21} = x_2 - x_1$ is the relative coordinate between the two vertices. The singular dependence of c_B on γ again signifies the importance of the local curvature of the Fermi surface. The second line in Eq. (59) represents the contribution from the fermion loop. The integration over the y momentum k' that runs within the fermion loop results in $\frac{1}{|q|}\delta(x_{21})$. Due to the δ-function, the nonzero contribution is concentrated at $x_{21} = 0$. As a result, Eq. (60) is independent of X_0.

Similarly, the fusion of $L+1$ quartic vertices in the RPA channel, as shown in Fig. 14(a), generates a L-loops diagram which is given by

$$\begin{aligned}\delta S_4^{(\mathrm{RPA},L)} &= \int\frac{dk_1dk_2dqd\omega_1d\omega_2d\nu}{(2\pi)^6}dx e^{2i\gamma(k_1-k_2)qx}V_{ij;ln}\chi_\theta(q)\left[-c_B\chi_\theta(q)\frac{|\nu|}{|q|}\right]^L\circ\circ\psi^*_{i,k_2}(\omega_2,x)\psi_{j,k_2+q}(\omega_2+\nu,x)\\ &\times\psi^*_{l,k_1+q}(\omega_1+\nu,x)\psi_{n,k_1}(\omega_1,x)\circ\circ\,. \qquad (61)\end{aligned}$$

For the derivation of Eq. (61), see Appendix B1. As is the case for the fusion of two vertices shown in Fig. 13, L relative coordinates between $L+1$ vertices are completely fixed by the L δ-functions that result from the wildly fluctuating flavors within the L fermion loops. Therefore, all operators generated from fusions in the RPA channel are independent of X_0. The infinite series of operators that are $O(1)$ can be summed over to renormalize the boson propagator to

$$\chi_\theta^{(\mathrm{RPA})}(\nu,q) = \frac{1}{|q^2+\mu^2|^{\theta/2}+c_B\frac{|\nu|}{|q|}}. \qquad (62)$$

Note that the $q \to 0$ limit of the quartic vertex is now well defined even in the $\mu \to 0$ limit. As a result, the IR divergence we encountered in integrations over y momentum [for example in Eq. (58)] in the $\mu \to 0$ limit is cured by the quantum corrections. Henceforth, we set $\mu = 0$ to focus on the critical point.

There are $O(1)$ contributions to the quadratic vertex as well. These are generated by contracting an extra pair of fermion fields in the diagrams that generate $O(1)$ correction to the quartic vertex. Diagrammatically, these are nothing but the RPA diagrams for the fermion self-energy as shown in Fig. 14(b), where the number of fermion loops matches with the number of relative coordinate between vertices. The $O(1)$ correction to the quadratic action is given by

$$\delta S_2^{(\mathrm{RPA})} = \int dx \frac{d\omega}{2\pi}\frac{dk}{2\pi}\psi^*_{i,k}(x,\omega)\Sigma^{(\mathrm{RPA})}_{ij}(\omega)\psi_{j,k}(x,\omega), \tag{63}$$

where the self-energy is

$$\Sigma^{(\mathrm{RPA})}_{ij}(\omega) = i\delta_{ij}c_F \mathrm{sgn}(\omega)|\omega|^{2/(\theta+1)}, \tag{64}$$

with

$$c_F = \frac{g^2 v}{2\pi^2} c_B^{\frac{1-\theta}{1+\theta}} \int_0^\infty dy\, y \ln\left(1+\frac{1}{y^{\theta+1}}\right). \tag{65}$$

It is noted that the integration over the y momentum (represented by y) in Eq. (65) is finite with $\mu = 0$ because the IR divergence is cured by the series of RPA diagrams. We emphasize that *the RPA diagrams are dynamically selected, not by hand.* As shown in the following section, all other diagrams vanish at least linearly in X_0 in the small X_0 limit due to the chiral nature of the theory. Those contributions necessarily contain larger powers of momentum or frequency, which are suppressed at low momentum/frequency.

2. Higher order in X_0

To illustrate the generic feature of operators generated from fusion in non-RPA channels, we compute the two-loop vertex correction shown in Fig. 15(a). Here three quartic operators are fused into one quartic vertex, which results in

$$\begin{aligned}\delta S_4^{(n\mathrm{RPA},3)} = -8\int \frac{dk_1 dk_2 dq d\omega_1 d\omega_2 d\nu}{(2\pi)^6} dx_1 e^{2i\gamma(k_1-k_2)qx_1} V_{i'j';ln}V_{il';n'i'}V_{l'j;j'n'}\chi_\theta(q)\int\frac{dq'd\nu'dk'd\omega'}{(2\pi)^4}\chi_\theta(q')\chi_\theta(q'-q)\\ \times\int_{\mathcal{C}} dx_{21}dx_{32}e^{2i\gamma(k'-k_2)qx_{21}}e^{2i\gamma(k'-k_2)(q-q')x_{32}}G_0(\omega',x_{21})G_0(\omega'+\nu',x_{32})G_0(\omega'+\nu,-x_{32}-x_{21})G_0(\omega_2+\nu',-x_{32})\\ \times \circ\!\circ\, \psi^*_{i,k_2}(\omega_2,x_1+x_{21})\psi_{j,k_2+q}(\omega_2+\nu,x_1+x_{32}+x_{21})\psi^*_{l,k_1+q}(\omega_1+\nu,x_1)\psi_{n,k_1}(\omega_1,x_1)\,\circ\!\circ,\end{aligned} \tag{66}$$

where x_{21} and x_{32} are the two relative coordinates of the three vertices integrated over the region of x space, $\mathcal{C} \equiv \cup_{\alpha=1}^6 \mathcal{C}_\alpha$, with $\mathcal{C}_\alpha$ defined in Eq. (B2). The y momentum k' running in the fermion loop generates $\delta(qx_{21}-(q'-q)x_{32})/2\gamma$, which fixes one of the relative coordinates (x_{32}). The integration over the other relative coordinate (x_{21}) gives rise to a factor of X_0. Since the remaining internal momentum and frequency integrals are UV finite, the resulting operator vanishes linearly in the $X_0 \to 0$ limit,

$$\begin{aligned}\delta S_4^{(n\mathrm{RPA},3)} = -\int \frac{dk_1 dk_2 dq d\omega_1 d\omega_2 d\nu}{(2\pi)^6} dx_1 e^{2i\gamma(k_1-k_2)qx_1} V_{i'j';ln}V_{il';n'i'}V_{l'j;j'n'}\chi_\theta(q)\Gamma^{(n\mathrm{RPA},3)}(\omega_2,\nu,q,X_0)\\ \times \circ\!\circ\, \psi^*_{i,k_2}(\omega_2,x_1)\psi_{j,k_2+q}(\omega_2+\nu,x_1)\psi^*_{l,k_1+q}(\omega_1+\nu,x_1)\psi_{n,k_1}(\omega_1,x_1)\,\circ\!\circ,\end{aligned} \tag{67}$$

where $\Gamma^{(n\mathrm{RPA},3)}(\omega_2,\nu,q,X_0)$ is proportional to X_0. The expression becomes simpler when one of the frequencies vanishes,

$$\begin{aligned}\Gamma^{(n\mathrm{RPA},3)}(\omega_2=0,\nu,q,X_0) = \frac{1}{2\pi^3\gamma}\int dq'\frac{\chi_\theta(q')\chi_\theta(q'+q)}{|q'|}\int_0^{X_0} dx_R\,\Theta\left(X_0-\frac{q}{q'}x_R\right)\Theta\left(\frac{q}{q'}\right)\int_0^{|\nu|}d\omega'\int_0^{\omega'}d\nu'\\ \times\ \exp\left[-\eta|x_R|\left(|\omega'|+\left|1+\frac{q}{q'}\right||\nu|-\omega'|+\left|\frac{q}{q'}\right|\{|\omega'-\nu'|+|\nu'|\}\right)\right].\end{aligned} \tag{68}$$

Although the integration over q' in the above expression is IR divergent in the $\mu \to 0$ limit, the divergence disappears once other operators which are also $O(X_0)$ are consistently included. The other diagrams which are $O(X_0)$ are the ones where the vertices and the fermion propagators in Fig. 15(a) are dressed by the RPA diagrams as shown in Fig. 15(b). Including all the $O(X_0)$ contributions amounts to replacing the bare vertices and the bare propagators in Eq. (66) with the dressed ones shown in Eqs. (62) and (64). Taking this into account, we obtain a finite expression,

$$\begin{aligned}&\Gamma^{(n\mathrm{RPA},3)}(\omega_2=0,\nu,q,X_0)\\ &= \frac{1}{2\pi^3}\frac{X_0|\nu|^{2/(\theta+1)}}{\gamma c_B^{2\theta/(\theta+1)}} f_1\left[c_F X_0|\nu|^{2/(\theta+1)}, \frac{q}{(c_B|\nu|)^{1/(\theta+1)}}\right],\end{aligned} \tag{69}$$

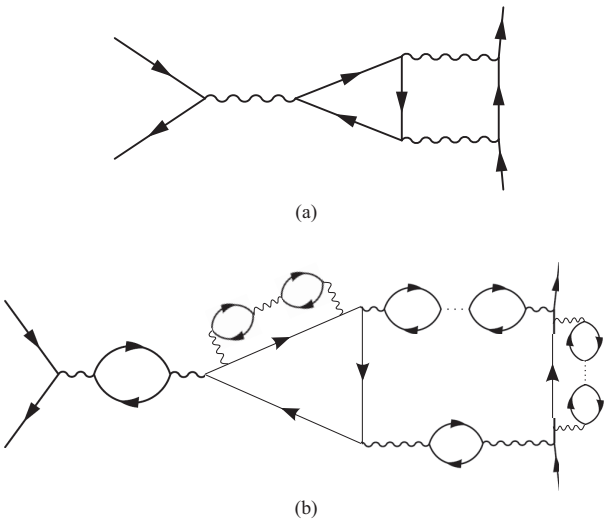

FIG. 15. A subleading correction to the quartic vertex. (a) With bare vertices and propagators, the resulting operator is IR divergent in the $\mu \to 0$ limit. (b) Once the vertices and propagators are dressed by all other $O(1)$ corrections, the resulting operator is finite as $\mu \to 0$.

where $f_1(x,y)$ is a finite universal function which has the following asymptotic behavior,

$$\lim_{x\to 0} f_1(x,1) \sim 1, \tag{70}$$

$$\lim_{x\to \infty} f_1(x,1) \sim x^{-1}. \tag{71}$$

It is noted that the non-RPA correction is suppressed by an extra factor of $X_0|\nu|^{2/(\theta+1)}$ in the small ν limit with fixed X_0.

3. General arguments

In this section we provide a general argument for the statement that all non-RPA diagrams contain positive powers of X_0 in the small X_0 limit. Consider a cluster of $(V+1)$ vertices which are to be fused into one vertex through a fusion channel with L_f fermion loops. They have V relative coordinates to be integrated over the range which is on the order of X_0. Integrating out the y momenta running in these loops yields L_f δ-functions for the relative coordinates, x_{ij}. After L_f relative coordinates are fixed, the remaining $V - L_f$ relative coordinates give rise to a factor of $X_0^{V-L_f}$. This implies that the only $O(1)$ contributions are the diagrams with $V = L_f$. These are exactly the RPA diagrams. All other diagrams, including higher-order vertices generated from the quartic vertex, necessarily include positive powers of X_0.

If the Wilsonian effective action were UV divergent in the $\Lambda X_0^{1/2}, \eta^{-1} X_0^{(\theta-1)/2} \to \infty$ limit, then $\Lambda X_0^{1/2}, \eta^{-1} X_0^{(\theta-1)/2}$ should be kept finite. In such a case, the extra power of X_0 in the non-RPA diagrams could be saturated by Λ or η^{-1}. In the present theory, there is no UV divergence due to chirality and $\theta > 1$. As a result, one can take the $\Lambda X_0^{1/2}, \eta^{-1} X_0^{(\theta-1)/2} \to \infty$ limit. Since there is no scale in the Wilsonian effective action, the extra powers of X_0 in the non-RPA diagrams should be accompanied by extra powers of momenta or frequency. This is why all non-RPA diagrams are suppressed in the low-momentum/frequency limit with fixed X_0.

4. The Wilsonian effective action

Including the corrections to the zeroth order in X_0, we obtain the Wilsonian effective action which is exact modulo irrelevant terms,

$$\begin{aligned} S_{X_0} = & \int \frac{dk}{2\pi}\frac{d\omega}{2\pi} dx \, {}^{\circ}_{\circ} \psi^*_{i,k}(\omega,x) \\ & \times [i c_F \mathrm{sgn}(\omega)|\omega|^{2/(\theta+1)} - i\partial_x] \psi_{i,k}(\omega,x) \, {}^{\circ}_{\circ} \\ & + \int \frac{dk_1 dk_2 dq d\omega_1 d\omega_2 d\nu}{(2\pi)^6} dx \; e^{2i\gamma(k_1-k_2)qx} \\ & \times \frac{V_{ij;ln}}{|q|^\theta + c_B \frac{|\nu|}{|q|}} \, {}^{\circ}_{\circ} \psi^*_{i,k_2}(\omega_2,x)\psi_{j,k_2+q}(\omega_2+\nu,x) \\ & \times \psi^*_{l,k_1+q}(\omega_1+\nu,x)\psi_{n,k_1}(\omega_1,x) \, {}^{\circ}_{\circ}, \end{aligned} \tag{72}$$

where c_B and c_F are positive constants. The effective action is local in the x direction but not in the τ direction, as can be seen from the terms that are nonanalytic in frequency. Once nonanalytic terms are allowed in the effective action, usually the standard RG procedure becomes less useful because, in principle, infinitely many marginal or relevant nonlocal operators can be generated. In the present case, however, the chiral nature of the theory puts a strong constraint on the form of nonlocal terms that are generated. The contributions from non-RPA diagrams are systematically suppressed by positive powers of $(|\omega|^{2/(\theta+1)}X_0)$, $(q^2 X_0)$, or $X_0\partial_x$ compared to the RPA contributions that are included in Eq. (72), where ω and q are external frequency and y momentum of the operator. Higher-order vertices such as ψ^6 are also generated. These vertices can be obtained by cutting open some internal lines from quartic vertices. As a result, they necessarily have less constraints on the relative coordinates of the vertices compared to the RPA diagrams. Since they are accompanied by positive powers of X_0, they are negligible in the low-energy limit. Therefore, the effective action in Eq. (72) includes all terms apart from the terms that are irrelevant by power counting. It is emphasized that RPA diagrams are dynamically selected to generate the leading-order terms in the Wilsonian effective action.

With the renormalized action, it is more convenient to use a new normal ordering scheme based on the dressed Green's function,

$$G(\omega,x_{12}) = -i\mathrm{sgn}(\omega)\Theta(-x_{12}\omega)\exp[-c_F|x_{12}||\omega|^{2/(\theta+1)}]. \tag{73}$$

The new normal ordering is related to the old one through

$$\begin{aligned} :\mathcal{O}: = \exp\Bigg[& -\sum_i \int dk d\omega dx_1 dx_2 (2\pi)^2 \\ & \times \{G(\omega,x_{12}) - G_0(\omega,x_{12})\} \\ & \times \frac{\delta}{\delta\psi^*_{i,k}(\omega,x_2)} \frac{\delta}{\delta\psi_{i,k}(\omega,x_1)} \Bigg] \, {}^{\circ}_{\circ} \mathcal{O} \, {}^{\circ}_{\circ}. \end{aligned} \tag{74}$$

This transformation modifies only the irrelevant operators in the action because the difference in the propagator vanishes in

the low-energy limit,

$$\begin{aligned} &G(\omega,x_{12}) - G_0(\omega,x_{12}) \\ &\quad = -i\Theta(-\omega x_{12})\mathrm{sgn}(\omega) \\ &\qquad \times [\exp(-c_F|x_{12}||\omega|^{2/(\theta+1)}) - \exp(-\eta|x_{12}\omega|)] \\ &\quad = -i\Theta(-\omega x_{12})\mathrm{sgn}(\omega)[-c_F|x_{12}||\omega|^{2/(\theta+1)} + \cdots]. \end{aligned} \tag{75}$$

From now on, all composite operators are understood to be normal ordered according to Eq. (20), with $G(\omega,x_{12})$ replacing $G_0(\omega,x_{12})$.

E. Wilsonian effective action vs quantum effective action

How was it possible for us to construct the Wilsonian effective action in Eq. (72) in the strongly coupled field theory? The answer to this question lies in the difference between the quantum effective action and the Wilsonian effective action. In the quantum effective action computed in Ref. [37], quantum fluctuations are fully incorporated, including the contributions from the gapless modes right on the Fermi surface. On the contrary, in the Wilsonian effective action constructed in Eq. (72), only the short-distance quantum fluctuations up to the length scale X_0 are included. Therefore, the diagrams that are of the same order as the RPA diagrams in the quantum effective action do not necessarily come in the same order in the Wilsonian effective action. In this section, we show that non-RPA diagrams are indeed subleading in the Wilsonian effective action although they are not suppressed in the full quantum effective action.

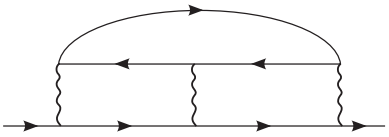

FIG. 16. A three-loop correction to the quadratic vertex. In the full quantum effective action, this is one of the infinite series of diagrams which is of the same order as the RPA corrections. In the Wilsonian effective action, this is subleading (see the text).

As a concrete example, we consider a three-loop diagram shown in Fig. 16, where three quartic vertices are fused into a quadratic vertex in the Wilsonian effective action. The resulting vertex is given by

$$\delta S_2^{(3)} = \int dx \frac{d\omega dk}{(2\pi)^2}\, \psi^*_{i,k}(\omega,x)\Sigma^{(3)}_{ij}(\omega,X_0)\psi_{j,k}(\omega,x), \tag{76}$$

where the self-energy is

$$\begin{aligned} \Sigma^{(3)}_{ij}(\omega,X_0) = \frac{i}{4\pi^5}\frac{c_B^{(1-3\theta)/(\theta+1)}}{c_F\gamma}\mathrm{sgn}(\omega)|\omega|^{2/(\theta+1)}V_{ij';j'n'}V_{m'l';j'i'} \\ \times V_{n'm';i'j} f_2(c_F X_0|\omega|^{2/(\theta+1)}). \end{aligned} \tag{77}$$

The dimensionless function $f_2(s)$ is

$$\begin{aligned} f_2(s) = s\int_0^1 dx \int_0^1 dt_1 \int_0^{1-t_1} dt_2 dt_3 \int_{-\infty}^{\infty} dy_1 dy_2 \Theta\left(-\frac{y_1}{y_2}\right)\Theta\left(1+\frac{y_1}{y_2}x\right) \\ \times \frac{|y_1|}{|y_1|^{\theta+1}+(t_1+t_2)}\frac{1}{|y_2|^{\theta+1}+(t_1+t_3)}\frac{|y_1-y_2|}{|y_1-y_2|^{\theta+1}+|t_2-t_3|} \\ \times \exp\left(-sx\left\{\left|1-\frac{y_1}{y_2}\right|t_1^{\frac{2}{(\theta+1)}} + \left[t_2^{\frac{2}{(\theta+1)}} + (1-t_1-t_2)^{\frac{2}{(\theta+1)}}\right] + \left|\frac{y_1}{y_2}\right|\left[t_3^{\frac{2}{(\theta+1)}} + (1-t_1-t_3)^{\frac{2}{(\theta+1)}}\right]\right\}\right), \end{aligned} \tag{78}$$

where $f_2(s)$ is finite for all s. It has the following asymptotic behaviors,

$$\lim_{s\to 0} f_2(s) \sim s, \tag{79}$$

$$\lim_{s\to\infty} f_2(s) \sim 1. \tag{80}$$

We note that the exponential factor in the last line of Eq. (78) is less than 1. In order to obtain an upper bound in the small s limit in Eq. (79), we can simply replace the exponential factor by 1. Since the rest of the integrals are finite, $f_2(s)$ should be proportional to s in the small s limit. The limit in Eq. (80) follows from the observation that the function multiplying sx in the exponent in Eq. (78) is strictly greater than 0 and is $\mathcal{O}(1)$. Therefore, as $s\to\infty$ the leading-order contribution to the x integral comes from the region $0 \leqslant x \lesssim 1/s$, resulting in the asymptotic behavior in Eq. (80). We numerically compute $f_2(s)$ and confirm the asymptotic behaviors as shown in Fig. 17.

In the Wilsonian effective action, we consider the low-energy limit with fixed X_0. In this case, the limit in Eq. (79) applies, and the three-loop self-energy has an extra factor of $c_F X_0|\omega|^{2/(\theta+1)}$ compared to the leading-order terms in Eq. (64). Therefore, the diagram does not contribute to the Wilsonian effective action to the leading order. In the full

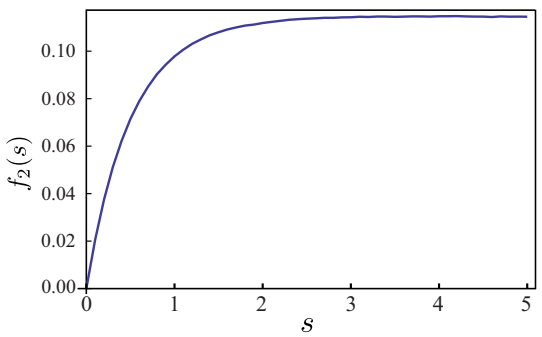

FIG. 17. (Color online) A plot of the function $f_2(s)$ in Eq. (78) for $\theta = 2$.

quantum effective action, on the other hand, we consider the limit $X_0 \to \infty$ with fixed external frequency. In this case, the limit in Eq. (80) applies, and the diagram has the same scaling behavior as the RPA contributions. In the RG, only short-distance quantum fluctuations are included in every step of coarse graining. In combination with the chiral nature of the theory which constrains the degree of UV/IR singularity of the theory, this allows one to compute the exact Wilsonian effective action to the leading order.

Having said that the Wilsonian effective action can be computed perturbatively in the low-momentum/frequency limit with fixed X_0, we note that physical observables are given by the full quantum effective action. If one wants to compute physical observables with external y momenta k using the effective action defined at a scale X_0 with $kX_0^{1/2} \ll 1$, one still has to include the quantum fluctuations between scales $X_0^{-1/2}$ and k, which are not included in the Wilsonian effective action. Therefore, the exact form of the n-point function, which is not dictated by the scaling, in general cannot be computed perturbatively.

VII. RENORMALIZATION GROUP

It is now straightforward to perform the RG analysis by increasing X_0 by a factor of e^{dl} in the Wilsonian effective action. The quantum correction obtained by increasing X_0 can be easily read from

$$\delta S = dl \frac{\partial S_{X_0}}{\partial \ln X_0}, \tag{81}$$

where S_{X_0} is the effective action in Eq. (72). The key observation is that S_{X_0} is independent of X_0 apart from irrelevant terms. This implies that there is no quantum correction to the leading order terms in the Wilsonian effective action.

Here we show that there is indeed no quantum corrections to the leading order through an explicit calculation. We divide the configuration space of operators into two parts. The first part represents the configurations where no two composite operators are closer than $X_0 e^{dl}$ along the x direction for an infinitesimally small dl. The second part represents the configurations where there is at least one pair of operators whose separation along the x direction is in

$$\Omega \equiv \{(x_1,x_2)|X_0 < |x_1 - x_2| \leqslant X_0 e^{dl}\}. \tag{82}$$

Two operators whose relative separation is in Ω are fused into one composite operator. The volume of the phase space where more than two operators fuse simultaneously is, at most, on the order of dl^2, which can be ignored.

Now we compute the quantum corrections explicitly. Figure 18 shows the channels where two quartic operators fuse into quadratic or quartic operators. The fusions generate the vertices

$$\Gamma_2^{(a)} = 0, \tag{83}$$

$$\Gamma_2^{(b)} = -\frac{idl}{4\pi^4} c_B^{-2\frac{\theta-1}{\theta+1}} \int dx \frac{dkd\omega}{(2\pi)^2} V_{n'm';il'} V_{m'j;l'n'} \, \mathrm{sgn}(\omega)|\omega|^{2/(\theta+1)} \circ\!\!\circ \psi^*_{i,k}(\omega)\psi_{j,k}(\omega) \circ\!\!\circ X_0|\omega|^{\frac{2}{\theta+1}} f^{(b)}(X_0|\omega|^{\frac{2}{\theta+1}}), \tag{84}$$

$$\Gamma_4^{(c)} = 0, \tag{85}$$

$$\begin{aligned}\Gamma_4^{(d)} = &-\frac{dl}{\pi^2} c_B^{-\frac{\theta-1}{\theta+1}} \int dx \frac{dk_1dk_2dqd\omega_1d\omega_2d\nu}{(2\pi)^6} X_0|\nu|^{\frac{2}{\theta+1}} f^{(d)}\left(X_0|\nu|^{\frac{2}{\theta+1}}, \frac{q}{|c_B\nu|^{\frac{1}{\theta+1}}}, \frac{\omega_1}{\nu}\right) \\ &\times \frac{V_{ij;l'n'}V_{ll';n'n}}{|q|^\theta + c_B|\nu|/|q|} e^{2i\gamma(k_1-k_2)qx} \circ\!\!\circ \psi^*_{i,k_2}(\omega_2)\psi_{j,k_2+q}(\omega_2+\nu)\psi^*_{l,k_1+q}(\omega_1+\nu)\psi_{n,k_1}(\omega_1) \circ\!\!\circ,\end{aligned} \tag{86}$$

$$\begin{aligned}\Gamma_4^{(e)} = &-\frac{dl}{2\pi^2} c_B^{\frac{1-2\theta}{\theta+1}} \int dx \frac{dk_1dk_2dqd\omega_1d\omega_2d\nu}{(2\pi)^6} e^{2i\gamma(k_1-k_2)qx} \frac{X_0|\Delta\omega^{(e)}|^{\frac{2}{\theta+1}}}{|\Delta\omega^{(e)}|^{\frac{\theta}{\theta+1}}} \\ &\times f^{(e)}\left[X_0|\Delta\omega^{(e)}|^{\frac{2}{\theta+1}}, \frac{q\,\mathrm{sgn}(\Delta\omega^{(e)})}{|c_B\Delta\omega^{(e)}|^{\frac{1}{\theta+1}}}, \frac{k_2-k_1}{|c_B\Delta\omega^{(e)}|^{\frac{1}{\theta+1}}}, \frac{\omega_2}{\Delta\omega^{(e)}}, \frac{\nu}{\Delta\omega^{(e)}}\right] \\ &\times V_{ij';l'n}V_{j'j;ll'} \circ\!\!\circ \psi^*_{i,k_2}(\omega_2)\psi_{j,k_2+q}(\omega_2+\nu)\psi^*_{l,k_1+q}(\omega_1+\nu)\psi_{n,k_1}(\omega_1) \circ\!\!\circ,\end{aligned} \tag{87}$$

$$\begin{aligned}\Gamma_4^{(f)} = &\frac{dl}{4\pi^2} c_B^{\frac{1-2\theta}{\theta+1}} \int dx \frac{dk_1dk_2dqd\omega_1d\omega_2d\nu}{(2\pi)^6} e^{2i\gamma(k_1-k_2)qx} \frac{X_0|\Delta\omega^{(f)}|^{2/(\theta+1)}}{|\Delta\omega^{(f)}|^{\theta/(\theta+1)}} \\ &\times f^{(f)}\left[X_0|\Delta\omega^{(f)}|^{\frac{2}{\theta+1}}, \frac{q}{|c_B\Delta\omega^{(f)}|^{\frac{1}{\theta+1}}}, \frac{k_2-k_1}{|c_B\Delta\omega^{(f)}|^{\frac{1}{\theta+1}}}, \frac{\omega_2}{\Delta\omega^{(f)}}, \frac{\nu}{\Delta\omega^{(f)}}, \mathrm{sgn}(\Delta\omega^{(f)})\right] \\ &\times V_{j'j;l'n}V_{ij';ll'} \circ\!\!\circ \psi^*_{i,k_2}(\omega_2)\psi_{j,k_2+q}(\omega_2+\nu)\psi^*_{l,k_1+q}(\omega_1+\nu)\psi_{n,k_1}(\omega_1) \circ\!\!\circ,\end{aligned} \tag{88}$$

where $\Delta\omega^{(e)} = \omega_2 - \omega_1$ and $\Delta\omega^{(f)} = \omega_1 + \omega_2 + \nu$. Here we suppress the reference to the x coordinate in $\psi_{i,k}(\omega,x)$ to simplify the notation. The universal crossover functions, $f^{(b,d,e,f)}$'s, are given by

$$\begin{aligned}f^{(b)}(s) = &\int_{-\infty}^{\infty} dy_1dy_2 \int_0^1 dt_1 \int_0^{1-t_1} dt_2 e^{2i\gamma c_B^{\frac{2}{\theta+1}} s y_1y_2} e^{-c_F s[t_1^{\frac{2}{\theta+1}} + t_1^{\frac{2}{\theta+1}} + (1-t_1-t_2)^{\frac{2}{\theta+1}}]} \\ &\times \frac{|y_1|}{|y_1|^{\theta+1} + |1-t_1|} \frac{|y_2|}{|y_2|^{\theta+1} + |1-t_2|},\end{aligned} \tag{89}$$

$$f^{(d)}(s,u,v) = \int_{-\infty}^{\infty} dy \int_0^1 dt e^{-c_F s[t^{\frac{2}{\theta+1}}+(1-t)^{\frac{2}{\theta+1}}]} e^{2i\gamma c_B^{\frac{2}{\theta+1}} suy} \frac{|y|}{|y|^{\theta+1}+|t+v|}, \tag{90}$$

$$f^{(e)}(s,u_1,u_2,v_1,v_2) = \int_{-\infty}^{\infty} dy \int_0^1 dt e^{-c_F s[t^{\frac{2}{\theta+1}}+(1-t)^{\frac{2}{\theta+1}}]} e^{2i\gamma c_B^{\frac{2}{\theta+1}} su_2 y} \frac{|y+u_1|}{|y+u_1|^{\theta+1}+|v_1-t|} \frac{|y|}{|y|^{\theta+1}+|v_1+v_2-t|}, \tag{91}$$

$$f^{(f)}(s,u_1,u_2,v_1,v_2,r) = \int_{-\infty}^{\infty} dy \int_0^1 dt e^{-c_F s[t^{\frac{2}{\theta+1}}+(1-t)^{\frac{2}{\theta+1}}]} e^{2i\gamma c_B^{\frac{2}{\theta+1}} sr(u_1+u_2+y)y} \frac{|y+u_1|}{|y+u_1|^{\theta+1}+|v_1-t|} \frac{|y|}{|y|^{\theta+1}+|v_1+v_2-t|}. \tag{92}$$

The absence of quantum corrections in Eqs. (83) and (85) is a consequence of the fact that the RPA diagrams are independent of X_0. All nonvanishing quantum corrections are proportional to X_0. Moreover, crossover functions are finite for $\theta > 1$. From dimensional ground, this implies that all quantum corrections come with an additional factor of momentum or frequency. Therefore, all quantum corrections in Fig. 18 are irrelevant relative to the terms that are already present in the effective action.

The scaling is easily determined from the scaling that leaves the Wilsonian effective action in Eq. (72) invariant. In order to put the cutoff structure to the original form after the coarse graining, we rescale frequency, x coordinate, y momentum, and the field as

$$\omega' = e^{zdl}\omega, \tag{93}$$

$$x' = e^{-dl}x, \tag{94}$$

$$k' = e^{\alpha dl}k, \tag{95}$$

$$\psi'_{i,k'}(\omega',x') = e^{\Delta_\psi dl}\psi_{i,k}(\omega,x). \tag{96}$$

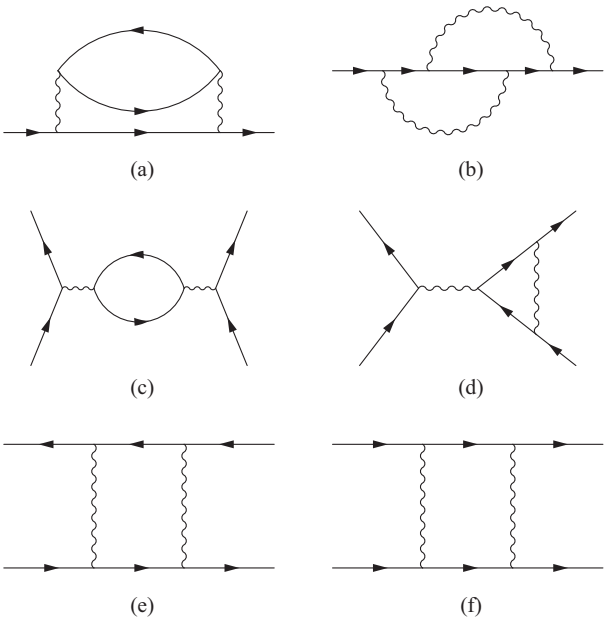

FIG. 18. The list of quantum corrections generated from the leading-order terms in the Wilsonian effective action at each step of coarse graining.

The dynamical critical exponent z, the scaling dimension of the fermion field Δ_ψ, and the dimension of y momentum α should be determined from the condition that the action is invariant. The condition that the marginal term $\psi^*\partial_x\psi$ should be scale invariant fixes the scaling dimension of the field to be

$$\Delta_\psi = -\tfrac{1}{2}(z+\alpha). \tag{97}$$

Then the β functions for c_F, c_B, γ, and $V_{ij;ln}$ are given by

$$\frac{dc_F}{dl} = \left(1-\frac{2z}{\theta+1}\right)c_F, \tag{98}$$

$$\frac{dc_B}{dl} = [\alpha(\theta+1)-z]c_B, \tag{99}$$

$$\frac{d\gamma}{dl} = (1-2\alpha)\gamma, \tag{100}$$

$$\frac{dV_{ij;ln}}{dl} = [1-z+\alpha(\theta-1)]V_{ij;ln}. \tag{101}$$

One can find a fixed point for the β functions if and only if we choose

$$\alpha = 1/2, \tag{102}$$

$$z = (\theta+1)/2. \tag{103}$$

This uniquely fixes the dynamical critical exponent and the scaling dimension of the field.

One can check that higher-order vertices that are generated from the quartic vertices are all irrelevant under the scaling in Eqs. (93)–(96). As an example, we compute the quantum correction where two quartic vertices fuse into a sixth-order vertex, as shown in Fig. 19. In the small X_0 limit,

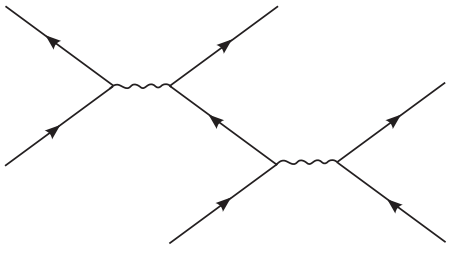

FIG. 19. A six-fermion vertex generated from two quartic vertices.

it becomes

$$\Gamma_6 = 4iX_0 dl \int \frac{dk_1 dk_2 dk_3 dq_1 dq_2 d\omega_1 d\omega_2 d\omega_3 d\nu_1 d\nu_2}{(2\pi)^{10}} dx\, e^{2i\gamma[(k_1-k_2)q_1+(k_3-k_1)q_2]x} \times \frac{V_{ij;ln'}V_{n'n;ms}}{|q_1|^\theta + c_B|\nu_1|/|q_1|} \frac{\mathrm{sgn}(\omega_1)}{|q_2|^\theta + c_B|\nu_2|/|q_2|} e^{-X_0[c_F|\omega_1|^{2/(\theta+1)}+2i\gamma\,\mathrm{sgn}(\omega_1)(k_1-k_3)q_2]} \times {}^\circ_\circ \psi^*_{i,k_2}(\omega_2,x)\psi_{j,k_2+q_1}(\omega_2+\nu_1,x)\psi^*_{l,k_1+q_1}(\omega_1+\nu_1,x)\psi_{n,k_1+q_2}(\omega_1+\nu_2,x)\psi^*_{m,k_3+q_2}(\omega_3+\nu_2,x)\psi_{s,k_3}(\omega_3,x){}^\circ_\circ . \quad (104)$$

According to the scaling in Eq. (103) and the expression of Δ_ψ in Eq. (97), this is irrelevant. This can be readily seen from the fact that the prefactor is proportional to X_0, which has scaling dimension -1. This is true for any higher-order vertices generated during the RG flow. Contributions from these higher-order vertices to the quadratic and quartic vertices are also irrelevant.

As expected, the scaling form in the chiral non-Fermi liquid state is fixed by the scaling in Eq. (36), where the interaction is kept invariant while the frequency-dependent term in the bare quadratic action is deemed strongly irrelevant. This implies that the theory flows to a strongly interacting non-Fermi liquid fixed point in the low-energy limit. It is remarkable that it is possible to obtain the exact scaling relation for the strongly interacting non-Fermi liquid fixed points. The scaling relation in Eq. (103) suggests that the exact fermion Green's function in the momentum space has the form

$$G^{-1}(k) = \delta_k\, g\left(\frac{|\omega|^{2/(\theta+1)}}{\delta_k}\right), \quad (105)$$

where $\delta_k = k_x + \gamma k^2$ and $g(x)$ is a universal function. Note that the one-loop Green's function obeys the scaling form in Eq. (105). In other words, chirality allows us to extract the scaling form of the exact Green's function, $G(k)$, from the one-loop Green's function. However, the dimensionless function $g(x)$ is not fixed by scaling, and the exact form of $g(x)$ can be, in principle, very different from what is inferred from the one-loop Green's function.

VIII. GENERAL PATCH THEORIES

The theory with the dynamical critical exponent $z = \frac{\theta+1}{2}$ captures the low-energy physics near the Fermi surface with nonzero quadratic curvatures. There exist special points where the quadratic curvature vanishes. In particular, the periodicity of the first Brillouin zone in the K_y direction guarantees that there exist inflection points as shown in Fig. 20. For example, the dispersion in Eq. (3) has two inflection points at $K_y = \pm\pi/2d$. In the neighborhood of one of the inflection points (say $K_y = -\pi/2d$), the dispersion can be written as $\epsilon_k = k_x - 2tdk_y + (td^3/3)k_y^3 + \mathcal{O}(k_y^5)$, where $\vec{k}$ is a deviation from the inflection point. Defining $k'_x = k_x - 2tdk_y$, $k'_y = k_y$, the local dispersion is written as

$$\epsilon_{k'} = k'_x + \gamma_3 {k'_y}^3, \quad (106)$$

with the cubic curvature given by $\gamma_3 = \frac{td^3}{3}$. Henceforth, we drop the prime in k'_x, k'_y. With some extra fine tuning, one can even have a higher inflection points with a local dispersion,

$$\epsilon_k = k_x + \gamma_u k_y^u, \quad (107)$$

with $u > 3$. Therefore, a general patch theory for chiral non-Fermi liquids can be parameterized by (u,θ),

$$S^{(u,\theta)} = \int \frac{d\omega d^2\vec{k}}{(2\pi)^3}\left(i\eta\omega + k_x + \gamma_u k_y^u\right)\psi^*_j(\omega,\vec{k})\psi_j(\omega,\vec{k}) + \frac{1}{2}\int \frac{d\nu d^2\vec{q}}{(2\pi)^3}\chi_\theta^{-1}(q)\phi_\alpha(-\nu,-\vec{q})\phi_\alpha(\nu,\vec{q}) + g\int \frac{d\omega d^2\vec{k}}{(2\pi)^3}\frac{d\nu d^2\vec{q}}{(2\pi)^3} \times \phi_\alpha(\nu,\vec{q})\psi^*_i(\omega+\nu,\vec{k}+\vec{q})T^\alpha_{ij}\psi_j(\omega,\vec{k}). \quad (108)$$

Here u is a positive integer greater than 1, and θ is an even integer for local theories.

A. UV finiteness and exact scaling

In this section, we show that each of the theory parameterized by (θ,u) in Eq. (108) describes a distinct and stable non-Fermi liquid fixed point for $1 < \theta < u + \frac{1}{2}$ and $u \geqslant 2$. For $\theta > u + \frac{1}{2}$, the theory should be modified by the $\lambda\phi^4$ term, which becomes relevant at the Gaussian fixed point. The RG analysis for general u is similar to that for the theory with $u = 2$ discussed in Secs. V–VII. In this section, we quickly recapitulate the key results from the previous sections that apply to general $u \geqslant 2$ and emphasize new features that are absent in the case with $u = 2$. In the mixed space of x coordinate and

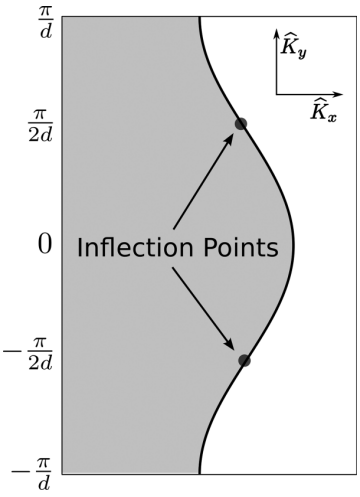

FIG. 20. Two inflections points on the chiral Fermi surface at which the quadratic curvature vanishes for the dispersion in Eq. (3).

frequency, the action is written as

$$S^{(u,\theta)} = \int \frac{dkd\omega}{(2\pi)^2} \int dx \psi^*_{i,k}(\omega,x)[i\eta\omega - i\partial_x]\psi_{i,k}(\omega,x) + \int \frac{dk_1dk_2dqd\omega_1d\omega_2d\nu}{(2\pi)^6} \int dx \exp\left[i\gamma_u x \sum_{m=1}^{u-1} \binom{u}{m} (k_1^m - k_2^m) q^{u-m}\right]$$
$$\times V_{ij;ln}\chi_\theta(q)\psi^*_{i,k_2}(\omega_2,x)\psi_{j,k_2+q}(\omega_2+\nu,x)\psi^*_{l,k_1+q}(\omega_1+\nu,x)\psi_{n,k_1}(\omega_1,x). \quad (109)$$

Again, k_i, q refer to y momenta. Two comments are in order for the general theory in Eq. (109). First, the phase factor in the quartic interaction includes u powers of y momenta, which is inherited from the dispersion in Eq. (107). As a result, the sliding symmetry associated with $\psi_{i,k} \to \psi_{i,k+\Delta k}$ is absent for $u > 2$. Second, the number of points with a common tangent vector determines the representation of the fermion field under the flavor group. For $u = 3$, the two inflection points have different tangent vectors, as shown in Fig. 20. Since the two are decoupled at low energies, only one point needs to be kept in the low-energy effective theory. As a result, one does not need to double the representation as in Eq. (8).

Now we consider the Wilsonian effective action with a running cutoff scale X_0, which is obtained by fusing operators whose separation in x direction is less than X_0. As is the case for $u = 2$ discussed in Sec. VI, the Wilsonian effective action is finite in the $\Lambda X_0^{1/2} \to \infty, \eta^{-1} X_0^{(\theta-1)/2} \to \infty$, and $\mu X_0^{1/2} \to 0$ limits. Since the integrations over internal frequencies are insensitive to the value of u, one can use the exactly same argument presented in Sec. VI B to show that they are finite: All internal frequencies are bounded by the external frequencies due to chirality. The integrations over y momenta are also UV convergent for $\theta > 1$. As is discussed in Sec. VI B 2, an integration over y momentum which goes through a boson propagator is UV convergent because it is suppressed as $q^{-\theta}$ at large momentum. The only exceptions are the fermion loops which are solely made of fermion propagators. This is because the fermion propagator does not depend on y momentum, and the integration over it diverges in the absence of the phase factor which cuts off the divergence. For example, the integration over y momentum in the RPA bubble reads

$$\int_{-\Lambda}^{\Lambda} dp \exp\left[i\gamma_u x_R \sum_{m=1}^{u-1} \binom{u}{m} p^m q^{u-m}\right] \sim \frac{1}{|qx_R|^{1/(u-1)}}, \quad (110)$$

in the $\Lambda \to \infty$ limit, where p is the y momentum that runs in the loop, q is the momentum transferred across the loop, and x_R is the relative coordinate between two vertices. The fact that the UV divergence from large y momenta is cut off by a length scale in the x direction is a consequence of the noncommutativity between the x coordinate and the y momentum as discussed in Sec. IV. Because $x_R \sim X_0$, this gives rise to a UV enhancement factor of $X_0^{-1/(u-1)}$ in the $X_0 \to 0$ limit for every fermion loop. Although Eq. (110) is singular in the $x_R \to 0$ limit, it is integrable for $u \geqslant 2$. (For $u = 2$, it gives rise to a δ-function for the relative coordinate.) Once the relative coordinate between vertices is integrated over, the RPA bubble is order of

$$\int_{-X_0}^{X_0} dx_R x_R^{-1/(u-1)} \sim X_0^{(u-2)/(u-1)} \quad (111)$$

for $u > 2$ and a constant independent of X_0 for $u = 2$.

Because the Wilsonian effective action is UV finite, one can take the $\Lambda X_0^{1/2} \to \infty, \eta^{-1} X_0^{(\theta-1)/2} \to \infty$ limit. Since there is no scale in the full quantum theory, the low-energy physics should be invariant under the scale transformation which leaves the rest of the terms in Eq. (109) invariant. In other words, the Wilsonian effective action should be invariant under the coarse graining $X_0 \to X_0 e^{dl}$ followed by a rescaling of the field and momenta dictated by the following scaling dimensions:

$$[x] = -1, \quad (112)$$
$$[k] = \frac{1}{u}, \quad (113)$$
$$z_{\theta,u} \equiv [\omega] = \frac{\theta + u - 1}{u}, \quad (114)$$
$$[\psi_i] = -\frac{\theta + u}{2u}, \quad (115)$$
$$[V] = 0, \quad (116)$$
$$[\eta] = -\frac{\theta - 1}{u}. \quad (117)$$

Equations (112)–(117) give the exact dynamical critical exponent and scaling dimensions.

B. The Wilsonian effective action

1. The RPA correction

In this section, we compute the Wilsonian effective action in the small X_0 limit. Let us estimate the magnitude of an operator generated by fusing V quartic vertices in the small X_0 limit. The fusion of V vertices involves $(V-1)$ relative coordinates that are integrated over the range of X_0. This leads to a factor of X_0^{V-1}. As is discussed in the previous section, each fermion loop gives rise to a UV enhancement factor of $X_0^{-1/(u-1)}$. This gives a net factor of

$$X_0^{V-1-L_f/(u-1)} \quad (118)$$

for a diagram with V vertices and L_f fermion loops. Indeed, Eq. (118) is the full answer for $u = 2$, as we have seen in in Sec. VI. For $u > 2$ we see that there are corrections to Eq. (118). To see this, we first consider the RPA diagrams which are largest in the small X_0 limit according to Eq. (118). The RPA bubble dresses the quartic vertex to (see Appendix C1 for derivation)

$$\chi^{(\mathrm{RPA})}_{u,\theta}(q,\nu,X_0) = \frac{1}{|q|^\theta + c_B^{(u)}(X_0)\xi_u[\mathrm{sgn}(\gamma_u \nu q)]\frac{|\nu|}{|q|^{1/(u-1)}}}, \quad (119)$$

with

$$c_B^{(u)}(X_0) = \left(\frac{g^2}{2\pi^2}\right)\frac{X_0^{(u-2)/(u-1)}}{|u\gamma_u|^{1/(u-1)}}. \tag{120}$$

The key difference from the $u=2$ case is that the RPA correction in the dressed quartic vertex vanishes in the $X_0 \to 0$ limit for $u > 2$ as shown in Eq. (111). It is crucial to include the leading quantum correction to the boson self-energy to dress the quartic vertex to cure the IR singularity as we have already seen in the $u=2$ case. Because the IR singularity is cut off by the RPA correction, which vanishes in the small X_0 limit, each integration over y momentum that goes through a boson propagator leads to an IR enhancement factor,

$$\int dq \frac{1}{|q|^\theta + c_B^{(u)}(X_0)\xi_u[\mathrm{sgn}(\gamma_u \nu q)]\frac{|\nu|}{|q|^{1/(u-1)}}} \sim X_0^{-(\theta-1)(u-2)/[\theta(u-1)+1]}. \tag{121}$$

Taking the IR enhancement factor into account, the naive power counting in Eq. (118) is modified as

$$X_0^{(V-1)+[-\frac{1}{u-1}]L_f+[-\frac{(\theta-1)(u-2)}{\theta(u-1)+1}]L_m} = X_0^{\frac{1}{2}(E-4)+\frac{u-2}{u-1}L_f+\frac{\theta+u-1}{\theta(u-1)+1}L_m}, \tag{122}$$

where L_m is the number of "mixed loops" that contain at least one boson propagator in contrast to fermion loops. We use the identity $V = \frac{E}{2} + L_m + L_f - 1$ and assume that only one boson propagator becomes singular at a time within each mixed loop. Since the coefficients of L_f and L_m are positive for $u > 2$, higher loop diagrams are suppressed in the small X_0 limit. For the fermion self-energy, the leading correction arises for $L_f = 0, L_m = 1, V = 1$ which is on the order of $X_0^{-\frac{(u-2)(\theta-1)}{\theta(u-1)+1}}$. See Appendix C 2 for an explicit computation of the leading correction to the quadratic action. Therefore, the Wilsonian effective action with the leading-order quantum corrections is written as

$$S_{X_0}^{(u,\theta)} = \int \frac{dk}{2\pi}\frac{d\omega}{2\pi}dx \circ \psi_{i,k}^*(\omega,x)\left[ic_F^{(u)}(X_0)\mathrm{sgn}(\omega)|\omega|^{\frac{u}{\theta(u-1)+1}} - i\partial_x\right]\psi_{i,k}(\omega,x) \circ + \int \frac{dk_1 dk_2 dq dv d\omega_1 d\omega_2}{(2\pi)^6}\int dx \times \frac{V_{ij;ln}\exp\left[i\gamma_u x\sum_{m=1}^{u-1}\binom{u}{m}(k_1^m - k_2^m)q^{u-m}\right]}{|q|^\theta + c_B^{(u)}(X_0)\xi_u[\mathrm{sgn}(\gamma_u\nu q)]\frac{|\nu|}{|q|^{1/(u-1)}}} \circ \psi_{i,k_2}^*(\omega_2,x)\psi_{j,k_2+q}(\omega_2+\nu,x)\psi_{l,k_1+q}^*(\omega_1+\nu,x)\psi_{n,k_1}(\omega_1,x) \circ, \tag{123}$$

where

$$c_F^{(u)}(X_0) \propto X_0^{-\frac{(u-2)(\theta-1)}{\theta(u-1)+1}}, \tag{124}$$

$$c_B^{(u)}(X_0) \propto X_0^{\frac{(u-2)}{(u-1)}}, \tag{125}$$

with

$$\xi_u[\mathrm{sgn}(\gamma_u\nu q)] = \begin{cases} \frac{u-1}{u-2}\int_0^\infty dy\cos(y^{u-1}) & \text{for even } u, \\ \frac{u-1}{u-2}\int_0^\infty dy e^{i\mathrm{sgn}(\gamma_u\nu q)y^{u-1}} & \text{for odd } u. \end{cases} \tag{126}$$

The expression in Eq. (126) is well defined for any $u \geqslant 2$. Note that ξ_u is complex for odd u and $\xi_u[\mathrm{sgn}(\gamma_u\nu q)] = \xi_u^*[-\mathrm{sgn}(\gamma_u\nu q)]$. This appears to break the inversion along the y direction under which q is mapped to $-q$. However, the full theory which includes the other patch with the opposite y momentum respects the inversion, as explained in Appendix C3.

It is noted that $c_F^{(u)}(X_0)$ in the fermion self-energy is singular in the $X_0 \to 0$ limit for $u > 2$, which reflects the fact that the IR divergence is cut off by the quantum correction, which vanishes in the $X_0 \to 0$ limit in Eq. (119). Although $c_F^{(u)}(X_0)$ diverges in the $X_0 \to 0$ limit for $u > 2$, its feedback to the Wilsonian effective action is subleading in the small X_0 limit. This can be seen from the dressed fermion propagator,

$$G(\omega,x_{12}) = -i\mathrm{sgn}(\omega)\Theta(-x_{12}\omega) \times \exp\left[-c_F^{(u)}(X_0)|x_{12}||\omega|^{\frac{u}{\theta(u-1)+1}}\right]. \tag{127}$$

Because $|x_{12}| < X_0$ for propagators that enter in OPE's for the Wilsonian effective action, we have $c_F^{(u)}(X_0)|x_{12}| < X_0^{\frac{\theta+u-1}{\theta(u-1)+1}} \to 0$ in the $X_0 \to 0$ limit. As a result, one can ignore the exponential factor in Eq. (127) to the leading order in X_0.

2. *Beyond the RPA correction*

Non-RPA corrections are suppressed in the small X_0 limit. For example, a non-RPA diagram with $L_f = 0$ and $L_m = 1$ shown in Fig. 21 contributes

$$\delta S_4^{(\mathrm{ph})} = -\int \frac{dk_1 dk_2 dq d\omega_1 d\omega_2 dv}{(2\pi)^6} dx\, V_{ij';l'n}V_{j'j;ll'} \times e^{i\gamma_u x\sum_{m=1}^{u-1}\binom{u}{m}(k_1^m - k_2^m)q^{u-m}}\Gamma^{(\mathrm{ph})}(k_1,k_2,q,\omega_1,\omega_2,\nu) \times \circ\, \psi_{i,k_2}^*(\omega_2,x)\psi_{j,k_2+q}(\omega_2+\nu,x) \times \psi_{l,k_1+q}^*(\omega_1+\nu,x)\psi_{n,k_1}(\omega_1,x)\, \circ, \tag{128}$$

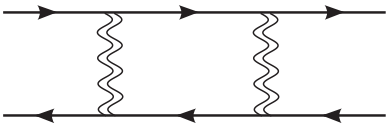

FIG. 21. A non-RPA contribution to the quartic vertex. The double wiggly line represents the RPA dressed quartic vertex.

where

$$\Gamma^{(\mathrm{ph})}(k_1,k_2,q,\omega_1,\omega_2,\nu) = \frac{1}{2\pi^2}\left[\frac{g^2}{2\pi^2|u\gamma_u|^{1/(u-1)}}\right]^{\frac{(u-1)(1-2\theta)}{\theta(u-1)+1}} X_0^{\frac{(\theta+1)-(\theta-1)(u-2)}{\theta(u-1)+1}} |\Delta\omega|^{\frac{1-(\theta-1)(u-1)}{\theta(u-1)+1}} \times f^{(\mathrm{ph})}\left[c_F X_0|\Delta\omega|^{\frac{u}{\theta(u-1)+1}}, \gamma_u \mathrm{sgn}(\Delta\omega) X_0\left(c_B^{(u)}|\Delta\omega|\right)^{\frac{u(u-1)}{\theta(u-1)+1}}, \frac{q}{\left(c_B^{(u)}|\Delta\omega|\right)^{\frac{u-1}{\theta(u-1)+1}}}, \frac{k_1}{\left(c_B^{(u)}|\Delta\omega|\right)^{\frac{u-1}{\theta(u-1)+1}}}, \frac{k_2}{\left(c_B^{(u)}|\Delta\omega|\right)^{\frac{u-1}{\theta(u-1)+1}}}, \frac{\nu}{\Delta\omega}, \frac{\omega_2}{\Delta\omega}\right], \tag{129}$$

with $\Delta\omega = \omega_1 - \omega_2$ and

$$f^{(\mathrm{ph})}(s_1,s_2,u_1,u_2,u_3,v_1,v_2) = \int_0^1 dxdt \int_{-\infty}^{\infty} dy e^{is_2x\sum_{m=1}^{u-1}\binom{u}{m}(u_2^m-u_3^m)y^{u-m}} e^{-s_1x[t^{\frac{u}{\theta(u-1)+1}}+(1-t)^{\frac{u}{\theta(u-1)+1}}]} \times \frac{|y-u_1|^{\frac{1}{u-1}}}{|y-u_1|^{\theta+\frac{1}{u-1}} + \xi_u(\mathrm{sgn}(\gamma_u(t+v_1+v_2)(y-u_1)))\,|t+v_1+v_2|} \times \frac{|y|^{\frac{1}{u-1}}}{|y|^{\theta+\frac{1}{u-1}} + \xi_u(\mathrm{sgn}(\gamma_u(t+v_2)y))\,|t+v_2|}. \tag{130}$$

Here, $\xi_u(x) = \xi_u[x]$ as in Eq. (126). Since the crossover function has complicated dependence on the dimensionless parameters, let us consider a particular limit to compare with the RPA correction. We consider the small frequency limit with fixed y momenta, where $s_i \ll 1$, $u_i \gg 1$ and $v_i \sim 1$. In this limit, the crossover function becomes

$$f^{(\mathrm{ph})}(0,0,u_1,u_2,u_3,v_1,v_2) \sim |u_1|^{-\theta}, \tag{131}$$

resulting in the quantum correction,

$$\Gamma^{(\mathrm{ph})}(k_1,k_2,q,\omega_1,\omega_2,\nu) \sim \left[\frac{g^2}{|\gamma_u|^{1/(u-1)}}\right]^{\frac{(u-1)(1-2\theta)}{\theta(u-1)+1}} (X_0|\Delta\omega|^{\frac{u}{\theta+u-1}})^{\frac{\theta+u-1}{\theta(u-1)+1}} |q|^{-\theta}. \tag{132}$$

This is smaller than the RPA dressed vertex in Eq. (123) in the limit under consideration.

There are diagrams which do not obey the counting in Eq. (122). For example, the diagram shown in Fig. 22 has a smaller power of X_0 than predicted in Eq. (122). In this diagram, there are two boson propagators (the ones outside the box in Fig. 22), which carry exactly same momentum. In the absence of the RPA correction to the quartic vertex, the two boson propagators become singular simultaneously. As a result, the integration over the y momentum that goes through the two boson propagators has a larger IR enhancement factor than predicted in Eq. (121). However, we cannot consider this diagram by itself because it is part of an infinite series of diagrams as shown in Fig. 23. The quartic vertex dressed by higher-loop boson self-energies can be written as

$$\int \frac{dk_1dk_2dqd\omega_1d\omega_2d\nu}{(2\pi)^6} dx \frac{V_{ij;ln}}{|q|^\theta + \Pi(k_1,k_2,q,\nu,X_0)} \times e^{i\gamma_u x\sum_{m=1}^{u-1}\binom{u}{m}(k_1^m-k_2^m)q^{u-m}} \times \circ\circ \psi^*_{i,k_2}(\omega_2,x)\psi_{j,k_2+q}(\omega_2+\nu,x) \times \psi^*_{l,k_1+q}(\omega_1+\nu,x)\psi_{n,k_1}(\omega_1,x) \circ\circ, \tag{133}$$

where

$$\Pi(k_1,k_2,q,\nu,X_0) = \Pi_u(k_1,q,\nu,X_0) + \Pi_{n\mathrm{RPA}}(k_1,k_2,q,\nu,X_0). \tag{134}$$

Here Π_u is the RPA correction defined in Eq. (C5) and $\Pi_{n\mathrm{RPA}}$ represents the corrections beyond the RPA level. $\Pi_{n\mathrm{RPA}}$ includes the subdiagram inside the box in Fig. 22. The one-particle irreducible non-RPA correction is suppressed compared to Π_u according to Eq. (122). Therefore, the RPA diagram dominates in the small X_0 limit.

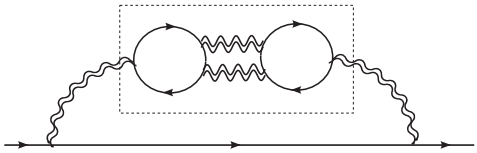

FIG. 22. A diagram where two quartic vertices (boson propagator) outside the box carry a same momentum. The double wiggly line represents the RPA dressed quartic vertex.

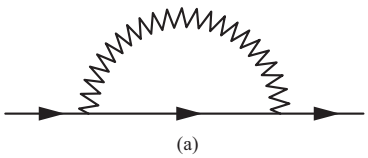

(a)

(b)

FIG. 23. (a) The diagram in Fig. 22 is a part of the "one-loop" fermion self-energy. (b) The zigzag line in (a) represents the quartic vertex dressed with an infinite series of the three-loop boson self-energy drawn inside the box in Fig. 22.

Although the diagram in Fig. 23(a) is consistent with Eq. (122), we do not have a systematic way of computing the exact dependence on X_0 for general diagrams. However, we emphasize that the scaling dimensions in Eq. (117) hold exactly irrespective of the magnitudes of individual diagrams in the small X_0 limit.

IX. THERMODYNAMIC RESPONSE

One full Fermi surface generally includes multiple patch theories with different values of u that belong to different universality classes. What is then the thermodynamic response of the whole system? Here we consider the case where the quadratic curvature is nonzero except for an isolated inflection point of the uth order.

Suppose there is an inflection, $\mathcal{P}^* \equiv (K_x^*, K_y^*)$ at which the fermion dispersion goes as $\epsilon_k = k_x + k_y^u$. The uth curvature γ_u is scaled to be 1. Let us consider a point $\mathcal{P}$ on the Fermi surface near $\mathcal{P}^*$. Let q be the difference in the y momentum between $\mathcal{P}$ and $\mathcal{P}^*$. The local energy dispersion around $\mathcal{P}$ includes the lower-order terms as

$$\epsilon_k = k_x + \sum_{n=2}^{u-1} \gamma_n(q) k_y^n + k_y^u, \tag{135}$$

where the term linear in k_y is absorbed into a redefinition of k_x, and the lower-order curvatures go to zero near $\mathcal{P}^*$ as $\gamma_n(q) = \tilde{\gamma}_n q^{u-n}$ with $\tilde{\gamma}_n \sim 1$. Consider the free-energy density per unit y momentum at temperature T : $\tilde{f}(T,q)$ is the contribution to the free-energy density from a unit segment of the Fermi surface at point $\mathcal{P}$. The total free-energy density is given by an integration over the momentum along the Fermi surface [42,50],

$$f(T) = \int_{-\Lambda}^{\Lambda} dq\, \tilde{f}(T,q), \tag{136}$$

where Λ is a UV cutoff set by the size of the Fermi surface. Equation (136) is a consequence of the fact that the y momentum q has a positive scaling dimension and the theory is local in the momentum space [51]. The scaling at the inflection point, $\mathcal{P}^*$, fixes the form of the free-energy density to be

$$\tilde{f}(T,q) = T^{1+1/z_{\theta,u}} h\left(\frac{q^u}{T^{1/z_{\theta,u}}}, \tilde{\gamma}_n\right). \tag{137}$$

Here we use the fact that the lower-order curvatures $\gamma_n(q)$'s are relevant perturbations with the scaling dimension $(u-n)/u$ to the inflection point which is described by the theory with the dynamical critical exponent $z_{\theta,u}$. $h(x)$ is a universal function that describes the crossover from the high-temperature scaling controlled by the inflection point to the low-temperature scaling controlled by the points with nonzero quadratic curvatures. Its asymptotic behaviors are given by

$$h(x,\tilde{\gamma}_n) \sim 1 \quad \text{for} \quad x \to 0, \tag{138}$$

$$h(x,\tilde{\gamma}_n) \sim x^{\frac{(u-2)(\theta-1)}{u(\theta+1)}} \quad \text{for} \quad x \to \infty. \tag{139}$$

Equation (138) is determined from the fact that the scaling dimension of $\tilde{f}(T,q=0)$ is $z_{\theta,u}+1$ at the inflection point, whereas Eq. (139) follows from the fact that $\tilde{f}(T,q) \to T^{1+1/z_{2,\theta}}$ in the $T \to 0$ limit with $\tilde{\gamma}_2 \neq 0$. If there was a hierarchy in the magnitudes of $\tilde{\gamma}_n$, there could be multiple crossovers. However, in this case, there is only one crossover from the multicritical point dictated by dispersion k_y^u to the critical point with dispersion k_y^2 because $\tilde{\gamma}_n \sim 1$ for all n, and the quadratic term is most relevant. Upon integrating along the Fermi surface, we obtain two universal terms for the free-energy density,

$$\begin{aligned} f(T) &\sim T^{1+\frac{1}{z_{\theta,u}}} \int_0^{T^{\frac{1}{uz_{\theta,u}}}} dq + T^{1+\frac{1}{z_{\theta,2}}} \int_{T^{\frac{1}{uz_{\theta,u}}}}^{\Lambda} dq q^{\frac{(u-2)(\theta-1)}{(\theta+1)}} \\ &\sim A T^{\frac{\theta+3}{\theta+1}} + B T^{\frac{\theta+2u}{\theta+u-1}}, \end{aligned} \tag{140}$$

where A, B are constants. The A term is the contribution from the extended region with nonzero quadratic curvatures, whereas the B term is from the region near the inflection point. Therefore, the specific heat scales as

$$c \sim A T^{\frac{2}{\theta+1}} + B T^{\frac{u+1}{\theta+u-1}}, \tag{141}$$

where the first term dominates in the low-temperature limit. In the presence of the most generic inflection point with $u=3$ for the quadratic dispersion of boson with $\theta=2$, the specific heat of the whole system goes as

$$c \sim A T^{\frac{2}{3}} + B T^{1}. \tag{142}$$

This analysis can be extended to other physical responses.

X. SUMMARY AND DISCUSSIONS

In this paper we considered a class of non-Fermi liquid states without time-reversal and parity symmetries in $(2+1)$ dimensions. The chiral non-Fermi liquid states can be potentially realized at quantum critical points where two-dimensional chiral Fermi surface is coupled with a critical boson associated with a spontaneous symmetry breaking. Chiral Fermi surface naturally arises on a stack of quantum Hall layers [45] or on the surface of three-dimensional Weyl metals [52–55]. The former example, however, is simpler because there are no gapless bulk degrees of freedom. In principle, chiral metals with multiple flavors can be realized by one stack of quantum Hall layers with $\nu > 1$. Alternatively, multiple chiral modes can arise at a junction of semiconductors with oppositely charged carriers in a uniform magnetic field.

In two-dimensional non-Fermi liquid states, the local patch description is valid due to the emergent locality in the momentum space [51]. General patch theories for the chiral non-Fermi liquid states can be classified by the local shape of the Fermi surface, the dispersion of the critical boson and the symmetry group. Although the non-Fermi liquid fixed points are described by strongly interacting quantum field theories, the stability of the fixed points can be established nonperturbatively, and the exact critical exponents can be computed. The main ingredient that makes an exact analysis possible is the chiral nature of the theory. Because of chirality, internal frequencies in scattering processes are strictly bounded by the external frequencies. Exploiting this property, it is possible to prove that the theory is UV finite below the upper critical dimension, which is the case for non-Fermi liquid states. The absence of UV divergence guarantees that the theory flows to a fixed point governed by the scaling which leaves

the interaction invariant in the bare action. We also confirm the general conclusion by computing the Wilsonian effective action explicitly in the low-momentum/frequency limit with a fixed running cutoff.

For the RG analysis, we formulate the low-energy excitations near the Fermi surface as a collection of one-dimensional fermions with a continuous flavor labeling the momentum along the Fermi surface. In this formalism, the curvature of the Fermi surface manifests itself through a noncommutative structure between a coordinate and momentum in different directions. The emergent noncommutativity leads to a UV/IR mixing in Fermi liquid states, where IR (UV) behavior of the system is sensitively controlled by UV (IR) structures. On the other hand, there is no prominent UV/IR mixing in non-Fermi liquid states due to the UV finiteness of the theory. The absence of nontrivial UV/IR mixing is what makes the patch description valid in the non-Fermi liquid states.

The chiral non-Fermi liquid states are two-dimensional cousins of the chiral Luttinger liquids in one dimension [44] whose stability is guaranteed by the absence of back scatterings. In the chiral Luttinger liquids, the scaling dimension of the fermionic operator is solely determined from the topological property of the system, independent of the microscopic details. Similarly, in the chiral non-Fermi liquids, the critical exponents only depend on the geometrical properties of the local Fermi surface and the dispersion of the critical boson. This is the reason why exact dimensions can be obtained.

Despite the similarity, the two-dimensional state cannot be obtained from a finite number of coupled one-dimensional chains. This is because the low-energy limit and the limit of infinite chains do not commute. The two-dimensional non-Fermi liquid state is obtained when one takes the limit of infinite chains before taking a low-energy limit. This is manifest from the fact that the momentum along the Fermi surface is continuous, and it has a nontrivial scaling dimension.

ACKNOWLEDGMENTS

We thank Djordje Minic, Subir Sachdev, Luiz Santos, T. Senthil, and Xiao-Gang Wen for helpful comments and discussions. The research was supported in part by the Natural Sciences and Engineering Research Council of Canada, the Early Research Award from the Ontario Ministry of Research and Innovation, and the Templeton Foundation. Research at the Perimeter Institute is supported in part by the Government of Canada through Industry Canada and by the Province of Ontario through the Ministry of Research and Information.

APPENDIX A: UV/IR MIXING

In this Appendix we compute the one-loop vertex function shown in Fig. 4. In this section, we focus on the critical point with $\mu = 0$. The one-loop vertex correction describes a process where a boson with $(\omega_p, \vec{p})$ creates a virtual particle-hole pair at $(\omega_k + \omega_p + \nu, \vec{k} + \vec{p} + \vec{q})$ and $(\omega_k + \nu, \vec{k} + \vec{q})$, which then scatter into the final state of a particle-hole pair with $(\omega_k + \omega_p, \vec{k} + \vec{p})$ and $(\omega_k, \vec{k})$. For convenience, we assume that $\vec{k} = 0, \omega_k = 0$ and the outgoing fermion is also on the Fermi surface; that is, $\epsilon_{k+p} = 0$. Then the resulting vertex function is a function of ω_p and p_y. In order to examine the interplay between UV and IR scales, we assume that the largest momentum along the Fermi surface is given by a finite UV cutoff Λ. As we see below, the Fermi liquid states with $\theta < 1$ and the non-Fermi liquid states with $\theta > 1$ show distinct behavior in terms of UV/IR mixing. In this Appendix, we use the conventional energy-momentum space representation.

First we consider the Fermi liquids with $\theta < 1$. We assume that the Yukawa coupling g is small and use the one-loop dressed propagators given by

$$G^{-1}(\omega, \vec{k}) = i c_F \omega + k_x + \gamma k_y^2, \tag{A1}$$

$$D^{-1}(\nu, \vec{q}) = |q_y|^\theta + c_B \frac{|\nu|}{|q_y|}, \tag{A2}$$

where c_F, c_B are constants. The one-loop vertex correction with $\vec{k} = \omega_k = 0$ and $\epsilon_p = 0$ is given by

$$\begin{aligned} &\Gamma_\theta(\omega_p, p_y; \Lambda) \\ &= g^3 \int \frac{d\nu d^2\vec{q}}{(2\pi)^3} G(\nu, \vec{q}) G(\omega_p + \nu, \vec{p} + \vec{q}) D(\nu, \vec{q}) \qquad \text{(A3)} \\ &= \frac{g^3}{2\pi^2} \frac{\Lambda^{1-\theta}}{c_F} \Upsilon_\theta(\alpha, L), \qquad \text{(A4)} \end{aligned}$$

where the crossover function is

$$\Upsilon_\theta(\alpha, L) = \frac{\alpha^2}{L^{1-\theta}} \int_0^L dy \frac{y}{y^2 + \alpha^2} \log\left(1 + \frac{1}{y^{\theta+1}}\right), \tag{A5}$$

with

$$L = \frac{\Lambda}{(c_B |\omega_p|)^{1/(\theta+1)}}, \tag{A6}$$

$$\alpha = \frac{c_F \mathrm{sgn}(\omega_p)}{2\gamma c_B^{1/(\theta+1)}} \frac{|\omega_p|^{\theta/(\theta+1)}}{p_y}. \tag{A7}$$

Here L and $1/\alpha$ correspond to the UV cutoff and the external y momentum scaled by the energy.

Now we examine the behavior of the vertex function as a function of p_y. Suppose that ω_p and Λ are fixed such that $L \gg 1$. A typical shape of the crossover function is shown in Fig. 24 for a fixed value of L. In the large p_y limit with $L \gg 1 \gg |\alpha|$, the vertex correction vanishes as

$$\Gamma_\theta(\omega_p, p_y; \Lambda) \sim \frac{c_F g^3}{c_B \gamma^2} \frac{|\omega_p|}{p_y^2} \log^2\left(\frac{c_F |\omega_p|^{\theta/(\theta+1)}}{\gamma c_B^{1/(\theta+1)} |p_y|}\right). \tag{A8}$$

As p_y decreases, α grows. For an intermediate regime with $L \gg |\alpha| \gg 1$, the vertex correction becomes

$$\Gamma_\theta(\omega_p, p_y; \Lambda) \sim \frac{g^3}{c_F} \left[\frac{c_F}{\gamma}\right]^{1-\theta} \left|\frac{\omega_p}{p_y}\right|^{1-\theta}. \tag{A9}$$

As p_y decreases, the vertex function tends to diverge as the number of virtual particle-hole pairs that can be excited within the energy provided by the boson increases. When the energy of the boson is ω_p, the range of q_y that the virtual particle and hole can take in the loop is given by $q_y \leqslant \frac{\omega_p}{2\gamma p_y}$, as shown in Fig. 5(a). This follows from the condition $\epsilon_{q+p} - \epsilon_q \leqslant \omega_p$. The volume of the phase space for the virtual excitations increases as p_y decreases. However, q_y is eventually bounded by Λ in the presence of the UV cutoff, and the vertex function

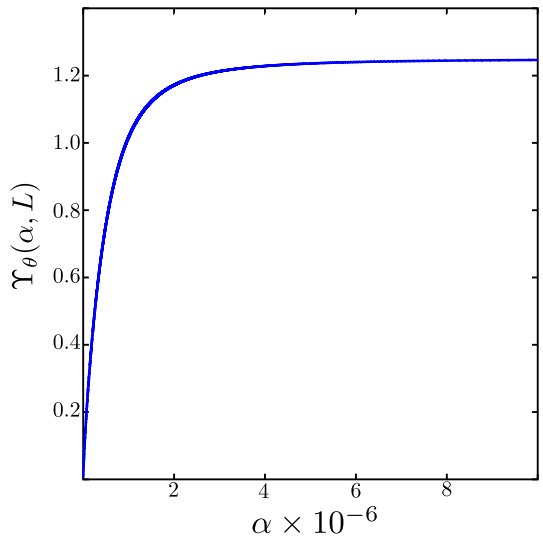

FIG. 24. (Color online) Plot of $\Upsilon_\theta(\alpha, L)$ as a function of α with $L = 10^6$ and $\theta = 0.2$.

saturates to a constant as

$$\Gamma_\theta(\omega_p, p_y; \Lambda) \sim \frac{g^3}{c_F} \Lambda^{1-\theta} \tag{A10}$$

in the small p_y limit with $\alpha \gg L \gg 1$. In other words, the maximum value of y momentum that virtual particles can have is determined by the condition

$$q_y^{\max} \sim \min\left(\frac{\omega_p}{\gamma p_y}, \Lambda\right). \tag{A11}$$

For $\frac{\omega_p}{\gamma p_y} \ll \Lambda$, the phase space of the virtual particle-hole excitations is controlled by the external momentum p_y. In the opposite limit, the UV-cutoff bounds the phase space. The two limits are illustrated in Fig. 5. From Eq. (A11), it is evident that $p_y \to 0$ and $\Lambda \to \infty$ limits do not commute.

It is interesting to note that the IR singularity that is present in Eq. (A9) is eventually cutoff by an IR scale $\tilde{p}_y \sim \frac{\omega_p}{\gamma \Lambda}$ which is set by the inverse of the UV cutoff Λ. This is a manifestation of UV/IR mixing where the IR behavior of the vertex function depends on the UV structure in a singular manner. The UV/IR mixing can be understood from a different perspective. For fixed ω_p, the vertex function tends to diverge as Λ increases as far as $\Lambda \ll \frac{\omega_p}{\gamma p_y}$, as shown in Eq. (A10). However, the UV divergence is cutoff by a scale $\tilde{\Lambda} \sim \frac{\omega_p}{\gamma p_y}$, which is set by the inverse of the IR scale p_y. This nontrivial interplay between UV and IR scales is a consequence of the fact that the low-energy fermions near $\vec{k} = 0$ "feel" the presence of other modes which carry large momenta. This situation commonly arises in quantum field theories above the upper critical dimensions. What is peculiar about the present case is that modes with large momenta are not necessarily high-energy modes because gapless modes on the Fermi surface can carry large momenta. Therefore, the modes at large momenta affect the low-energy behavior in a singular way. This is the origin of the UV/IR mixing.

In the Fermi liquids, the UV/IR mixing is driven by the UV sensitive volume of the phase space for low-energy particle-hole excitation available near the Fermi surface. In the non-Fermi liquid state with $\theta > 1$, on the other hand, the couplings that are nonlocal in momentum space are suppressed. This is due to the fact that the energy of boson increases steeply at large momentum. As a result, the intermediate states of particle-hole pairs with large momenta get dynamically suppressed, although those states are equally available as in Fermi liquids. This makes the vertex correction to be insensitive to the virtual processes occurring at large momenta. Therefore, the UV cutoff is not important to the low-energy processes for $\theta > 1$. To see this explicitly, we use the one-loop dressed fermion propagator,

$$G^{-1}(\omega, \vec{k}) = i c_F \mathrm{sgn}(\omega) |\omega|^{2/(\theta+1)} + \epsilon_k, \tag{A12}$$

to compute the vertex correction,

$$\Gamma_\theta(\omega_p, p; \Lambda) = \frac{g^3 c_B^{\frac{1-\theta}{\theta+1}}}{2\pi^2 c_F} \alpha^2 \int_0^1 dt \int_0^L dy \frac{y}{y^{\theta+1} + t} \times \frac{(1-t)^{\frac{2}{\theta+1}} + t^{\frac{2}{\theta+1}}}{y^2 + \alpha^2 \left[(1-t)^{\frac{2}{\theta+1}} + t^{\frac{2}{\theta+1}}\right]^2}, \tag{A13}$$

with

$$\alpha = \frac{c_F \mathrm{sgn}(\omega_p)}{2\gamma c_B^{1/(\theta+1)}} \frac{|\omega_p|^{1/(\theta+1)}}{p_y} \tag{A14}$$

and L is as defined in Eq. (A6). In Eq. (A13), the integration is convergent in the large L limit even when $p_y = 0$ unlike the case in Fermi liquids. For $L, \alpha \gg 1$, the vertex function saturates to a constant,

$$\Gamma_\theta(\omega_p, p) \sim \frac{1}{c_F c_B^{\frac{\theta-1}{\theta+1}}}, \tag{A15}$$

independent of the ratio $\frac{\omega_p}{\gamma p_y \Lambda}$ in contrast to the nontrivial crossover that is present in Fermi liquid state. In this case there is no UV/IR mixing in the vertex function. The insensitivity of the physics near $\vec{k} = 0$ to the gapless modes at large momenta is the reason for the emergent locality in the momentum space [51]. As a result, one can use the patch description in non-Fermi liquid states. On the contrary, all low-energy modes remain coupled with each other in the Fermi liquid state, and one has to keep the entire Fermi surface in the low-energy description. Landau Fermi liquid theory indeed includes Landau parameters associated with the forward scattering across the entire Fermi surface as the low-energy data.

APPENDIX B: THE RPA CORRECTION FOR THE PARABOLIC FERMI SURFACE

In this section we compute the RPA vertex correction and the RPA self-energy and derive the expressions for c_B and c_F in Eqs. (60) and (65), respectively.

1. RPA vertex correction

The four-fermion vertex correction generated from the L-loop RPA diagram shown in Fig. 14(a) is written as

$$\delta S_4^{(\mathrm{RPA},L)} = \int \frac{dk_1 d\omega_1 dk_2 d\omega_2 dq d\nu}{(2\pi)^6} dx_1 e^{2i\gamma(k_1-k_2)qx_1} V_{ij;ln}\chi_\theta(q) \sum_{\alpha=1}^{(L+1)!} \int_{\mathcal{C}_\alpha} \prod_{i=1}^{L} dx_{i+1,i}$$
$$\times \left[-\frac{g^2}{4\pi^2}\chi_\theta(q)\right]^L \prod_{j=1}^{L}\left[\int d\omega_j dp_j e^{2i\gamma x_{j+1,j}(k_1-p_j)q} G_0(\omega_j, -x_{j+1,j}) G_0(\omega_j+\nu, x_{j+1,j})\right]$$
$$\times \,^{\circ}_{\circ}\, \psi^*_{i,k_2}(\omega_2,x_1)\psi_{j,k_2+q}(\omega_2+\nu,x_1)\psi^*_{l,k_1+q}(\omega_1+\nu,x_{L+1})\psi_{n,k_1}(\omega_1,x_{L+1}) \,^{\circ}_{\circ}\,. \tag{B1}$$

Here x_i is the coordinate of the ith vertex in the chain of RPA bubbles and $x_{i+1,i} = x_{i+1} - x_i$. $\mathcal{C}_\alpha$ represents nonoverlapping sets of configurations of the x coordinates of the vertices whose separations from their neighboring vertices are less than X_0. For example, when there are three vertices at x_1, x_2, and x_3, there exist six distinct sets of configurations given by

$$\begin{aligned}
\mathcal{C}_1 &= \{(x_1,x_2,x_3)|x_1 > x_2 > x_3\},\\
\mathcal{C}_2 &= \{(x_1,x_2,x_3)|x_1 > x_3 > x_3\},\\
&\vdots\\
\mathcal{C}_6 &= \{(x_1,x_2,x_3)|x_3 > x_2 > x_1\}.
\end{aligned} \tag{B2}$$

In the present case, only two of the $(L+1)!$ sets contribute to the diagram due to the chiral nature of the theory. To see this, we first deduce the constraints on the relative coordinates of the vertices. From the Θ functions in the propagators, we have

$$-\nu x_{j+1,j} > \omega_j x_{j+1,j} > 0. \tag{B3}$$

These inequalities not only put a bound on the internal frequencies $\{\omega_j\}$, but also impose constraints on relative coordinates $\{x_{ij}\}$: for any pair $\{ij\}$ with $i > j$, x_i and x_j are strictly ordered depending on the sign of ν; i.e.,

(i) $x_{L+1} > x_L > \cdots > x_2 > x_1$ for $\nu < 0$,
(ii) $x_{L+1} < x_L < \cdots < x_2 < x_1$ for $\nu > 0$.

The implication of the strict ordering is that for a fixed ν all x_{ij} possess the same sign and $|x_{ij}| \in (0, X_0]$. The integration over each p_j leads to a δ-function whose support is localized in the neighborhood of $x_{j+1} = x_j$. The width of the δ-function goes to zero in the limit where the UV cutoff of p_j's is sent to ∞. As a result, the RPA diagram generates a vertex which is ultralocal in the x direction,

$$\delta S_4^{(\mathrm{RPA},L)} = \int \frac{dk_1 d\omega_1 dk_2 d\omega_2 dq d\nu}{(2\pi)^6} dx\, e^{2i\gamma(k_1-k_2)qx}$$
$$\times V_{ij;ln}\chi_\theta(q)\Gamma_4^{(\mathrm{RPA},L)}(q,\nu,X_0)$$
$$\times \,^{\circ}_{\circ}\, \psi^*_{i,k_2}(\omega_2,x)\psi_{j,k_2+q}(\omega_2+\nu,x)\psi^*_{l,k_1+q}$$
$$\times (\omega_1+\nu,x)\psi_{n,k_1}(\omega_1,x) \,^{\circ}_{\circ}\,, \tag{B4}$$

where

$$\Gamma_4^{(\mathrm{RPA},L)}(q,\nu,X_0) = \left\{\left[-\frac{g^2}{4\pi^2}\chi_\theta(q)\right]|\nu|\int_{-\infty}^{\infty} dp \right.$$
$$\left. \times \int_0^{X_0} dx_R e^{-2i\gamma\,\mathrm{sgn}(\nu)x_R(p-k_1)q} e^{-\eta|x_R||\nu|}\right\}^L$$
$$\equiv [-\Pi_2(q,\nu,X_0)\chi_\theta(q)]^L, \tag{B5}$$

with

$$\Pi_2(q,\nu,X_0) = \left(\frac{g^2}{4\pi^2}\right)|\nu|\int_0^{X_0} dx_R$$
$$\times \int_{-\infty}^{\infty} dp e^{-2i\gamma\,\mathrm{sgn}(\nu)x_R pq} e^{-\eta|x_R||\nu|} \tag{B6}$$
$$= \left(\frac{g^2}{4\pi^2}\right)|\nu|\frac{\pi}{\gamma|q|} \times \frac{1}{2}\int_{-X_0}^{X_0} dx_R \delta(x_R) e^{-\eta|x_R||\nu|} \tag{B7}$$
$$= c_B \frac{|\nu|}{|q|} \tag{B8}$$

and

$$c_B = \frac{g^2}{8\pi\gamma}. \tag{B9}$$

It is noted that the dependence of $\Gamma_4^{(L)}$ on k_1 drops out as k_1 is absorbed into the p in Eq. (B5).

2. RPA self-energy

The quantum correction generated from the L-loop RPA diagrams shown in Fig. 14(b) is

$$\delta S_2^{(\mathrm{RPA},L)} = \int \frac{dk d\omega}{(2\pi)^2} dx_1\, \Sigma_{ab}^{(\mathrm{RPA},L)}(k,\omega) \,^{\circ}_{\circ}\, \psi^*_{a,k}(\omega,x_1)$$
$$\times \psi_{b,k}(\omega,x_1) \,^{\circ}_{\circ}\,, \tag{B10}$$

where

$$\Sigma_{ab}^{(\mathrm{RPA},L)}(k,\omega) = 2^{L+1} V_{al_1;j_1 i_1} V_{i_1 j_1;j_2 i_2} \cdots V_{i_L j_L;l_1 b} \int \frac{dq d\nu}{(2\pi)^2}$$
$$\times \int_{\mathcal{C}} \prod_{l=1}^{L} [dx_{l+1,l} P_2(q,\nu,x_{l+1,l})][\chi_\theta(q)]^{L+1}$$
$$\times G_0(\omega+\nu, -x_{L+1,1}), \tag{B11}$$

with

$$P_2(q,\nu,x_{l+1,l}) = \int \frac{dp_l d\nu_l}{(2\pi)^2} e^{2i\gamma q(k-p_l)x_{l+1,l}} G_0(\nu+\nu_l, x_{l+1,l})$$
$$\times G_0(\nu_l, -x_{l+1,l}) \tag{B12}$$
$$= |\nu|\Theta(-\nu x_{l+1,l}) \int \frac{dp_l}{(2\pi)^2} e^{2i\gamma q p_l x_{l+1,l}} e^{-\eta|x_{l+1,l}\nu|}. \tag{B13}$$

The product of the V's in Eq. (B11) yields

$$V_{al_1;j_1i_1}\cdots V_{i_Lj_L;l_1b}=\delta_{ab}\left(-\frac{g^2v}{2}\right)\left(-\frac{g^2}{2}\right)^L, \quad \text{(B14)}$$

where v is defined in Eq. (24). Before integrating over y momentum p_l in Eq. (B13), we use the constraints imposed by the $(L+1)$ Θ functions in Eq. (B11) to write

$$\begin{aligned}&\int_C\prod_{l=1}^{L}[dx_{l+1,l}\Theta(-x_{l+1,l}v)]\Theta(x_{L+1,1}(v+\omega))\\&=\Theta(v)\Theta(-v-\omega)\int_{-X_0}^{0}\prod_{l=1}^{L}dx_{l+1,l}\\&\quad+\Theta(-v)\Theta(v+\omega)\int_{0}^{X_0}\prod_{l=1}^{L}dx_{l+1,l}. \quad \text{(B15)}\end{aligned}$$

Now we integrate over p_l and use the property

$$\int_0^a dx\delta(x)=\frac{1}{2}, \quad \text{(B16)}$$

along with results in Eqs. (B13)–(B15) to obtain

$$\begin{aligned}\Sigma^{(\mathrm{RPA},L)}_{ab}(k,\omega)&=i\delta_{ab}\mathrm{sgn}(\omega)\frac{g^2v}{(2\pi)^2}\int_{-\infty}^{\infty}dq\int_0^{|\omega|}dv\\&\quad\times\chi_\theta(q)\left[-c_B\frac{|v|}{|q|}\chi_\theta(q)\right]^L. \quad \text{(B17)}\end{aligned}$$

The net contribution to the quadratic term from all RPA diagrams can be written as

$$\delta S_2=\int\frac{dkd\omega}{(2\pi)^2}dx\,\Sigma^{(\mathrm{RPA})}_{ab}(k,\omega)\circ\psi^*_{a,k}(\omega,x)\psi_{b,k}(\omega,x)\circ, \quad \text{(B18)}$$

where the RPA self-energy is

$$\Sigma^{(\mathrm{RPA})}_{ab}(k,\omega)=\sum_{L=0}^{\infty}\Sigma^{(\mathrm{RPA},L)}_{ab}(k,\omega). \quad \text{(B19)}$$

Here $\Sigma^{(RPA,0)}_{ab}(k,\omega)$ is the Fock term in Eq. (23). After summing over all loops in Eq. (B19) we obtain

$$\begin{aligned}\Sigma^{(\mathrm{RPA})}_{ab}(k,\omega)&=i\delta_{ab}\mathrm{sgn}(\omega)\frac{g^2v}{(2\pi)^2}\int_{-\infty}^{\infty}dq\int_0^{|\omega|}dv\,\chi^{(\mathrm{RPA})}_\theta(q,v)\\&=i\delta_{ab}c_F\mathrm{sgn}(\omega)|\omega|^{2/(1+\theta)}, \quad \text{(B20)}\end{aligned}$$

where $\chi^{(\mathrm{RPA})}_\theta(q,v)$ is given by Eq. (62) and

$$c_F=\frac{g^2v}{2\pi^2}c_B^{\frac{1-\theta}{1+\theta}}\int_0^\infty dy\,y\ln\left(1+\frac{1}{y^{\theta+1}}\right) \quad \text{(B21)}$$

for $\mu=0$. As expected, the quantum corrections removes the spurious IR singularity at $\mu=0$.

APPENDIX C: THE RPA CORRECTION FOR GENERAL SHAPES OF THE LOCAL FERMI SURFACE

In this section we compute the RPA correction to the Wilsonian effective action for the patch theory with a general shape of the local Fermi surface.

1. RPA vertex correction

The four-fermion vertex correction generated from the L-loop RPA diagrams shown in Fig. 14(a) is

$$\begin{aligned}\delta S^{(\mathrm{RPA},L)}_{4,u}&=\int\frac{dk_1d\omega_1dk_2d\omega_2dqdv}{(2\pi)^6}dx_1\exp\left[i\gamma_ux_1\sum_{m=1}^{u-1}\binom{u}{m}(k_1^m-k_2^m)q^{u-m}\right]V_{ij;ln}\chi_\theta(q)\sum_{\alpha=1}^{(L+1)!}\int_{\mathcal{C}_\alpha}\prod_{i=1}^{L}dx_{i+1,i}\\&\times\left[-\frac{g^2}{4\pi^2}\chi_\theta(q)\right]^L\int\prod_{j=1}^{L}\left\{d\omega_jdp_j\exp\left[i\gamma_ux_{j+1,j}\sum_{m=1}^{u-1}\binom{u}{m}(k_1^m-p_j^m)q^{u-m}\right]G_0(\omega_j,-x_{j+1,j})G_0(\omega_j+v,x_{j+1,j})\right\}\\&\times\sum_{m=0}^{\infty}\frac{(x_{(L+1)1})^m}{m!}\circ\psi^*_{i,k_2}(\omega_2,x_1)\psi_{j,k_2+q}(\omega_2+v,x_1)\partial_{x_1}^m\left[\psi^*_{l,k_1+q}(\omega_1+v,x_1)\psi_{n,k_1}(\omega_1,x_1)\right]\circ, \quad \text{(C1)}\end{aligned}$$

where in the last line we have Taylor expanded the local operator $\psi^*_{l,k_1+q}(\omega_1+v,x_{L+1})\psi_{n,k_1}(\omega_1,x_{L+1})$ around x_1. We first compute the leading-order term in the Taylor expansion which renormalizes the marginal four-fermion vertex in the action [Eq. (109)]. Later we comment on the subleading terms in the Taylor expansion.

a. The leading-order term

The leading contribution to the four-fermion vertex from the L-loop RPA diagram is

$$\begin{aligned}\delta S^{(\mathrm{RPA},L)}_{4,u}&=\int\frac{dk_1d\omega_1dk_2d\omega_2dqdv}{(2\pi)^6}dx\;\exp\left[i\gamma_ux\sum_{m=1}^{u-1}\binom{u}{m}(k_1^m-k_2^m)q^{u-m}\right]V_{ij;ln}\chi_\theta(q)\Gamma^{(\mathrm{RPA},L)}_{4,u}(k_1,q,v,X_0)\\&\times\circ\,\psi^*_{i,k_2}(\omega_2,x)\psi_{j,k_2+q}(\omega_2+v,x)\psi^*_{l,k_1+q}(\omega_1+v,x)\psi_{n,k_1}(\omega_1,x)\,\circ, \quad \text{(C2)}\end{aligned}$$

where

$$\Gamma^{(\mathrm{RPA},L)}_{4,u}(k,q,\nu,X_0)=\left[-\frac{g^2}{4\pi^2}\chi_\theta(q)\right]^L\sum_{\alpha=1}^{(L+1)!}\int_{\mathcal{C}_\alpha}\prod_{i=1}^{L}dx_{i+1,i}\prod_{j=1}^{L}\Bigg\{\int d\omega_j dp_j\exp\left[-i\gamma_u x_{j+1,j}\sum_{m=1}^{u-1}\binom{u}{m}(p_j^m-k^m)q^{u-m}\right]$$
$$\times\, G_0(\omega_j,-x_{j+1,j})G_0(\omega_j+\nu,x_{j+1,j})\Bigg\}. \tag{C3}$$

Due to chirality, as discussed in Appendix B, the x coordinates are strictly ordered. Hence, Eq. (C3) factorizes as

$$\Gamma^{(\mathrm{RPA},L)}_{4,u}(k,q,\nu,X_0)=[-\Pi_u(k,q,\nu,X_0)\chi_\theta(q)]^L, \tag{C4}$$

where

$$\Pi_u(k,q,\nu,X_0)=\left(\frac{g^2}{4\pi^2}\right)|\nu|\int_{-\infty}^{\infty}dp\int_0^{X_0}dx_R\exp\left[i\gamma_u\mathrm{sgn}(\nu)x_R\sum_{m=1}^{u-1}\binom{u}{m}(p^m-k^m)q^{u-m}\right]e^{-\eta|x_R||\nu|}. \tag{C5}$$

Unlike the case with $u=2$, $\Pi_u(k,q,\nu,X_0)$ in Eq. (C5) for general $u>2$ depends not only on q but also on one of the external y momentum because k^m cannot be absorbed by p^m in Eq. (C5). This is due to the fact that the inflection point breaks the sliding symmetry along the Fermi surface. By scaling

$$p\mapsto\frac{y}{|u\gamma_u x_R q|^{1/(u-1)}}\quad\text{and}\quad x_R\mapsto X_0 x, \tag{C6}$$

we rewrite Eq. (C5) as

$$\Pi_u(k,q,\nu,X_0)=\left(\frac{g^2}{4\pi^2}\right)X_0^{\frac{u-2}{u-1}}\frac{|\nu|}{|u\gamma_u q|^{1/(u-1)}}\int_0^1\frac{dx}{|x|^{1/(u-1)}}e^{-i\mathrm{sgn}(\nu)\gamma_u X_0 x\sum_{m=1}^{u-1}\binom{u}{m}k^m q^{u-m}}\;e^{-\eta X_0|x||\nu|}h_u[|\gamma_u X_0 q^u x|,\mathrm{sgn}(\gamma_u\nu),\mathrm{sgn}(q)], \tag{C7}$$

where

$$h_u(\alpha_u,s_{\gamma\nu},s_q)=\int_{-\infty}^{\infty}dy\exp\left[is_{\gamma\nu}\sum_{m=1}^{u-1}\binom{u}{m}\frac{\alpha_u^{\frac{u-m-1}{u-1}}s_q^{u-m}}{u^{m/(u-1)}}y^m\right]. \tag{C8}$$

We can further simplify Eq. (C8) by appealing to the parity of the integer u. For even u, we have

$$h_u(\alpha_u,s_{\gamma\nu},s_q)=2\int_0^{\infty}dy\exp\left[is_{\gamma\nu}\sum_{m=1}^{(u-2)/2}\binom{u}{2m}\frac{\alpha_u^{\frac{u-2m-1}{u-1}}}{u^{2m/(u-1)}}y^{2m}\right]\cos\left[y^{u-1}+\sum_{m=1}^{(u-2)/2}\binom{u}{2m-1}\frac{\alpha_u^{\frac{u-2m}{u-1}}}{u^{\frac{2m-1}{u-1}}}y^{2m-1}\right], \tag{C9}$$

and for odd u,

$$h_u(\alpha_u,s_{\gamma\nu},s_q)=2\int_0^{\infty}dy\exp\left[is_{\gamma\nu}s_q\sum_{m=1}^{(u-1)/2}\binom{u}{2m}\frac{\alpha_u^{\frac{u-2m-1}{u-1}}}{u^{2m/(u-1)}}y^{2m}\right]\cos\left[\sum_{m=1}^{(u-1)/2}\binom{u}{2m-1}\frac{\alpha_u^{\frac{u-2m}{u-1}}}{u^{\frac{2m-1}{u-1}}}y^{2m-1}\right]. \tag{C10}$$

To the leading order in $X_0|q|^u\ll 1$, $\Pi_u(k,q,\nu,X_0)$ takes the form

$$\Pi_u(k,q,\nu,X_0)=\left(\frac{g^2}{2\pi^2}\right)X_0^{(u-2)/(u-1)}\frac{|\nu|}{|u\gamma_u q|^{1/(u-1)}}\left\{\xi_u[\mathrm{sgn}(\gamma_u\nu q)]+f_u\left(X_0^{1/u}q,X_0^{1/u}k,\eta X_0|\nu|\right)\right\}, \tag{C11}$$

where ξ_u was defined in Eq. (126). The dimensionless function $f_u(s,t,v)\to 0$ as $s\to 0$ and is regular in the $t,v\to 0$ limit. Therefore, to the leading order in $X_0^{1/u}q$, $X_0^{1/u}k$, and $\eta X_0|\nu|$,

$$\Gamma^{(\mathrm{RPA},L)}_{4,u}(k,q,\nu,X_0)=\left\{-\left(\frac{g^2}{2\pi^2}\right)X_0^{\frac{u-2}{u-1}}\xi_u[\mathrm{sgn}(\nu q)]\frac{|\nu|\chi_\theta(q)}{|u\gamma_u q|^{1/(u-1)}}\right\}^L. \tag{C12}$$

It is of note that $\Gamma^{(L)}_{4,u}$ is independent of k to the leading order in X_0.

The infinite series of the RPA diagrams combined with the bare four-fermion vertex,

$$S_4^{(u,\theta)}=\int\frac{dk_1dk_2dqd\nu d\omega_1d\omega_2}{(2\pi)^6}\int dx\,V_{ij;ln}\chi_\theta(q)\exp\left[i\gamma_u x\sum_{m=1}^{u-1}\binom{u}{m}(k_1^m-k_2^m)q^{u-m}\right]$$
$$\times\,{}^{\circ}_{\circ}\,\psi^*_{i,k_2}(\omega_2,x)\psi_{j,k_2+q}(\omega_2+\nu,x)\psi^*_{l,k_1+q}(\omega_1+\nu,x)\psi_{n,k_1}(\omega_1,x)\,{}^{\circ}_{\circ}\,, \tag{C13}$$

gives the renormalized four-fermion vertex,

$$S_4^{(u,\theta)} + \sum_{L=1}^{\infty} \delta S_{4,u}^{(\mathrm{RPA},L)} = \int \frac{dk_1 d\omega_1 dk_2 d\omega_2 dq d\nu}{(2\pi)^6} dx \exp\left[i\gamma_u x \sum_{m=1}^{u-1} \binom{u}{m} (k_1^m - k_2^m) q^{u-m} \right] V_{ij;ln} \chi_{u,\theta}^{(\mathrm{RPA})}(q,\nu,X_0)$$
$$\times \circ\!\circ \psi_{i,k_2}^*(\omega_2,x)\psi_{j,k_2+q}(\omega_2+\nu,x)\psi_{l,k_1+q}^*(\omega_1+\nu,x)\psi_{n,k_1}(\omega_1,x) \circ\!\circ , \tag{C14}$$

where

$$\chi_{u,\theta}^{(\mathrm{RPA})}(q,\nu,X_0) = \left\{ |q|^\theta + c_B^{(u)}(X_0)\xi_u[\mathrm{sgn}(\gamma_u \nu q)] \frac{|\nu|}{|q|^{1/(u-1)}} \right\}^{-1}, \tag{C15}$$

with

$$c_B^{(u)}(X_0) = \left(\frac{g^2}{2\pi^2} \right) \frac{X_0^{(u-2)/(u-1)}}{|u\gamma_u|^{1/(u-1)}}. \tag{C16}$$

b. The subleading terms

Now we consider the subleading terms with $m > 0$ in Eq. (C1). As we discussed in the main text, for $u = 2$ all the relative coordinates between vertices in the RPA diagrams are fixed by the δ-functions arising from the fermion loops. As a result, the terms with $m > 0$ in Eq. (C1) are absent for $u = 2$. For $u > 2$ the fermion loops do not produce δ-functions. Consequently, one has to consider the full gradient expansion in Eq. (C1). In this section, we show that the gradient expansion is well defined when external momenta are small with fixed X_0. This is less trivial than it naively looks because the two vertices at the end of the L-loop RPA chains can be as far as LX_0. Since L can be arbitrarily large, one has to show that the contribution from large L is small.

The coefficient of the m derivative term, $\psi^*\psi\partial^m[\psi^*\psi]$ in Eq. (C1) is at most

$$\tilde{C}_{m,L} = \frac{(L\tilde{X}_0)^m}{m!} \tilde{X}_0^{\frac{u-2}{u-1}L}, \tag{C17}$$

where $\tilde{X}_0 \sim X_0|q|^u, X_0 q_x, X_0\omega^{1/z}$ are small dimensionless parameters associated with external momentum or frequency (q, q_x, ω) measured in the unit of X_0^{-1} (q refers to y momentum). Here we used the fact that $x_{(L+1)1} \leqslant LX_0$ and the fact that each fermion loop contributes a factor of $X_0^{(u-2)/(u-1)}$. The question is how $\tilde{C}_{m,L}$ behaves in the large m and L limit with a fixed value of $\tilde{X}_0 \ll 1$.

From Eq. (C17) it is obvious that at fixed m, $\tilde{C}_{m,L}$ is exponentially suppressed as a function of L because of the exponential suppression in $\tilde{X}_0^{\frac{u-2}{u-1}L}$. In order to understand the behavior of $\tilde{C}_{m,L}$ in the large m limit, we consider the logarithm of $\tilde{C}_{m,L}$,

$$\ln \tilde{C}_{m,L} = -\ln m! - \left(m + \frac{u-2}{u-1} L \right) \ln\left(\tilde{X}_0^{-1}\right) + m \ln L \tag{C18}$$
$$\approx -L\left(\frac{u-2}{u-1} \ln\left(\tilde{X}_0^{-1}\right) + \left(\frac{m}{L}\right)\left\{ \left[\ln\left(\tilde{X}_0^{-1}\right) - 1 \right] + \ln\left(\frac{m}{L}\right) \right\} \right). \tag{C19}$$

Since $\tilde{X}_0^{-1} \gg 1$ and $x \ln x$ is bounded from below, the expression within the square brackets in Eq. (C19) is positive definite for any $(m/L) \in [0,\infty)$. Consequently, $\tilde{C}_{m,L}$ is exponentially suppressed as a function of m when $m \gg 1$. This shows that both in the large m and large L limits $\tilde{C}_{m,L} \ll 1$. Therefore, the derivative terms with $m > 0$ in the Taylor expansion in Eq. (C1) are suppressed compared to the leading term at the low-momentum/frequency limit with fixed X_0.

2. RPA self-energy

Here we compute the contributions of the RPA diagrams to the quadratic action. The procedure is identical to the one used in Appendix B2.

The self-energy generated from the L-loop RPA diagrams is

$$\delta S_2^{(\mathrm{RPA},L)} = \int \frac{dk d\omega}{(2\pi)^2} dx_1 \; \Sigma_{ab}^{(\mathrm{RPA},L)}(k,\omega,X_0) \circ\!\circ \psi_{a,k}^*(\omega,x_1)\psi_{b,k}(\omega,x_1) \circ\!\circ , \tag{C20}$$

where

$$\Sigma_{ab}^{(\mathrm{RPA},L)}(k,\omega,X_0) = 2^{L+1} V_{al_1;j_1 i_1} V_{i_1 j_1; j_2 i_2} \cdots V_{i_L j_L; l_1 b} \int \frac{dq d\nu}{(2\pi)^2} [\chi_\theta(q)]^{L+1} \int_{\mathcal{C}} \prod_{l=1}^{L} [dx_{l+1,l}] G_0(\omega+\nu, -x_{L+1,1})$$
$$\times \prod_{l=1}^{L} \left[\int \frac{dp_l d\nu_l}{(2\pi)^2} G_0(\nu_l, -x_{l+1,l}) G_0(\nu_l+\nu, x_{l+1,l}) e^{i\gamma_u x_{l+1,l} \sum_{m=1}^{u-1} \binom{u}{m} (k^m - p_l^m) q^{u-m}} \right]. \tag{C21}$$

Note that Eq. (C20) is the leading term in the gradient expansion. The terms with derivatives are dropped because they are irrelevant at low momentum as discussed in Appendix C 1 b. Integrating over ν_l in Eq. (C21) and using the constraints imposed by the Θ functions in Eq. (C21), we obtain

$$\Sigma^{(\mathrm{RPA},L)}_{ab}(k,\omega,X_0) = i\delta_{ab}\frac{g^2 v}{(2\pi)^2}\int dq\,\chi_\theta(q)\int d\nu[\Theta(-\nu)\Theta(\omega+\nu)-\Theta(\nu)\Theta(-\omega-\nu)][-\tilde{\Pi}_u(k,q,\omega,\nu,X_0)\chi_\theta(q)]^L \tag{C22}$$

$$= i\delta_{ab}\frac{g^2 v}{(2\pi)^2}\int dq\,\chi_\theta(q)\int_0^{|\omega|} d\nu\{\Theta(\omega)[-\tilde{\Pi}_u(k,q,\omega,-\nu,X_0)\chi_\theta(q)]^L-\Theta(-\omega)[-\tilde{\Pi}_u(k,q,\omega,\nu,X_0)\chi_\theta(q)]^L\}, \tag{C23}$$

where

$$\tilde{\Pi}_u(k,q,\omega,\nu,X_0) = \left(\frac{g^2}{4\pi^2}\right)|\nu|\int_{-\infty}^{\infty}dp\int_0^{X_0}dx_R\exp\left[i\gamma_u\mathrm{sgn}(\nu)x_R\sum_{m=1}^{u-1}\binom{u}{m}(p^m-k^m)q^{u-m}\right]e^{-\eta|x_R||\omega|}. \tag{C24}$$

Note that $\tilde{\Pi}_u$ differs from Π_u defined in Eq. (C5) because of the different frequency dependence of the exponential damping factor.

We write the contribution from the Fock diagram in Eq. (23), which is valid for all u, as

$$S_2' = i\delta_{ab}\frac{g^2 v}{(2\pi)^2}\int\frac{dkd\omega}{(2\pi)^2}dx_1\int dq\,\chi_\theta(q)\int_0^{|\omega|}d\nu[\Theta(\omega)-\Theta(-\omega)]\,{}^{\circ}_{\circ}\,\psi^*_{a,k}(\omega,x_1)\psi_{b,k}(\omega,x_1)\,{}^{\circ}_{\circ}\,. \tag{C25}$$

To the Fock diagram we add the contributions $\delta S_2^{(\mathrm{RPA},L)}$ from $L=1$ to $L=\infty$ to obtain the RPA self-energy,

$$\Sigma^{(\mathrm{RPA})}_{ab}(k,\omega,X_0) = i\delta_{ab}\frac{g^2 v}{(2\pi)^2}\int dq\int_0^{|\omega|}d\nu[\Theta(\omega)\tilde{\chi}_{u,\theta}(k,q,\omega,-\nu,X_0)-\Theta(-\omega)\tilde{\chi}_{u,\theta}(k,q,\omega,\nu,X_0)], \tag{C26}$$

where

$$\tilde{\chi}_{u,\theta}(k,q,\omega,\nu,X_0) = \frac{1}{|q|^\theta+\tilde{\Pi}_u(k,q,\omega,\nu,X_0)}. \tag{C27}$$

As in the case of Π_u in Eq. (C11), to the leading order in $X_0|q|^u$, we have

$$\tilde{\Pi}_u(k,q,\omega,\nu,X_0) = c_B^{(u)}(X_0)\xi[\mathrm{sgn}(\gamma_u q\nu)]\frac{|\nu|}{|q|^{1/(u-1)}}. \tag{C28}$$

Accordingly, the renormalized vertex becomes

$$\chi^{(\mathrm{RPA})}_{u,\theta}(q,\nu,X_0) = \frac{1}{|q|^\theta+c_B^u(X_0)\xi[\mathrm{sgn}(\gamma_u q\nu)]\frac{|\nu|}{|q|^{1/(u-1)}}} \tag{C29}$$

to the leading order. Using Eq. (C29) in Eq. (C26), we obtain the leading-order contribution to the self-energy,

$$\Sigma^{(\mathrm{RPA})}_{ab}(k,\omega,X_0) = i\delta_{ab}\frac{g^2 v}{(2\pi)^2}\mathrm{sgn}(\omega)\int dq\int_0^{|\omega|}d\nu\,\chi^{(\mathrm{RPA})}_{u,\theta}(q,\nu,X_0) \tag{C30}$$

$$= i\delta_{ab}c_F^{(u)}(X_0)\mathrm{sgn}(\omega)|\omega|^{\frac{u}{u(\theta-1)+1}}. \tag{C31}$$

Here $c_F^{(u)}(X_0)$ is a constant given by

$$c_F^{(u)}(X_0) = \frac{g^2 v}{4\pi^2}\left[c_B^{(u)}(X_0)\right]^{\frac{(u-1)(1-\theta)}{\theta(u-1)+1}}\int_0^1 dt\int_{-\infty}^{\infty}dy\frac{|y|^{1/(u-1)}}{|y|^{\frac{\theta(u-1)+1}{u-1}}+\xi_u[\mathrm{sgn}(\gamma_u yt)]|t|}. \tag{C32}$$

Note that $c_F^{(u)}(X_0)$ depends on X_0 through $c_B^{(u)}(X_0)$. Since $c_B^{(u)}(X_0)\propto X_0^{(u-2)/(u-1)}$, we have

$$c_F^{(u)}(X_0)\propto X_0^{\frac{(u-2)(1-\theta)}{\theta(u-1)+1}}. \tag{C33}$$

3. Inversion symmetry along the y direction in the patch description

In this section we show that the theory of the full Fermi surface respects the inversion symmetry along the y direction as it should be although a single patch theory breaks the symmetry for odd u. The effective action for even u in Eq. (123) is manifestly invariant under reversing y momenta : $q\to -q$, $k_i\to -k_i$. For odd u, the symmetry is less obvious because the four-fermion vertex includes an imaginary components in ξ_u, which is odd under $q\to -q$ transformation as shown in Eq. (126). In order to see the symmetry of the full theory, one has to include the other patch connected by the inversion.

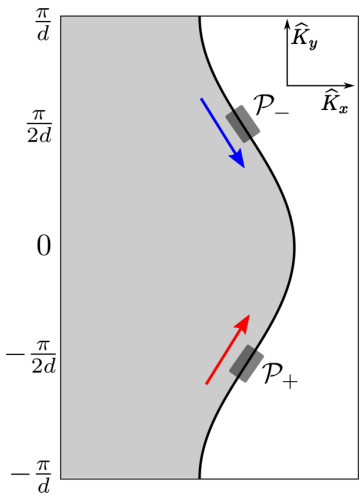

FIG. 25. (Color online) Under the inversion along the y direction the two patches are exchanged. Momentum defined away from the inversion points in each patch are also exchanged. For example, a particle-hole pair denoted as an arrow in patch $\mathcal{P}_+$ is mapped to the other arrow in patch $\mathcal{P}_-$.

This is necessary even though the two patches are, in general, decoupled at low energies because they have different tangent vectors.

The inversion symmetry of the full Fermi surface guarantees that the inflection points with odd u arise in pairs. For example, there is a pair of inflection points with $u = 3$ in generic chiral Fermi surfaces as shown in Fig. 25. Suppose that the local dispersions near a pair of such inflection points are given by

$$\epsilon_k^{(\sigma)} = k_x + \gamma_\sigma k_y^u, \tag{C34}$$

where $\vec{k}$ measures the deviation of momenta away from the inflection points, $\sigma = +,-$ and $\gamma_+ = -\gamma_-$, where $\gamma_+ > 0$. The fermion field in each local patch is related to the original field through

$$\psi_i^{(\sigma)}(\omega,k_x,k_y) \equiv \psi_i(\omega,k_x,-\sigma K_y^* + k_y), \tag{C35}$$

where we assume that the inflection points are at $(K_x,K_y) = (0,\pm K_y^*)$. Under the inversion of the y component of momentum, the original field transforms as

$$\psi_i(\omega,k_x,-K_y^*+k_y) \mapsto \psi_i(\omega,k_x,K_y^*-k_y). \tag{C36}$$

Therefore, the inversion exchanges $\psi^{(+)}$ and $\psi^{(-)}$ as

$$\psi_i^{(\sigma)}(\omega,k_x,k_y) \mapsto \psi_i^{(-\sigma)}(\omega,k_x,-k_y). \tag{C37}$$

In the mixed-space representation, the effective action for the two patches is given by

$$S_{X_0}^{(u,\theta)} = \sum_{\sigma=\pm}\int dx\Big[\int \frac{dkd\omega}{(2\pi)^2}\mathcal{L}_2^{(u,\theta,\sigma)}(x,k,\omega,X_0) + \int \frac{dk_1dk_2dqd\omega_1d\omega_2d\nu}{(2\pi)^6} \times \mathcal{L}_4^{(u,\theta,\sigma)}(x,k_1,k_2,q,\omega_1,\omega_2,\nu,X_0)\Big], \tag{C38}$$

where

$$\mathcal{L}_2^{(u,\theta,\sigma)}(x,k,\omega,X_0) = \psi_{i,k}^{(\sigma)*}(\omega,x)\big[ic_F^{(u)}(X_0)\mathrm{sgn}(\omega)|\omega|^{\frac{u}{\theta(u-1)+1}} - i\partial_x\big]\psi_{i,k}^{(\sigma)}(\omega,x), \tag{C39}$$

$$\mathcal{L}_4^{(u,\theta,\sigma)}(x,k_1,k_2,q,\omega_1,\omega_2,\nu,X_0) = V_{ij;ln}\chi_{u,\theta}^{\mathrm{RPA}(\sigma)}(q,\nu,X_0) \times \exp\left[i\gamma_\sigma x\sum_{m=1}^{u-1}\binom{u}{m}\big(k_1^m-k_2^m\big)q^{u-m}\right]\psi_{i,k_2}^{(\sigma)*}(\omega_2,x) \times\psi_{j,k_2+q}^{(\sigma)}(\omega_2+\nu,x)\psi_{l,k_1+q}^{(\sigma)*}(\omega_1+\nu,x)\psi_{n,k_1}^{(\sigma)}(\omega_1,x), \tag{C40}$$

with

$$\chi_{u,\theta}^{\mathrm{RPA}(\sigma)}(q,\nu,X_0) = \left\{|q|^\theta + c_B^{(u)}(X_0)\xi_u[\mathrm{sgn}(\gamma_\sigma\nu q)]\frac{|\nu|}{|q|^{1/(u-1)}}\right\}^{-1}. \tag{C41}$$

It is now easy to check that $S_{X_0}^{(u,\theta)}$ is invariant under inversion of the y component of momenta because

$$\chi_{u,\theta}^{\mathrm{RPA}(-\sigma)}(-q,\nu,X_0) = \chi_{u,\theta}^{\mathrm{RPA}(\sigma)}(q,\nu,X_0). \tag{C42}$$

[1] L. Landau, Sov. Phys. JETP **3**, 920 (1957).
[2] J. Polchinski, in *Proceedings of the 1992 TASI*, edited by J. Harvey and J. Polchinski (World Scientific, Singapore, 1993).
[3] R. Shankar, Rev. Mod. Phys. **66**, 129 (1994).
[4] T. Holstein, R. E. Norton, and P. Pincus, Phys. Rev. B **8**, 2649 (1973).
[5] M. Y. Reizer, Phys. Rev. B **40**, 11571 (1989).
[6] P. A. Lee, Phys. Rev. Lett. **63**, 680 (1989).
[7] P. A. Lee and N. Nagaosa, Phys. Rev. B **46**, 5621 (1992).
[8] B. I. Halperin, P. A. Lee, and N. Read, Phys. Rev. B **47**, 7312 (1993).
[9] B. L. Altshuler, L. B. Ioffe, and A. J. Millis, Phys. Rev. B **50**, 14048 (1994).
[10] J. Polchinski, Nucl. Phys. B **422**, 617 (1994).
[11] Y. B. Kim, A. Furusaki, X.-G. Wen, and P. A. Lee, Phys. Rev. B **50**, 17917 (1994).
[12] Ar. Abanov and A. V. Chubukov, Phys. Rev. Lett. **84**, 5608 (2000); **93**, 255702 (2004).
[13] O. I. Motrunich and M. P. A. Fisher, Phys. Rev. B **75**, 235116 (2007).
[14] H. v. Lohneysen, A. Rosch, M. Vojta, and P. Wölfle, Rev. Mod. Phys. **79**, 1015 (2007)
[15] P. Coleman, in *The Handbook of Magnetism and Advanced Magnetic Materials*, edited by Helmut Kronmuller and Stuart Parkin (Wiley & Sons, New York, 2007), Vol. 1, pp. 95–148.
[16] T. Senthil, Phys. Rev. B **78**, 045109 (2008).

[17] D. Podolsky, A. Paramekanti, Y. B. Kim, and T. Senthil, Phys. Rev. Lett. **102**, 186401 (2009).

[18] V. Oganesyan, S. A. Kivelson, and E. Fradkin, Phys. Rev. B **64**, 195109 (2001).

[19] W. Metzner, D. Rohe, and S. Andergassen, Phys. Rev. Lett. **91**, 066402 (2003)

[20] L. Dell'Anna and W. Metzner, Phys. Rev. B **73**, 045127 (2006); Phys. Rev. Lett. **98**, 136402 (2007).

[21] H.-Y. Kee, E. H. Kim, and C.-H. Chung, Phys. Rev. B **68**, 245109 (2003).

[22] M. J. Lawler, D. G. Barci, V. Fernandez, E. Fradkin, and L. Oxman, Phys. Rev. B **73**, 085101 (2006); M. J. Lawler and E. Fradkin, *ibid.* **75**, 033304 (2007).

[23] J. Rech, C. Pepin, and A. V. Chubukov, Phys. Rev. B **74**, 195126 (2006).

[24] P. Wolfe and A. Rosch, J. Low Temp. Phys. **147**, 165 (2007).

[25] D. L. Maslov and A. V. Chubukov, Phys. Rev. B **81**, 045110 (2010).

[26] J. Quintanilla and A. J. Schofield, Phys. Rev. B **74**, 115126 (2006).

[27] H. Yamase and H. Kohno, J. Phys. Soc. Jpn. **69**, 2151 (2000).

[28] H. Yamase, V. Oganesyan, and W. Metzner, Phys. Rev. B **72**, 035114 (2005).

[29] C. J. Halboth and W. Metzner, Phys. Rev. Lett. **85**, 5162 (2000).

[30] P. Jakubczyk, P. Strack, A. A. Katanin, and W. Metzner, Phys. Rev. B **77**, 195120 (2008).

[31] M. Zacharias, P. Wölfle, and M. Garst, Phys. Rev. B **80**, 165116 (2009).

[32] E.-A. Kim, M. J. Lawler, P. Oreto, S. Sachdev, E. Fradkin, and S. A. Kivelson, Phys. Rev. B **77**, 184514 (2008).

[33] Y. Huh and S. Sachdev, Phys. Rev. B **78**, 064512 (2008).

[34] O. I. Motrunich, Phys. Rev. B **72**, 045105 (2005).

[35] S.-S. Lee and P. A. Lee, Phys. Rev. Lett. **95**, 036403 (2005).

[36] P. A. Lee, N. Nagaosa, and X.-G. Wen, Rev. Mod. Phys. **78**, 17 (2006), and references therein.

[37] S.-S. Lee, Phys. Rev. B **80**, 165102 (2009).

[38] M. A. Metlitski and S. Sachdev, Phys. Rev. B **82**, 075127 (2010); **82**, 075128 (2010).

[39] H.-C. Jiang, M. S. Block, R. V. Mishmash, J. R. Garrison, D. N. Sheng, O. I. Motrunich, and M. P. A. Fisher, Nature (London) **493**, 39 (2013).

[40] C. Nayak and F. Wilczek, Nucl. Phys. B **430**, 534 (1994).

[41] D. F. Mross, J. McGreevy, H. Liu, and T. Senthil, Phys. Rev. B **82**, 045121 (2010).

[42] D. Dalidovich and S.-S. Lee, Phys. Rev. B **88**, 245106 (2013).

[43] A. L. Fitzpatrick, S. Kachru, J. Kaplan, and S. Raghu, Phys. Rev. B **88**, 125116 (2013).

[44] X.-G. Wen, Phys. Rev. B **41**, 12838 (1990).

[45] L. Balents and M. P. A. Fisher, Phys. Rev. Lett. **76**, 2782 (1996).

[46] For example, see M. R. Douglas and N. A. Nekrasov, Rev. Mod. Phys. **73**, 977 (2001); R. J. Szabo, Phys. Rep. **378**, 207 (2003).

[47] S. Minwalla, M. V. Raamsdonk, and N. Seiberg, J. High Energy Phys. 02 (2000) 020.

[48] J. Polchinski, *String Theory* (Cambridge University Press, Cambridge, UK, 1998), Vol. 1.

[49] J. Cardy, *Scaling and Renormalization in Statistical Physics* (Cambridge University Press, Cambridge, UK, 1996).

[50] T. Senthil, Phys. Rev. B **78**, 035103 (2008).

[51] S.-S. Lee, Phys. Rev. B **78**, 085129 (2008).

[52] F. R. Klinkhamer and G. E. Volovik, Int. J. Mod. Phys. A **20**, 2795 (2005).

[53] X. Wan, A. M. Turner, A. Vishwanath, and S. Y. Savrasov, Phys. Rev. B **83**, 205101 (2011).

[54] K.-Y. Yang, Y.-M. Lu, and Y. Ran, Phys. Rev. B **84**, 075129 (2011).

[55] A. A. Burkov and L. Balents, Phys. Rev. Lett. **107**, 127205 (2011).

CHAPTER 5

CONCLUSION AND OUTLOOK

In this thesis we studied the low energy scaling properties of critical points that arise at symmetry breaking, continuous phase transitions in metals with extended Fermi surfaces. The $\vec{Q}_{ord} = 0$ state is unique, since it is the only NFL state in two dimensions whose exact scaling properties are known. The NFL states arising at the $\vec{Q}_{ord} \neq 0$ transitions are amongst the first examples of their kind, whose critical exponents are obtained within a controlled computation.

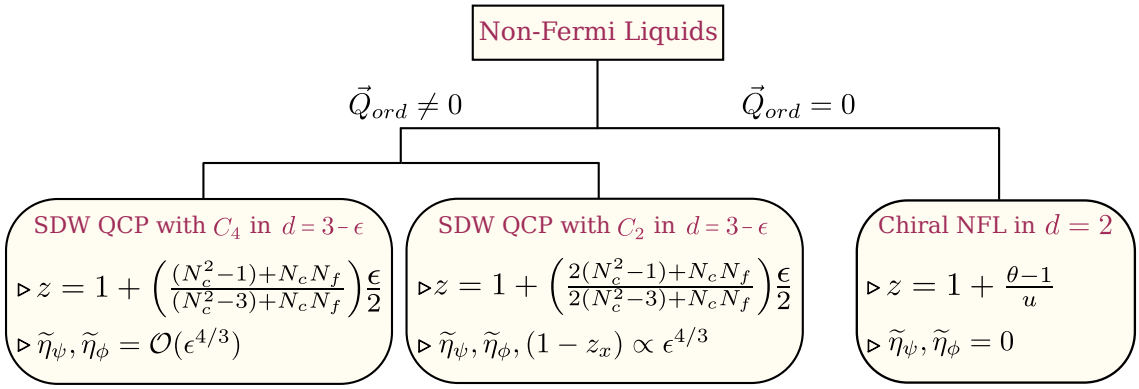

Figure 5.1: The three classes of NFLs studied in this thesis. Here we distinguish them by the momentum carried by the order parameter, and the critical exponents. (from left to right) The parameters are defined in Chapters 2, 3 and 4, respectively.

Different types of NFL states that emerge at metallic QCPs in two and higher dimensions

can be classified according to,

- the symmetry groups,
- local curvature of the Fermi surface,
- dispersion of the boson,
- number of spatial dimensions,
- dimension (or equivalently codimensions) of the Fermi surface.

In Fig. 5.1 we summarize the critical exponents for the three examples of NFL.

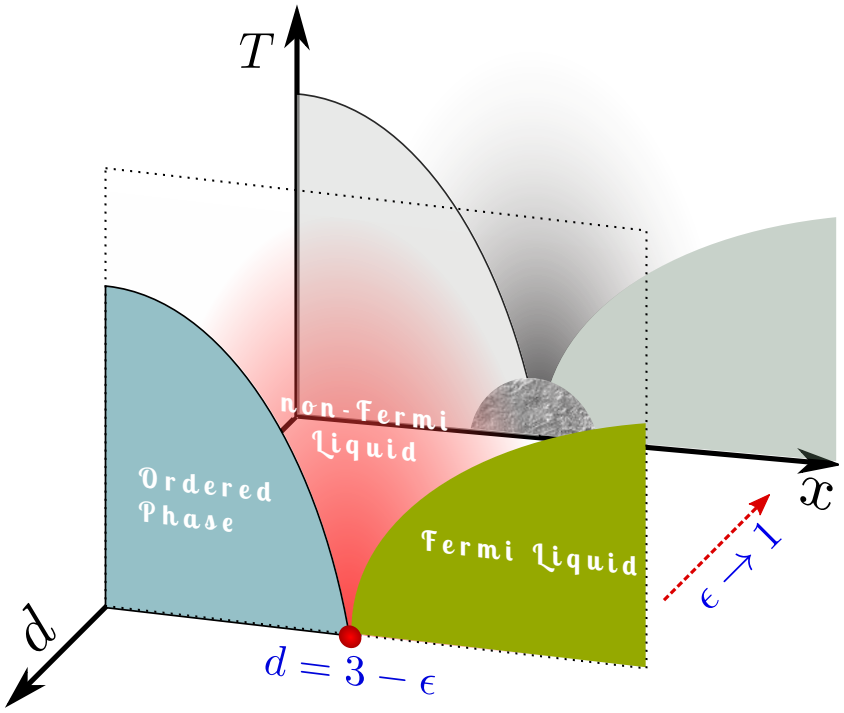

Figure 5.2: Full phase diagram for SDW criticality. Here x, T, and d represent non-thermal tuning parameter, temperature and spatial dimensions, respectively. We have uncovered stable NFL phases close to three dimensions where $\varepsilon \ll 1$. The stability implies a naked QCP. However, in two dimensional systems a dome, representing an additional ordered state, hides the QCP. An important future research direction is to study the implication of our analysis as $\varepsilon \to 1$.

Although we have obtained a few controlled examples of NFL fixed points at metallic QCPs by studying their scaling behavior, there are still many open questions. Some of the less understood aspects are listed below:

- Although, the critical theories for the SDW critical points flow to stable fixed points near the upper critical dimension, the putative QCPs can be unstable in two space dimensions. As the dimension is tuned towards two an instability may develop below a certain dimension. Indeed we observed enhancements of several pairing and CDW susceptibilities in Chapter 2. It is thus of great interest to understand whether the two dimensional NFL is unstable, and if so, what is the leading instability (Fig. 5.2).

- In a recent work, Hartnoll, *et al.* [73] showed that the incoherent hotspot electrons alone are unable to produce the experimentally observed transport properties in the quantum critical region of the phase diagrams of the SDW critical points. Further, the authors suggested that scattering of the SDW fluctuations with electrons away from the hot-spots (*lukewarm* electrons) may be strong enough to produce NFL response in two dimensions. Interestingly, within a perturbative framework, the interaction between lukewarm electrons and the SDW fluctuations weakens with decreasing energy as we deduced in Chapters 2 and 3. However, it is possible that as the spatial dimension of the model gets closer to two, certain operators that were irrelevant near three dimensions become marginal or relevant near two dimensions. This would introduce qualitatively new features to the low energy physics. Given this dichotomy, which exists within perturbative approaches to the problem, it is interesting to investigate whether and how the interactions between the lukewarm electrons and the SDW fluctuations become important at low energy. Finding a controlled way to answer these questions is of general significance to the physics of antiferromagnetic quantum critical points.

- As we deduced in Chapter 3, metals most likely do not undergo a continuous transition into commensurate CDW states below three dimensions. One of the possibilities is a continuous transition into an incommensurate CDW state. However, the current formulation of the (co)dimensional regularization scheme does not allow us to study QCPs arising at incommensurate density wave transitions of metals, because the $2\vec{K}_F$

CDW, that is required to push the two dimensional theory to three dimensions, pins the sliding mode of the incommensurate density wave. Therefore, a suitable generalization of the dimensional regularization scheme will open up a number of important QCPs for controlled perturbative analyses, including the study of competing density wave orderings in metals.

As the thesis reaches its conclusion, in Fig. 5.3, we summarize the progress made in the study of non-Fermi liquids over the last 42 years, since its theoretical discovery in 1973.

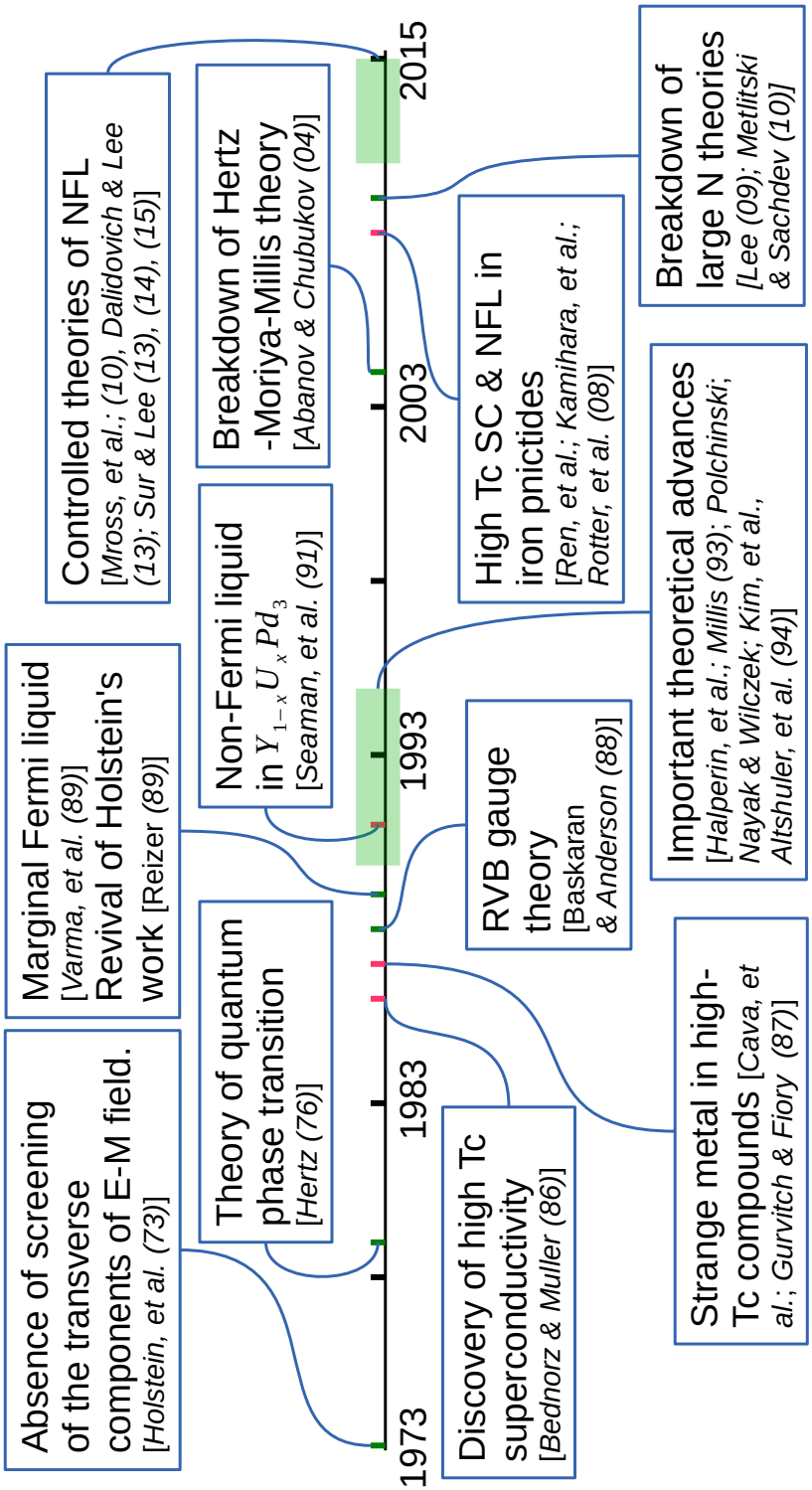

Figure 5.3: A historical timeline highlighting selected developments in the field of non-Fermi liquids since its first theoretical discovery 42 years back! The shaded regions represent periods of theoretical advances that have led to significant improvements in the understanding of NFL states. The green (red) ticks represent theoretical (experimental) advances.

BIBLIOGRAPHY

[1] T. Andrews, Phil. Trans. R. Soc. Lond. **159**, 575 (1869).

[2] J. W. Gibbs, Transactions of the Connecticut Academy of Sciences **2**, 382 (1873).

[3] J. D. van der Waals, Ph.D. thesis, University of Leiden (1873).

[4] P. Weiss, J. Phys. Radium (Paris) **6**, 667 (1907).

[5] L. D. Landau, Phys. Z. Sowjun. **11**, 26 (1937).

[6] L. D. Landau, Zh. Eksp. Teor. Fiz. **7**, 19 (1937).

[7] C. Domb, *The Critical Point* (Taylor & Francis (London), 1996).

[8] N. Goldenfeld, *Lecture on Phase Transitions and the Renormalization Group* (Levant Books (Kolkata), 2005).

[9] A. P. Levanyuk, Sov. Phys. JETP **36**, 571 (1959).

[10] V. L. Ginzburg, Sov. Phys. Sol. State **2**, 1824 (1960).

[11] L. P. Kadanoff, Physics **2**, 263 (1966).

[12] K. G. Wilson, Phys. Rev. B **4**, 3174 (1971).

[13] K. G. Wilson, Phys. Rev. B **4**, 3184 (1971).

[14] T. Senthil, A. Vishwanath, L. Balents, S. Sachdev, and M. P. A. Fisher, Science **303**, 1490 (2004).

[15] R. K. Kaul, A. Kolezhuk, M. Levin, S. Sachdev, and T. Senthil, Phys. Rev. B **75**, 235122 (2007).

[16] M. Suzuki, Progr. Theor. Phys. **56**, 1454 (1976).

[17] M. T. Beal-Monod, Solid State Commun. **14**, 677 (1974).

[18] J. A. Hertz, Phys. Rev. B **14**, 1165 (1976).

[19] S. Sachdev, *Quantum Phase Transitions* (Cambridge University Press (Cambridge), 2011), 2nd ed.

[20] L. Savary, E.-G. Moon, and L. Balents, Phys. Rev. X **4**, 041027 (2014).

[21] L. D. Landau, Sov. Phys. JETP **3**, 920 (1957).

[22] L. D. Landau, Sov. Phys. JETP **5**, 101 (1957).

[23] C. M. Varma, Z. Nussinov, and W. van Sarloos, Physics Reports **361**, 267 (2002).

[24] A. J. Schofield, Contemporary Physics **40**, 95 (1999).

[25] A. A. Abrikosov, L. P. Gorkov, and I. E. Dzyaloshinski, *Methods of Quantum Field Theory in Statistical Physics* (Dover Publications, 1975).

[26] R. Shankar, Rev. Mod. Phys. **66**, 129 (1994).

[27] J. Polchinski, Proceedings of the 1992 TASI (World Scientific, Singapore, 1993) [arXiv:hep-th/9210046] (1993).

[28] J. Bardeen, L. N. Cooper, and J. R. Schrieffer, Phys. Rev. **106**, 162 (1957).

[29] J. Bardeen, L. N. Cooper, and J. R. Schrieffer, Phys. Rev. **108**, 1175 (1957).

[30] G. Baym and C. Pethick, *Landau Fermi-Liquid Theory* (John Wiley & Sons Inc., 1991).

[31] S. Tomonaga, Progress in Theoretical Physics **5**, 544 (1950).

[32] J. M. Luttinger, Journal of Mathematical Physics **4**, 1154 (1963).

[33] D. C. Mattis and E. H. Lieb, Journal of Mathematical Physics **6**, 304 (1965).

[34] F. D. M. Haldane, J. Phys. C: Solid State Phys. **14**, 2585 (1981).

[35] T. Holstein, R. E. Norton, and P. Pincus, Phys. Rev. B **8**, 2649 (1973).

[36] J. G. Bednorz and K. A. Müller, Z. Physik B **64**, 189 (1986).

[37] R. J. Cava, B. Batlogg, R. B. van Dover, D. W. Murphy, S. Sunshine, T. Siegrist, J. P. Remeika, E. A. Rietman, S. Zahurak, and G. P. Espinosa, Phys. Rev. Lett. **58**, 1676 (1987).

[38] M. Gurvitch and A. T. Fiory, Phys. Rev. Lett. **59**, 1337 (1987).

[39] C. L. Seaman, M. B. Maple, B. W. Lee, S. Ghamaty, M. S. Torikachvili, J.-S. Kang, L. Z. Liu, J. W. Allen, and D. L. Cox, Phys. Rev. Lett. **67**, 2882 (1991).

[40] Z.-A. Ren, W. Lu, J. Yang, W. Yi, X.-L. Shen, Z.-C. Li, G.-C. Che, X.-L. Dong, L.-L. Sun, F. Zhou, et al., Chin. Phys. Lett. **25**, 2215 (2008).

[41] Y. Kamihara, T. Watanabe, M. Hirano, and H. Hosono, J. Am. Chem. Soc. **130**, 3296 (2008).

[42] M. Rotter, M. Tegel, and D. Johrendt, Phys. Rev. Lett. **101**, 107006 (2008).

[43] M. Y. Reizer, Phys. Rev. B **40**, 11571 (1989).

[44] P. A. Lee and N. Nagaosaa, Phys. Rev. B **46**, 5621 (1992).

[45] B. L. Altshuler, L. B. Ioffe, and A. J. Millis, Phys. Rev. B **50**, 14048 (1994).

[46] J. Polchinski, Nucl. Phys. B **422**, 617 (1994).

[47] B. I. Halperin, P. A. Lee, and N. Read, Phys. Rev. B **47**, 7312 (1993).

[48] C. Nayak and F. Wilczek, Nucl. Phys. B **430**, 534 (1994).

[49] P. A. Lee, N. Nagaosa, and X.-G. Wen, Rev. Mod. Phys. **78**, 17 (2006).

[50] H. Watanabe and A. Vishwanath, PNAS **111**, 16314 (2014).

[51] Y. B. Kim, A. Furusaki, X.-G. Wen, and P. A. Lee, Phys. Rev. B **50**, 17917 (1994).

[52] S.-S. Lee, Phys. Rev. B **80**, 165102 (2009).

[53] M. A. Metlitski and S. Sachdev, Phys. Rev. B **82**, 075127 (2010).

[54] M. A. Metlitski and S. Sachdev, Phys. Rev. B **82**, 075128 (2010).

[55] C. Nayak and F. Wilczek, Nucl. Phys. B **417**, 359 (1994).

[56] D. F. Mross, J. McGreevy, H. Liu, and T. Senthil, Phys. Rev. B **82**, 045121 (2010).

[57] T. Holder and W. Metzner, arXiv:1503.05089 (2015).

[58] D. Dalidovich and S.-S. Lee, Phys. Rev. B **88**, 245106 (2013).

[59] C. M. Varma, P. B. Littlewood, S. Schmitt-Rink, E. Abrahams, and A. E. Ruckenstein, Phys. Rev. Lett. **63**, 1996 (1989).

[60] Q. Si and E. Abrahams, Phys. Rev. Lett. **101**, 076401 (2008).

[61] L. de' Medici, G. Giovannetti, , and M. Capone, Phys. Rev. Lett. **112**, 177001 (2014).

[62] A. V. Chubukov, D. V. Efremov, and I. Eremin, Phys. Rev. B **78**, 134512 (2008).

[63] S. Chakravarty, R. E. Norton, and O. F. Syljuåsen, Phys. Rev. Lett. **74**, 1423 (1995).

[64] A. L. Fitzpatrick, S. Kachru, J. Kaplan, and S. Raghu, Phys. Rev. B **88**, 125116 (2013).

[65] T. Senthil and R. Shankar, Phys. Rev. Lett. **102**, 046406 (2009).

[66] A. V. Chubukov, Europhys. Lett. **44**, 655 (1998).

[67] A. Abanov and A. V. Chubukov, Phys. Rev. Lett. **84**, 5608 (2000).

[68] P. Dai, J. Hu, and E. Dagotto, Nature Physics **8**, 709 (2012).

[69] I. Mandal and S.-S. Lee, arXiv:1407.0033 (2014).

[70] S.-S. Lee, Phys. Rev. B **78**, 085129 (2008).

[71] L. Balents and M. P. A. Fisher, Phys. Rev. Lett. **76**, 2782 (1996).

[72] X.-G. Wen, Phys. Rev. B **41**, 12838 (1990).

[73] S. A. Hartnoll, D. M. Hofman, M. A. Metlitski, and S. Sachdev, Phys. Rev. B **84**, 125115 (2011).